ISSN 1694-7398
journals.manas.edu.kg

JUNE 2022
Volume 10, Issue 1

# MANAS JOURNAL OF ENGINEERING

## MJEN

BISHKEK 2022

KYRGYZ TURKISH MANAS UNIVERSITY
MANAS JOURNAL OF ENGINEERING (MJEN)

ISSN: 1694- 7398
Year: 2021
Volume: 10
Special Issue: 1
http://journals.manas.edu.kg
journals@manas.edu.kg

**PUBLICATION PERIOD**

Manas Journal of Engineering (MJEN) is published twice year, MJEN is a peer reviewed journal.



CORRESPONDENCE ADDRESS
Kyrgyz Turkish Manas University
Chyngyz Aitmatov Avenue 56 Bishkek, KYRGYZSTAN
URL: http://journals.manas.edu.kg
e-mail: journals@manas.edu.kg
Tel : +996 312 492763- Fax: +996 312 541935

KYRGYZ TURKISH MANAS UNIVERSITY
MANAS JOURNAL OF ENGINEERING (MJEN)

## Content

MANAS Journal of Engineering
ISSN 1694-7398 | e-ISSN 1694-7398

*Volume 10, Issue 1, (2022) Pages – 1-16*
*https://doi.org/10.51354/mjen 914000*

# Performance analysis of static var compensators for distance protection of Nigerian 132-kV sub-transmission network using Matlab/ Simulink model

Akintunde S. Alayande[1], Sunday O. Akınbode[2], Ignatius K. Okakwu[3], Ajibola O. Oyedejı[4,*]

[1] Department of Electrical and Electronics Engineering, University of Lagos, Akoka, Nigeria.
aalayande@unilag.edu.ng
[2] Department of Electrical and Electronics Engineering, University of Lagos, Akoka, Nigeria.
[3] Department of Electrical and Electronics Engineering, Olabisi Onabanjo University, Ago-Iwoye, Nigeria.
okakwu.ignatius@oouagoiwoye.edu.ng
[4] Department of Computer Engineering, Olabisi Onabanjo University, Ago-Iwoye, Nigeria.
oyedeji.ajibola@oouagoiwoye.edu.ng, ORCID: 0000-0002-0180-492X

**ABSTRACT**

In this paper, the influence of the Static Var Compensators (SVC) on distance relay protection when connected to the sub-transmission network of the Nigerian 132-kV grid system is investigated. This is carried out by monitoring the error margin of the fault locator associated with the distance protective relays when SVC is connected to the transmission line. The location of the SVC is selected such that there is a common primary source of power to the sub-transmission network (Ikorodu-Sagamu 132-kV transmission line) and the SVC, which is a shunt-connected device located on Ikorodu 132-kV bus. The fault is simulated at 33.6 km and 60.4 km respectively from the Ikorodu 132-kV sub-station in MATLAB/ Simulink model and the simulation results obtained are used to investigate the influence of SVC on distance protective relay when connected to the 132-kV power transmission line. The results of the line faults are obtained with respect to earth for both zones one (1) and two (2) when SVC is connected and disconnected for all shunt type of faults. Thus, indicating under-reach and over-reach characteristics of the distance relay, when the SVC is connected and disconnected, while the transmission line protection showed no under-reach or over-reach characteristics for line-to-line fault for both zones with the SVC connected or disconnected. The results of this study show that though SVCs improve the quality of power to consumers, there is a tendency for under-reach and over-reach characteristics of the protective relay to be displayed when the relays are disconnected and connected, which introduces error margins to the fault locator in distance protective relays. Therefore, more detailed dynamic simulations are recommended for reducing the error margin.

**ARTICLE INFO**

***Research article***

*Received: 12.04.2021*
*Accepted: 7.02.2022*

***Keywords:***
*Static var compensators,*
*distance relay protection,*
*error margins,*
*flexible alternating current transmission systems,*
*voltage profile*

**Corresponding author*

## 1 Introduction

Static Var Compensators (SVC) are one of the most basic Flexible Alternating Current Transmission Systems (FACTS) available today [2]. SVC's are versatile in their application as they are used to correct and maintain the voltage profiles of power transmission lines and also to improve the amount of power delivered through the transmission lines [2]. The control of reactive power is the SVC's primary responsibility as it either injects or absorbs reactive power when connected to the grid network. When the voltage profile is low, the thyristors trigger the capacitive mode to add reactive power for the voltage profile to return to normal. Similarly, when the voltage profile of the transmission line is high, the thyristors trigger the inductive mode and the SVC adds reactive power for the voltage profile to return to normal [2].

Globally, many industries have employed the use of SVCs due to their dual functionality of maintaining a normal voltage when the network variables or reactive component in the power system are either highly capacitive or inductive [1]. Industries such as power companies, railway, oil & gas companies, steel companies, mining industries have all switched to the use of SVC's because of lower maintenance costs, increased plant and energy efficiency, lower overall

system losses [1]. In Africa, the use of SVC is gaining popularity as companies such as Eskom located in South Africa improved the quality of power delivered by connecting five (5) -50/250MVAR and -10/35MVAR to their 400kV and 132kV power grid respectively [2]. In Nigeria, the popularity of SVC is just getting a boost as the Transmission Company of Nigeria (TCN) is geared towards improving the quality of power delivered. TCN recently commissioned 25-MVar and 60-MVar Fixed Capacitor Banks at Keffi and Apo 132/33kV Substation located at Nassarawa and Abuja (F.C.T.) respectively. The project is an emergency approach aimed at improving the voltage profile being supplied by TCN under the $13 Million Japanese International Cooperation Agency (JICA) grant. NISSIN Electric, a Japanese power company conducted detailed research on the voltage deficit to Abuja and environs [3].

FACTS controllers are numerous and their point of application for optimum performance differ. They are used in distribution and transmission networks for voltage profile correction and reactive power control. Distance protective relays are vital at ensuring distribution and transmission lines are adequately protected in the event of a fault. Electrical signal quantities (Voltage and current) are utilised by the distance protective relay to calculate apparent impedance. The distance protective relay has many types of architectures such as lens, mho, modified, mho, peanut, impedance, quadrilateral and elliptical [4].

This study attempts to focus on the mho architecture for distance protective relays as it can accommodate up to six (6) zones of protection but primarily only four (4) will be considered. These four zones are zone one (1), zone two (2), zone three (3) and zone four (4) which is also known as zone three (3) reverse. Zone one (1) usually covers 80-90% of the protected line, zone two (2) covers 100% of the protected line plus 20-50% of the next neighbouring line, zone three (3) covers 100% of the protected line plus 125% of the next neighbouring line, zone four (4) is a zone with its direction of protection placed in the reverse approach and its reach is 10-25% of the protected line. time and current grading coordination of all protective relays in the grid network must be done to avoid unnecessary tripping [5].

The benefits that could be derived from the application of distance relay protection in power systems are numerous. These include, but not limited to, improving the stability of the grid, providing protection to the transmission network against transient, semi-transient and permanent faults, providing backup protection to the feeder and transformer, increasing the efficiency of the grid network, causing a significant reduction in the maintenance costs and reducing transmission line losses. Besides, the introduction of SVCs as indicated in this research will help at improving grid stability, reduced fluctuations of Voltage profile, reduction in transmission line losses and an improvement in overall grid efficiency. The under-reach and overreach tendencies of distance protective relays for shunt faults observed in this research is a result of the introduction of SVCs.

## 2. Material and methods

It is well-known that distribution systems are affected by stochastic events such as faults on lines, sudden failures of power plants and random variations in demand.

The occurrence of faults on transmission lines is inevitable. However, the influence of their occurrence is not expected to have a significant impact on the operation of the system by the timely isolation of affected parts from the healthy parts of the system. These faults are usually classified into Line-to-Earth (L-E) fault, Line-to-Line-to-Earth (L-L-E) fault, Line-to-Line-to-Line-to-Earth (L-L-L-E) fault, Line to Line (L-L) fault.

### *2.1. Single line-to-earth*

This is the most common type of fault. It is averaged that 80% of most transmission line faults are single phase to earth in nature. The type of faults can be either a result of lightning strikes, external or internal events. For reference, we will adopt Phase A as our reference phase [6]. If phase A is subjected to SLG fault, as shown in Figure 1, the magnitude of the current flowing through the ground can be expressed as follows:

$$I_{FA} = \frac{V_{AF}}{Z_F} \quad (1)$$

$$I_{FB} = 0 \quad (2)$$

The equivalent circuit is drawn from all the Thevenin's equivalent impedances derived from the zero, negative and positive sequences as shown in Figure 2 [1,6].

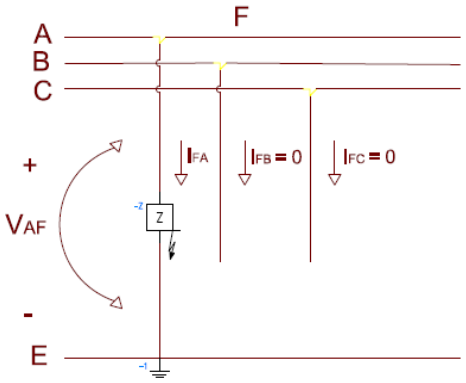


**Figure 1.** *Diagram showing a Single Line-to-Earth Fault (L-E)* [8].

From equivalent circuit, shown in Figure 2, we can write

$$\begin{bmatrix} I_a \\ I_b \\ I_c \end{bmatrix} = \begin{bmatrix} 1 & 1 & 1 \\ 1 & a^2 & a \\ 1 & a & a^2 \end{bmatrix} \begin{bmatrix} I_{a0} \\ I_{a1} \\ I_{a2} \end{bmatrix} \quad (3)$$

$$I_{a0} = I_{a1} = I_{a2} = \frac{1}{3}(I_a) \quad (4)$$

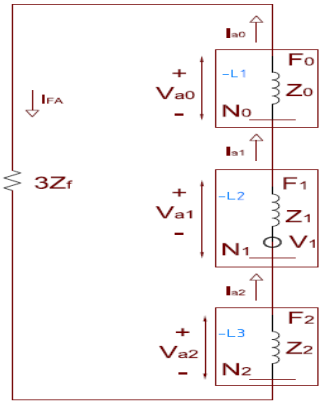


**Figure 2.** *Sequence diagram for a Single Line-to-Earth Fault (L-E)* [8].

Considering the voltages, we have

$$\begin{bmatrix} V_{a0} \\ V_{a1} \\ V_{a2} \end{bmatrix} = \begin{bmatrix} 0 \\ V_F \\ 0 \end{bmatrix} - \begin{bmatrix} Z_0 + Z_F & 0 & 0 \\ 0 & Z_1 + Z_F & 0 \\ 0 & 0 & Z_2 + Z_F \end{bmatrix} . \begin{bmatrix} I_{a0} \\ I_{a1} \\ I_{a2} \end{bmatrix} \quad (5)$$

Therefore, the fault current through A is

$$I_{FA} = \frac{3\ X\ V_F}{Z_0 + Z_1 + Z_2 + 3Z_F} \quad (6)$$

*2.2. Double Line to Earth Fault*

This type of fault can easily manifest to L-L-L-E fault if not cleared within the shortest possible time and it is represented in Figure 3. The interconnection of the positive, negative and zero sequence networks is shown in Figure 4.

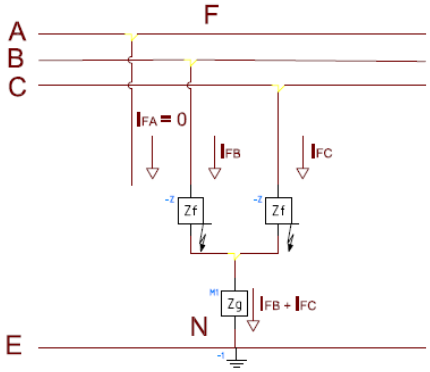


**Figure 3.** *A Diagram showing a Line-to-line-to-Earth fault (L-L-E)*[8].

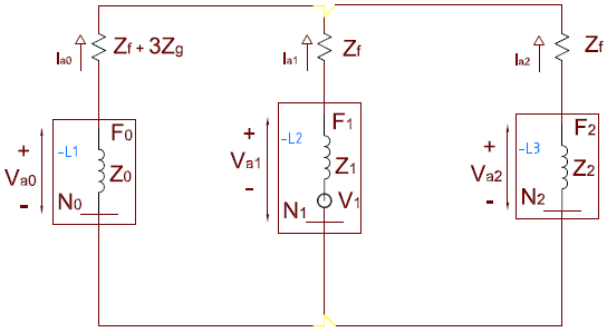


**Figure 4.** *Sequence for a Line-to-line-to-Earth fault (L-L-E)* [8].

From Figure 4,

$$I_{a1} = \frac{V_F}{(Z_1 + Z_F) + \left(\frac{(Z_2 + Z_F)(Z_0 + Z_F + 3Z_g)}{Z_0 + Z_2 + 2Z_F + 3Z_g}\right)} \quad (7)$$

$$I_{a2} = -\left(\frac{(Z_0 + Z_F + 3Z_g)}{(Z_2 + Z_F)(Z_0 + Z_F + 3Z_g)}\right).I_{a1} \quad (8)$$

$$I_{a0} = -\left(\frac{(Z_2 + Z_F)}{(Z_2 + Z_F)(Z_0 + Z_F + 3Z_g)}\right).I_{a1} \quad (9)$$

If $Z_g = 0$,

$$I_{a1} = \frac{V_F}{(Z_1) + \left(\frac{(Z_2)(Z_0 + 3Z_F)}{Z_0 + Z_2 + 3Z_F}\right)} \quad (10)$$

$$I_{a2} = -\left(\frac{(Z_0 + 3Z_F)}{(Z_2 + Z_0 + 3Z_F)}\right).I_{a1} \quad (11)$$

$$I_{a0} = -\left(\frac{Z_2}{(Z_2 + Z_0 + 3Z_F)}\right).I_{a1} \quad (12)$$

If $Z_F = 0$ & $Z_g = 0$,

$$I_{a1} = \frac{V_F}{(Z_1) + \left(\frac{Z_2 x\ Z_0}{Z_0 + Z_2}\right)} \quad (13)$$

$$I_{a2} = -\left(\frac{Z_0}{(Z_2 + Z_0)}\right).I_{a1} \quad (14)$$

$$I_{a0} = -\left(\frac{Z_2}{Z_2 + Z_0}\right).I_{a1} \quad (15)$$

The total fault current through the neutral is given by

$$I_n = 3I_{a0} = I_B + I_C \quad (16)$$

Considering the voltage equations, we have

$$= \begin{bmatrix} 0 \\ V_F \\ 0 \end{bmatrix} - \begin{bmatrix} Z_0 + Z_F & 0 & 0 \\ 0 & Z_1 + Z_F & 0 \\ 0 & 0 & Z_2 + Z_F \end{bmatrix} . \begin{bmatrix} I_{a0} \\ I_{a1} \\ I_{a2} \end{bmatrix} \quad (17)$$

For $Z_F = 0 \ and \ Z_g = 0$

$$V_{a0} = V_{a1} = V_{a2} = V_F - (I_{a1}.Z_1) \quad (18)$$

Considering the phase voltages, we have

$$V_A = V_{a0} + V_{a1} + V_{a2} = 3V_{a1} \quad (19)$$
$$V_A = V_C = 0 \quad (20)$$

Considering the line-to-line voltages, we have

$$V_{AB} = V_A - V_B = V_A \quad (21)$$
$$V_{BC} = V_B - V_C = 0 \quad (22)$$
$$V_{CA} = V_C - V_A = -V_A \quad (23)$$

### 2.3. Three Phase-to-Earth Fault

A balanced three-phase fault is shown in Figure 5 whose impedance diagram is depicted in Figure 6. It is the most severe type of fault but rarely occurs. The zero and negative sequences are zero in this type of fault. Consequently, only the positive sequence represents the interpretation of the fault. When the magnitude of the fault voltage is not known, it is usually assumed to be 1.05∠0°V [7].

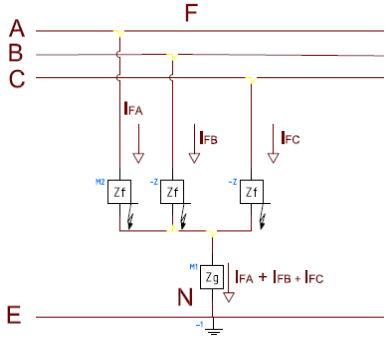


**Figure 5.** *A Line-to-Line-to-Line-to-Earth fault (L-L-L-E)* [8].

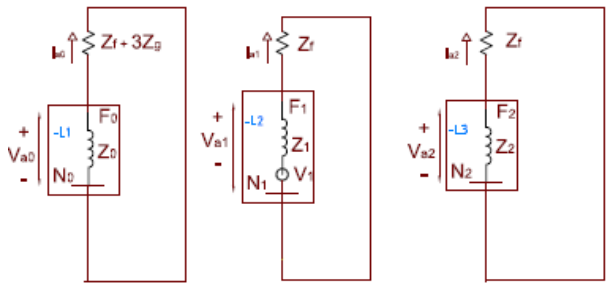


**Figure 6.** *Sequence network for a Line-to-Line-to-Line-to-Earth fault (L-L-L-E)* [8].

From Figure 6, the phase voltages are,

$$V_A = I_A Z_F = V_{a1} \quad (24)$$
$$V_B = a^2 V_{a1} \quad (25)$$
$$V_C = aV_{a1} \quad (26)$$

The line-to-line voltages can be expressed as

$$V_{AB} = V_A - V_B = (1 - a^2)V_A = \sqrt{3} I_a Z_F \angle 30° \quad (27)$$
$$V_{BC} = V_B - V_C = (a^2 - a)V_A = \sqrt{3} I_a Z_F \angle -9 \quad (28)$$
$$V_{CA} = V_C - V_A = (a - 1)V_A = \sqrt{3} I_a Z_F \angle 150° \quad (29)$$

### 2.4. Phase-to-Phase Fault

This is a fault that occurs on the two phases B and C simultaneously as shown in Figure 7. The sequence network for such a system is shown in Figure 8 and the resulting equations are as follows:

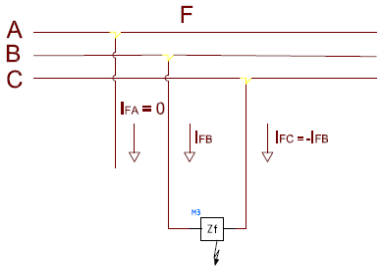


**Figure 7.** *A diagram showing a Line-Line fault (L-L)* [8].

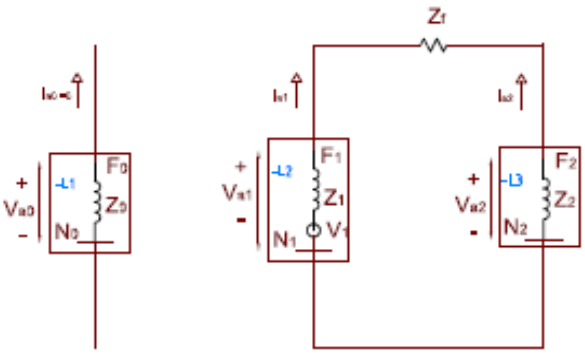


**Figure 18.** *Network sequence for a Line-Line fault (L-L)* [8]

$$I_A = 0 \quad (30)$$
$$I_B = -I_C \quad (31)$$
$$I_{a1} = -I_{a2} \quad (32)$$
$$V_B - V_C = I_B Z_F \quad (33)$$
$$\begin{bmatrix} I_{a0} \\ I_{a1} \\ I_{a2} \end{bmatrix} = \frac{1}{3} . \begin{bmatrix} 1 & 1 & 1 \\ 1 & a & a^2 \\ 1 & a^2 & a \end{bmatrix} . \begin{bmatrix} 0 \\ I_B \\ -I_B \end{bmatrix} = \begin{bmatrix} 0 \\ (a - a^2)I_B \\ (a^2 - a)I_B \end{bmatrix} \quad (34)$$

When

$$V_{a0} = 0, I_{a1} = -I_{a2} = \frac{V_F}{Z_1 + Z_2 + Z_F} \quad (35)$$

The current through the phase B and the phase voltages at A, B and C are expressed respectively as

$$I_B = \frac{j\sqrt{3}V_F}{Z_1 + Z_2 + Z_F} = \frac{\sqrt{3}\angle 90°X\ V_F}{Z_1 + Z_2 + Z_F} \quad (36)$$

$$\begin{bmatrix} V_A \\ V_B \\ V_C \end{bmatrix} = \begin{bmatrix} 1 & 1 & 1 \\ 1 & a^2 & a \\ 1 & a & a^2 \end{bmatrix} \begin{bmatrix} 0 \\ V_{a1} \\ V_{a2} \end{bmatrix} \quad (37)$$

The line-to-line voltages are then

$$V_{AB} = V_A - V_B \quad (38)$$
$$V_{BC} = V_B - V_C \quad (39)$$
$$V_{CA} = V_C - V_A \quad (40)$$

*2.5. Concept of distance protection*

To accurately determine the fault point on a very long transmission line, a distance relay is of utmost importance. Consider the circuit shown in Figure 9, it is assumed that the relay is located at point A and the relay has a reach of Zset. If an internal fault occurs (F1), the relay will trip but if an external fault occurs (F3) the relay will be restrained. From Figure 9, Distance relay zones can be mainly categorised into three (3) zones of protection. Zone 1, Zone 2 and Zone 3.

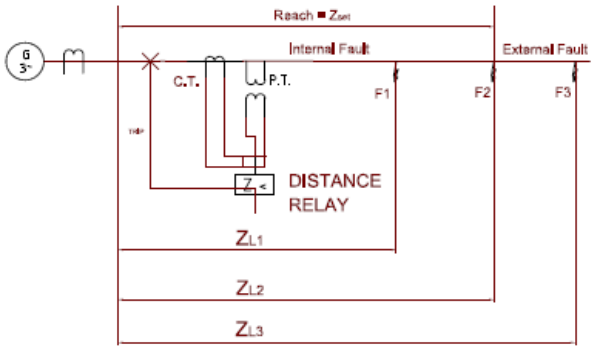


**Figure 9.** *Zones of protection of a transmission line*

*2.6. Choice between Impedance, Reactance and Mho Algorithm*

The reactance relay is preferred for use as a grounding relay because it is more stable when used on short lines rather than long lines. Consequently, the relay becomes unstable during power surges unless if an additional relay is installed to prevent such mal-operation. Mho type is preferred for phase-to-phase faults, long line and lines with heavy power surges. When a mho relay is used for the protection of a line section, its operating characteristics cover the least space in the R-X diagram. Impedance relay is preferred for phase faults related to lines of moderate length. Arc resistance affects impedance relay more than reactance relay but less than mho distance relay. In this paper, mho relay is explored for our analysis [9].

## 3. Results and discussions

The one-line diagram of the network used as a case study is as shown below;

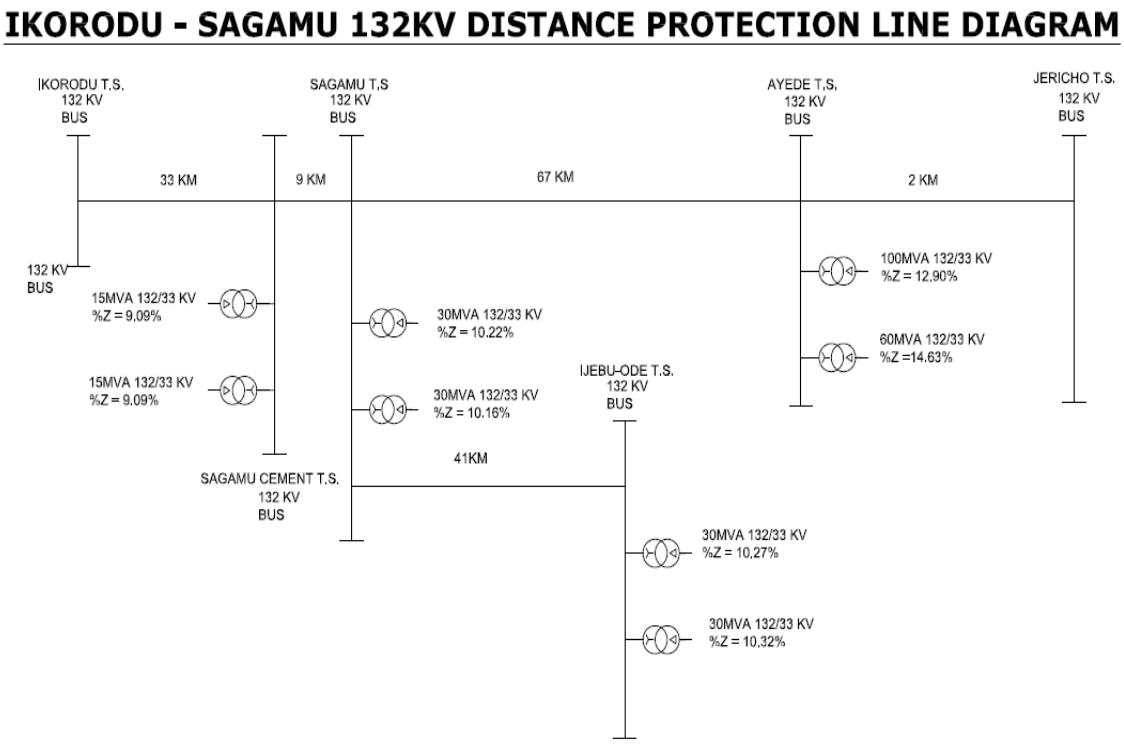


**Figure 10.** *One line diagram of Ikorodu-Sagamu 132kV distance protective scheme*

A brief description of each of the components modelled in the MATLAB/ SIMULINK environment is presented as follows:

### *3.1. The Distance Relay Simulink Model*

The MATLAB/SIMULINK simulation is used to model a variety of protective relays through current measurement (which represents the current transformer), voltage measurement (which represents the voltage transformer), logic operations, Math operators, signal attributes and routing etc.

The distance relay is accurately modelled through the measurement of current and voltage parameters. The measured impedance is compared to the calculated impedance setting of the line, thus, the zone in which the fault impedance occurs is identified. The distance relay also sends out a trip signal to the circuit breaker to isolate the faulted area of the network [6]. In MATHLAB/SIMULINK, each block is separately modelled and thereafter connected. The main blocks responsible for the proper modelling and operation of the distance relay, in this paper, include Fault Detection & Identification Block, Impedance Measurement Block, Zone Detection & Time delay Block, Fault Locator Block and Tripping Signal Block [6]. The complete model for the transmission line incorporated with a distance relay and the SVC is depicted in Figure 10. The Static Var compensator (SVC) is a shunt connected device and it is usually applied at the primary location of the distance relay. In this study, our primary location is Ikorodu 132/33kV Sub-Station. In our study, we considered an SVC designed by Pierre Giroux and Gibert Sybille (Hydro-Quebec) for (MATHWORKS) MATLAB which is sized as one (1) no Thyristor controlled reactor (TCR) 109MVAR and three (3) nos Thyristor switched Capacitor (TSC) of 94MVAR each. The +300MVar/-100MVar SVC model designed by Pierre Giroux and Gibert Sybille (Hydro-Quebec) is connected to a 735kV 60Hz transmission line and 200MW load. The SVC model Voltage and frequency parameters were adjusted to match our input voltage of 132kV and 50Hz respectively while all other parameters remained the same as the original model designed [10].

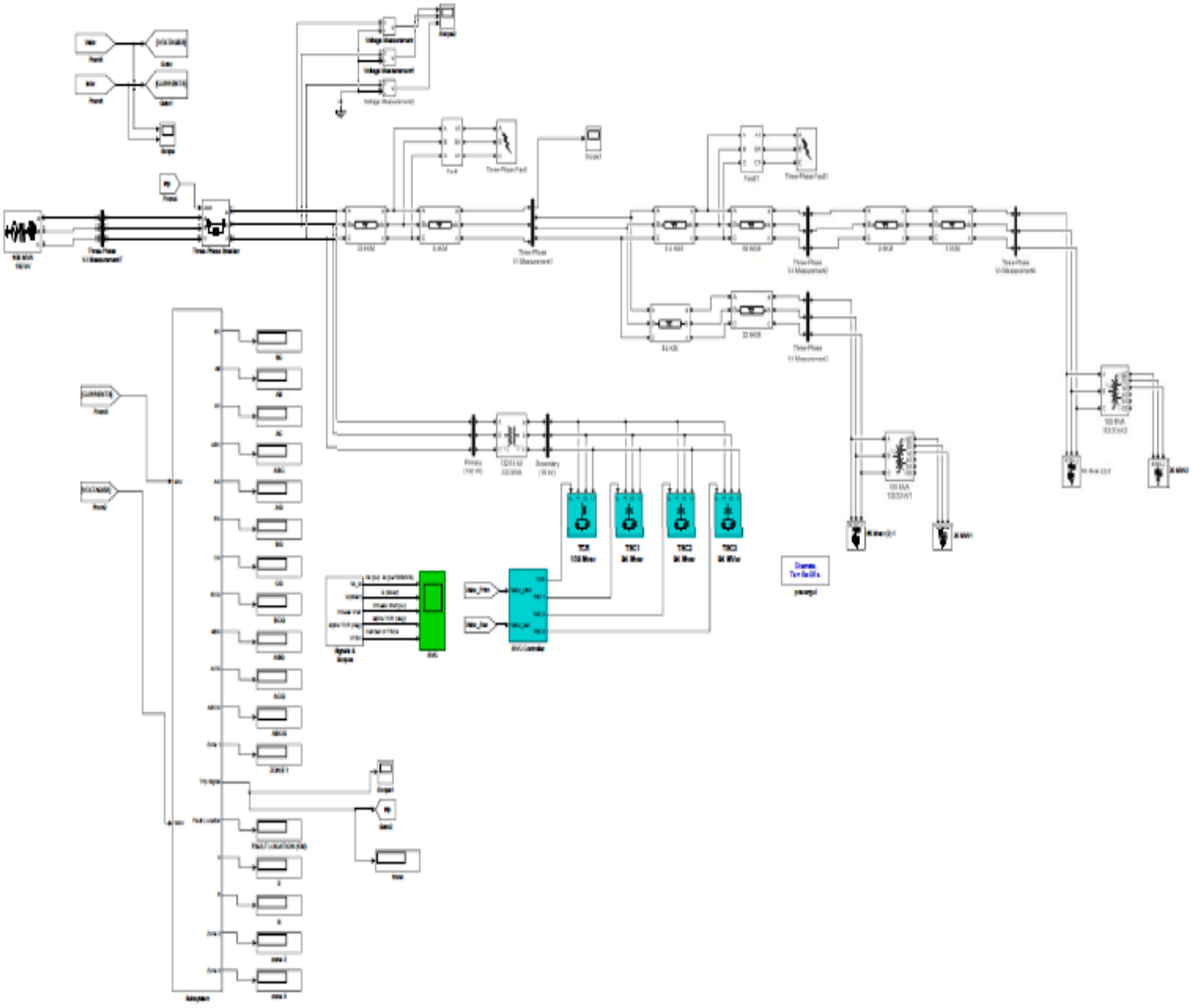

**Figure 11.** *The Complete transmission line, distance relay and static var compensator model.*

### *3.2. The mho circle characteristics simulink model*

The Mho Characteristic graph is drawn using the MATLAB M-file and it shows the relationship between resistance and reactance on a transmission line. In Figure 12, each Mho circle represents a zone of protection as illustrated by the Legend of the Mho Circle Graph. MATLAB codes was used for representing the zones of protection on a Mho Circle Graph. Figure 12 shows the picture of the Mho Circle Characteristics graph.

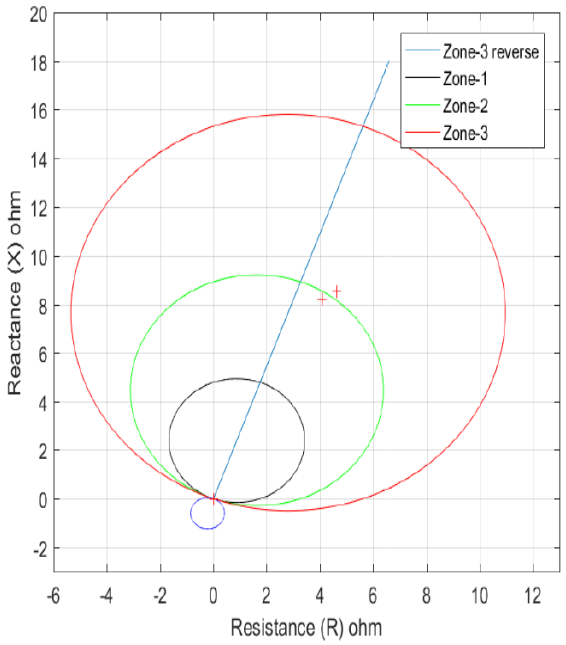


**Figure 12.** *Mho Circle plot*

### *3.3.The Complete Distance Relay Simulink Model*

The complete distance relay as shown in Figure 13 is a combination of the fault detection and identification block, impedance measurement block, zone detection and time delay block, fault locator block and the mho circle characteristics graph.

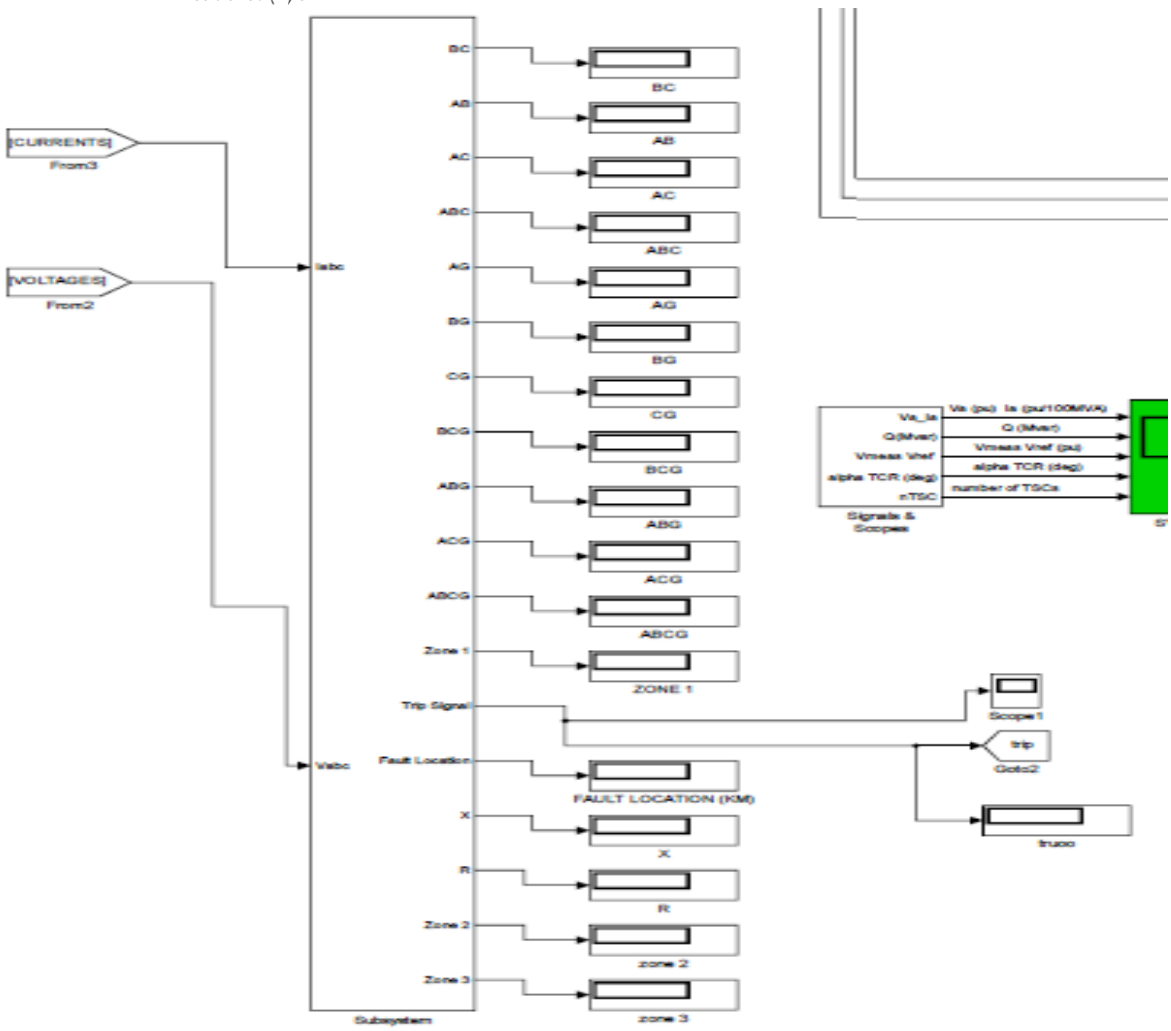


**Figure 13.** *The Complete Distance Relay Model*

### *3.4.The Static Var Compensator (Svc) Simulink Model*

SVCs are shunt-connected devices. This particular model of SVC was designed by Pierre Giroux and Gibert Sybille (Hydro-Quebec) for (MATHWORKS) MATLAB and used to study the impact of harmonics, transients and stresses on power components during fault conditions. The model has been modified to fit the parameters of this research project which seeks to understand the consequence of SVC on transmission line protection.

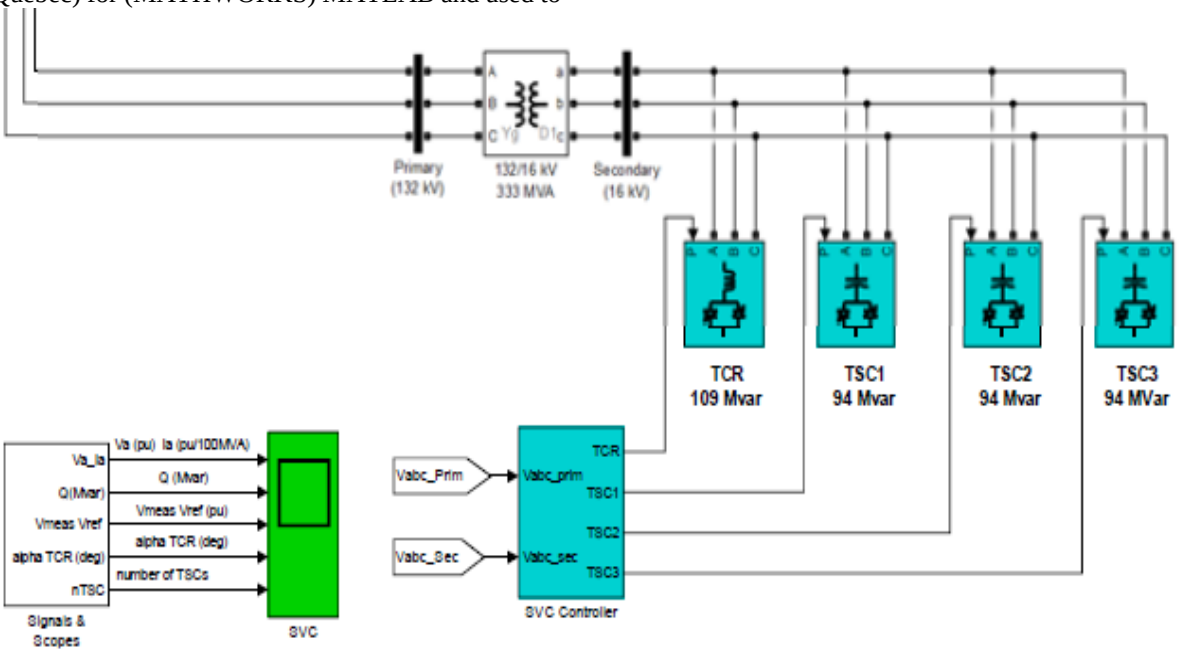


**Figure 14.** *The Static Var Compensator (SVC) model*

The SVC model has one (1) TCR of 109MVAR rating, three (3) TSC of 94MVAR rating each and an SVC Controller [10]. The modifications that affected this model includes modifying the voltage and frequency parameters to suit the required parameters for this paper. Figure 14 shows the basic structure of the SVC model used for the simulation.

### *3.5.The Svc Control System*

The SVC control system is responsible for the controlled firing of the thyristors to inject or absorb VAR into the system based on the inherent system parameters. The SVC Control system consists of four (4) components which include the measurement system, voltage regulator, distribution unit and firing unit [9,11].

The simulations were carried out considering faults occurring in zone one (1) and zone two (2) of the distance relay protective scheme. The results obtained are presented in Table 1.

**Table 1**. *Simulation result for the impedance and fault location as seen by the distance relay modelled in MATLAB/Simulink*

| Protection zone | SVC connection status | | Types of fault | | | | |
|---|---|---|---|---|---|---|---|
| | | | L-E fault | L-L fault | L-L-L fault | L-L-E fault | L-L-L-E fault |
| zone 1 | with svc | apparent impedance | 2.296 + j4.553 (5.099) | 1.698 + j3.752 (4.118) | 1.997 + j4.954 (5.341) | 2.296 + j4.551 (5.097) | 1.997 + j4.153 (4.608) |
| | | fault location | 33.6 km | 27.14 km | 35.19 km | 33.58 km | 30.36 km |
| zone 1 | without svc | apparent impedance | 2.296 + j4.553 (5.099) | 1.698 + j3.752 (4.118) | 1.997 + j4.954 (5.341) | 1.824 + j3.888 (4.295) | 1.997 + j4.954 (5.341) |
| | | fault location | 33.6 km | 27.14 km | 35.19 km | 28.29 km | 35.19 km |
| summary for zone 1 distance relay | | | Same | Same | Same | over reach | under reach |
| zone 2 | with svc | apparent impedance | 4.073 + j8.211 (9.166) | 4.066 + j8.201 (9.154) | 4.066 + j8.777 (9.672) | 4.073 + j8.211 (9.166) | 4.073 + j8.211 (9.166) |
| | | fault location | 60.39 km | 60.31 km | 63.73 km | 60.39 km | 60.39 km |
| zone 2 | without svc | apparent impedance | 4.073 + j8.766 (9.666) | 4.066 + j8.202 (9.155) | 4.066 + j8.776 (9.672) | 4.073 + j8.766 (9.666) | 4.073 + j8.767 (9.666) |
| | | fault location | 63.69 km | 60.32 km | 63.73 km | 63.69 km | 63.69 km |
| summary for zone 2 distance relay | | | under reach | Same | Same | under reach | under reach |

Table 1 presents the results obtained when the SVC is connected and disconnected from the transmission line for both faults in zone 1 and zone 2. As shown in Table 1, our analysis was based on the simulation of five different types of faults on the network considering zone one (1) and zone two (2). For instance, in zone one (1), considering the Single Line-to-Earth (L-E) fault, the Resistance-Reactance (R-X) diagram for the distance relay when SVC is connected with the transmission line is shown in Figure 15 (a) while Figure 15 (b) shows the Resistance-Reactance (R-X) diagram for the distance relay when SVC is not connected for the same L-E type of fault. Figure 15a and Figure 15b clearly show plotted points (purple and red) at the same magnitude of Resistance (R) of 2.296Ω and Reactance (X) j4.553Ω as shown in Table 1 for both Line-to-Earth faults with and without the SVC connected to the bus. Consequently, in both conditions, the distance relay was observed to have tripped at 33.6km. Thus, indicating that during line-to-earth (L-E) fault conditions with SVC connected or not connected the distance relay fault location accuracy is not affected.

When the simulation is carried out for Phase-to-Phase (L-L) faults, the Resistance-Reactance (R-X) diagram for the distance relay when SVC is connected with the transmission line is shown in Figure 16 (a) while the Resistance-Reactance (R-X) diagram for the same Phase-to-Phase (L-L) fault with the distance relay but without the SVC is shown in Figure 16 (b). Figure 16a and Figure 16b clearly show plotted points (purple and red) at the same magnitude of Resistance (R) of 1.698Ω and Reactance (X) j3.752Ω as shown in Table 1 for both Line-to-Earth faults with and without the SVC connected to the bus. Consequently, in both conditions, the distance relay was observed to have tripped at 27.14km. Thus, indicating that during Phase-to-Phase (L-L) fault conditions with SVC connected or not connected, the distance relay fault location accuracy is not affected.

For Double-Line-to-Earth faults (L-L-E), Figure 17 (a) shows the Resistance-Reactance (R-X) diagram for the distance relay when SVC is connected while Figure 17 (b) shows the Resistance-Reactance (R-X) diagram for the distance relay when SVC is not connected. Figure 17a and Figure 17b clearly show plotted points (purple and red) at the different magnitude of Resistance (R) and Reactance (X). The purple plotted dot in Figure 17 (a) has a Resistance (R) magnitude of 2.296Ω and Reactance (X) Magnitude of j4.551Ω as shown in Table 1 for Double-Line-to-Earth (L-L-E) with SVC connected while the red plotted dot in Figure 17 (b) has a Resistance (R) magnitude

of 1.824Ω and Reactance (X) Magnitude of j3.888Ω as shown in Table 1 for Double-Line-to-Earth (L-L-E) without SVC connected. Consequently, the distance relay, with and without SVC connected was observed to have tripped at 33.58km and 28.29km respectively. Thus, indicating that during Double-line-to-Earth (L-L-E) fault conditions, the distance relay over-reaches with the SVC connected.

For Three-Phase-to-Earth faults (L-L-L-E), Figure 18 (a) shows the Resistance-Reactance (R-X) diagram for the distance relay when SVC is connected while Figure 18 (b) shows the Resistance-Reactance (R-X) diagram for the distance relay when SVC is not connected. Figure 18a and Figure 18b clearly show plotted points (purple and red) at the same magnitude of Resistance (R) and different magnitude of Reactance (X). The purple plotted dot in Figure 18 (a) has a Resistance (R) magnitude of 1.997Ω and Reactance (X) Magnitude of j4.153Ω as shown in Table 1 for Three-phase-to-Earth (L-L-L-E) with SVC connected while the red plotted dot in Figure 18 (b) has a Resistance (R) magnitude of 1.997Ω and Reactance (X) Magnitude of j4.954Ω as shown in Table 1 for Three-phase-to-Earth (L-L-L-E) without SVC connected. Consequently, the distance relay, with and without SVC connected was observed to have tripped at 30.36km and 35.19km respectively. Thus, indicating that during Three-phase-to-Earth (L-L-L-E) fault conditions, the distance relay under-reaches with the SVC connected.

a

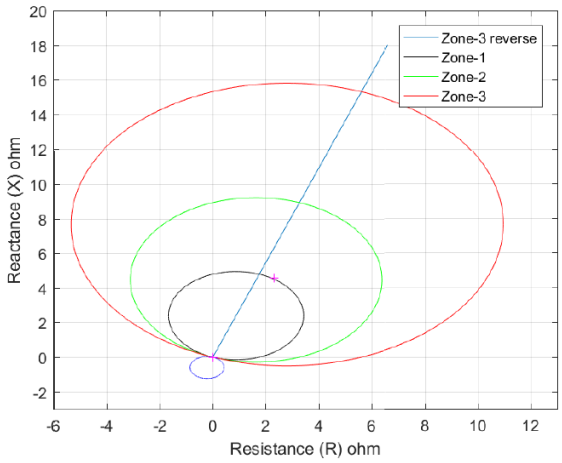


b

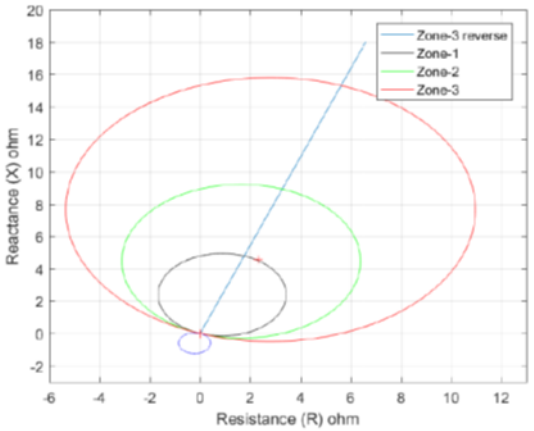


**Figure 15.** *Resistance-Reactance (R-X) plot of a zone 1 for Line-to-Earth (L-E) fault with (a) with SVC (b) without SVC*

a

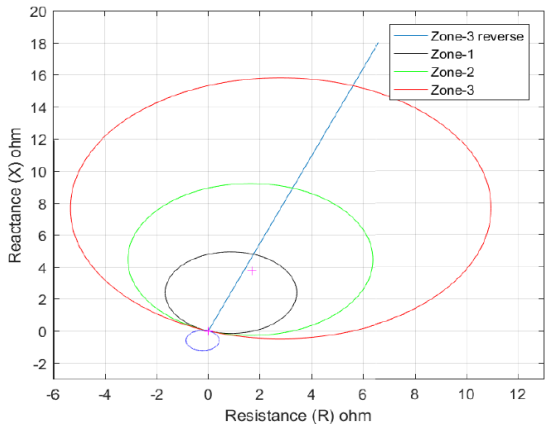


b

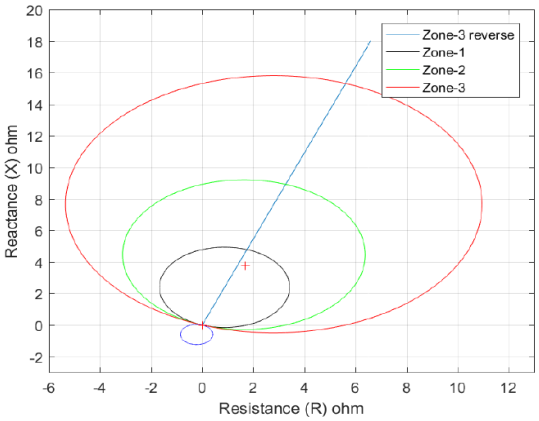


**Figure 16.** *Resistance-Reactance (R-X) plots of a zone 1 for Phase-to-Phase (L-L) fault with (a) with SVC (b) without SVC*

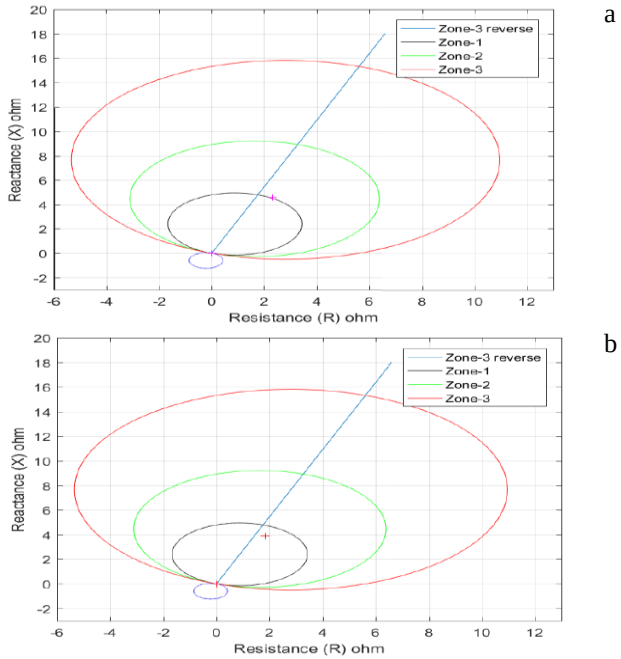


**Figure 17.** *Resistance-Reactance (R-X) plots of a zone 1 for Double-Line-to-Earth (L-L-E) fault with (a) with SVC (b) without SVC*

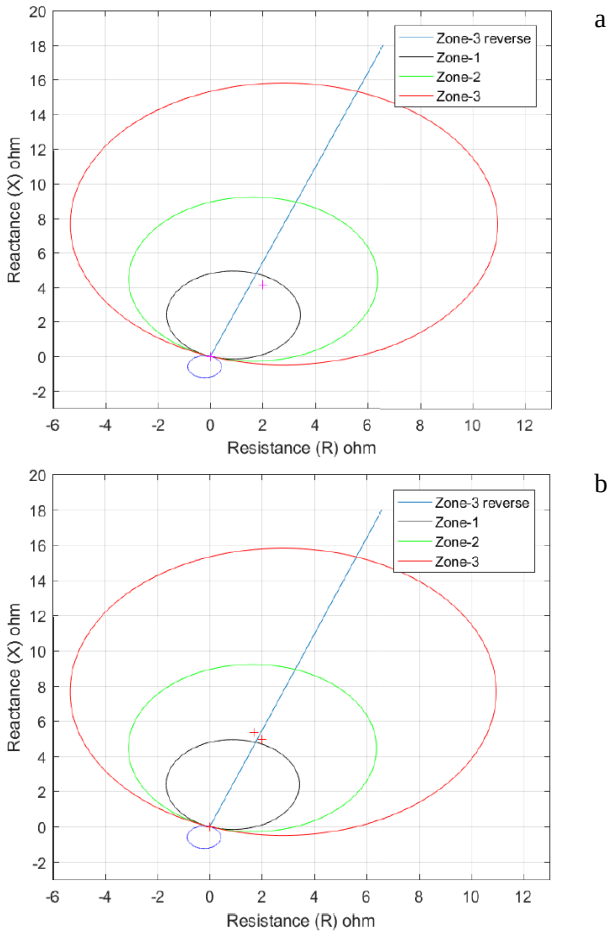


**Figure 18.** *Resistance-Reactance (R-X) plots of a zone 1 for Three-phase-to-Earth (L-L-L-E) fault with (a) with SVC (b) without SVC*

**Considering zone 2, f**or Single Line-to-Earth (L-E) fault the Resistance-Reactance (R-X) diagram for the distance relay when SVC is connected with the transmission line is shown in Figure 19 (a) while Figure 19 (b) shows the Resistance-Reactance (R-X) diagram for the distance relay when SVC is not connected for the same Single Line-to-Earth (L-E) type of fault. Figure 19a and Figure 19b clearly show plotted points (purple and red) at the same magnitude of Resistance (R) and different magnitude of Reactance (X). The purple plotted dot in Figure 19 (a) has a Resistance (R) magnitude of 4.073Ω and Reactance (X) Magnitude of j8.211Ω as shown in Table 1 for Single Line-to-Earth (L-E) with SVC connected while the red plotted dot in Figure 19 (b) has a Resistance (R) magnitude of 4.073Ω and Reactance (X) Magnitude of j8.766Ω as shown in Table 1 for Single Line-to-Earth (L-E) without SVC connected. Consequently, the distance relay, with and without SVC connected was observed to have tripped at 60.39km and 63.69km respectively. Thus, indicating that during Single Line-to-Earth (L-E) fault conditions, the distance relay under-reaches with the SVC connected.

When the simulation is carried out for the Phase-to-Phase (L-L) faults, the Resistance-Reactance (R-X) diagram with the connection of the distance relay and installation of the SVC is shown in Figure 20 (a) while the Resistance-Reactance (R-X) diagram for the same L-L fault with the distance relay but without the SVC is shown in Figure 20 (b). Figure 20a and Figure 20b clearly show plotted points (purple and red) at the same magnitude of Resistance (R) of 4.066Ω and Reactance (X) j8.201Ω as shown in Table 1 for both Phase-to-Phase (L-L) faults with and without the SVC connected to the bus. Consequently, in both conditions, the distance relay was observed to have tripped at 60.32km. Thus, indicating that during phase-to-phase (L-L) fault conditions with SVC connected or not connected, the distance relay fault location accuracy is not affected.

For Double-Line-to-Earth faults (L-L-E), Figure 21 (a) shows the Resistance-Reactance (R-X) diagram for the distance relay when SVC is connected while Figure 21 (b) shows the Resistance-Reactance (R-X) diagram for the distance relay when SVC is not connected. Figure 21 (a) and Figure 21 (b) clearly shows plotted points (purple and red) at different magnitude of Resistance (R) and Reactance (X). The purple plotted dot in Figure 21 (a) has a Resistance (R) magnitude of 4.073Ω and Reactance (X) Magnitude of j8.766Ω as shown in Table 1 for Double-Line-to-Earth (L-L-E) with SVC connected while the red plotted dot in Figure 21 (b) has a Resistance (R) magnitude of 4.073Ω and Reactance (X) Magnitude of j8.766Ω as shown in Table 1 for Double-Line-to-Earth (L-L-E) without SVC connected. Consequently, the distance relay, with and without SVC connected was observed to have tripped at 60.39km and 63.69km respectively. Thus, indicating that during Double-line-to-Earth (L-L-E) fault

conditions, the distance relay under-reaches with the SVC connected.

For Three-phase-to-Earth faults (L-L-L-E), Figure 21 (a) shows the Resistance-Reactance (R-X) diagram for the distance relay when SVC is connected while Figure 22 (b) shows the Resistance-Reactance (R-X) diagram for the distance relay when SVC is not connected. Figure 22 (a) and Figure 22 (b) clearly shows plotted points (purple and red) at the same magnitude of Resistance (R) and different magnitude of Reactance (X). The purple plotted dot in Figure 22 (a) has a Resistance (R) magnitude of 4.073Ω and Reactance (X) Magnitude of j8.211Ω as shown in Table 1 for Three-phase-to-Earth (L-L-L-E) with SVC connected while the red plotted dot in Figure 22 (b) has a Resistance (R) magnitude of 4.073Ω and Reactance (X) Magnitude of j8.767Ω as shown in Table 1 for Three-phase-to-Earth (L-L-L-E) without SVC connected. Consequently, the distance relay, with and without SVC connected was observed to have tripped at 60.39km and 63.69km respectively. Thus, indicating that during Three-phase-to-Earth (L-L-L-E) fault conditions, the distance relay under-reaches with the SVC connected.

a

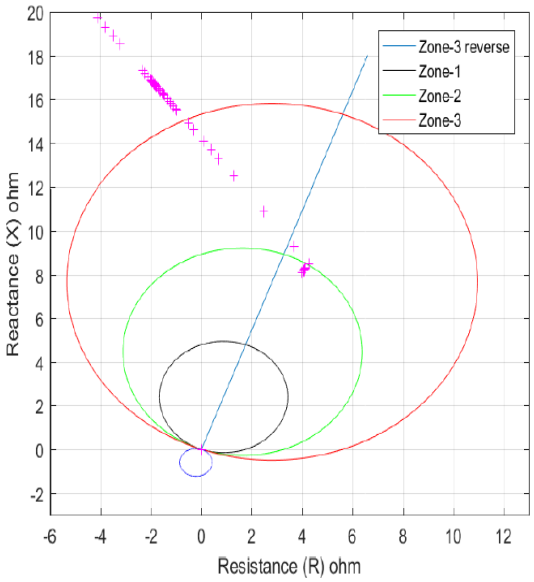


b

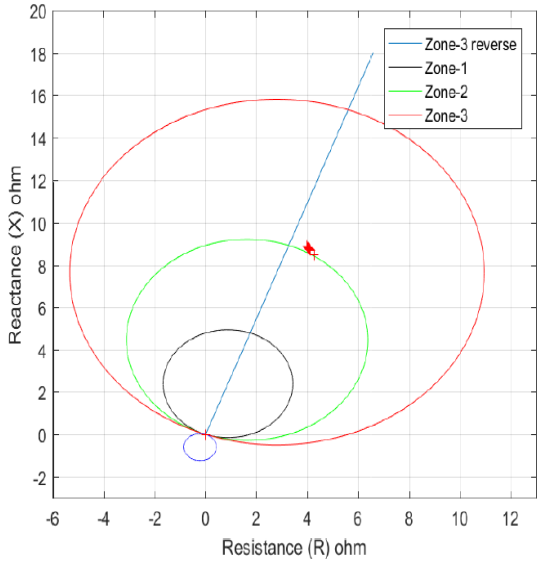


**Figure 19.** *Resistance-Reactance (R-X) plots of a zone 2 for Single Line-to-Earth (L-E) fault with (a) with SVC (b) without SVC*

a

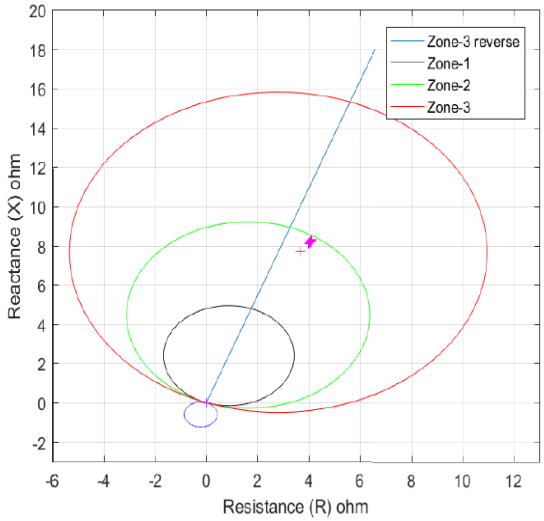

b

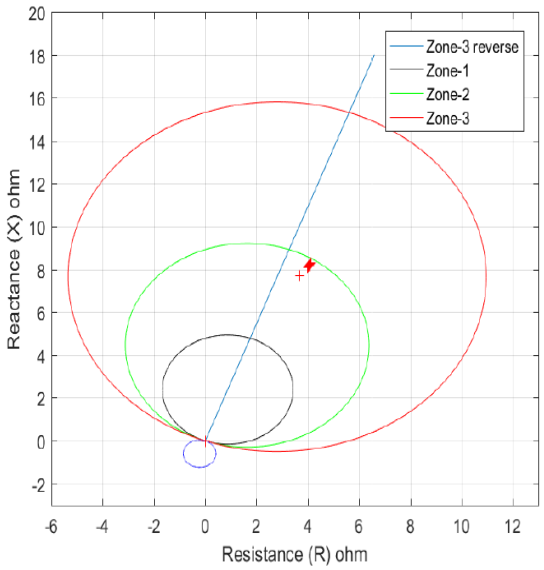


**Figure 20.** *Resistance-Reactance (R-X) plots of a zone 2 for Phase-to-Phase (L-L) fault with (a) with SVC (b) without SVC*

a

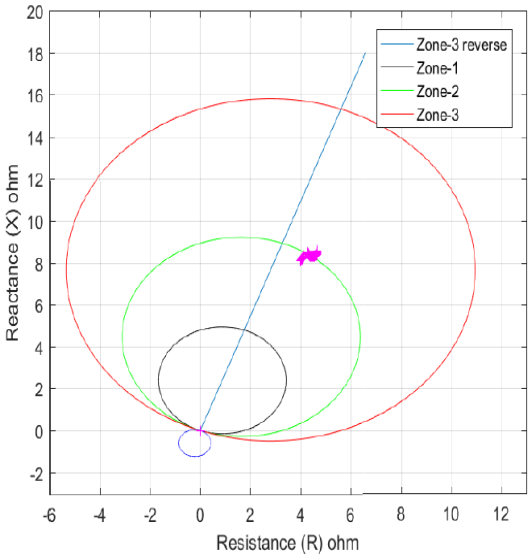


b

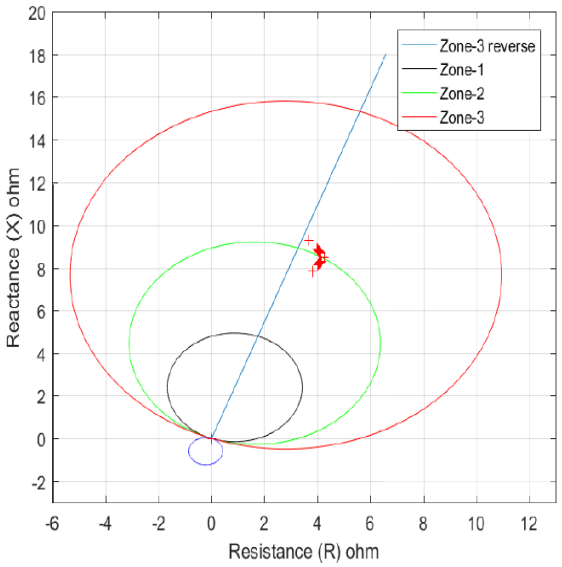


**Figure 21.** *Resistance-Reactance (R-X) plots of a zone 2 for Double-Line-to-Earth (L-L-E) fault with (a) with SVC (b) without SVC*

a

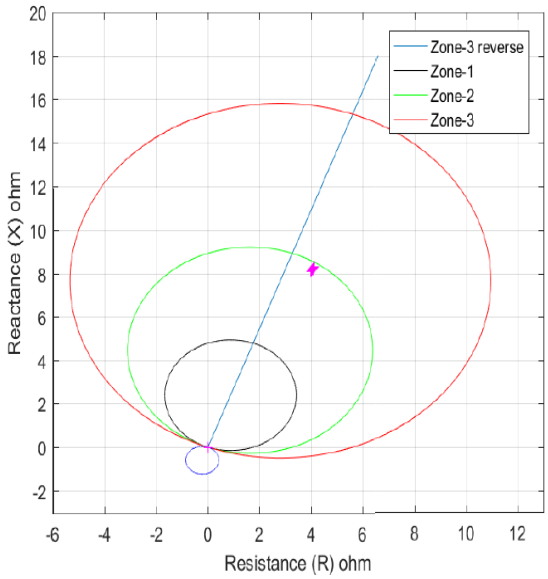

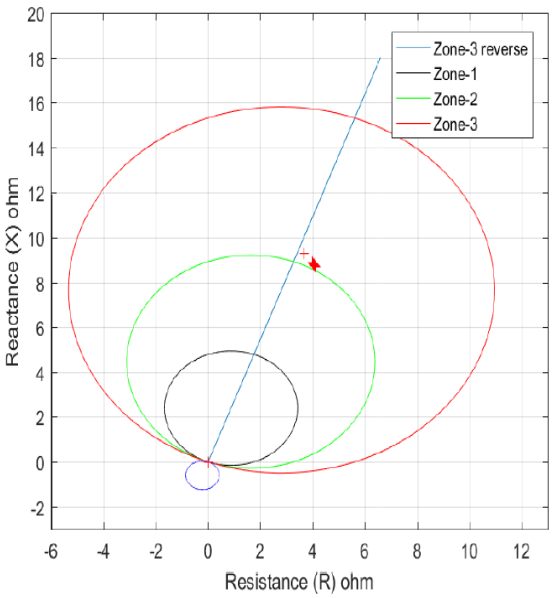


b

**Figure 22.** *Resistance-Reactance (R-X) plots of a zone 2 for Three-Phase-to-Earth (L-L-L-E) fault with (a) with SVC (b) without SVC*

*3.6.Summary of Results*

The simulation result when a highly inductive load of 130MVAR is applied into the real-life scenario setting of the Ikorodu-Sagamu 132kV transmission line setting being fed from a source of 600MVA short circuit. The simulation result shows a case of very high voltage despite the highly inductive load due to the surplus amount of source power. From the simulation results obtained for zone one (1) and zone two (2) as represented in Table 1 and Figure 23, the following observations were made during the simulation;

The known fault application points are 33.6km and 60.4km respectively. When SVC is applied, the simulation result shows us that the SVC takes care of the over-voltage condition by stabilizing the voltage, as this is evident in the fault location results, which are close to the applied point of fault. Table 1 shows that the fault locations for both zone one (1) and zone two (2) lies close to the point of fault application. For zone one (1), the fault is applied at 33.6km (80% of protected line settings) and the distance relay sees fault locations such as 33.6km, 27.14km, 35.19km, 33.58km, 30.36km and 28.29km. For zone two (2), the fault is applied at 60.4km (143.8% of protected line settings) and the distance relay sees fault locations such as 60.39km, 60.31km, 63.73km, 63.69km and 60.32km.

Furthermore, the distance protective relays see these fault locations as either over-reach or under-reach. The over-reach and under-reach are evidence that error margins are introduced when SVCs are connected. Static Var Compensators do not affect Phase to phase faults. The tabulated data of Table 1 and plotted dots in Figure 16 and Figure 20 clearly shows that for Phase-to-Phase (L-L) faults, the distance protective relay sees the same magnitude of Resistance (R) and Reactance (X) for both zone one (1) and zone two (2). Similarly, Figure 23 shows a Bar chart comparison for each fault type with and without SVC connected. The similar magnitudes of Resistance (R) and reactance (X) for both zone one (1) and zone two (2) can easily be seen deduced.

Static Var Compensators appear to be more consistent in their operation for zone two (2) faults. From the tabulated data in Table 1, the result shows that for all shunts faults in zone two (2), the distance protective relay under-reaches for all shunt faults to Earth faults and no effect for all phase to phase faults. For zone 1, the distance protective relay under-reaches for Three-Phase-to-Earth (L-L-L-E), over-reaches for Double-Line-to-Earth (L-L-E) and no effect for all phase-to-phase faults (L-L) and Single Line-to-Earth (L-E) faults. Figure 22 shows graphically that zone two (2) fault results appear to be more consistent for all shunt faults, unlike zone one (1) shunt faults which varies from no effect to under-reach and over-reach distance relay tendencies.

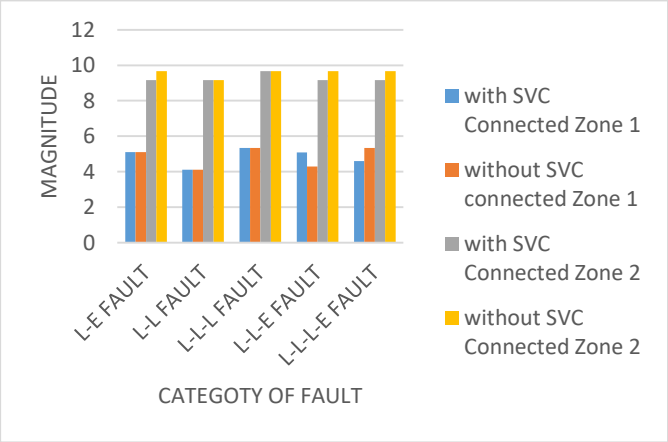


**Figure 23.** *Distance relay response with and without the installation of SVC*

## 1. Conclusion

The efficiency of transmission lines is very vital. The need to expand the grid means that the quality of power supplied must be improved upon. The use of Static VAR Compensators is encouraged by its lower cost compared to STATCOM. In this research, the results gotten and analysed satisfies the objectives of this study. The study's comparison of results between when an SVC is connected to the transmission grid and without the SVC connected shows that there are under-reach and over-reach tendencies for faults that occur both in Zone one (1) and Zone two (2).

Figure 22 clearly shows the under reach and overreach fault locations of the distance protective relay when different types of fault occur. The research revealed that for Phase-to-Phase

(L-L) faults in both Zone One (1) and Zone Two (2), they are unaffected by the presence of SVC in the grid network. From Figure 22, the magnitude of Resistance (R) and Reactance (X) for both phase-to-phase (L-L) faults of zone one (1) with and without SVC connected are the same. Similarly, the magnitude of Resistance (R) and Reactance (X) for both Phase-to-Phase (L-L) faults of zone two (2) with and without SVC connected are the same.

It is of paramount importance to note that there is an error margin when an SVC is connected to the transmission grid and without the SVC connected. The under-reach and over-reach tendencies are clear proofs that the relay sees an error margin when the SVC is connected for both zone one (1) and zone two (2). However, the distance protective relays did not show any error margins to Phase-to-Phase (L-L) faults for both scenarios. Site Adaptive setting is encouraged to be implemented since each line section has various parameters introducing errors into the fault location calculations as seen by the distance relays.

Further research on algorithm development to mitigate the inaccuracies in fault locator introduced by the presence of SVC in the Transmission Company of Nigeria (TCN) 132kV Power Grid Network. Further study in the use of other types of FACTS devices is highly recommended using this same methodology. Researchers can also simulate Zone three (3) zone of protection to show if the same behaviours in this research are observed.

Although, the linear predictor is used to obtaining forecast values in this study, it is recommended that other approaches such as Auto-Regressive Moving Average (ARMA) model can be used to enhance the accuracy of the model equation. Also, the study can be further carried out to show the trend of individual fault occurrence which will help the transmission company to have better plans towards mitigation the occurrence of faults and maintenance strategy so as to improve customer satisfaction.

**References**

[1]. IndustryArc, “Static VAR Compensator Market: By Type (Thyristor-Based SVC, & Magnetically Controlled Reactor-Based SVC) By End-Use Industry (Electric Utility, Renewable, Railway, Industrial, Oil & Gas, & Others), By Component & Geography - Forecast (2018 - 2023),” 2018. [Online]. Available: https://industryarc.com/Report/15449/static-var-compensator-market.html.

[2]. P.S. (AEG G. H. Pesch, S. Ranade, M. Schubert, “Static VAR-Compensators for stabilizing traction and transmission systems in South Africa,” Berlin, 2007.

[3]. Anumihe, “FG obtains $13m JICA grant to fix power supply in Nasarawa State,” Sun News Online, 2019. [Online]. Available: https://www.sunnewsonline.com/fg-obtains-13m-jica-grant-to-fix-power-supply-in-nasarawa-state/. [Accessed: 19-Nov-2020].

[4]. Aptransco, Technical Reference Book. HYDERABAD: TRANSMISSION CORPORATION OFANDHRA PRADESH LIMITED, 2004.

[5]. Mohamed Zellagui A.C., “Impact of svc devices on distance protection setting zones in 400 kv transmission line,” U.P.B. Sci. Bull., Ser. C, (2013), 75, 2, 249–262.

[6]. Lamture J., “DEVELOPMENT OF DISTANCE RELAY IN MATLAB,” Int. J. Adv. Comput. Eng. Netw., (2015), 3, 9, 77–80.

[7]. . Xiaoyao Zhou H.W Aggarwall R.K., Phil Beaumont, “The Impact of STATCOM on Distance Relay,” in 15th Power Systems Computation Conference (PSCC’05), (2005), 1–7.

[8]. Altaie A.S., “Design of a New Digital Relay for Transmission Line Fault Detection, Classification and Localization Based on a New Composite Relay and Artificial Neural Network Approach,” Western Michigan University, (2015).

[9]. Ngo Minh Khoa D.T.V., Nguyen Huu Hieu2, “A Study of SVC’s Impact Simulation and Analysis for Distance Protection Relay on Transmission Lines,” Int. J. Electr. Comput. Eng., (2017), 7, 4, 1686–1695.

[10]. Sybille P.G., “SVC (Detailed Model).” [Online]. Available: https://www.mathworks.com/help/physmod/sps/examples/svc-detailed-model.html. [Accessed: 08-Jul-2019].

[11]. Al-Husban A.N., “An Eigenstructure Assignment for a Static Synchronous Compensator,” Am. J. Eng. Appl. Sci., (2009), 2, 4, 812–816.

[12]. Le Ngoc Giang T.T.N., Nguyen Thi Dieu Thuy, “Assessment study of STATCOM’s effectiveness in improving transient stability for power system,” TELKOMNIKA, (2013), 11, 10, 6095–6104.

MANAS Journal of Engineering
ISSN 1694-7398 | e-ISSN 1694-7398

*Volume 10, Issue 1, (2022) Pages 17-20*
*https://doi.org/10.51354/mjen. 940760*

# Estimation of the moisture content, volatile matter, ash content, fixed carbon and calorific values of saw dust briquettes

Francis Inegbedion

Department of Production Engineering, University of Benin, Benin City, Nigeria, francis.inegbedion@uniben.edu,
ORCID: 0000-0002-2142-8079

**ABSTRACT**

Briquetting is one way of making efficient use of existing resources. It involves collecting combustible waste materials due to lack of density, and compressing them into solid fuels of convenient shape that can be burnt like wood or charcoal". "Biomass briquette is one of the proven ways of generating energy from waste". "The excessive use of fossil fuels, wood fuels and natural gas has led to serious environmental issues and deforestation". "This work focused on estimating the heating values of sawdust briquettes to ascertain its suitability for domestic use and small-scale industrial cottage application". The calorific value of the briquettes was determined using a bomb calorimeter. "The following heating values of sawdust briquettes were obtained: average percentage moisture content 5.04%, average percentage volatile matter 10.80%, average percentage ash content 3.85%, average percentage fixed carbon 80.95% and average percentage calorific value 26918.02KCal/Kg. These results indicate that the briquettes made from sawdust have high heating values enough for domestic use and small-scale industrial cottage applications

**ARTICLE INFO**

***Research article***

*Received: 21.05.2021*
*Accepted: 7.02.2022*

***Keywords:***
*Moisture content,*
*volatile matter,*
*ash content,*
*fixed carbon,*
*calorific values,*
*sawdust briquettes*

*Corresponding author

## 1 Introduction

"The primary source of energy for such vital activities as cooking and space heating is burning wood, charcoal and other agricultural products". "An increasing population using dwindling resource of combustible materials (fossil and wood fuels) for cooking and heating purposes will eventually result in the shortage of those materials unless urgent steps are taken to reverse the trend". "One way of making efficient use of existing resources is briquetting". "Briquetting involves collecting combustible waste materials that are not usable due to lack of density, compressing them into solid fuels of convenient shape that can burn like wood or charcoal" [3].

Biomass briquetting is the densification of loose agro residues with or without binding agents to produce compact solids with the application of pressure". "A briquette is the product formed from the physic-mechanical conversion of dry, loose and tiny particle size material with or without the addition of an additive into a solid state characterized by a regular shape". "Briquettes are mainly used for heat applications (steam generation, melting metals, space heating, brick kilns, tea curing, etc) and power generation through gasification of biomass briquettes and for domestic uses" [4].

Developing countries are faced with the huge problem of waste management of agro residues". "Agro and sawmill residues are usually burnt on roadside or dump yards, which results in environmental pollution. "These residues are very difficult to handle, store and if they are burnt directly results in very poor thermal efficiency and create lots of air pollution". "These problems can be avoided by briquetting these wastes into usable energy generating fuel." [1]
"Biomass briquettes are a proven way of generating energy from waste". "Different types of waste have been utilized to develop biomass briquettes". "It has been revealed that the fabrication of biomass briquettes derived from municipal waste stream could result in feasible on–site fuel production [6]". "In another report, briquettes have been produced from sawdust, date palm trunk and different plastic wastes, without the use of external binding agent" [7].

"It has been reported that briquettes were prepared using cow dung, wheat flour and paper pulp as binding agents". "These

briquettes were tested for calorific value and compressive strength by varying percentage by volume of binders. The minimum energy costs for production of these briquettes were also calculated." [2]. "In an effort to substitute briquettes for firewood in the rural households in Nigeria Bio briquettes were prepared from elephant grass, spear grass and bio coal at moderate pressure and temperature". "Proximate analysis was carried out on these briquettes and results were compared with wood samples". [8]

"In this research paper, I estimated the heating values of briquettes produced from sawdust".

## 2. Materials and methods

### *2.1. Determination of moisture content of the briquettes*

"The percentage moisture content (PMC) was determined by weighing 1.5g of the briquette sample in a crucible of known mass and placed in an oven set at 105°C ± 5°C for 1 hour". "The crucible and its content were removed from the oven allowed to cool to room temperature and reweighed". "This process was repeated until the weight after cooling became constant and the value was recorded as the final weight". This process was repeated using three (3) different samples of the briquettes and results are tabulated in Table 1. "The sample's moisture content was determined using equation (1)".

$$PMC = \frac{W_1 - W_2}{W_2} \times 100\% \quad (1)$$

"Where, $W_1$ is the initial weight of briquette sample and $W_2$ is the final weight of briquette sample".

### *2.2. Determination of volatile matter of the briquettes*

"The percentage volatile matter (PVM) was determined by placing 1.5g of the briquettes sample in a crucible and kept in a furnace for 8 minutes, at temperature of 550ºC ± 5°C and weighted after cooling". This process was repeated using three (3) different samples of the briquettes and results are tabulated in Table 2. "The percentage volatile matter of the sample was determined using equation (2)"

$$PVM = \frac{W_2 - W_3}{W_3} \times 100\% \quad (2)$$

"Where, $W_2$ is the weight of the oven-dried sample in grams; $W_3$ is the weight of the sample after 8 min in the furnace at 550 °C in grams"

### *2.3. Determination of ash content of the briquettes*

"1.5g of the briquettes samples was placed in a closed furnace and burnt completely". "The weight of the residue was taken with an electronic balance". This process was repeated using three (3) different samples of the briquettes and results are tabulated in Table 3. "The percentage weight of residue gives the ash contained in the sample and its determined using equation (3)".

$$PAC = \frac{W_4}{W_2} \times 100\% \quad (3)$$

### *2.4. Determination of fixed carbon of the briquettes*

The percentage fixed carbon (PFC) is given by equation (4) [9] and results are tabulated in Table 4.

$$PFC = 100\% - (PMC + PVM + PAC) \quad (4)$$

### *2.5. Determination of calorific value of the briquettes*

"The calorific value of the briquettes were determined using a bomb calorimeter". "1.5g of the briquettes sample was burnt completely in oxides of oxygen". "The liberated heat was absorbed by the water and calorimeter". "The heat lost by burning briquette was the heat gained by water and calorimeter". "The calorific value (CV) of three (3) different samples of the fuel was calculated from the measured data [5] using equation (5)" and results are tabulated in Table 5.

$$CV = \frac{BFx\ \Delta t - 2.3\ length\ of\ wire}{W} \quad (5)$$

"Where: BF = Burn Factor; Δt = Change of temperature ($t_2$ – $t_1$)ºC; $t_2$ = final temperature; $t_1$ = initial temperature; W = mass of the sample used and BF = constant = 13,257.32"

## 3. Results and discussion

"The physico-chemical properties of the briquettes produced from sawdust were limited to determination of the percentage moisture content, percentage volatile matter, percentage ash content, percentage fixed carbon and calorific value".

**Table 1**. *Percentage values of moisture content for sawdust briquettes*

| Sample | PMC (%) |
|---|---|
| 1 | 5.10 |
| 2 | 5.09 |
| 3 | 4.92 |
| **Average** | **5.04** |

"Table 1, showed the average percentage moisture content for the sawdust briquette produced as 5.04%". "Moisture content of briquette increased with increase in binder concentration and decreased with increase in compaction pressure for all

briquettes [10]". "Results obtained agreed with the recommendation of 5% – 10% moisture content for quality briquettes [11]". "When moisture content is low, briquettes will easily ignite, and higher calorific values are expected from the briquette [9]". The moisture content obtained indicates that the briquettes produced can easily ignite; higher calorific values are expected and are of high quality.

**Table 2.** *Percentage values of volatile matter for sawdust briquettes*

| Sample | PVM (%) |
|---|---|
| 1 | 10.95 |
| 2 | 10.56 |
| 3 | 10.88 |
| **Average** | **10.80** |

"Table 2, showed the average percentage volatile matter for the sawdust briquette produced as 10.80%". "High volatile matter indicates ease of ignition, rapid burning and proportionate increase in flame length but low heating values". "The sawdust briquette produced has a percentage volatile matter that falls within the range 10% to 25% for good quality briquettes [10]". This indicates that the briquette produced can easily ignite, burns rapidly and has proportionate increase in flame lenght.

"**Table 3**. *Percentage values of ash content for sawdust briquettes*

| Sample | PAC (%) |
|---|---|
| 1 | 4.15 |
| 2 | 3.81 |
| 3 | 3.60 |
| **Average** | **3.85** |

"Ash content of briquettes tells the extent of clogging up of the burning medium". "Table 3, showed the average percentage ash content for the sawdust briquette produced as 3.85%". "Low ash content offers higher heating value for briquettes but high ash content results in dust emissions that lead to air pollution [5]". "High ash content lower calorific value which affects combustion volume and efficiency [12]". Since the ash content of the briquette produced is low, it will offer higher heating value.

**Table 4.** *Percentage values of fixed carbon for sawdust briquettes*

| Sample | PFC (%) |
|---|---|
| 1 | 80.50 |
| 2 | 81.24 |
| 3 | 81.10 |
| **Average** | **80.95** |

"Table 4, showed the average percentage fixed carbon for the sawdust briquette produced as 80.95%". "This result agrees with the reported suitability of briquettes with fixed carbon as 80.5% for domestic applications [11]". "The higher the fixed carbon of a fuel, the greater the calorific value, the smaller the volatile matter, the lower the ash and moisture content and the better the quality of the fuel [13]". The percentage fixed cardon obtained from the briquette produced is indicative of the fact that the briquette has high calorific value, lower volatile matter, lower ash and moisture content.

**Table 5.** *Calorific values for sawdust briquettes*

| Sample | CV (KCal/Kg) |
|---|---|
| 1 | 26,914.98 |
| 2 | 26,926.21 |
| 3 | 26,912.88 |
| **Average** | **26,918.02** |

"The calorific value determines the amount of heat energy present in a material". "Results from Table 5, showed that the average percentage calorific value for the sawdust briquette produced is 26918.02KCal/Kg". "The briquette samples produced were of high heating value enough for domestic use and small-scale industrial cottage applications".

## 4. Conclusion

"Fossil fuels and wood fuels are the major source for energy in Nigeria today". "The excess use of these fuels will lead to serious environmental issues like global warming, air pollution and deforestation". "It is high time we convert biomass wastes to useful briquettes, which will be the substitute for these fuels". "Using Crucible furnace and the bomb calorimeter were used to perform the various experiments, this work focused on estimating the heating values of sawdust briquettes to ascertain its suitability for domestic use and small-scale industrial cottage application". "Results obtained indicate that the briquettes made from sawdust have high heating value enough for domestic use and small-scale industrial cottage applications".

## References

[1]. Agidi G., Efomah A.N. and Alake S.A., "Assessment of the Performance of a Disc Actuated Briquette Production Machine Developed at the National Cereals Research Institute, Badeggi," Global Journal of Engineering Science and Research Management, Gbabo., 2(7), (2015), 35–40.

[2]. DahamShyamalee A.D., Amarasinghe, U.S. and Senanayaka, N.S., "Evaluation of different binding materials in forming biomass briquettes with sawdust", International Journal of Scientific and Research Publications, 5(3), (2015), 210–218.

[3]. Khadatkar S.B. and Gangwani D., "Automated Briquetting Machine for Bio Coal Manufacturing,"

International Journal of Engineering and Technical Research (IJETR), 4(1), (2016), 105–111.

[4]. Mordi F.A., "Production of SawDust/Charcoal Briquette for Export (2007) (www.groundreport.com).

[5]. Obi O.F., Akubuo C.O. and Okonkwo W.I., "Development of an Appropriate Briquetting Machine for Use in Rural Communities," International Journal of Engineering and Advanced Technology, 2(4), (2013), 578–582.

[6]. Romallosa A.R.D. and Kraft E., "Feasibility of biomass briquette production from municipal wastestreams by integrating the informal sector in the Philippine," Resources, 6, (2017), 12.

[7]. Garrido M.A., Conesa J.A., Garcia M.D., "Characterization and production of fuel briquettes made from biomass and plastic wastes", Energies, 10, (2017), 850.

[8]. Onuegbu T.U., Ogbu I.M., Ejikeme C., "Comparative analyses of densities and calorific values of wood and briquettes samples prepared at moderate pressure and ambient temperature," Int. J. Plant Anim. Environ. Serv., 2, (2011), 40–45.

[9]. Akowuah J., Kemausuor F. and Mitchual J.S., "Physiochemical characteristics and market potential of sawdust charcoal briquettes," International Journal of Energy and Environmental Engineering, 3(20), (2012), 1−6.

[10]. Akintaroa A.O., Musab A.I., Ajobo J.A. and Oyewusi T.F., "The Potentials of Using Carbonized Corncob to Produced Briquettes as an Alternative to Fuel wood," FUTA Journal of Research in Sciences, 13(1), (2017), 137–145

[11]. Pallavi H.V., Srikantaswamy S., Kiran B.M., Vyshnavi D.R. and Ashwin C.A., "Briquetting Agricultural Waste as an Energy Source," Journal of Environmental Science, Computer Science and Engineering & Technology, 2(1), (2013), 160–172.

[12]. Chaney J.O., "Combustion Characteristics of Biomass Briquettes," Fuel Processing Technology, 30(2), (2010), 219–230.

[13]. Moore W., and Johnson D., "Procedures for the Chemical Analysis of Wood and Wood Products," Forest Products Laboratory Department of Agriculture. Madison, U.S.A 1999.

MANAS Journal of Engineering
ISSN 1694-7398 | e-ISSN 1694-7398

*Volume 10, Issue 1, (2022) Pages 21-34*
*https://doi.org/10.51354/mjen. 943729*

# Structural and compressibility properties of weft-knitted rib fabrics from glass yarn

Mehmet Erdem İnce

Gaziantep University, Engineering Faculty, Textile Engineering Department, 27310 Gaziantep, Turkey
einceg@gantep.edu.tr, meince@ncsu.edu, ORCID: 0000-0001-7537-9172

**ABSTRACT**

The structural and compressibility properties of the weft-knitted glass yarn fabrics from 1x1, 2x2, English, and fisherman rib architectures were investigated in this study. Due to their tight structures; 2x2 and fisherman rib fabric architectures exhibited higher loop density, and shorter loop length than 1x1 and English rib fabric architectures. English and fisherman rib fabric architectures displayed higher fiber volume fraction than 1x1 and 2x2 rib architectures in multi-layer compaction and recovery tests where the pressure was varied between 2 and 200 kPa. Number of layer increased the fiber content that pointed the nesting between the fabric layers. As a result of lack of complete recovery from compression; the fabrics exhibited lower thicknesses (i.e. higher fiber volume fractions) during the recovery periods than they did during the compression periods. A second order polynomial regression model with 0,89 $R^2$ (coefficient of determination) was developed to estimate the fiber volume fraction by means of knit architecture, number of fabric layers, pressure, and measurement period.

**ARTICLE INFO**

***Research article***

*Received: 27.05.2021*
*Accepted: 7.04.2022*

***Keywords:***
*Glass yarn,*
*weft-knitted fabric,*
*fabric structural properties,*
*fabric compressibility*

**Corresponding author*

## 1 Introduction

Due to their better specific strength, impact resistance, and non-corrosible features than the conventional materials; the use of fiber reinforced polymers (FRPs) is increasing in all segments of industrial areas ranging from automotive to marine, aerospace, and defense. FRPs principally consist of two constituents – fiber and polymeric resin – while the low density resin surrounding the fibers protects them from severe environmental conditions and transfers the applied load on to them; high performance fiber improves mechanical properties of the integrated body. The mechanical properties of FRPs for a given direction are controlled by the relative amount (volume fraction) of fibers lying in that direction. This makes the FRPs designable depending on the forces applied during their use [1, 2].

Fiber volume fraction (FVF) of a FRP is a function of the reinforcement's structural and compressibility properties. Therefore, measuring the reinforcement fabric's response in compression and relaxation periods plays a critical role to predict the FVF of the composite product. The compaction behaviour of the reinforcement is also central to design a firm mold and to estimate the mold filling time [3-5]. This study is about the structural properties and compaction behaviors of glass yarn weft knit fabrics and the relevant studies are given in the following paragraphs.

Pearce and Summerscales [6] studied compaction behaviour of plain woven glass fabrics, where one-layer fabric displayed higher fiber content than multi-layer fabrics. While lack of nesting was observed between layers, the fiber content was increased by the repeated compaction. Lekakou, Johari and Bader [7] developed a nonlinear elastic compaction model and confirmed it with the liquid molding of layered 2D plain woven glass fabrics. The number of fabric layers decreased the in-plane resin flow permeability, which pointed out the inter-layer nesting.

Robitaille and Gauvin [8] reviewed the studies about the compaction and relaxation of glass fiber nonwoven and woven fabrics. The researchers reported that while both the number of layers and number of compaction cycles increased the stiffness (compaction resistance), only the number of cycles improved the fiber content due to lack of nesting between layers. Luo and Verpoest [9] measured the compactions of a multi-layer fabric (a plain weft-knitted glass fabric was sewn between two plies of random glass mats), its constituents, and a 2D plain woven glass fabric. The number of layers improved the fiber content of the plain knitted fabric that was associated with the interlocked loopy fabric structure allowing nesting.

Potluri and Sagar [10] developed an energy-minimization-based compaction model considering the compression and bending of the yarn, and confirmed it via 2D and 3D woven

glass fabrics. The researchers measured the nesting for 2D fabric and obtained good agreement between the model and the practice. Lomov and Molnár [11] studied the existence of nanofiber interleaves on the compaction of 2D plain woven carbon fiber fabrics. The scientists stated that successive compaction cycles improved the fiber content through increasing the stiffness of the stack, and both fabric stacks with/without nanofiber exhibited the nesting.

Yousaf, Potluri and Withers [12] examined the influence of pattern (plain, twill and sateen) and the number of layers on the compression of 2D woven glass fabrics. Due to its tight and less bendable structure, the plain woven fabric exhibited the highest compaction resistance. While all weave patterns displayed nesting, the plain weave showed the highest nesting that was attributed to its shorter yarn float length.

Due to its low cost, flexible, and fast production; the use of weft-knitting in composite industry is growing. Easily stretchable and formable weft knit fabrics make it possible to produce complex and seamless 2D or 3D preforms in one step. Because of their 3D form loops and porous structure allowing nesting, the composites reinforced by weft knit fabrics show improved impact resistance as compared with the other textile fabrics.

However, due to their loose structure and low load-carrying capability caused by low fiber content with lack of fiber directionality; weft-knitted fabrics are disadvantageous for in-plane strengthening [13–16]. This disadvantage of the weft knit fabrics makes their compaction critical. However, no particular attention was paid to the compaction of glass yarn weft knitted fabrics with various architectures in the literature. Focus in previous studies was mostly directed to the compaction of commercially available mat and woven fabrics. We hypothesized that the compaction of glass yarn weft knit fabrics yarn can be controlled by knit architecture and number of fabric layers.

## 2. Materıal and methods

The three-ply E-glass multi-filament yarn with a single-ply yarn count of 136 tex and fiber diameter of 9 microns was used to produce fabrics on the Brother KH-864 flat, weft knitting machine with 5 gauge fineness. Table 1 shows the experimental plan. Figure 1 illustrates technical notations and hand-drawn views of the weft knit fabrics; Figure 2 shows the simulations of the knits from filament yarn; and Figure 3 displays the real pictures of the knit fabrics, both under tension on the knitting machine and on the bench in stress-free form.

**Table 1.** *Experimental study plan*

| Variable: | Knit architecture | Number of fabric layer | Measurement period | Pressure [kPa] |
|---|---|---|---|---|
| Levels: | 1x1 rib<br>2x2 rib<br>English rib<br>Fisherman rib | 1<br>2<br>3 | compression recovery | 2 - 200 |

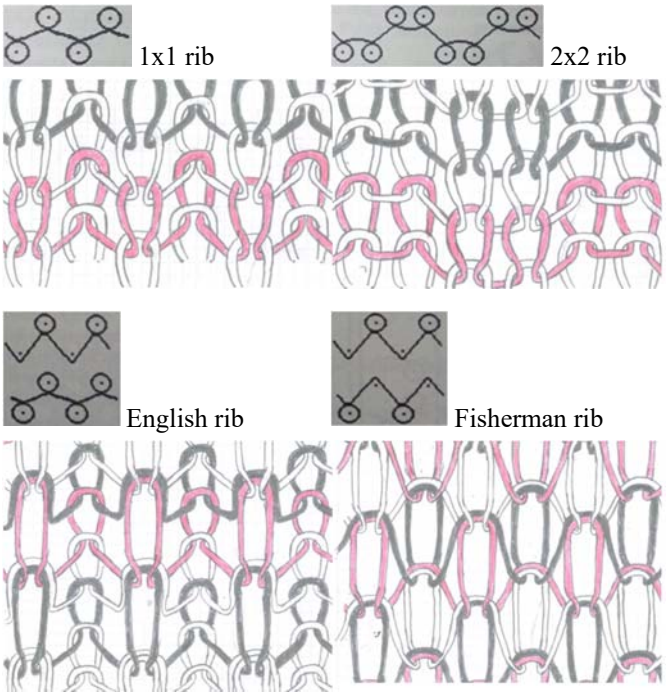


**Figure 1.** *Technical notations [17, 18] and hand-drawn views of the knit architectures*

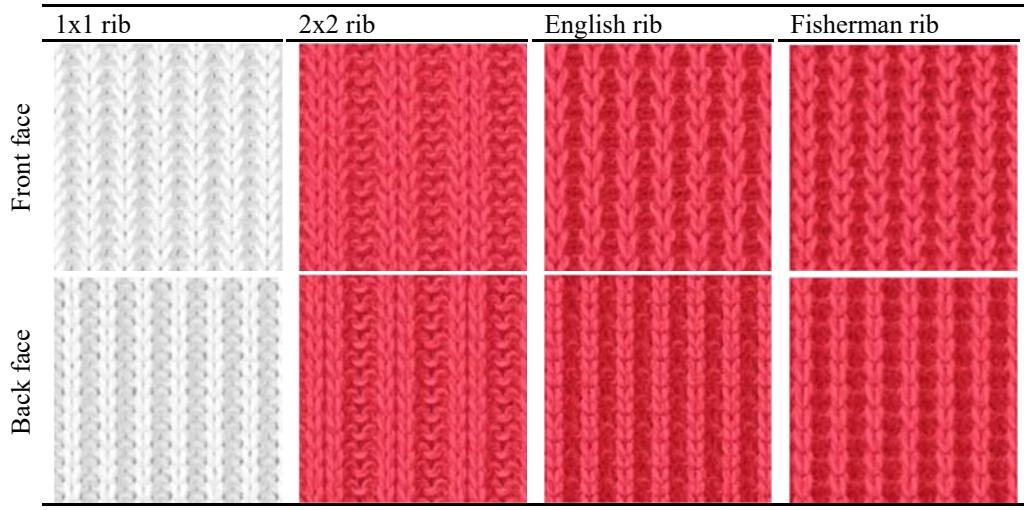


**Figure 2.** *The simulations of the knit architectures from filament yarn*

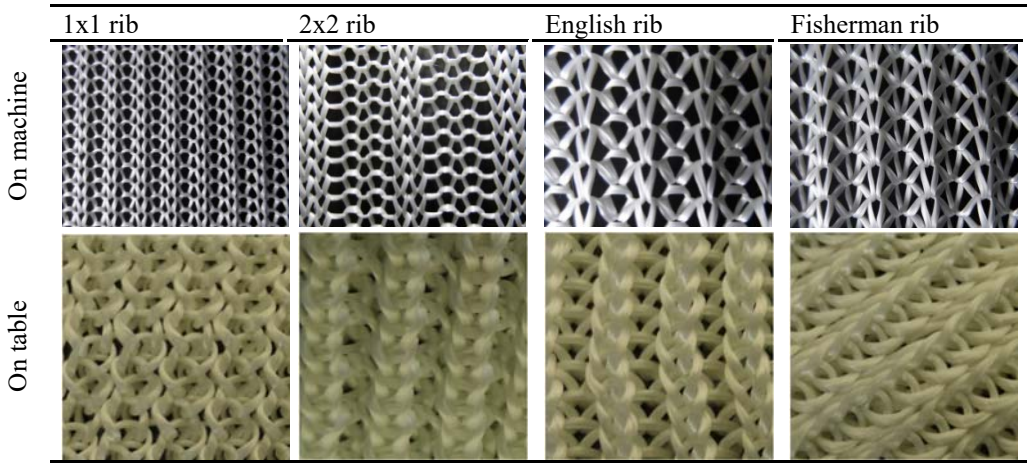


**Figure 3.** *Real pictures of the knit architectures*

*2.1. Measurement of physical and structural properties of single-layer fabrics*

*2.1.1. Thickness*

The digital thickness gauge (Figure 4) was used to measure the thicknesses of the fabrics. The gauge has gradually-increased weights to apply pressures from 2 to 200 kPa. Thicknesses measured under 200 kPa were utilized for the thickness and fiber content analyses of the one-layer fabrics.

**Figure 4.** *The thickness gauge and its additional weights*

*2.1.2. Areal density*

The weights of 5x5 cm$^2$ single-layer pieces cut from fabrics by a special die cutter were measured in line with ASTM D3776 [19]. The fiber volume percent were calculated using the thickness (measured under 200 kPa pressure) and the areal density along with Equation 1 where $A_f$, $\rho_f$ , $t$ are fabric areal density, fiber volumetric density, and fabric thickness, respectively. Glass fiber material density was assumed to be 2,5 g/cm$^3$.

$$Fiber\ volume\ percent\ [\%] = \frac{A_f}{\rho_f * t} * 100 \qquad (1)$$

*2.1.3. Course density, wale density, and loop length*

ASTM D8007 [20] was followed to determine the course and wale densities. The loop density (number of loops for every centimeter square) was calculated from the product of the relevant course and wale densities. The loop length was measured according to BS 5441 [21].

*2.2. Measurement of the thickness of single and multi-layer fabrics*

Knitted fabrics (in single-, or multi-layer form) were placed on the anvil of the digital thickness gauge (Figure 4). The presser foot with compaction pressure of 2 kPa was lowered onto the fabric. After at least 30-second wait, once the gauge's display became invariant, the thickness was recorded. Thereafter, extra masses were sequentially added on the presser foot. After the adding of each mass, at least 30 seconds was waited to record the thickness on the steady screen of the thickness gauge. When the compaction was terminated at 200 kPa, the masses on the presser foot were removed sequentially and the relaxation thickness for each removal was recorded. The each measured thickness was converted into fiber volume percent using Equation 2 where $n$, $A_f$, $\rho_f$, $t$ are number of fabric layers, average areal density of single-layer fabric, fiber volumetric density, and fabric stack thickness, respectively. A trial form of the Jump® [22] software was used for drawing graphs and analysis.

$$Fiber\ volume\ percent\ [\%] = \frac{n * A_f}{\rho_f * t} * 100 \qquad (2)$$

## 3. Results and discussion

*3.1. Physical and structural properties of single-layer fabrics*

*3.1.1. Thickness, areal density, and fiber volume percent*

Tuck stitches contracted English and fisherman ribs in both width and length direction and increased their thickness (Figure 5 and Table 2). Similarly, the number and position of the tuck stitches in single-bed cotton yarn weft knit fabrics significantly affected the properties of the fabric and the tuck stitch increased the fabric thickness and areal density in the previous studies [23-25]. İnce and Yıldırım [26] also observed that the tuck stitch increased the thickness and areal density in single-bed glass yarn weft knit fabrics because of left to right turning and nesting of the loop bars.

On the other hand, the successive placement of binary face and back plain loop bars increased the internal tension that dramatically narrowed the knit architecture of 2x2 rib in the course direction after removal from the machine. Thus, due to shortening in the fabric width direction, 2x2 rib exhibited higher thickness than 1x1 rib. Pairwise comparisons showed that the thickness difference between fisherman and 2x2 ribs did not reach a statistically significant level, as was the difference between English and 1x1 ribs. The low internal stress resulting from the architecture revealed a loose knit structure for the 1x1 rib fabric that exhibited the lowest thickness. Parallel results were detected for the influences of knit architecture on areal density and fiber volume percent. The 2x2 rib knit architecture and the architectures incorporating tuck stitches showed higher areal density and fiber content than 1x1 rib.

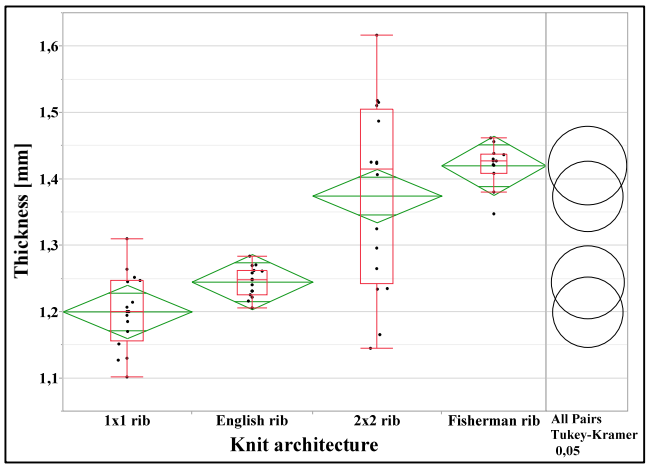


a

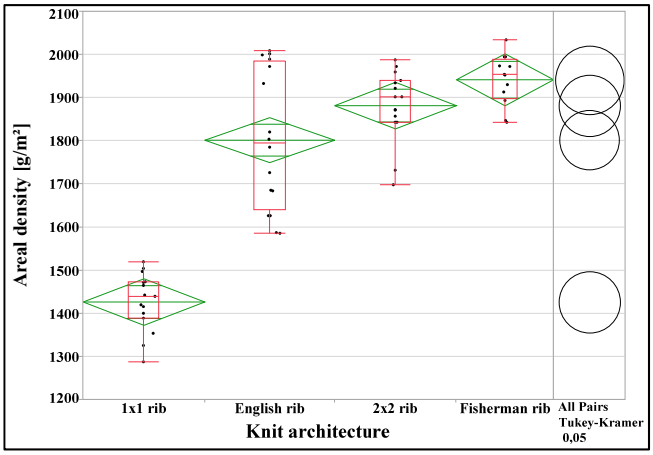


b

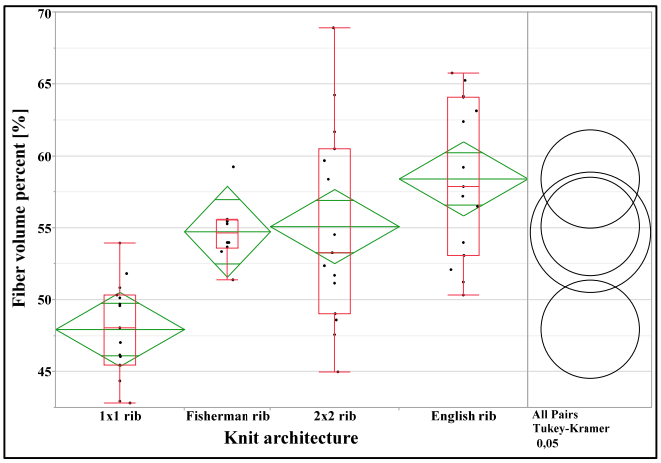


**c**

**Figure 5.** *The effect of knit architecture on thickness (a), areal density (b) and fiber volume percent (c)*

**Note:** The space between the upper and lower corners of the green parallelogram represents the 95% confidence interval. One comparison circle is given in the right-hand column for the mean of each knit architecture level. Comparison circles representing significantly different means are either non-intersecting or slightly intersecting.

**Table 2.** *The effect of knit architecture on thickness, areal density and fiber volume percent*

| Property | Knit architecture | | | | n | mean | sd | LL | UL | p-value |
|---|---|---|---|---|---|---|---|---|---|---|
| Thickness [mm] | Fisherman rib | A | | | 13 | 1,42 | 0,03 | 1,40 | 1,44 | < 0,0001 |
| | 2x2 rib | A | | | 16 | 1,37 | 0,14 | 1,30 | 1,45 | |
| | English rib | | B | | 15 | 1,24 | 0,02 | 1,23 | 1,26 | |
| | 1x1 rib | | B | | 16 | 1,20 | 0,06 | 1,17 | 1,23 | |
| Areal density [g/m$^2$] | Fisherman rib | A | | | 12 | 1941,78 | 59,18 | 1904,2 | 1979,4 | < 0,0001 |
| | 2x2 rib | A | B | | 15 | 1881,99 | 82,08 | 1836,5 | 1927,4 | |
| | English rib | | B | | 16 | 1801,83 | 161,47 | 1715,8 | 1887,9 | |
| | 1x1 rib | | | C | 15 | 1426,46 | 66,99 | 1389,4 | 1463,6 | |
| Fiber volume percent [%] | English rib | A | | | 15 | 58,41 | 5,45 | 55,40 | 61,43 | < 0,0001 |
| | 2x2 rib | A | | | 15 | 55,10 | 6,84 | 51,31 | 58,88 | |
| | Fisherman rib | A | | | 10 | 54,74 | 2,05 | 53,27 | 56,21 | |
| | 1x1 rib | | B | | 15 | 47,94 | 3,31 | 46,11 | 49,78 | |

**Note:** Levels not united with the same alphabetical capital letter are significantly different (α = 0,05). **n**: number of measurements, **sd**: standard deviation, **LL**: lower limit, **UL**: upper limit. The limits are based on a 95% confidence level. p-values less than 0,05 are indicative of statistical significance and are red.

*3.1.2. Course-, wale-, and loop-density*

The knit architecture played a statistically significant role on course-, wale-, and loop-density; and the knit architecture of 2x2 ribs overwhelmed the other architectures in terms of these densities (Figure 6, Table 3). The fabric with 2x2 rib architecture showed a dramatic contraction in the course direction that increased the fabric's tightness. After removal of the fabric from the machine, the tuck stitches on both faces of the fisherman rib fabric rotated the loop bars in clockwise direction (Figure 3). As a result of this rotation, the loop bars nested under each other that increased the loop density of the fisherman rib fabric. On the other hand, because of its loose structure with less internal tension, 1x1 rib fabric showed the lowest loop density.

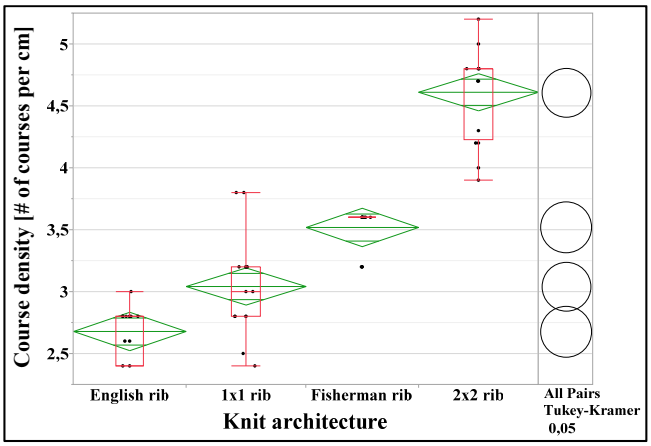


**a**

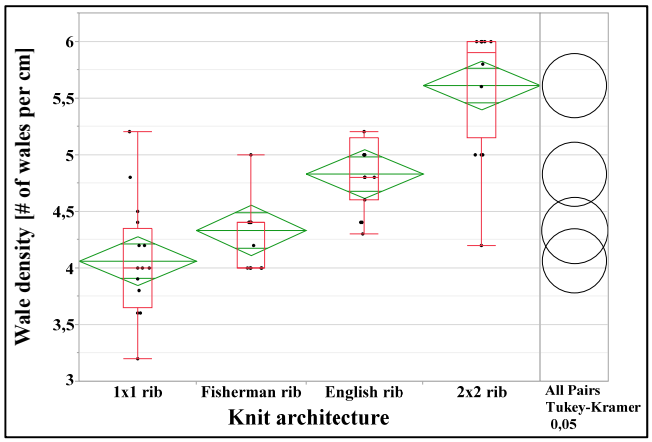


b

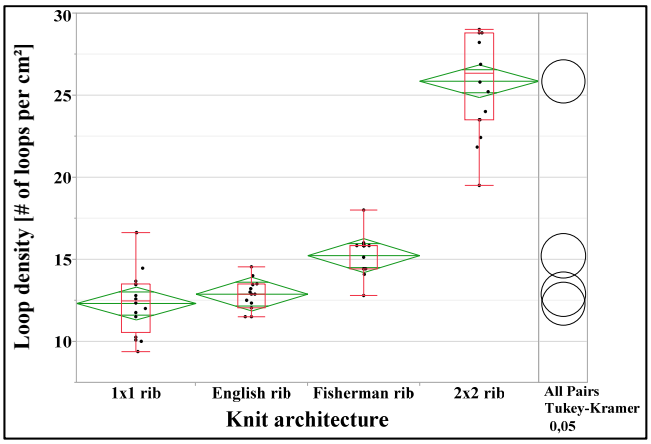


c

**Figure 6.** *The effects of knit architecture on course- (a), wale- (b), and loop-density (c)*

**Table 3.** *The effects of knit architecture on course-, wale-, and loop-density*

| Property | Knit architecture | | | | n | mean | sd | LL | UL | p-value |
|---|---|---|---|---|---|---|---|---|---|---|
| Course density [#/cm] | 2x2 rib | A | | | 16 | 4,61 | 0,37 | 4,41 | 4,81 | < 0,0001 |
| | Fisherman rib | | B | | 15 | 3,52 | 0,17 | 3,43 | 3,61 | |
| | 1x1 rib | | | C | 16 | 3,04 | 0,38 | 2,84 | 3,25 | |
| | English rib | | | | D | 15 | 2,68 | 0,20 | 2,57 | 2,79 |
| Wale density [#/cm] | 2x2 rib | A | | | 16 | 5,61 | 0,54 | 5,32 | 5,90 | < 0,0001 |
| | English rib | | B | | 16 | 4,83 | 0,30 | 4,67 | 4,99 | |
| | Fisherman rib | | | C | 15 | 4,33 | 0,33 | 4,15 | 4,51 | |
| | 1x1 rib | | | C | 16 | 4,06 | 0,50 | 3,80 | 4,33 | |
| Loop density [#/cm²] | 2x2 rib | A | | | 16 | 25,86 | 3,09 | 24,22 | 27,51 | < 0,0001 |
| | Fisherman rib | | B | | 15 | 15,24 | 1,21 | 14,57 | 15,91 | |
| | English rib | | | C | 15 | 12,90 | 1,02 | 12,33 | 13,46 | |
| | 1x1 rib | | | C | 16 | 12,32 | 1,88 | 11,32 | 13,32 | |

### *3.1.3 Loop length*

Among many structural parameters, the loop length is the most effective one that controls the properties of the knitted fabric. The shorter the loop length, the tighter (more compact) the fabric is. The knit architecture showed a statistically significant effect on the loop length (Figures 7, and Table 4). While the 1x1 rib fabric exhibited the longest loop length, the fisherman rib demonstrated the shortest one. The presence of tuck stitches in English and fisherman ribs, and the shrinkage in the direction of knitting line in 2x2 rib decreased the loop length.

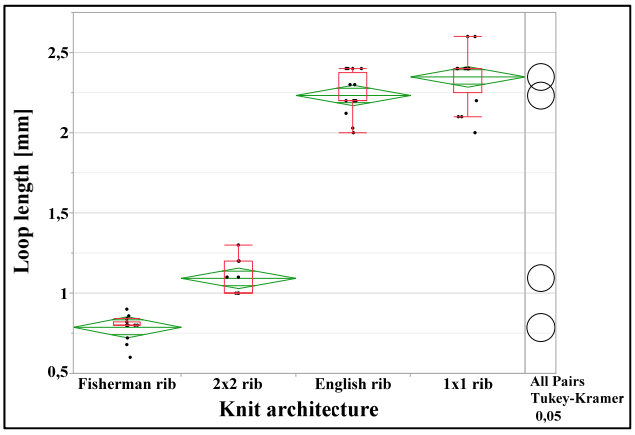


**Figure 7.** *The effects of knit architecture on loop length*

**Table 4.** *The effects of knit architecture on loop length*

| | Knit architecture | | | | n | mean | sd | LL | UL | p-value |
|---|---|---|---|---|---|---|---|---|---|---|
| Loop length [mm] | 1x1 rib | A | | | 16 | 2,35 | 0,17 | 2,26 | 2,44 | < 0,0001 |
| | English rib | A | | | 16 | 2,23 | 0,13 | 2,17 | 2,30 | |
| | 2x2 rib | | B | | 16 | 1,09 | 0,12 | 1,03 | 1,16 | |
| | Fisherman rib | | | C | 15 | 0,79 | 0,07 | 0,75 | 0,83 | |

### *3.2. Thickness analysis based on multi-layer fabric thickness measurement*

#### *3.2.1. The effect of knit architecture on thickness*

The 2x2 rib fabric displayed the highest thickness, while 1x1 rib fabric showed the lowest one (Figure 8 and Table 5). The only statistically significant difference in thickness was observed between 1x1 and 2x2 rib fabrics. The thickness difference between the other knit architectures could not reach a statistically significant level (α = 0,05). These findings are in line with the analysis of the influence of knit architecture on the thickness of single-layer fabrics, which was measured under 200 kPa compaction pressure (Figure 5-a, Table 2).

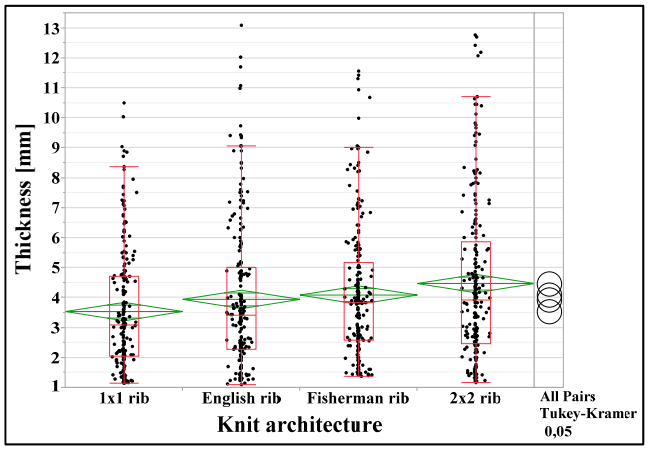


**Figure 8.** *The effect of knit architecture on single- and multi-layer fabric thicknesses*

**Table 5.** *The effect of knit architecture on single- and multi-layer fabric thicknesses*

| Property | Knit architecture | | | n | mean | sd | LL | UL | p-value |
|---|---|---|---|---|---|---|---|---|---|
| Thickness [mm] | 2x2 rib | A | | 225 | 4,48 | 2,66 | 4,13 | 4,82 | 0,0004 |
| | Fisherman rib | A | B | 225 | 4,09 | 2,23 | 3,80 | 4,38 | |
| | English rib | A | B | 225 | 3,95 | 2,42 | 3,63 | 4,27 | |
| | 1x1 rib | | B | 225 | 3,54 | 2,01 | 3,28 | 3,80 | |

#### *3.2.2. The effect of knit architecture on fiber content*

Fisherman rib knit architecture exhibited the highest fiber volume percent, while 1x1 rib knit architecture showed the lowest one (Figure 9 and Table 6). Significant fiber content change (α = 0,05) was only observed between fisherman and 1x1 rib architectures. The tuck stitches narrowed the fabric in both width and length direction that formed a compact and tight fabric structure. In 2x2 rib knit fabric architecture: the side-by-side placement of binary face and back loop bars increased the fabric internal tension in the course direction. After removal of the fabric from the machine; this inner pull shrank the fabric in the course direction, and thus increased the tightness of the fabric. These findings agreed with the Figure 5-c, Table 2 where the influence of knit architecture on the fiber volume percent of single-layer fabrics under 200 kPa compaction pressure was displayed.

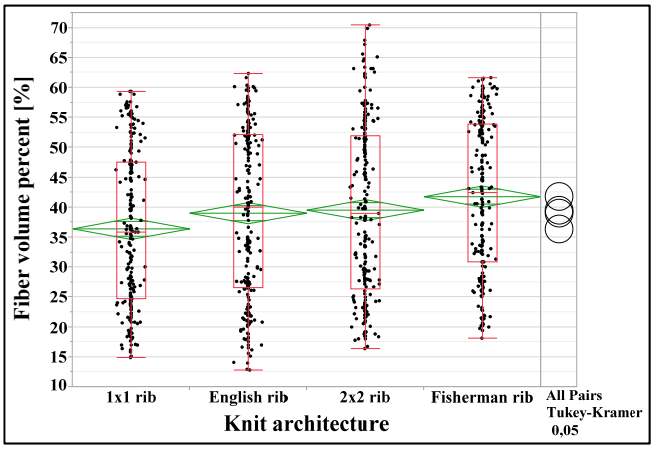


**Figure 9.** *The effect of knit architecture on fiber volume percent*

**Table 6.** *The effect of knit architecture on fiber volume percent*

| Property | Knit architecture | | | n | mean | sd | LL | UL | p-value |
|---|---|---|---|---|---|---|---|---|---|
| Fiber volume percent [%] | Fisherman rib | A | | 225 | 41,79 | 12,66 | 40,13 | 43,46 | **0,0005** |
| | 2x2 rib | A | B | 225 | 39,54 | 14,37 | 37,65 | 41,43 | |
| | English rib | A | B | 225 | 39,03 | 14,16 | 37,16 | 40,89 | |
| | 1x1 rib | | B | 225 | 36,42 | 12,75 | 34,75 | 38,10 | |

*3.2.3. The effect of the number of fabric layers on the normalized thickness and fiber volume percent*

The number of fabric layers decreased the normalized thickness (Figure 10-a, and Table 7). Although this decrease did not reach a statistically significant level, it proved the nesting tendency in compacted multi-layer weft-knitted fabrics. On the other hand, the number of fabric layers increased the fiber volume percent at a statistically significant level (Figure 10-b and Table 7). This result, parallel with Luo and Verpoest's study [9] where the nesting was observed for the weft-knitted glass yarn plain fabric, also proved the nesting in weft-knitted glass yarn rib fabrics with various architectures. The stretchable and flexible weft knitted fabrics from 3D, porous and intertwined loops exhibit higher nesting tendency than woven and random mat fabrics. Lack of important difference (α = 0,05) was detected between 3-layer fabrics with single- and 2-layer fabrics in terms of fiber content. However, the 2-layer fabric exhibited significantly greater fiber volume percent than the one-layer fabric.

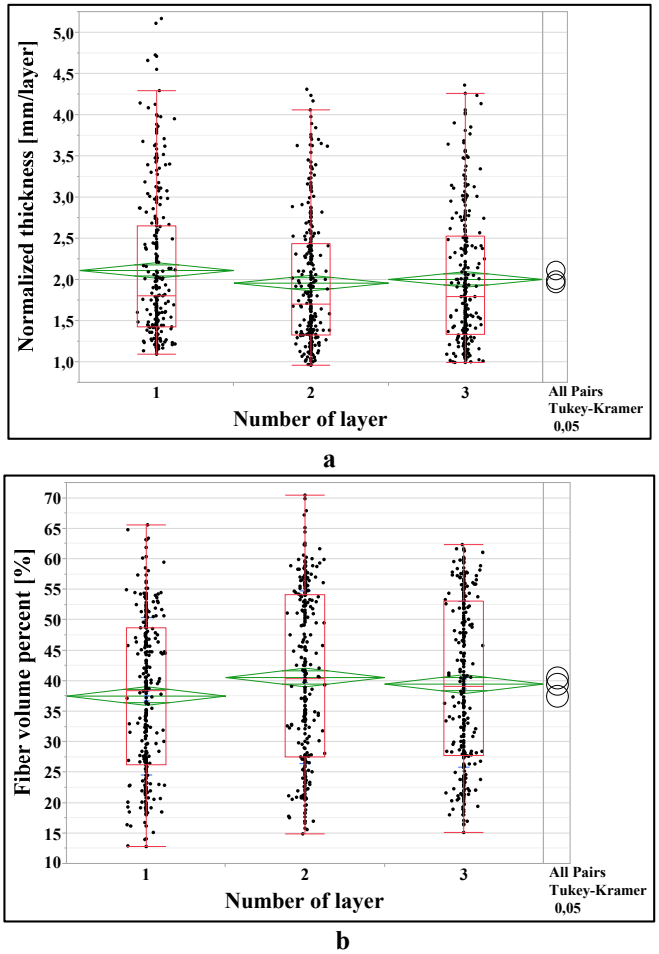


**Figure 10.** *The effects of the number of fabric layers on normalized thickness (a) and fiber volume percent (b)*

**Table 7.** *The effects of the number of fabric layers on normalized thickness and fiber volume percent*

| Property | Number of layer | | | n | mean | sd | LL | UL | p-value |
|---|---|---|---|---|---|---|---|---|---|
| Normalized thickness [mm/layer] | 1 | A | | 300 | 2,11 | 0,88 | 2,01 | 2,21 | 0,0654 |
| | 3 | A | | 300 | 2,00 | 0,80 | 1,91 | 2,10 | |
| | 2 | A | | 300 | 1,96 | 0,80 | 1,87 | 2,05 | |
| Fiber volume percent [%] | 2 | A | | 300 | 40,57 | 14,18 | 38,96 | 42,18 | **0,0210** |
| | 3 | A | B | 300 | 39,48 | 13,60 | 37,94 | 41,03 | |
| | 1 | | B | 300 | 37,52 | 12,92 | 36,06 | 38,99 | |

*3.2.4. The effect of force type (compression or recovery period) on thickness and fiber content*

Because the first compaction crushed and repositioned the fibers in the fabric stacks, the stacks exhibited lower thickness during the subsequent recovery (relaxation) period (Figure 11-a and Table 8). Lower thicknesses in the recovery periods increased the fiber volume percent calculated in these periods.

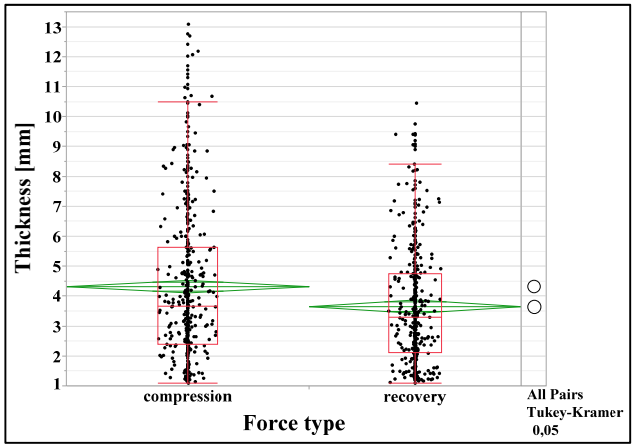


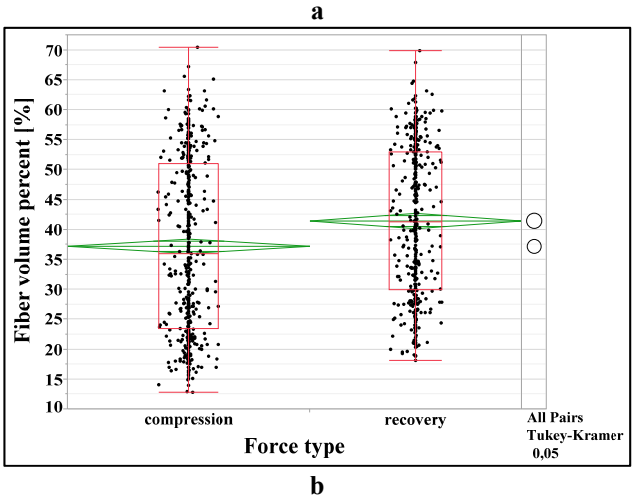


**Figure 11**. *The effect of measurement period on thickness (a) and fiber content (b)*

**Table 8.** *The effect of measurement period on thickness and fiber content*

| Property | Measurement period | | n | mean | sd | LL | UL | p-value |
|---|---|---|---|---|---|---|---|---|
| Thickness [mm] | compression | A | 480 | 4,33 | 2,61 | 4,09 | 4,56 | < 0,0001 |
| | recovery | B | 420 | 3,66 | 1,99 | 3,47 | 3,85 | |
| Fiber volume percent [%] | recovery | A | 420 | 41,44 | 12,49 | 40,24 | 42,64 | < 0,0001 |
| | compression | B | 480 | 37,23 | 14,26 | 35,95 | 38,51 | |

*3.2.5. The effect of pressure on fiber content*

Figure 12 shows the relationship (grouped by compression and recovery periods) between pressure and fiber volume percent. The effect of pressure on the fiber volume percent exhibited a power-law character. The fiber volume percent increased vertically in the initial pressure steps then slowed down and evolved into a plateau in the higher pressure steps. Due to crushing and stiffening effect of the initial compaction, the recovery curve exhibited a higher fiber content than the compression curve did. This result was consistent with the previous studies [6, 8, 11] indicating that repeated relaxation and reloading to maximum compaction increased the rigidity and the fiber content of the fabric stack. The power law equations developed for the overall compression and recovery curves plotted in Figure 12 are given below.

General compression behaviour ($R^2$: 0,92; p-value < 0,0001):

$$Fiber\ volume\ percent\ [\%] = 14{,}94 * (Pressure\ [kPa])^{0{,}25} \quad (3)$$

General recovery behaviour ($R^2$: 0,90; p-value < 0,0001):

$$Fiber\ volume\ percent\ [\%] = 21{,}00 * (Pressure\ [kPa])^{0{,}21} \quad (4)$$

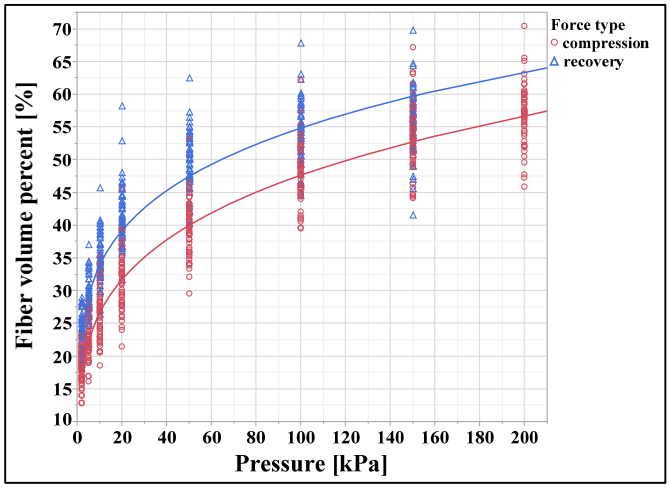


**Figure 12.** *The effect of pressure on fiber volume percent*

*3.2.6. Development of fiber volume percent estimation equation*

A regression equation was developed 1) to estimate the fiber volume percent using experimental study plan input variables and 2) to illustrate in detail how the fiber volume percent is influenced by the input variables. Among the various options, the second degree polynomial model resulted in the highest $R^2$ (0,888 i.e. 88,8% of the total variation in the fiber volume percent results was explained by the model) and the residuals with a nearly normal distribution. The ANOVA test for the model resulted in a p-value of less than 0,0001 that indicated the significance of the model. The black dots given in Figure 13-a were as close as possible to the linear red continuous line with the slope of one and the black dots given in Figure 13-b were almost symmetrically distributed on both sides of the blue dashed horizontal zero line. All these reinforced the reliability of the developed model. The model residuals showed a nearly normal (p = 0,0376) distribution (Figure 13-c). Equation 5 shows the developed estimation equation. All the inputs and their coefficients given in Equation 5 were statistically significant (p-values less than 0,05).

$$
\begin{aligned}
&Fiber\ volume\ percent\ [\%] \\
&= 28{,}13 \\
&+ Match(Knit\ architecture)\begin{pmatrix} 1x1\ rib & \Rightarrow & -3{,}49 \\ 2x2\ rib & \Rightarrow & -0{,}95 \\ Fisherman\ rib & \Rightarrow & 1{,}84 \\ English\ rib & \Rightarrow & 2{,}59 \end{pmatrix} \\
&+ Match(Number\ of\ layer)\begin{pmatrix} 1 & \Rightarrow & 0 \\ 2 & \Rightarrow & 2{,}98 \\ 3 & \Rightarrow & 1{,}98 \end{pmatrix} \\
&+ Match(Force\ type)\begin{pmatrix} compression & \Rightarrow & -3{,}28 \\ recovery & \Rightarrow & 3{,}28 \end{pmatrix} + 0{,}27 \\
&* (Pressure\ [kPa]) + (Pressure\ [kPa] - 58{,}31) \\
&* (Pressure\ [kPa] - 58{,}31) * (-0{,}001278)
\end{aligned}
\tag{5}
$$

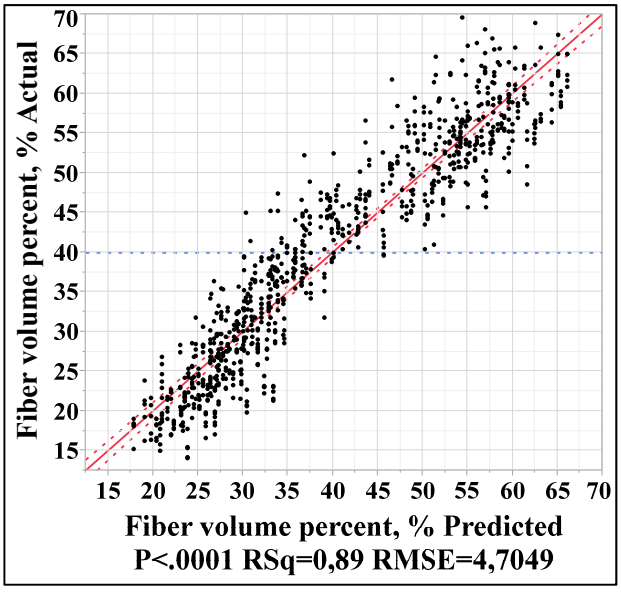


a

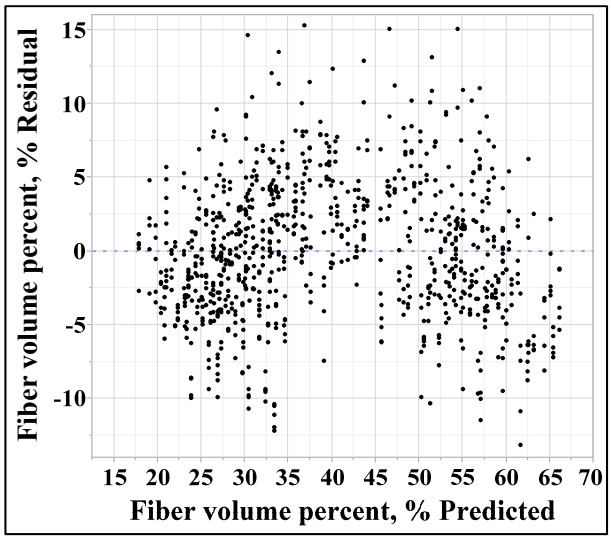


b

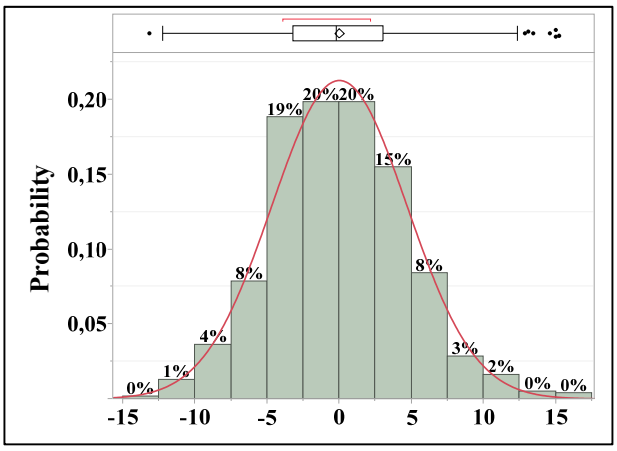


c

**Figure 13.** *Predicted versus actual (a), predicted versus residual (b), and the distribution of residual (c) fiber volume percents*

The prediction profilers given in Figure 14 reveal the effects of number of fabric layers, force type and pressure on the fiber volume percent of fabrics with different knit architecture. At all of the knit architecture levels, the other input variables exhibited the same effect on the fiber volume percent. The number of fabric layers increased the fiber volume percent and the 2-layer fabric stacks exhibited higher fiber volume percent than the 3-layer fabric stacks. Due to the hardening effect of the first compression, the fabrics showed a higher fiber volume percentage during the recovery period than the compression period. The relationship between pressure and fiber volume percent conforms to the power law model: for low pressures the curve increases perpendicularly and then it becomes a plateau for high pressures. The parallels observed in the interaction plots matrix indicated the lack of interactions between input variables (Figure 15). Figure 16 illustrates the effects of knit architecture, pressure, number of layer, and force type (compression or recovery period) on fiber volume percent in the form of 3D graphs.

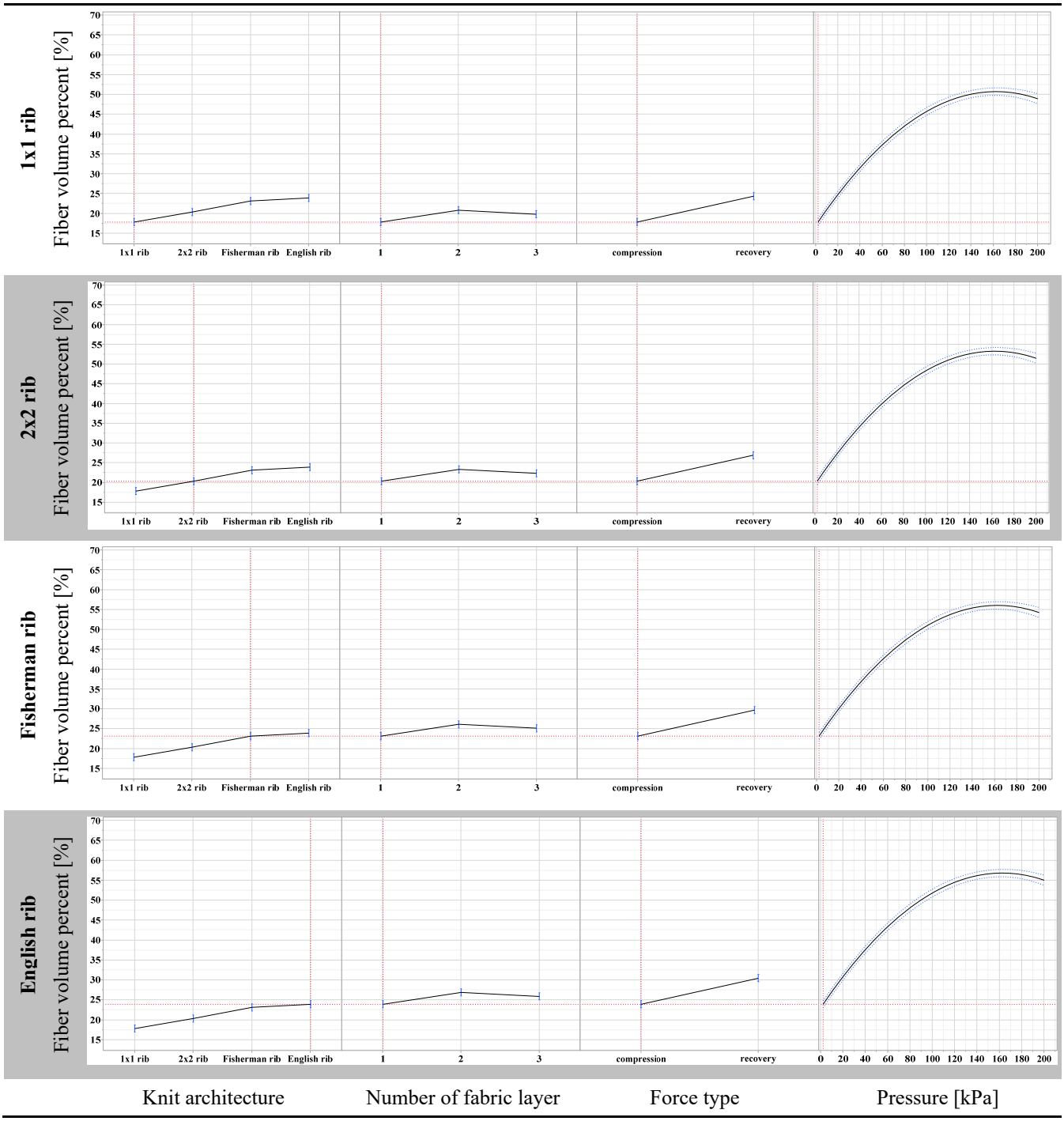


**Figure 14.** *The prediction profilers for fiber volume percent*

**Note**: The red vertical dashed line for each input variable on the horizontal axis indicates the current level of the input variable. The red horizontal dashed line indicates the fiber volume percent for the selected levels of the input variables. Continuous vertical error bar lines and the dashed lines showing the 95% confidence interval limits are blue.

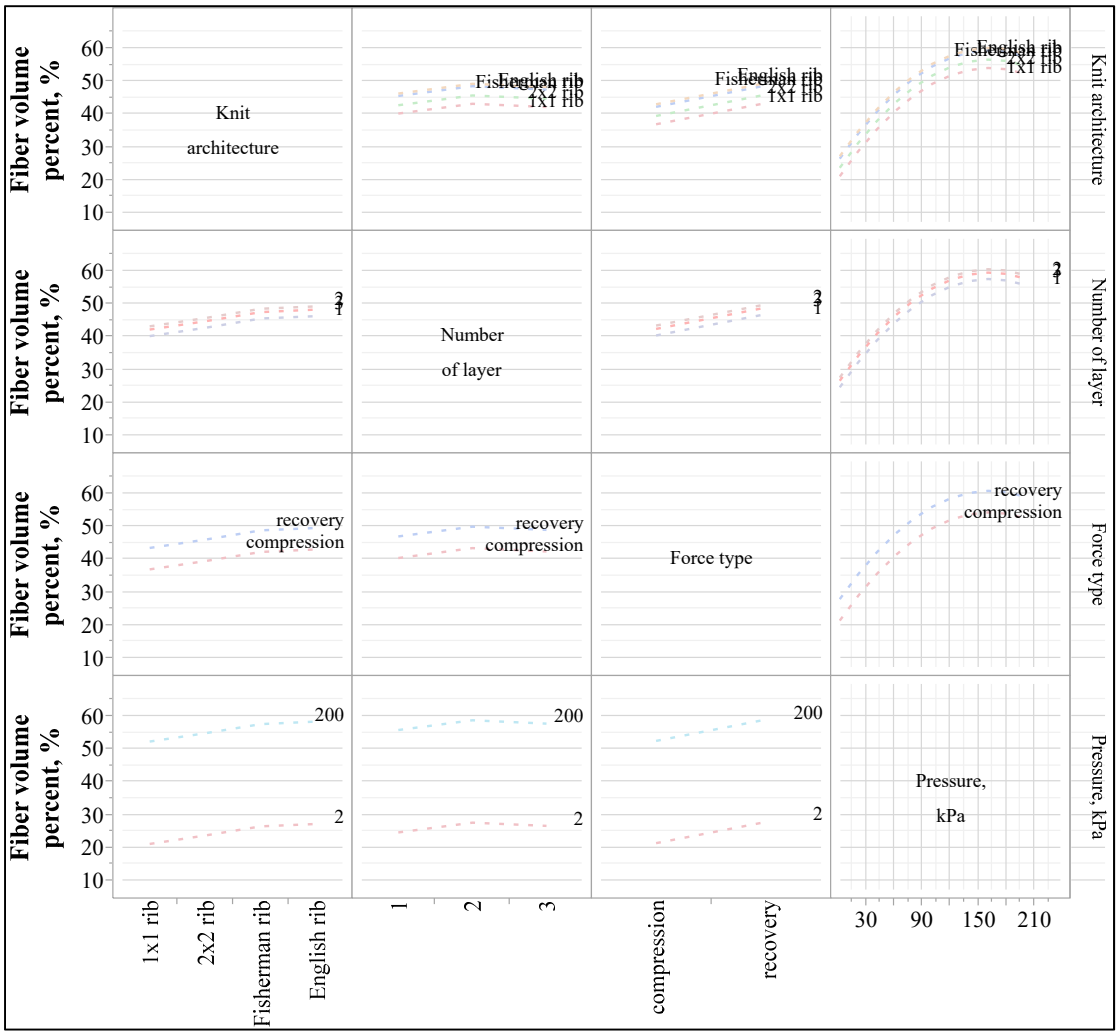


**Figure 15.** *Interaction plots matrix*

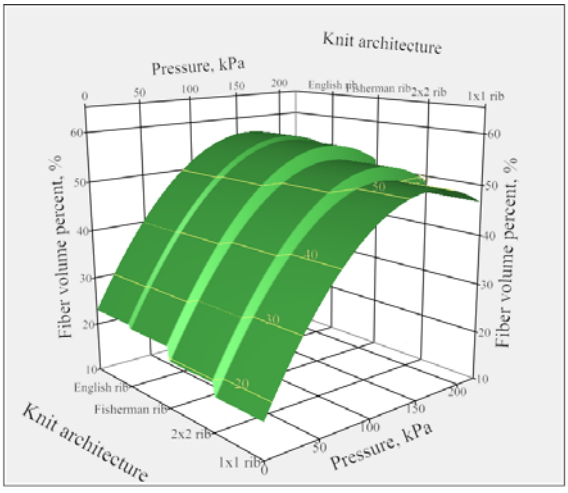


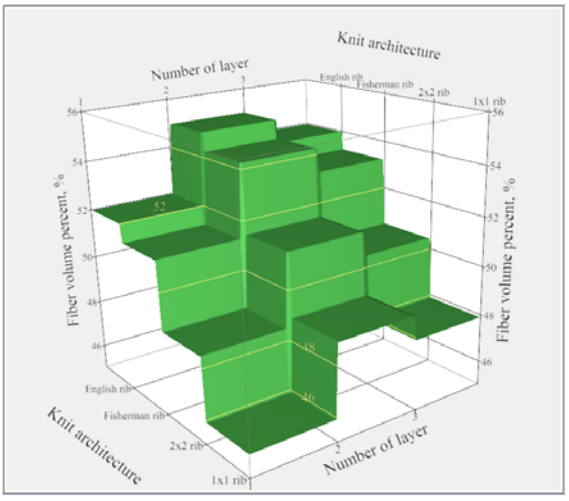

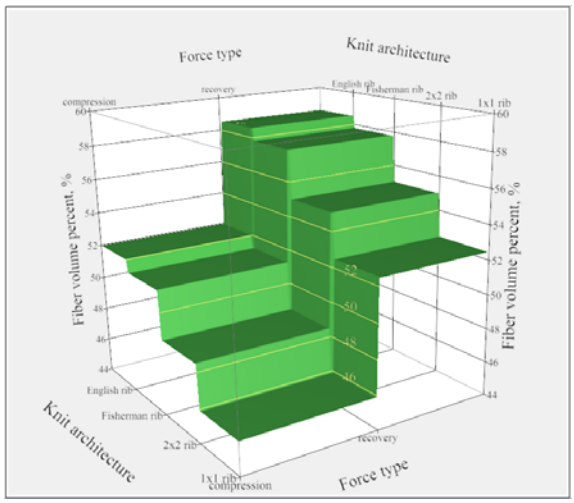


**Figure 16.** *Surface profilers for fiber volume percent*

## 4. Conclusion

In this study, weft knitted fabrics with 1x1, 2x2, English and fisherman rib architectures from glass yarn were produced and their structural and compressibility properties were analyzed in detail. The main findings of the single-layer fabric structural properties of the fabrics are:

**i.** The contractions in the width and/or length of the fabric, which vary in quantity depending on the knit architecture, control the structural properties of the fabric.

**ii.** While fabrics with 2x2 and fisherman rib knit architectures exhibited the highest thickness, the maximum fiber volume percent, the highest loop density and the shortest loop length; the fabric with 1x1 rib knit architecture displayed exactly the opposite of the relevant properties.

**iii.** These findings were related to the tendency of the fabric to shrink in the course direction for 2x2 rib knitted fabrics, while they were associated with the presence of tuck stitches for fisherman rib knitted fabrics.

Thereafter, the effects of knit architecture and the number of fabric layers on the compaction and relaxation behavior of the fabric stacks were discussed. The main findings of this discussion are:

**i.** The knit architecture affected the thickness and fiber content of single and multi-layer fabrics in the same trend.

**ii.** While a statistically non-significant negative association between the number of fabric layers and the normalized thickness (mm/layer) pointed out the beginning of the nesting; the number of fabric layers increased the fiber volume percent at a statistically significant level.

**iii.** The repeated compaction and relaxation processes reduced the thickness and increased the fiber volume percent.

**iv.** The power-law relationships with $R^2$s of greater than 0,90 between pressure and fiber volume percent were observed for both compaction and relaxation periods.

## Acknowledgement

This work was supported by the Bilimsel Araştırma Projeleri (BAP) unit of Gaziantep University, Turkey under the grant number of MF.YLT.18.02.

## References

[1]. Chawla K.K., Composite Materials: Science and Engineering. New York, Springer, 2019.

[2]. Mazumdar S.K., Composites manufacturing: materials, products, and process engineering. Boca Raton Fla, CRC Press, 2002.

[3]. Hammami A., Gebart B.R., "Analysis of the Vacuum Infusion Molding Process", Polymer Composites, 21, (2000), 28-40.

[4]. Correia N.C., Robitaille F., Long A.C., Rudd C.D., Simacek P., Advani S.G. "Use of Resin Transfer Molding Simulation to Predict Flow, Saturation, and Compaction in the VARTM Process", Journal of Fluids Engineering, 126, (2004), 210-215.

[5]. Govignon Q., Bickerton S., Morris J., Kelly P.A. "Full field monitoring of the resin flow and laminate properties during the resin infusion process", Composites Part A: Applied Science and Manufacturing, 39, (2008), 1412-1426.

[6]. Pearce N., Summerscales J., "The compressibility of a reinforcement fabric", Composites Manufacturing, 6, (1995), 15-21.

[7]. Lekakou C., Johari M.A.K.B., Bader M.G. "Compressibility and flow permeability of two-dimensional woven reinforcements in the processing of composites", Polymer Composites, 17, (1996), 666-672.

[8]. Robitaille F., Gauvin R., "Compaction of Textile Reinforcements for Composites Manufacturing. I: Review of Experimental Results", Polymer Composites", 19, (1998), 198-216.

[9]. Luo Y., Verpoest I., "Compressibility and Relaxation of a New Sandwich Textile Preform for Liquid

Composite Molding, Polymer Composites", 20, (1999), 179-191.

[10]. Potluri P., Sagar T.V., "Compaction modelling of textile preforms for composite structures", Composites Structures, 86, (2008), 177-185.

[11]. Lomov P., Molnár K., "Compressibility of carbon fabrics with needless electrospun PAN nanofibrous interleaves", Express Polymer Letters, 10, (2016), 25-35.

[12]. Yousaf Z., Potluri P., Withers P.J. "Influence of tow architecture on compaction and nesting in textile preforms", Applied Composite Materials, 24, (2017), 337-350.

[13]. Gommers B., Verpoest I., Van Houtte P. "Analysis of knitted fabric reinforced composites", Composites Part A: Applied Science and Manufacturing, 29, (1998), 1579-1588.

[14]. Pandita S.D., Falconet D., Verpoest I. "Impact properties of weft knitted fabric reinforced composites", Composite Science and Technology, 62, (2002), 1113-1123.

[15]. Pamuk G., Çeken F., "Manufacturing of Weft-Knitted Fabric Reinforced Composite Materials: A Review", Materials and Manufacturing Processes, 23, (2008), 635-640.

[16]. Ciobanu L., "Development of 3D Knitted Fabrics for Advanced Composite Materials", in Advances in Composite Materials – Ecodesign and Analysis, Edited by Brahim Attaf, InTech, 2011, pp. 161-192.

[17]. Marmaralı A.B., Atkı Örmeciliğine Giriş, İzmir, E.Ü Tekstil ve Konfeksiyon Araştırma – Uygulama Merkezi, 2004.

[18]. Marmaralı A., Kretzshmar S.D., Örme Terimleri ve Tanımlamaları, İzmir, E.Ü Tekstil ve Konfeksiyon Araştırma – Uygulama Merkezi, 2004.

[19]. Standard Test Methods for Mass per Unit Area (Weight) of Fabric, ASTM D3776, 2009.

[20]. Standard Test Methods for Wale and Course Count of Weft Knitted Fabrics, ASTM D8007, 2015.

[21]. British Standard Methods of test for Knitted Fabrics, BS 5441, 1998.

[22]. Statistical Software / JMP Software from SAS, 2021. [Online]. Available: https://www.jmp.com/en_us/home.html. [Accessed: May 27, 2021].

[23]. Kane C.D., Patil U.J., Sudhakar P. "Studies on the Influence of Knit Structure and Stitch Length on Ring and Compact Yarn Single Jersey Fabric Properties", Textile Research Journal, 77, (2007), 572-582.

[24]. Uyanık S., Değirmenci Z., Topalbekiroğlu M., Geyik F., "Examining the relation between the number and location of tuck stitches and bursting strength in circular knitted fabrics", Fibres & Textiles, 24, (2016), 114-119.

[25]. Uyanık S., Topalbekiroğlu M., "The effect of knit structures with tuck stitches on fabric properties and pilling resistance", The Journal of the Textile Institute, 108, (2017), 1584-1589.

[26]. İnce M.E., Yildirim H., "Air permeability and bursting strength of weft-knitted fabrics from glass yarn. Part II: knit architecture effect", The Journal of the Textile İnstitute, 110, (2019), 1072-1084..

MANAS Journal of Engineering
ISSN 1694-7398 | e-ISSN 1694-7398

*Volume 10, Issue 1, (2022) Pages 35-41*
*https://doi.org/10.51354/mjen. 986631*

# Parking lot occupancy prediction using long short-term memory and statistical methods

Ercan Avşar[1*], Yusuf Can Anar[2], Abdurrahman Özgür Polat[3]

[1] Dokuz Eylül University, Department of Computer Engineering, İzmir, Turkey, ercan.avsar@deu.edu.tr, ORCID: 0000-0002-1356-2753
[2] Çukurova University, Department of Electrical and Electronics Engineering, Adana, Turkey, yusufcan2617@gmail.com, ORCID: 0000-0002-2227-768X
[3] Karamanoğlu Mehmet Bey University, Department of Electrical and Electronics Engineering, Karaman, Turkey, ozgrpolat@kmu.edu.tr, ORCID: 0000-0002-4922-6567

**ABSTRACT**

In crowded city centers, drivers looking for available parking space generate extra traffic and in addition, the resulting excessive exhaust gases cause air pollution. Therefore, directing the drivers to a parking spot in an intelligent way is an important task for smart city applications. This task requires the prediction of occupancy states of parking lots which involves appropriate processing of the historical parking data. In this work, Long-Short Term Memory (LSTM) and Autoregressive Integrated Moving Average (ARIMA) methods were applied to parking data collected from curbside parking spots of Adana, Turkey for predicting the parking lot occupancy rates of future values. The experiments were performed for making predictions with different prediction horizons that are 1 minute, 5 minutes, and 15 minutes. The performances of the methods were compared by calculating root mean squared error (RMSE) and mean absolute error (MAE) values. The experiments were performed on data from five different days. According to the results, when the prediction horizon is set to 1 minute, LSTM achieved RMSE and MAE values of 0.98 and 0.72, respectively. For the same prediction horizon, ARIMA achieved RMSE and MAE values of 0.62 and 0.35, respectively. On the other hand, LSTM achieved smaller error values for larger prediction horizons. In conclusion, it was shown that LSTM is more suitable for larger prediction horizons, however, ARIMA is better at predicting near-future values.

**ARTICLE INFO**

***Research article***

*Received: 24.08.2021*
*Accepted: 12.03.2022*

***Keywords:***
*ARIMA,*
*deep learning,*
*LSTM,*
*parking occupancy,*
*smart parking,*
*time series prediction*

**corresponding author*

## 1 Introduction

As a result of increment in world population, city centers are getting more crowded every day. Finding an available parking spot in such city centers is a challenging and frustrating task. Besides, extra time and fuel are consumed while looking for a parking spot. In addition, searching action of drivers causes slowing down the traffic movements and this recursive action causes more traffic problems. It is reported that parking spot searching drivers cause more than 1/3 of the traffic congestions [1]. Another source for this problem has emerged due to the Covid-19 situation. Today, more people started to prefer personal vehicles instead of urban transportation to decrement the risk of being infected. Hence, more vehicles may be present in traffic when compared to pre-pandemic times. Consequently, finding a parking spot is becoming critical for the economy, health, and air pollution.

To address this parking problem, various technologies such as wireless communication, sensors, and machine learning are used in smart city applications. Within the scope of Internet of Things (IoT) systems, a network of low-cost and low-power sensors may provide a useful infrastructure for a smart parking system. Such a system should involve more features than showing the instantaneous information for available parking spots to the users. Because of the dynamic properties of the parking problem, a smart parking system needs to be capable of organizing the drivers in an intelligent way. One key feature may be the processing of historical parking data using machine learning methods to make statistical inferences and future predictions.

There are various cities in the world that are being equipped with various smart city features with high investment costs. In general, sensors are one type of the important tools for these

systems. For smart parking applications, sensors placed at the curbside parking spots make it possible to collect both spatial and temporal data. Some of the cities in which sensor-based parking lot occupancy data collection scheme is deployed are San Francisco, USA [2], Melbourne, Australia [3], and Westminster, England [4].

Recent advancements in various technologies enable the widespread usage of the sensors in smart city applications. One example of these technologies is the wireless communication protocols. Relatively recent protocol "long range wide area network" (LoRaWAN) makes wireless data transmission possible over distances up to 15 kilometers while consuming very small amount of power. Investments on other enabling technologies like cloud computing, big data analytics, and embedded systems triggers deployment of more smart parking systems in various cities. As a result, the amount of collected parking data increases and it becomes necessary to analyze the data using advanced methods. Analysis of such data involves performing statistical analysis on the previous data as well as predicting the parking space availability for a particular area.

Machine learning methods are suitable for such time-series prediction problems; hence, various machine learning methods are utilized for prediction of parking spot states. Among the traditional machine learning methods, Artificial Neural Networks (ANN) [5], Support Vector Machines (SVM) [6] and Regression Trees (RT) [6, 7] are widely used for this purpose. On the other hand, Long Short-Term Memory (LSTM), an architecture based on Recursive Neural Networks (RNN) for time-series prediction, is a commonly used deep learning method [8].

In this work, Autoregressive Integrated Moving Average (ARIMA) and LSTM methods are applied to parking data collected from curbside parking spots of Adana, Turkey. ARIMA is a statistical method where the data is regressed on its own prior values. LSTM is a deep learning method that can handle the long-term dependencies in the data with the help of memory cells in its structure. Both of these methods are developed for time-series analysis problems, hence this study compares the performances of these methods on the parking data and underlines the advantages of one method over other.

The rest of the paper is organized as follows. In section 2, related literature review is given. The background information about the LSTM and ARIMA models are provided in section 3. Section 4 contains the details about the dataset and the experiments. The results are given in section 5 and the paper is concluded with section 6.

## 2. Literature review

The importance of parking lot occupancy prediction has been mentioned in the literature frequently with an increased rate in the recent years. The reason for this situation may be the emergence of IoT concept and its widespread applications. Within the scope of smart cities, the prediction of occupancy rates contributes to various aspects such as reduction in traffic congestion and environmental pollution. One other useful application can be given as efficient pricing for the smart parking systems. A machine learning based pricing system was proposed by Saharan et al., where on-street occupancy rates are predicted using four well-known methods, namely, linear regression, decision tree (DT), neural networks (NN), and random forest (RF) [9].

Typically, machine learning methods are utilized for solving this prediction problem. In a recent study by Awan et al., prediction performances of multilayer perceptron, k-nearest neighbors (KNN), DT, RF, and an ensemble of these methods were compared and it was shown that the voting-based ensemble method outperforms the others [10]. The ensemble methods attracted the attention of different researchers. For example, Sampathkumar et al. proposed a majority voting ensemble model that combines outputs of seven different prediction methods for predicting parking availability in a smart city [11]. On the other hand, further analysis of different ensemble methods for parking space availability was performed by Tekouabou et al. using four regression methods that are bagging, RF, adaptive boosting, and gradient boosting [12]. Instead of considering only the occupancy rate, Provoost et al, defined state of a parking area using occupancy rate as well as in- and out-flux of the vehicles [13]. They showed that this definition is less sensitive to the prediction horizon. Furthermore, there is a large amount of publications for this problem utilizing different variants of machine learning methods. These studies include road segment clustering and kalman filter based prediction [14], neural networks considering dynamic distribution characteristics [15], and wavelet neural networks [16].

Strategies utilizing deep learning methods for parking availability prediction is also very common [17]. For example, a hybrid approach was proposed by Qiu et al., where the parameters of an RNN model were optimized using genetic algorithm [18]. In the work proposed by Yang et al., several traffic data sources such as parking meter transactions, traffic speed, and weather conditions were used as input parameters to a Graph-Convolutional Neural Network (GCNN) models [19]. It was shown that GCNN has better prediction performance than the baseline LSTM and lasso models. Usage of ensemble learners together with deep learning models is also available in the literature. Lv et al. proposed an ensemble learning algorithm with an RNN model [20]. The optimized values for the parameters of the algorithm were determined using particle swarm optimization. At this point it is worth to mention that the number studies using time series analysis is limited when compared to machine learning and deep learning based methods [21, 22].

## 3. Background

### 3.1. Long short-term memory

LSTM is a type of RNN architecture and has been applied in various problems such as language modeling, speech-to-text transcription, machine translation and time-series prediction. LSTM networks are able to learn long-term dependencies in the data with the repeating memory cells in its structure. There are three main building blocks of the memory cells which are input, output and forget gates. These gates process the data from the previous hidden state ($h_{t-1}$), previous cell state ($C_{t-1}$) and the current input ($x_t$). The previous hidden state and the current input data are processed together by concatenating them to form current information ($I_t$). Specifically, forget gate decides whether to keep or forget the previous state of the cell by passing the current information through a sigmoid activation function. In the input gate, the important information within the current information is determined to allow the less important ones be removed from the cell. The outputs of these two gates are summed to update the cell state. This updated cell state ($C_t$) is passed to a tanh function and then multiplied with the sigmoid output of the current information. This final step is called the output gate because it outputs the updated hidden state ($h_t$) for the cell. A memory cell and corresponding operations are illustrated in Figure 1.

Repeating structure of such cells can be achieved by providing the output states of a cell as inputs to the next one, eventually yielding an LSTM network. The weights associated with the gates can be learned appropriately when a sequence data is used for training the network. As a result, the dependencies between the states of the sequence are modelled using these networks. An LSTM network having a visible layer with one input and a hidden layer with four neurons is used in this work.

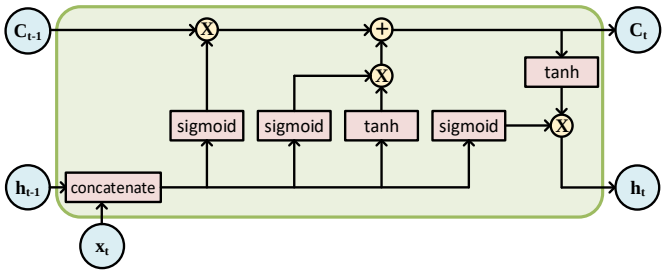


**Figure 1**. *Memory cell of an LSTM network*

### 3.2. Auto regressive integrated moving average

ARIMA is a statistical method particularly for time series analysis by which future values are predicted. It involves three main parts that are auto regression (AR), moving average (MA) and integration (I) of these two.

For a time series data, $y_t$, AR can be described as a model that depends on linear combination of its past values, $y_{t-n}$. Thus, it is a regression model based on its own lagged version. $AR(p)$ notation is used to denote an AR model of order $p$ and is defined as

$$y_t = c + \sum_{i=1}^{p} \varphi_i y_{t-i} + n_t \quad (1)$$

where $c$ is a constant number, $\varphi_i$ are the model parameters, and $n_t$ is the white noise.

On the other hand, rather than past values, MA method uses linear combination of previous prediction errors and current error to model the current value of a variable. MA model of order q can be defined as

$$y_t = \mu + \varepsilon_t + \theta_1 \varepsilon_{t-1} + \theta_2 \varepsilon_{t-2} + \cdots + \theta_q \varepsilon_{t-q} \quad (2)$$

where $\mu$ is the mean of the time series, $\varepsilon_t$ are the white noise error terms, $\theta_i$ are the model parameters.

The combination of AR and MA methods cannot capture the non-stationary properties in the data. To overcome this situation, "integrated" part (I) of the ARIMA model is introduced. In this step the difference between the data points and their previous values are calculated. The data points are replaced with these difference values. This differencing process may be repeated more than once. Generally, the order of the integrated step is denoted with $d$ and represents the number of consecutive differencing operations. As a result, an ARIMA $(p, d, q)$ model is defined as

$$y'_t = c + \sum_{i=1}^{p} \varphi_i y'_{t-i} + \varepsilon_t + \theta_1 \varepsilon_{t-1} + \theta_2 \varepsilon_{t-2} + \cdots + \theta_q \varepsilon_{t-q} \quad (3)$$

where $y'_t$ is the differenced version of the time series $y_t$. Obviously, for such a model, $p$ is the order of AR part; $d$ is the number of differencing operations, and $q$ is the order of MA part.

In this work and ARIMA$(1,1,0)$ model is used to make predictions on the parking data.

## 4. Materials and methods

### 4.1. The dataset

The dataset used in this work is taken from Adana Metropolitan Municipality. It contains data for a curbside parking lot in the city center for five working days. The raw data was recorded in a vehicle-based format where each record

contained enter and exit time of a vehicle. A preprocessing step was performed to convert this data into a time-series format in which each sample denotes the total number of vehicles for one minute of a day. A sample parking data after preprocessing is shown in Figure 2. Since the curbside parking system is active only during the daytime, the data belonging to intervals of hours [00:00,09:00] and [17:00,23:59] are all zero. When performing the experiments, these hours are simply ignored and only the data for active hours is used and this corresponds to nearly 500 samples of the time series data.

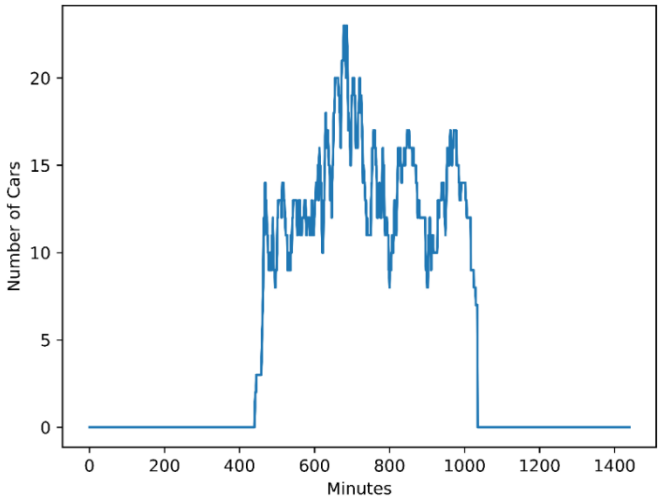


**Figure 2**. *Parking lot occupancy data for one day*

*4.2. Experiments*

For both ARIMA and LSTM methods, three different experiments were performed to predict the parking lot occupancy of 1, 5, and 15 minutes ahead. These experiments were applied separately to the days of data. In other words, the data belonging to each day is processed individually.

The sliding window approach is employed for making the predictions for one-step ahead. If $x_t$ denotes the t[th] sample in the time-series data, $x_{t+1}$ is predicted by training the model on all the samples from $x_1$ to $x_t$. Next, the samples from $x_1$ to $x_{t+1}$ are used to predict $x_{t+2}$. This procedure is continued until the end of the time-series data. For this purpose, 66% of the one-day data is taken as the training set and the next single record in the dataset is used as test data. The remaining 34% of the one-day data is predicted in this manner and each prediction result is stored for performance analysis.

When training the LSTM model, five most recent data (i.e. $x_{t-i}$ where $i \in \mathbb{Z}$ and $0 \leq i \leq 4$) are used as lookback features and the training is performed for 30 epochs. These values are determined by increasing the lookback features and the training epochs gradually. It was observed that larger values for these hyperparameters have no considerable improvement in the performance of the model. The learning curve showing the training loss for different epochs is given in Figure 3. These parameters are not usable in the ARIMA model because it makes new predictions according to total updated history.

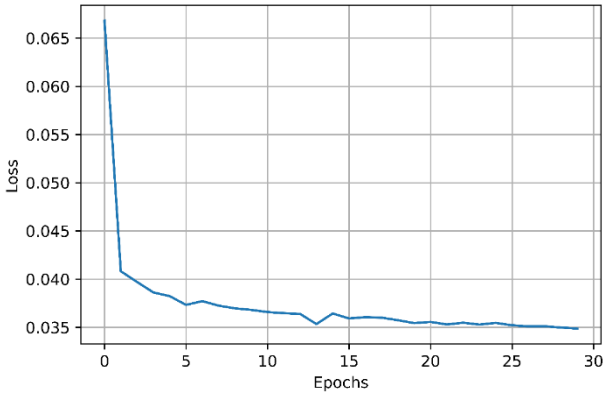


**Figure 3**. *Change of the training loss in LSTM*

The performances of the models are evaluated by computing root mean squared error (RMSE) and mean absolute error (MAE) which are given by the following equations:

$$RMSE = \sqrt{\frac{\sum_{k=1}^{n}(p_k - a_k)^2}{n}} \quad (4)$$

$$MAE = \frac{1}{n}\sum_{k=1}^{n}|a_k - p_k| \quad (5)$$

where $p_k$, $a_k$, and $n$ denote the predicted values, actual values, and the total number of samples, respectively.

## 5. Results and discussion

As indicated earlier, the dataset contains data for five different days and future predictions for three different times (1, 5 and 15 minutes ahead) are performed. The prediction results for LSTM and ARIMA methods are given in Tables 1 and 2, respectively.

As can be seen from the tables, the minimum error for both methods are achieved when predicting one minute ahead. This is an expected situation as the problem of predicting the future values gets more difficult as the prediction horizon increases. This is consistent with the obtained results because the amount of error increases when the prediction horizon is larger. The increment is observable in all of the experimented days with different prediction horizons for both LSTM and ARIMA methods as well as both performance metrics. Sample predictions of both methods for different times are provided in Figures 4 and 5 where there is an apparent shift in case of 5-minute ahead predictions. In addition, the shift in the predicted values, there is a slight distortion and hence, the calculated error values increase eventually.

**Table 1.** *Prediction Results for LSTM*

| | 1 minute | | 5 minutes | | 15 minutes | |
|---|---|---|---|---|---|---|
| | **RMSE** | **MAE** | **RMSE** | **MAE** | **RMSE** | **MAE** |
| **Day 1** | **0.98** | **0.72** | 1.13 | 0.89 | 1.88 | 1.57 |
| **Day 2** | 1.13 | 0.83 | 1.50 | 1.23 | 2.39 | 1.94 |
| **Day 3** | 1.19 | 0.90 | 1.56 | 1.23 | 2.28 | 1.84 |
| **Day 4** | 1.04 | 0.77 | 1.05 | 0.81 | 1.29 | 1.04 |
| **Day 5** | 1.14 | 0.85 | 1.29 | 1.00 | 1.91 | 1.51 |
| **Mean** | 1.10 | 0.81 | 1.31 | 1.03 | 1.95 | 1.58 |

**Table 2.** Prediction Results for ARIMA

| | 1 minute | | 5 minutes | | 15 minutes | |
|---|---|---|---|---|---|---|
| | **RMSE** | **MAE** | **RMSE** | **MAE** | **RMSE** | **MAE** |
| **Day 1** | **0.62** | **0.35** | 1.47 | 1.07 | 2.82 | 2.47 |
| **Day 2** | 0.75 | 0.48 | 1.96 | 1.55 | 3.05 | 2.47 |
| **Day 3** | 0.73 | 0.47 | 1.63 | 1.21 | 2.71 | 2.17 |
| **Day 4** | 0.66 | 0.43 | 1.45 | 1.10 | 2.21 | 1.83 |
| **Day 5** | 0.78 | 0.48 | 1.71 | 1.27 | 2.26 | 1.83 |
| **Mean** | 0.71 | 0.44 | 1.64 | 1.24 | 2.61 | 2.15 |

According to the results presented in Tables 1 and 2, for all the experiments with a prediction horizon of 1 minute, ARIMA has lower error rate, while the error rate achieved by LSTM is generally lower when the prediction horizon is 5 minutes or 15 minutes. Thus, it is possible to compare the overall performances of the methods. On average, ARIMA is able to predict the future values when the prediction horizon is smaller. However, for larger values of prediction horizon the relative error for ARIMA gets higher than those for LSTM. It means that LSTM may be a better choice than ARIMA in case of a large prediction horizon.

This information can be handy when developing a hands-on application for a smart city parking system. If the driver is looking for a parking lot a nearby location, then ARIMA will be more suitable method for generation suggestions to the user. On the other hand, in case of a user looking for a parking lot a distant location (in other words, it will take some time for the driver to reach to the target location), usage of LSTM will allow the user to find a parking lot with a higher probability.

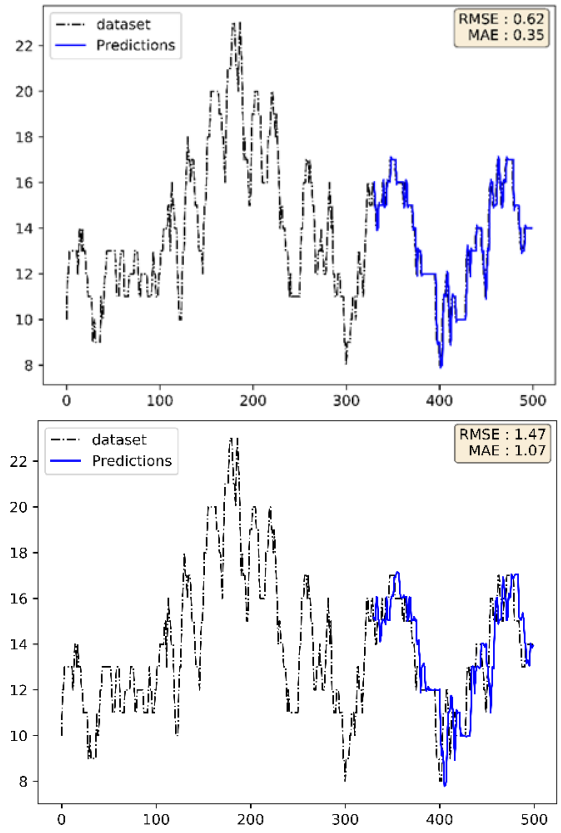


**Figure 4**. *Prediction results of ARIMA belonging to "Day 1" for (a) 1 minute and (b) 5 minutes ahead*

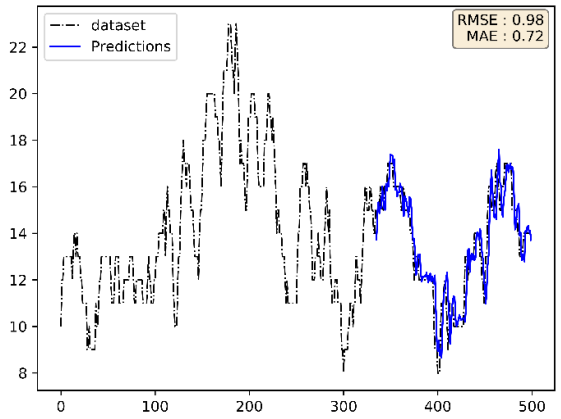

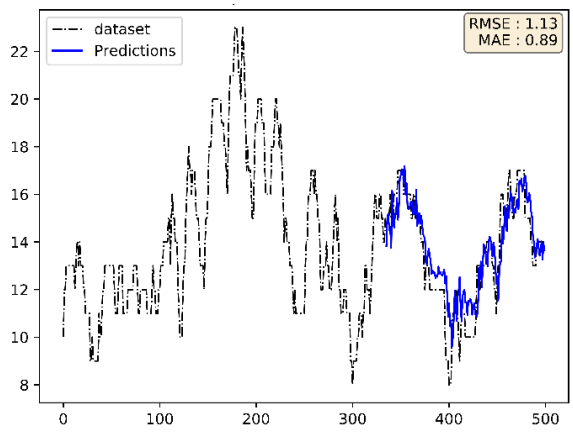


(b)

**Figure 5.** *Prediction results of LSTM belonging to "Day 1" for (a) 1 minute and (b) 5 minutes ahead*

## 6. Conclusion

As the city centers get more crowded, it becomes a necessity to organize and manage the facilities of the cities in an intelligent way. Car parking problem is one of the consequences of high population, which brings about several other issues such as generating extra traffic and increased carbon emission to the atmosphere. The machine learning and data analysis methods available today may allow for predicting the occupancy status of a specific parking spot, thereby it becomes possible to direct the drivers to the available place. In this work, ARIMA and LSTM methods are used to predict parking lot occupancy rate using the parking data collected from Adana, Turkey. For both of the methods, the experiments were performed with three different prediction horizons that are 1 minute, 5 minutes and 15 minutes. According to the results, it was observed that ARIMA outperforms LSTM when the prediction horizon is smaller. On the other hand, for the increased prediction horizons, the performance of LSTM is higher. This situation may be due to the presence of memory cells in the structure of LSTM that enables considering the long-term dependencies when making predictions. Since the predictions with horizons more than one minute are more feasible in practical applications, it may be concluded that LSTM method is more suitable than ARIMA for such problems. Increasing the amount of data for training the model as well as inclusion of traditional machine learning methods in the experiments are planned as the future works.

## References

[1]. Shao W., Zhang Y., Guo B., Qin K., Chan J., Salim F.D., "Parking availability prediction with long short term memory model," in International Conference on Green, Pervasive, and Cloud Computing, Springer, (2018), 124-137.

[2]. https://www.sfmta.com/demand-responsive-parking-pricing, Accessed: 24 August 2021.

[3]. https://www.melbourne.vic.gov.au/about-council/governance-transparency/open-data/Pages/on-street-parking-data.aspx, Accessed: 24 August 2021.

[4]. https://www.smartparking.com/latest/case-studies/city-of-westminster, Accessed: 24 August 2021.

[5]. Vlahogianni E.I., Kepaptsoglou K., Tsetsos V., Karlaftis M.G., "A Real-Time Parking Prediction System for Smart Cities," Journal of Intelligent Transportation Systems, (2015), 20, 2, 192-204, doi: 10.1080/15472450.2015.1037955.

[6]. .Yanxu Zheng S.R, Christopher Leckie, "Parking Availability Prediction for Sensor-Enabled Car Parks in Smart Cities," 2015 IEEE Tenth International Conference on Intelligent Sensors, Sensor Networks and Information Processing (ISSNIP) Singapore, 2015.

[7]. Alajali W., Wen S., Zhou W., "On-Street Car Parking Prediction in Smart City: A Multi-source Data Analysis in Sensor-Cloud Environment," in Security, Privacy, and Anonymity in Computation, Communication, and Storage, (Lecture Notes in Computer Science, (2017), ch. Chapter 58, 641-652.

[8]. Li Xiangdong C.Y., CEN Gang, Xu Zengwei, "Prediction of short-term available parking space using LSTM model," The 14th International Conference on Computer Science & Education (ICCSE 2019).

[9]. Saharan S., Kumar N., Bawa S., "An efficient smart parking pricing system for smart city environment: A machine-learning based approach," Future Generation Computer Systems, vol. 106, pp. 622-640, 2020, doi: 10.1016/j.future.2020.01.031.

[10]. Awan F.M., Saleem Y., Minerva R., Crespi N., "A Comparative Analysis of Machine/Deep Learning Models for Parking Space Availability Prediction," Sensors (Basel), (2020), 20, 1, doi: 10.3390/s20010322.

[11]. Sampathkumar R.M.A., Pon Harshavardhanan, S. Murugan, P. Jayarajan, V. Sivasankaran, "Majority Voting based Hybrid Ensemble Classification Approach for Predicting Parking Availability in Smart City based on IoT," 11th ICCCNT 2020.

[12]. Koumetio Tekouabou S.C., Abdellaoui Alaoui E.A., Cherif W., Silkan H., "Improving parking availability prediction in smart cities with IoT and ensemble-based model," Journal of King Saud University - Computer and Information Sciences, (2020), doi: 10.1016/j.jksuci.2020.01.008.

[13]. Jesper L.J.J.W. C. Provoost, Sander J. van der Drift, Maurice van Keulen, Andreas Kamilaris, "Short Term Prediction of Parking Area states Using Real Time Data and Machine Learning Techniques," 2019.

[14]. Sergio Di Martino A.A., "Exploiting Recurrent Patterns to Improve Scalability of Parking Availability Prediction Systems," Electronics (2020), 9, 838.

[15]. Zhao Z., Zhang Y., Zhang Y., Ji K., Qi H., "Neural-Network-Based Dynamic Distribution Model of Parking Space Under Sharing and Non-Sharing Modes," Sustainability, (2020), 12, 12, doi: 10.3390/su12124864.

[16]. Liu J., Wu J., Sun L., "Control method of urban intelligent parking guidance system based on Internet of Things," Computer Communications, (2020), 153, 279-285, doi: 10.1016/j.comcom.2020.01.063.

[17]. Jamie Arjona M. P. L., Josep Casanovas-Garcia, Juan José Vázquez, "Improving Parking Availability Information Using Deep Learning Techniques," 22nd EURO Working Group on Transportation Meeting, EWGT 2019, 2020.

[18]. Qiu J., Tian J., Chen H., Lu X., "Prediction Method of Parking Space Based on Genetic Algorithm and RNN," in Advances in Multimedia Information Processing – PCM 2018, (Lecture Notes in Computer Science, (2018), ch. Chapter 79, 865-876.

[19]. Yang S., Ma W., Pi X., Qian S., "A deep learning approach to real-time parking occupancy prediction in transportation networks incorporating multiple spatio-temporal data sources," Transportation Research Part C: Emerging Technologies, (2019), 107, 248-265, doi: 10.1016/j.trc.2019.08.010.

[20]. Kedi Lv H.C., Yingda Lv, "Parking Space Predicting Algorithm Based on Recurrent Neural Network and Ensemble Learning Algorithm," Proceedings of CCIS2019.

[21]. Zhao Z., Zhang Y., Zhang Y., "A Comparative Study of Parking Occupancy Prediction Methods considering Parking Type and Parking Scale," Journal of Advanced Transportation, (2020), 1-12, doi: 10.1155/2020/5624586.

[22]. Stolfi D.H., Alba E., Yao X., "Can I Park in the City Center? Predicting Car Park Occupancy Rates in Smart Cities," Journal of Urban Technology, (2019), 1-15, doi: 10.1080/10630732.2019.1586223.

MANAS Journal of Engineering
ISSN 1694-7398 | e-ISSN 1694-7398

*Volume 10, Issue 1, (2022) Pages 42-51*
*https://doi.org/10.51354/mjen. 1000248*

# Launching to an orbit with a chemical propellant staged rocket systems

Erk Inger

Airframe and Powerplant Maintenance Department, Atilim University, Ankara, Turkey, ORCID ID: https://orcid.org/0000-0002-1857-8180

**ABSTRACT**

There is one way to explore space by using the space launch vehicles, which is known as rockets, and it can carry useful load named simply as payload of satelite from Earth into Space. In this study, performance predictions of the multi rocket motors are discussed and compared with single rocket motor with the same amount of propellant used for space travel.
In this article in serial or tandem staging schemes, the boosting stage is usually the largest, the second stage and subsequent upper stages are above it, usually decreasing in size are used. In boosting stage parallel staging schemes solid or liquid rocket boosters are used to assist with launch. At low level starting to high altitude higher density fuel solid fuels, kerogen and cryogenic hydrogen(-250°C) are used as fuel. In solid propellants oxidizer is generally ammonium per chloride is used but in cryogenic liquid propellants oxygen(183.3°C) are used.
In the first stage, both liquid propellant in a booster and five solid rocket propellent are used to reach about a certain altitude and velocity. In second stage, after reducing the weight by ejecting the five solid rocket propellent and only liquid propellant is used only to reach the an extra altitudes and velocities at low earth orbit (LEO). Drag and gravity effects are successfully used in all of the calculations.
The added total result of velocities and altidudes found by these staged rockets are higher than the first single staged case. The advantage of multistage rockets, having same amount of propellant in staged rockets where total velocity will be increased by separating and removing waste from the system weight out of the system. Use of staged rocket system are usefull for increasing the amount of payload and decreasing the cost per unit weight as well.

**ARTICLE INFO**

***Research article***

*Received: 24.09.2022*
*Accepted: 3.02.2022*

***Keywords:***
*Staged and single stage rocket,*
*useful load,*
*payload,*
*low earth orbit (LEO),*
*apogee,*
*perigee*

*Corresponding author

## 1 Introduction

Most modern, high-performance rocket, particularly those used in space application are the multi-stage rocket systems. Multi-staging is an excellent way to attain higher velocity and higher altitude or more payload by using staged model. Staging is a concept where one engine's velocity is added to an already existing velocity of another, engine one engine's altitude is added to an already existing altitude of another engine. If you keep the velocity same then you can increase your payload for making more economical flight. Mathematical calculation of this case study is presented in three parts as staged rocket calculations.

Tsiolkovsky's Rocket Equation states that the rocket velocity is the function of exhaust velocity and the propellant to total mass change while the propellant is consumed

$$V = V_e \mathrm{Ln} \frac{m_0}{m} \tag{1.1}$$

where ,
$V$, required velocity change,
$V_e$, is exhaust velocity,
$m_0$ the initial mass and
$m$ the mass of the rocket at each time

$$V_e = I_{SP} g_0 \tag{1.2}$$

$I_{SP}$ is the specific impulse,
$g_0 = 9.80665 \ \frac{m}{s^2}$, is the gravitational acceleration at sea level.

Specific impulse (usually abbreviated Isp) is a measure of how efficiently a reaction mass engine (a rocket using propellant or a jet engine using fuel) creates thrust. For engines whose

reaction mass is only the fuel they carry, specific impulse is exactly proportional to exhaust gas velocity. Specific impulse which may be expressed as total impulse namely thrust time per unit weight of propellant is a fuel property and for solid propellants 180-250s, liquid propellant 300-475s have been used.

**Table 1.** *Practical Isp values for common rocket propellants[1]*

| **Propellant type** | ***Isp [sec]*** |
|---|---|
| Solid | 180 - 270 |
| *N2O4/MMH<br>**N2O4/UDMH | 260 - 310 |
| Kerogene/LO2 | 300 - 350 |
| ***LH2/LO2 | 455 |

*(N2O4 Dinitrogen Tetraoxide) (MMH Monomethylhydrazine) (UDMH
**Unsymmetrical Dimethylhydrazine ((CH3)2NNH2))
***(LH2/LO2 Liquid H2/O2)

## 2. Theory

In this article, two fundamental types of rocket stages, five solid propellant boosters (SRB) with liquid propellant center core booster (CCB) are at the same time are fired in parallel Fig (1) and Fig (2). A popular method for producing large first stage has been to cluster several SRB rockets together to provide greater combined thrust without actually having to build the larger rocket. Number of solid rocket boosters may be change starting from two to seven. In this article taken as five and when those SRB rockets rocket motors are completely consumed, ejected away in the flight. Until the end of CCB liquid booster continues to burn as booster. After ejection of SRB system since the total weight is reduced CCB may be referred as vertically staging sustainer rocket.

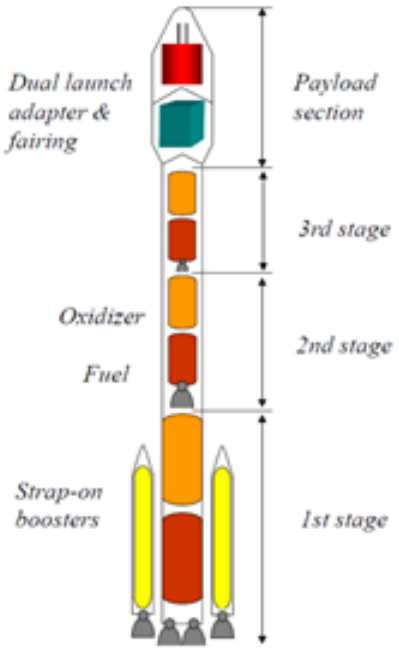


**Figure 1.** *Three staged Rocket System [2]*

The total rocket system mass is composed of n units of SRB, one CCB with solid and liquid propellant

$$m_T = nm_{SRB} + m_{LCCB} + m_{L1S} + m_{L2S} \quad (1.3)$$

$n$ , *number solid rocket booster*
$m_{SRB}$, *solid rocket booster mass*
$m_{SRBP}$, *solid rocket booster propellant mass*
$m_{LCCB}$, *total center core mass*
$m_{LRBP}$, *center core propellant mass*
$m_{LB}$ , total center core mass of the first stage
$m_{L1S}$ , mass of first stage rocket motor
$m_{L2S}$ , mass of second stage rocket motor

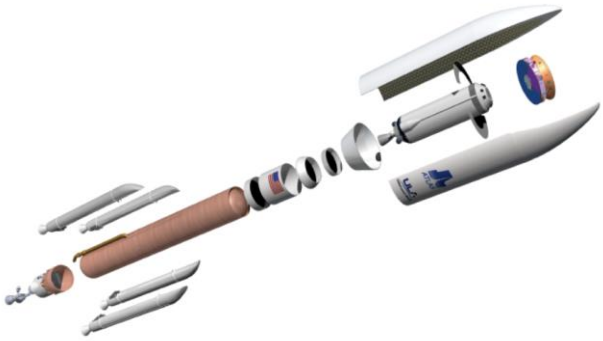

**Figure 2.** *Multiple Rocket System Configurations [3]*

In the calculation of the altitude of any potential rocket, one must take into account the weights of the rockets and the forces produced by both the thrust of the engine and the gravitational pull of the Earth. A simplified approach can be developed for estimating altitude performance of model rocket vehicles.

**Table 2.** *U.S. Standard Atmosphere Air Properties - SI Units[4]*

| Geo potential Altitude above Sea Level - h - (m) | Temperature - t - (°C) | Acceleration of Gravity - g - ($m/s^2$) | Absolute Pressure - p - ($10^4$ N/$m^2$) | Density - ρ - ($10^{-1}$ kg/$m^3$) | Dynamic Viscosity - μ - ($10^{-5}$ N.s/$m^2$) |
|---|---|---|---|---|---|
| -1000 | 21.50 | 9.810 | 11.39 | 13.47 | 1.821 |
| 0 | 15.00 | 9.807 | 10.13 | 12.25 | 1.789 |
| 1000 | 8.50 | 9.804 | 8.988 | 11.12 | 1.758 |
| 2000 | 2.00 | 9.801 | 7.950 | 10.07 | 1.726 |
| 3000 | -4.49 | 9.797 | 7.012 | 9.093 | 1.694 |
| 4000 | -10.98 | 9.794 | 6.166 | 8.194 | 1.661 |
| 5000 | -17.47 | 9.791 | 5.405 | 7.364 | 1.628 |
| 6000 | -23.96 | 9.788 | 4.722 | 6.601 | 1.595 |
| 7000 | -30.45 | 9.785 | 4.111 | 5.900 | 1.561 |
| 8000 | -36.94 | 9.782 | 3.565 | 5.258 | 1.527 |
| 9000 | -43.42 | 9.779 | 3.080 | 4.671 | 1.493 |
| 10000 | -49.90 | 9.776 | 2.650 | 4.135 | 1.458 |
| 15000 | -56.50 | 9.761 | 1.211 | 1.948 | 1.422 |
| 20000 | -56.50 | 9.745 | 0.5529 | 0.8891 | 1.422 |
| 25000 | -51.60 | 9.730 | 0.2549 | 0.4008 | 1.448 |
| 30000 | -46.64 | 9.715 | 0.1197 | 0.1841 | 1.475 |
| 40000 | -22.80 | 9.684 | 0.0287 | 0.03996 | 1.601 |
| 50000 | -25 | 9.654 | 0.007978 | 0.01027 | 1.704 |
| 60000 | -26.13 | 9.624 | 0.002196 | 0.003097 | 1.584 |
| 70000 | -53.57 | 9.594 | 0.00052 | 0.0008283 | 1.438 |
| 80000 | -74.51 | 9.564 | 0.00011 | 0.0001846 | 1.321 |

*2.1. First Boosting Stage Five Rockets with Solid and Liquid Propellant in CCB*

To calculate time and velocity at burn out solid rockets and half of the liquid used the Newton's second law;

$$m_{SLB} = m_T - \frac{5m_{SRBP}}{2} - \frac{m_{LRBP1}}{2} \quad (1.4)$$

$\boldsymbol{m_{SLB}}$, average mass of the rocket system .
$m_{LRBP1}$ , center core first liquid propellant mass of the first stage

Where, the liquid propellant is used with 5 solid propellant rocket is fired then the rest of liquid propellant continue to burn in CCB.

In the configuration design, n unit $d_{SB}$, diameter of solid rocket boosters are added symmetrically to peripheral of central core booster with diameter $d_{CCB}$. The aerodynamic cross section areas $A_{SLB}$ are calculated below.

$$A_{SLB} = \frac{\pi}{4}[d_{CCB}^2 + 5d_{SRB}^2] \quad (1.5)$$

*2.1.1. Burn out time at boosting stage*

$F = m_{SLB}.a$

$\boldsymbol{F = m_{SLB}.\frac{\partial v}{\partial t}}$

$T_{SB} = n.T_{SRB}$ (1.6)

$\boldsymbol{T_{LB}}$ , ***Thrust Force of Liquid Booster***

$\boldsymbol{T_{SRB}}$, ***Thrust Force of SRB***

$T_{SLB} = n.T_{SRB} + T_{LB}$ (1.7)

The drag force, $F_D = \frac{1}{2}\rho_{AIR}v^2C_DA_{SLB}$ (1.8)

Where, ρ is the air density, and V is the instantaneous speed of the rocket.
The drag coefficient $C_D$ is related to the geometry of the rocket and the quality of flow (laminar, turbulent, etc. ) over the surface of the rocket. The quantity A is a reference area to indicate rocket size." $k$" is air drag coefficient in kg/m and defined as [4,5,6];

$$k_{SLB} = \frac{1}{2}\rho_{AIR}.\sigma_{SLB}C_D.A_{SLB} \quad (1.9)$$

Air density, $\rho_{AIR}$ = 1.223 kg/m³

Drag coefficient, $C_D$ = 0.75

$$m_{SLB}.\frac{\partial v}{\partial t} = T_{SLB} - m_{SLB}.g - k_{SLB}.v^2$$

$$\partial t = \frac{m_{SLB}.\partial v}{k_{SLB}\frac{T_{SB}-m_{SLB}.g}{k_{SLB}} - k_{SLB}.v^2}$$

The terminal velocity of solid and liquid propellant booster phase is given below;

$$\boldsymbol{q_{SLB} = \sqrt{\frac{T_{SLB}-m_{SLB}.g}{k_{SLB}}}} \quad (1.10)$$

$$\boldsymbol{\partial t = \frac{m_{SLB}.\partial v}{k_{SLB}.q^2 - k_{SLB}.v^2}}$$

$$\int \partial t = \frac{m_{SLB}}{k_{SLB}}\int_0^v \frac{\partial v}{q_{SLB}^2 - v^2}$$

The burnout time of solid and liquid boosters

$$\boldsymbol{t_{SLB} = \frac{m_{SLB}}{k_{SLB}}\frac{1}{2q_{SLB}}ln\frac{q_{SLB}+v}{q_{SLB}-v}} \quad (1.11)$$

*2.1.2 Burn out velocity at boosting stage*

$$\frac{2.q_{SB}.k_{SLB}}{m_{SLB}}t = ln\frac{q_{SLB}+v}{q_{SLB}-v}$$

Let $x_{SB} = \frac{2.q_{SLB}.k_{SLB}}{m_{SLB}}$

So that

$$-x_{SLB}t = ln\frac{q_{SLB}-v_{SLB}}{q_{SLB}+v_{SLB}}$$

$$e^{-x_{SLB}t} = \frac{q_{SLB}-v_{SLB}}{q_{SLB}+v_{SLB}}$$

$$e^{-x_{SLB}.t}.q_{SLB} + e^{-x_{SLB}.t}.v_{SLB} = q_{SLB} - v_{SLB}$$

The burnout velocity solid and liquid boosters are expressed as

$$v_{SLB} = q_{SLB}\frac{1+e^{-x_{SLB}t}}{1-e^{-x_{SLB}t}} \quad (1.12)$$

*2.1.3. Burn out altitude at boosting stage*

For finding burnout altitude similarly Newtons second law is used.

$$F = m_{SLB}\frac{\partial v}{\partial h}\frac{\partial h}{\partial t} = m_{SLB}\frac{\partial v}{\partial h}v$$

$$T_{SLB} - m_{SLB}.g - k_{SLB}v^2 = m_{SLB}.v\ .\frac{\partial v}{\partial h}$$

$$\partial h = \frac{m_{SLB\cdot}}{T_{SLB}-m_{SLB}.g-k_{SLB}v^2}\, v\, \partial v$$

$$\int \partial h = \frac{m_{SLB\cdot}}{2k_{SLB}} \int \frac{1}{T_{SLB}-m_{SLB}.g-k_{SLB}v^2}\, \partial v$$

The burnout altitude solid and liquid booster is found as

$$h_{SLB} = \frac{m_{SLB\cdot}}{2.k_{SLB}}\, ln\, \frac{T_{SLB}-m_{SLB}.g}{T_{SLB}-m_{SLB}.g-k_{SLB}.v_{SLB}{}^2} \quad (1.13)$$

Velocity and Total Altitude of the Rocket System.

$$v_{BT1} = v_{SLB} \quad (1.14)$$
$$h_{BT1} = h_{SLB} \quad (1.15)$$

*2.2 Second Boosting Stage with only Liquid Propellant in CCB*

After n solid rockets ejected from the system, new calculations are made for the liquid stage of center core booster with reduced weight of the system. To calculate time and velocity at burnout stage used the Newton's second law;

$$m_{LB} = m_T - n.m_{SRB} - m_{LRBP1} - \frac{m_{LRBP2}}{2}$$

$m_{LB}$ , average mass of system after ejected five rockets $m_{LRBP2}$, center core second liquid propellant mass of the first stage

After ejections of n unit $d_{SRB}$ diameter solid rockets, the cross-section area central core booster with diameter $d_{CCB}$ is calculated.

$$A_{LB} = \frac{\pi}{4}[d_{CCB}^2] \quad (1.16)$$

*2.2.1. Burnout time at boosting stage*

$$F = m_{LB}.a$$
$$\boldsymbol{F = m_{LB}.\frac{\partial v}{\partial t}}$$

$$F = T_{LB} - m_{LB}.g - k_{LB}.v^2$$

"$k$" is air drag coefficient in kg/m and defined as;

$$k_{LB} = \frac{1}{2}\rho_{AIR}.C_D.A_{LB} \quad (1.17)$$

Air density ,$\rho_{AIR}$ = 1.223 kg/m³

Drag coefficient , $C_D$ = 0.75

Mean altitude value, $\sigma_{BL}$

$$m_{LB}.\frac{\partial v}{\partial t} = T_{LB} - m_{LB}.g - k_{LB}.v^2$$

$$\partial t = \frac{m_{LB}.\partial v}{k_{LB}\frac{T_{LB}-m_{LB}.g}{k_{LB}} - k_{LB}.v^2}$$

$$\boldsymbol{q_{LB}{}^2 = \frac{T_{LB}-m_{LB}.g}{k_{LB}}}$$

$$\boldsymbol{q_{LB} = \sqrt{\frac{T_{LB}-m_{LB}.g}{k_{LB}}}} \quad (1.18)$$

Above liquid propellant booster phase terminal velocity is found.

$$\boldsymbol{\partial t = \frac{m_{LB}.\partial v}{k_{LB}.q^2 - k_{LB}.v^2}}$$

$$\boldsymbol{\int \partial t = \frac{m_{LB}}{k_{LB}} \int_0^v \frac{\partial v}{q_{LB}{}^2 - v^2}}$$

The burnout time half of only CCB

$$\boldsymbol{t_{LB} = \frac{m_{LB}}{k_{LB}} \frac{1}{2q_{LB}}\, ln\, \frac{q_{LB}+v}{q_{LB}-v}} \quad (\mathbf{1.19})$$

*2.2.2. Burn out velocity at boosting stage*

$$\frac{2.q_{LB}.k_{LB}}{m_{LB}}\, t = ln\, \frac{q_{LB}+v}{q_{LB}-v}$$

$$Let \qquad x_{LB} = \frac{2.q_{LB}.k_{LB}}{m_{LB}} \quad (1.20)$$

$$x_{LB}.t = ln\, \frac{q_{BL}+v}{q_{BL}-v}$$

$$-x_{LB}t = ln\, \frac{q_{LB}-v}{q_{LB}+v}$$

$$e^{-x_{LB}t} = \frac{q_{LB}-v}{q_{LB}+v}$$

$$e^{-x_{LB}.t}.q_{LB} + e^{-x_{LB}.t}.v = q_{LB} - v$$

$$s_{LB} = \frac{q+v_{SLB}}{q-v_{SLB}} \quad (1.21)$$

$$v_{LB} = q_{LB}\, \frac{s_{LB}-e^{-x_{LB}t}}{s_{LB}+e^{-x_{LB}t}} \quad (1.22)$$

*2.2.3. Burn out altitude at boosting stage*

For finding burnout altitude similarly Newtons second law is used.

$$F = m_{LB}\frac{\partial v}{\partial h}\frac{\partial h}{\partial t} = m_{LB}\frac{\partial v}{\partial h}v = m_{LB}v\frac{\partial v}{\partial h}$$

$$T_{LB} - m_{LB}.g - k_{LB}v^2 = m_{LB}.v.\frac{\partial v}{\partial h}$$

$$\partial h = \frac{m_{LB\cdot}}{k_{LB}q^2 - k_{LB}v^2}\partial v$$

$$\int \partial h = \frac{m_{LB\cdot}}{k_{LB}} \int \frac{v}{{q_{LB}}^2 - v^2}\partial v$$

$$h_{LB} = \frac{m_{LB\cdot}}{2.k_{LB}}\ ln\frac{T_{LB} - m_{LB}.g - k_{LB}{v_{SB}}^2}{T_{LB} - m_{LB}.g - k_{LB}{v_{LB}}^2} \quad (1.23)$$

Velocity and Total Altitude of the Rocket System.

$$v_{BT2} = v_{SLB} + v_{LB} \quad (1.24)$$
$$h_{BT2} = h_{SLB} + h_{LB} \quad (1.25)$$

*2.3. Calculation Of Time, Velocity And Altitude At Stage 1*

Average mass of system after the ejection of center core booster, at first stage

$$m_{L1} = m_T - 5m_{SRB} - m_{LB} - \frac{m_{L1P}}{2} \quad (1.26)$$

$m_{L1}$ , avarage mass of system after the ejection of center core booster, at first stage
$m_{L1S}$, 1. stage liquid propellant rocket mass with its structural mass
$m_{L1SP}$, 1. stage liquid propellant

The cross section of first stage with a diameter of $d_{L1}$

$$A_{L1} = \frac{\pi}{4}[d_{L1}^2] \quad (1.27)$$

*2.3.1 Burn out time at first stage*

$$F = m_{L1}.a$$

$$\boldsymbol{F = m_{L1}.\frac{\partial v}{\partial t}}$$

$$F = T_{L1} - m_{L1}.g - k_{L1}.v^2$$

$T_{L1}$ , thrust of first stage

" $k_{L1}$" is air drag coefficient in kg/m and defined as;

$$k_{L1} = \frac{1}{2}\rho_{AIR}.\sigma_{L1}C_D.A_{L1} \quad (1.28)$$

Air density ,$\rho_{AIR}$ = 1.223 kg/m³

Drag coefficient , $C_D$ = 0.75

$$m_{L1}.\frac{\partial v}{\partial t} = T_{L1} - m_{L1}.g - k_{L1}.v^2$$

$$\partial t = \frac{m_{L1}.\partial v}{k_{L1}\frac{T_{L1} - m_{L1}.g}{k_{L1}} - k_{L1}.v^2}$$

$${q_{L1}}^2 = \frac{T_{L1} - m_{L1}.g}{k_{L1}}$$

$$q_{L1} = \sqrt{\frac{T_{L1} - m_{L1}.g}{k_{L1}}} \quad (1.29)$$

Above liquid propellant sustainer phase terminal velocity is found.

$$\boldsymbol{\partial t = \frac{m_{L1}.\partial v}{k_{L1}.{q_{L1}}^2 - k_{L1}.v^2}}$$

$$\boldsymbol{\int \partial t = \frac{m_{L1}}{k_{L1}} \int_0^v \frac{\partial v}{q^2 - v^2}}$$

$$t_{L1} = \frac{m_{L1}}{k_{L1}}\frac{1}{2q_{L1}}\ln\frac{q_{L1}+v}{q_{L1}-v} \quad (1.30)$$

*2.3.2 Burn out velocity at boosting stage*

$\frac{2.q_{L1}.k_{L1S}}{m_{L1}}t = ln\frac{q_{L1}+v}{q_{L1}-v}$ , Let $x_{L1} = \frac{2.q_{L1}.k_{L1}}{m_{L1}}$ (1.29)

So that $x_{L1}.t = ln\frac{q_{L1}+v}{q_{L1}-v}$

$$-x_{L1}t = ln\frac{q_{L1}+v}{q_{L1}-v}$$
$$e^{-x_{L1}t} = \frac{q_{L1}-v}{q_{L1}+v}$$
$$e^{-x_{L1}.t}.q_{L1} + e^{-x_{L1}.t}.v = q_{L1} - v$$
$$\boldsymbol{s_{L1} = \frac{1+v_{BT2}}{1-v_{BT2}}} \quad (1.31)$$

the burnout velocity half of only CCB ($t = t_{L1}$)

$$\boldsymbol{v_{L1} = q_{L1}\frac{s_{L1} - e^{-x_{L1}t}}{s_{L1} + e^{-x_{L1}t}}} \quad (1.32)$$

*2.3.3 Burnout altitude at boosting stage*

For finding burnout altitude similarly Newtons second law is used.

$$F = m_{L1}\frac{\partial v}{\partial h}\frac{\partial h}{\partial t} = m_{L1}\frac{\partial v}{\partial h}v = m_{L1}v\frac{\partial v}{\partial h}$$
$$T_{L1} - m_{L1}.g - k_{L1}v^2 = m_{L1}.v.\frac{\partial v}{\partial h}$$
$$\partial h = \frac{m_{L1}.g}{k_{L1}{q_{L1}}^2 - k_{L1}v^2}\partial v$$
$$\int \partial h = \frac{m_{L1}.g}{k_{L1}} \int \frac{v}{{q_{L1}}^2 - v^2}\partial v$$

The burnout altitude at the second half of only CCB:

$$h_{L1} = \frac{m_{L1}.g}{2.k_{L1}}.ln\frac{T_{L1} - m_{L1}.g - k_{L1}{v_{BT_2}}^2}{T_{L1} - m_{L1}.g - k_{L1}{v_{L1}}^2} \quad (1.33)$$

Velocity and Total Altitude of the Rocket System.

$$v_{TS2} = v_{SLB} + v_{LB} + v_{L1} \quad (1.34)$$
$$h_{TS2} = h_{SLB} + h_{LB} + h_{L1} \quad (1.35)$$

*2.4. Calculation of time, velocity and altitude at stage 2*

$$m_{L2} = m_T - 5m_{SRB} - 2m_{LB} - m_{CCBS} - m_{L1P} - m_{1S} - \frac{m_{L2P}}{2} \quad (1.36)$$

$m_{L2}$ , avarage mass of system during the second stage.
$m_{L2}$ 2. Stage liquid rocket mass
$m_{L2P}$ 2. Stage liquid rocket propellant mass

The cross section of second stage with a same diameter of $d_{L2}$

$$A_{L2} = \frac{\pi}{4}[d_{L2}^2] \quad (1.37)$$

$$k_{L2} = \frac{1}{2}\rho_{AIR}.C_D.A_{L2} \quad (1.38)$$

$T_{L2}$ = Thrust of first stage rocket after booster

Burn out time at first stage,
Terminal velocity of the first stage after booster:

$$q_{L2} = \sqrt{\frac{T_{L2} - m_{L2}.g}{k_{L2}}} \quad (1.39)$$

$$x_{L2} = \frac{2.q_{L2}.k_{L2}}{m_{L2}} \quad (1.40)$$

$$s_{L2} = \frac{q_{L2} + v_{T1}}{q_{L2} - v_{T1}} \quad (1.41)$$

$$v_{L2} = q_{L2}\frac{s_{L1} - e^{-x_{L1}t}}{s_{L1S} + e^{-x_{L1}t}} \quad (1.42)$$

$$h_{L2} = \frac{m_{LB}}{2.k_{L2}}\ln\frac{T_{CCB} - m_{L2}.g - k_{L2}{v_{T1}}^2}{T_{CCB} - m_{L2}.g - k_{L2}{v_{L2}}^2} \quad (1.43)$$

All velocity and altitude calculations were made for booster and sustainer rockets before are added to find out Total Velocity and Total Altitude of the Rocket System:

$$v_{T2} = v_{SLB} + v_{BL} + v_{L1} + v_{L2} \quad (1.44)$$
$$h_{T2} = h_{SLB} + h_{LB} + h_{L1} + h_{L2} \quad (1.45)$$

In the remaining system of the two-stage booster and two stage sustainer rockets with some constructional mass, completes its mission with orbit engines running with some chemical fuel and of course with some payload.

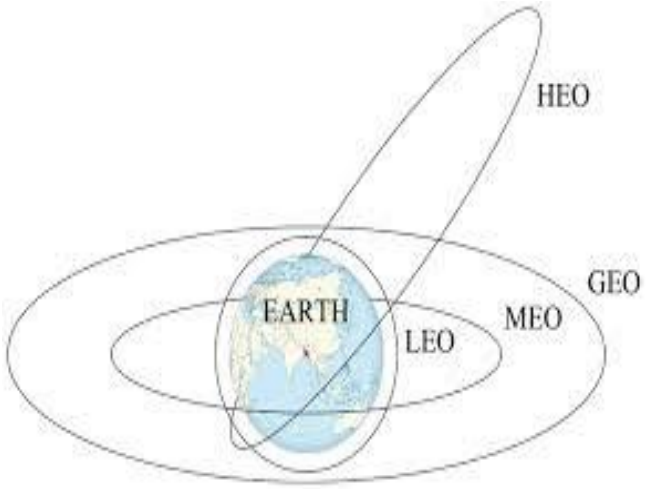


**Figure 3.** *Orbit altitudes[3] LEO satellites are confined between 500 to 1500 km. altitude. The GEO satellite altitude is of around 36,000 km, MEO satellites altitude is in the range of 10,000 to 15,000 km. and MEO and LEO satellites are referred to as Non-Geostationary Orbit (NGSO) satellites.*

LEO orbits are confined between 500 to 1500 km. altitude. The GEO satellite altitude is of around 36,000 km, MEO satellites altitude are in the range of 10,000 to 15,000 km. and MEO and LEO orbit are referred as Non-Geostationary Orbit (NGSO) Fig (3). In this study designer is to replace the payload to orbit in LEO. Then it is possible to send the payload to GEO or even to the Moon with this infrastructure.

## 3. Scope of work, results and discussion

In this study, a vehicle with multistage rockets to reach a Low Earth Orbit were designed. The rocket used as solid propellants in five solid rocket booster (SRB) and a liquid propellant in common core booster (CCB) which divided in two tanks.

At the boosting (first stage), the solid propellants in the five solid rocket booster and liquid propellant in CCB is ignited for 90 seconds. After the five solid rockets with pay rejected from the rocket, the other liquid propellant in the boosting stage. The duration of this stage is about 180 second. The table (3) shows all data which are partially taken for design vehicle in boosting phase [7].

**Table 3.** *Principal boosting phase design data[7]*

| Item BOOSTING PHASE | Total |
|---|---|
| Mass of launch vehicle (kg) | 467000 |
| **SOLID ROCKET BOOSTERS(SRB)** | |
| Solid Rocket Booster (SRB ) no. | 5 |
| Fuel mass (Kg) | 41000x5=205000 |
| Structure mass (Kg) | 5740x5=28700 |
| Burning Time(s) | 90 |
| I sp (s) | 275 |
| Diameter (m) | 1.55 |
| Total Thrust (N) | 5x1688400=8442000 |
| **COMMON CORE BOOSTERS CCB** | |
| Fuel mass1 (Kg), $m_{LRBP}$ =90s(1030)kg/s=61800kg | 92700 |
| Fuel mass2 (Kg), $m_{LRBP}$ = 90s(1030)kg/s=92700kg | 92700/185400 |
| Structure mass(Kg) | 21173 |
| Burning Time(s) | 90/90+ |
| Specific Impulse (Isp) (s) | 460 |
| Diameter (m) | 3.81 |
| Thrust (n) at sea level | 3827000 |
| Thrust (n) at airless(vacuum) | 4152000 |

$m_T = (nm_{SRB} + m_{LCCB}) + m_{L1S} + m_{L2S}$

$n$ *number solid rocket booster =5*
$m_{SRB}$ *solid rocket booster mass =47000kg*
$m_{SRBP}$ *solid rocket booster propellant mass =41000kg*

$m_{CCBS}$ *structural mass of the CCB* $= 21173kg$
$m_{LBP1}$ *common core propellant mass* $= 185400kg$
$m_{LCCB}$ *total center core mass =206573kg*

$m_{L1S}$, 1. *stage liquid propellant with structural mass* $= 22247k$
$m_{L1SP}$, 1. *stage liquid propellant* $= 20000kg$

$m_{L2S}$, 2. *stage liquid propellant with structural mass =2018kg*
$m_{L2SP}$, 2. *stage liquid propellant* $= 1850kg$

*3.1. First Boosting Stage Five Rockets with Solid and Liquid Propellant in CCB For 90 Seconds*

*D= Overall Diameter*
*D =3.82+1.58=5.4*
*A = rocket cross-sectional area in m2* $A_{SLB}$ *=22.9m2*
*t=90s*
$m_{SRBP} = 41000kg$
$m_{LRBP}$ *=1030kg/s(90s)= 92700kg*

$$m_{SLB} = m_T - \frac{5m_{SRBP}}{2} - \frac{m_{LRBP1}}{2} = 308250kg$$

$T_{SRBT} = 5(1680000N) = 8400000N$ *Thrust of Solid Booster*
$T_{LRB} = 3827000N$ *=Thrust of Liquid Booster*

*Air density,* $\rho_{AIR} = 1.223\ kg/m^3$ *Drag coefficient,* $C_D = 0.75$

**Table 4.** *First boosting stage five rockets with solid and liquid propellant in ccb for 90 seconds*

| BST* | $k_{SLB}(\frac{kg}{m})$ | $q_{SLB}(\frac{m}{s})$ | $v_{SLB}(\frac{m}{s})$ | $h_{SLB}(m)$ | $v_{BT1}(\frac{m}{s})$ | $h_{BT1}(m)$ |
|---|---|---|---|---|---|---|
| | 10.5 | 931 | 927 | 57644 | 927 | 57644 |

*3.2 Second boosting stage liquid propellant ın CCB for 90-180 seconds*

*D=* $d_{CCB}$ *= Overall Diameter*
*D =3.82+1.58=5.4m*
*A = rocket cross-sectional area in m2 A =* $A_{SLB}$ *=22.9m2*
$m_{CCBS} = 21173kg$
$m_{LBP}$ *=1030kg/s(90s)=92700kg*

$$m_{LB} = m_T - \frac{5m_{SRB}}{2} - m_{LRBP} - \frac{m_{LRBP}}{2} = 467000 - 5(47000) - 92700 - \frac{92700}{2} = 82950kg$$

$T_{LB} = 3827000N$ *=Thrust of liquid booster*

*t=90s*

**Table 5.** *Second boosting stage liquid propellant in CCB for 90-180 seconds*

| CCB liquid prop | $k_{SLB}(\frac{kg}{m})$ | $q_{SLB}(\frac{m}{s})$ | $v_{SLB}(\frac{m}{s})$ | $h_{SLB}(m)$ | $v_{BT1}(\frac{m}{s})$ | $h_{BT1}(m)$ |
|---|---|---|---|---|---|---|
| Results | 10.5 | 535 | 535 | 23480 | 1362 | 81124 |

$v_{BT2} = v_{SLB} + v_{LB} = 927\frac{m}{s} + 535\frac{m}{s} = 1362\frac{m}{s}$
$h_{BT2} = h_{SB} + h_{LB} = 57644m + 23480\text{m} = 81124\text{m}$

In the typical case, the first-stage and booster engines fire to propel the entire rocket upwards. When the boosters run out of fuel, they are detached from the rest of the rocket (usually with some kind of small explosive charge or explosive bolts) and fall away. The first stage then burns to completion and falls off. This leaves a smaller rocket, with the second stage on the bottom, which then fires.

Known in rocketry circles as staging, this process is repeated until the desired final velocity is achieved. In some case with serial staging, the upper stage ignites before the separation—the inter stage ring is designed with this in mind, and the thrust is used to help positively separate the two vehicles.
In this article at start 467ton of three stage rocket system first stage which is called as booster's final altitude is found as 81 km. It is in the range of LEO and vertical velocity is found as 1362 m/s. 205 tons of solid propellant and 185.4 tons liquid propellants are consumed. Additionally,30tons of solid rocket and 21.173tons of used bile load reduced the weight of the system and are creating smaller drag forces on the system at higher altitudes.

*3.3. First stage after boosting*

The RL10 is a liquid fuel cryogenic rocket engine built in the United States by Aerojet Rocketdyne that burns cryogenic liquid hydrogen and liquid oxygen propellants. Modern versions produce up to 110 kN (24,729 lbf) of thrust per engine in vacuum.

Inert mass: 2,247 kg (4,954 lb) Length: 12.68 m (42 ft
Fuel: Liquid Hydrogen Oxidizer: Liquid oxygen
Fuel and Oxidizer mass: 12000kg
Thrust: 99.2 kN (22,300 lbf)
Burn time: Variable, t=100s (842 s on Atlas V)

$$m_{L1} = m_T - 5m_{SRB} - 2m_{LB} - m_{CCBS} - \frac{m_{L1P}}{2}$$
$$=467000\text{-}5(47000)\text{-}92700 - 92700 - 21173 - \frac{20000}{2} = 5427kg$$

$$A_{L1} = \frac{\pi}{4}[d_{L1}^2] = \frac{\pi}{4}[1.51^2] = 1.79m2$$

$$T_{L1} = 198400\ N$$

**Table 6.** *First stage after boosting*

| Stage 1 | $k_{L1}(\frac{kg}{m})$ | $q_{L1}(\frac{m}{s})$ | $v_{L1}(\frac{m}{s})$ | $h_{SLB}(m)$ | $v_{TL1}(\frac{m}{s})$ | $h_{TL1}(m)$ |
|---|---|---|---|---|---|---|
| Results | 0.0012 | 6262 | 2556 | 505260 | 4018 | 586384 |

$v_{TL1}=927\frac{m}{s}+535\frac{m}{s}+2556=4018\frac{m}{s}$
$h_{TL1} = 57644m + 23480m+505260m = 586384m$

$$V_{OR1} = \sqrt{\frac{\left(6.67\times10^{-11}\frac{Nm^2}{kg^2}\right)(5.98\times10^{24}kg)}{6378000\,m+586000\,m}} = \sqrt{\frac{\left(6.67\times10^{-11}\frac{Nm^2}{kg^2}\right)(5.98\times10^{24}kg)}{69.6400}} = 7568m/s$$

At 586 km altitude the orbit velocity 7568m/s which is still higher than 4018 m/s and not able to enter the orbit at 586 km altitude.

*3.4. Second stage after booster*

Engine Mass,168kg(restartable) Engine Length,2.32m
Engine Diameter,1.51m
Propellant, Hydrazine Attitude Control,4X40N Thrusters

$$m_{L2} = m_T - 5m_{SB} - 2m_{LB} - m_{CCBS} - m_{L1P} - m_{1S}$$
$m_{L3}$= 467000- 5(47000)- 185400 − 21173 − 20000 − 2247kg = 3180kg

So far booster and first stage rocket motors has an 586km altitude and 4018 m/s velocity. If its velocity is increased to very close to 8000 m/s, at appropriate altitude the orbit transfer can be completed. According to calculations for this purpose 1847kg of fuel should be added the system for the required fuel to make the velocity around 8000m/s which means we need second stage rocket.

$$m_{LP2} = 3180\left(1 - e^{-\frac{4000}{4600}}\right) = 1847kg$$

In order to reach orbit velocity, required mass=1847kg has been taken as 1850kg

Engine dry-weight: 168 kg

$$m_{L3} = m_{L2} - \frac{1850}{2} = 3180\text{-}925 = 2255kg$$
$$A_{L2} = \frac{\pi}{4}[d_{L2}^2] = \frac{\pi}{4}[1.51^2] = 1.79m2$$
$$T_{L2} = 99200\ N$$
$$t = \frac{m_{L2}}{k_{L2}}\frac{1}{2q_{L2}}\ln\frac{q_{L2}+v}{q_{L2}-v} = \frac{2255}{0.0006(11334)2}ln\frac{11334+4018}{11334-4018} = 123s$$
$$t_{L3} = 100s$$
$$v_{L2} = q_{L2}\frac{s_{L2}-e^{-x_{L2}t}}{s_{L2}+e^{-x_{L2}t}} = 11334\frac{2.10-0.55}{2.10+0.55} = 6629\frac{m}{s}$$
$$t_{L2} = 80s$$

**Table 7.** *Second stage after boosting*.

| Stage 11 | $k_{L2}(\frac{kg}{m})$ | $q_{L2}(\frac{m}{s})$ | $v_{L2}(\frac{m}{s})$ | $h_{L2}(m)$ | $v_{TL2}(\frac{m}{s})$ | $h_{TL2}(m)$ |
|---|---|---|---|---|---|---|
| Results | 0.0006 | 11314 | 4273 | 879042 | 8291 | 1586560 |

$v_{TL2}=927\frac{m}{s}+535\frac{m}{s}+2556+4273\frac{m}{s}=8291\frac{m}{s}$
$h_{TL2} = 57644m + 23480m+647534+879042m = 1586560m$

The staged rocket system either the velocity and altitude calculated above can enter the orbit below the 1500 km which we define as LEO. The corresponding orbit velocity at 1500 km found as

$$V_{OR1500} = \sqrt{\frac{\left(6.67\times10^{-11}\frac{Nm^2}{kg^2}\right)(5.98\times10^{24}kg)}{6378000\,m+1500000\,m}} = \sqrt{\frac{\left(6.67\times10^{-11}\frac{Nm^2}{kg^2}\right)(5.98\times10^{24}kg)}{78.78000}} = 7116m/s$$

This means whenever second stage system enters to orbit at any height it may it may go to the higher altitudes by elliptic orbit transfer or even go to the other space regions.

In the literature, artificial satellites are first launched into the desired altitude by conventional liquid/solid propelled rockets after which the satellite may use onboard propulsion systems for orbital station keeping. Once in the desired orbit, they often need some form of attitude control so that they are correctly pointed with respect to the Earth, the Sun, and possibly some astronomical object of interest.[9] They are also subject to drag from the thin atmosphere, so that to stay in orbit for a long period of time some form of propulsion is occasionally necessary to make small corrections (orbital station-keeping).[10] Many satellites need to be moved from one orbit to another from time to time, and this also requires propulsion.[11] A satellite's useful life is usually over once it has exhausted its ability to adjust its orbit.

**Table 8.** *Satellite orbit engines working with chemical fuel*

| Thrust Power (kW) | Battery Weight (kg) | Power Distribution Control Unit (kg) | Power Sub Unit (kg) | Solar Antenna (kg) | Total Weight |
|---|---|---|---|---|---|
| | | | | 88 | 163 |
| 5 | 25 | 20 | 30 | 39 | 114 |
| | | | | 35 | 110 |
| | | | | 162 | 267 |
| 10 | 25 | 30 | 50 | 72 | 177 |
| | | | | 65 | 170 |
| | | | | 250 | 385 |
| 15 | 25 | 40 | 70 | 111 | 246* |
| | | | | 100 | 235 |

## 4. Conclusions

In this article a multistage rocket is required to reach orbital speed,7116m/s and successively verified by 3 stage system is the velocity of 8291m/s at 1500km altitude.

Payload is the object or the entity which is being carried by an aircraft or launch vehicle. For a rocket, the payload can be a satellite, space probe, or spacecraft carrying humans, animals or cargo.

Firstly in [8], the travelling to Moon is discussed. By using the data Table (3) and the results of the article, it is possible to travel to Moon. The payload is found as 758 kg which may be considered as a reasonable payload. The vehicle 3180m payload by consuming nearly 407 kg Lunar Transfer Fuel for a hyperbola that encounters the Moon for 6 days, total velocity change has been expected approximately 4000m/s having at least with 7116 m/s launcher velocity. The mass driver starts orbiting at 1500km at this Earth altitude to Lunar Orbit of 100km height of Moon orbit Table (9).

**Table 9.** *Direct transfers from 185-km circular Earth orbits to 100-km prograde lunar orbits, given in inertial frame[8].*

| $m_{L2}(kg)$ | $m_{LP2}$(kg) | Total Lunar Transfer Fuel(kg) | 2ndStage Mass(kg) | Payload(kg) |
|---|---|---|---|---|
| 3180 | 1847 | 407 | 168 | 758 |

Secondly if this vehicle is separated from main mass body, 168kg of 2nd stage the new capsule is satellite may go to the to Geosynchronously Equatorial Orbit in Space at 35,786m altitude[9].

**Table 10.** *Direct transfers from 80-km circular Earth orbits to 42164-km GEO satellite orbits, given in inertial frame[10].*

| $m_{L2}(kg$ | $m_{LP2}$ (kg) | Apogee / Perigee Fuel (kg) | Orbit engine (kg) | 2.Stage Mass (kg) | Payload (kg) |
|---|---|---|---|---|---|
| 3012 | 1847 | 38/246 (284) | 246 *Table (10) | 168 | 467 |

This results are evaluated from perigee to apogee circular orbit transfers consuming approximately 284 kg of fuel and using 15kw power satellite orbit engine Table(10). Finally, reasonable mass of payload is found as 467kg.

In the scope of this article, mathematical modelling of gravity and drag calculations with changing density of the air with altitude are introduced by a successfully. It is found that multi staged chemical rockets are advantageous with respect to single rockets which has almost 90% of system propellant mass where the system is found highly expensive due to limited amount of payload.

In the literature, rather than relying on high temperature and fluid dynamics to accelerate the reaction mass to high speeds, there are a variety of methods that use electrostatic or electromagnetic forces to accelerate the reaction mass directly by a stream of ions such an engine typically uses electric power, first to ionize atoms, and then to create a voltage gradient to accelerate the ions to high exhaust velocities by using solar, nuclear electric rockets. But, power generation adds significant mass to the spacecraft, and ultimately the weight of the power source limits the performance of the vehicle. Ion thrusters, electro thermal thrusters, electromagnetic thrusters and mass drivers for propulsion are the typical examples of electromagnetic methods.

## References

[1]. Ezgi Civek Coşkun, Multistage Launch Vehicle Design with Thrust Profile and Trajectory Optimization, Ph.D.

DissertationSeptember 2014, DOI:10.13140/RG.2.2.13871.02725

[2]. Three staged Rocket System,https://mars.nasa.gov/internal_resources/784/

[3]. Eliott Wertheimer, Multiple Rocket System, http://ftp.demec.ufpr.br/foguete/bibliografia/curso_Udemy/Launchers%203%20-%20Multiple%20Stages.pdf

[4]. U.S. Standard Atmosphere Air Properties - SI Units, https://www.engineeringtoolbox.com/standard-atmosphere-d_604.html

[5]. John C. Eward, CALCULATION OF ROCKET VERTICAL-FLIGHT PERFORMANCE, EXPLORING IN AEROSPACE ROCKETRY 3. CALCULATION OF ROCKET VERTICAL -FLIGHT PERFORMANCE Lewis Research Center Cleveland, Ohio NASA TM X-52390, Ohio 1966-67

[6]. http://www.rocketmime.com/rockets/rckt_eqn.html

[7]. David Shortt • May 05, 2017 Learn the rocket equation, part 1-part 2

[8]. Erk Inger , “Mass Driver Design Traveling Earth to Moon” , Atılım Üniversitesi, Sivil Havacılık Yüksek Okulu, Gövde ve Motor Bakımı Bölümü, 06839 İncek-Ankara DOI:10.1109/ACCESS.2019.2950882 IEEE Access PP(99):1-1, November 2019

[9]. Erk Inger IE Electromagnetic Launching Systems to Geosynchronously Equatorial Orbit in Space and Cost Calculations , IEEE TRANSACTIONS ON PLASMA SCIENCE, VOL. 45, NO. 7, JULY 2017 1663

[10]. Phillips, Tony (May 30, 2000). "Solar S'Mores". NASA. Archived from the original on June 19, 2000. Retrieved 2007-07-30.

[11]. Olsen, Carrie (September 21, 1995). "Hohmann Transfer & Plane Changes". NASA. Archived from the original on 2007-07-15. Retrieved 2007-07-30.

MANAS Journal of Engineering
ISSN 1694-7398 | e-ISSN 1694-7398

*Volume 10, Issue 1, (2022) Pages 52-59*
*https://doi.org/10.51354/mjen. 1021241*

# From traditional density to compaction index: the example of Van province

Ahmet Aktaş[1], Burak Uyar[2,*]

[1] Van Yüzüncü Yıl University, Graduate School of Natural and Applied Sciences, Department of Statistics, Van, Turkey, karatahta49@gmail.com, ORCID: 0000-0002-7322-8642
[2] Van Yüzüncü Yıl University, Faculty of Economics and Administrative Sciences, Department of Econometrics, Van, Turkey, burak.uyar@yyu.edu.tr, ORCID: 0000-0002-3178-4157

**ABSTRACT**

Due to the spread of epidemic diseases such as Covid 19, through the mobility and interaction of infected people, rates of transmission, infection and death are even higher in urban areas with higher density. Density is a measurement obtained by dividing the number of people by the area; we can call it "Traditional Density". However, traditional density alone is not enough for cities that are growing and developing day by day and becoming increasingly complex. In the study, the average compaction index for Van province was calculated as 3788.67 person/km$^2$ (one person in Van province lives with 3788.67 persons in one square kilometer). According to the traditional population density, there are 57.69 people per square kilometer in Van throughout the province. While the traditional density for the city center of Van is 1368.39 person/km$^2$, this value is 7164.92 person/km$^2$ according to the compaction index. The Compaction Index, weighted density by population, is an alternative to the traditional density scale, which is the total population divided by the total area. The compaction index is the average of the densities of the subareas of a larger area weighted by the populations of the subareas. Urban sprawl is directly related to compaction, and the selection of the appropriate density scale is crucial for a developing city. Although both types of density are positively related to the size of urban areas, the compaction index takes a different density aspect compared to conventional density. Compaction index; It is a scale that should be considered in situations such as health, transportation, urban life, education, fire, natural disaster management and coordination. Therefore, it is a useful alternative in most cases.

**ARTICLE INFO**

***Research article***

*Received: 9.10.2021*
*Accepted: 7.02.2022*

***Keywords:***
*Population density,*
*population weighted density,*
*compaction ındex,*
*Van province*

**corresponding author*

## 1 Introduction

Population Density is one of the most fundamental characteristics for an urban area. The basic idea of Population Density refers to the number of people per area. Traditional Density is a measurement obtained by dividing the number of people by the area. However, traditional density alone is not sufficient for cities that are growing and developing day by day and becoming increasingly complex. Population-weighted density is more explanatory and guiding in expressing the compaction of an urban area. The Compaction Index is an alternative density scale, commonly referred to as population-weighted density, which is an alternative to the traditional density, consisting of the average of the densities of small sub-areas weighted by the populations of the whole subregional areas. It is a scale that reflects the average density of urban area populations, whose densities are weighted according to sub-area populations, within their own sub-areas. Population-weighted density has been used in a variety of ways. The simplest is that it is often used as a descriptive intensity scale compared to conventional intensity.

Craig [7] examined the conventional density and compaction index (including the geometric mean) for the whole of Great Britain using sub-areas of different sizes. In a subsequent article, he compared traditional and population-weighted densities in regions and counties of England and Wales according to Craig [8].

Dorling and Atkins [11] presented more detailed and up-to-date results on the subject.

Coombes and Raybould [6] evaluated the metrics of settlement patterns used to allocate funds to local authorities in England in the context of policymaking. They then evaluated additional measures, including population-weighted

density, looking for relationships to improve their proposed indexes.

Barnes [2] used both population- and employment-weighted densities as scales of land use when examining the impact on various aspects of travel behavior in the United States, taking into account studies of transportation and the environment. In this study, the author defined the population-weighted density scale as a "new" scale, which he named "perceived density".
Castro [5] evaluated both traditional and population-weighted density relationships, taking into account regional income convergence in Europe. He examined how economic factors affect crowding.

Lee and Lee [15] showed in their study that higher population-weighted density is associated with larger reductions in carbon dioxide greenhouse gas emissions from domestic travel and residential energy use in the one hundred and twenty-five largest urbanized regions of the United States. In addition, population-weighted density was calculated using block group data. "We use this alternative measure because it better captures the population density that typical residents of an urban area experience in their daily lives than traditional density measures," the authors explained.
Bradford [4] and Davies [9] view the traditional density scale as an "irrational" scale of density.

According to Avent [1], Bradford [4], the compaction Index is a more meaningful or informative density scale than traditional density.

According to Florida Richard [13], the Compaction Index is the best way to measure density.

The compaction index is a valid alternative to traditional density, which captures aspects that the other scale does not [16].

Since the population shapes the economic, social, health and physical conditions of a city, the most important element that makes up the city is the demographic element [10].

According to Başer [3], Pandemics are spread through the movement of infected people and the interaction between them, and these interactions occur more frequently where the Compaction index is high. As such, it has been associated with higher rates of transmission, infection and death in urban areas where density is higher during pandemics such as Covid-19. According to the traditional density, while there are 109 people per square kilometer in Turkey, this value rises to 3,868 people according to the compaction index. On average, a person in Turkey lives with 3,868 people in one square kilometer.

The Organization for Economic Cooperation and Development (OECD), which has been working on rural areas since 1988, defines rural areas according to arithmetic population density criteria by emphasizing the human-space relationship. The OECD has defined the amount of population per square kilometer as a determining criterion, and if this amount is less than 150 people, it defines that settlement as rural. The European Union (EU) uses this criterion to facilitate comparisons between countries [17].

An incorrect perception has been created that the geographical area of the metropolitan municipalities within the borders of the provinces they are located in is entirely the city area and that rural areas are not included in this area.

Rural areas; These are areas with a unique lifestyle, where economic activities such as agriculture, animal husbandry, hunting, and forestry make a living, the population is low, and natural geographical conditions are dominant, apart from urban settlements. The European Commission advocates that rural areas should not be evaluated with one-dimensional criteria such as population density, agriculture and natural resources [14].

In this study, all neighborhoods of Van province were specified in accordance with both various satellite maps (Google Earth) images and international density criteria used in the determination of urban and rural areas in order to obtain better results and to minimize the impact of the compaction index on vacant lands far from the living area.

### *1.1. Van province*

Van Province is located in the Eastern Anatolia Region and is the 19th province of Turkey, the largest in this region in terms of population. As of the end of 2020, its population is 1 149 342 people (TUIK, 2020). It is bordered by Ağrı in the north, Bitlis in the west, Siirt in the southwest, Hakkari provinces in the south, and Iran in the east. On the shores of Lake Van, the largest closed basin of Anatolia; It is a settlement center with fertile soils, abundant streams and very favorable climatic conditions. It is one of the oldest inhabited cities in the world.


**Figure 1.** *Van province and districts map [12].*

As of the end of 2020, the total area of Van (areas of 691 neighborhoods) with a population of 1 149 342 people is 19 922 square kilometers. While the population growth rate is

1.11% compared to the previous year, the traditional population density is 58. The districts with the highest and lowest population growth rates are İpekyolu (2.60%) and Bahçesaray (-2.19%).

### *1.2. Districts of Van province*

According to the data of the Turkish Statistical Institute (TUIK) [18] on February 04, 2021, there are 13 districts of the province of Van and a total of 691 neighborhoods in these districts. Of the 13 districts, İpekyolu, Edremit and Tusba are central districts and the others are provincial districts.

**Table 1.** *Numerical information about the population of Van province and its districts [18]*

| District | Population 2019 | Population 2020 | Difference | P.Growth (%) | Num. of Neigh. | Area ($km^2$) | Density (D) |
|---|---|---|---|---|---|---|---|
| Bahçesaray | 14 701 | 14 379 | -322 | -2.19 | 20 | 372 | 39 |
| Başkale | 48 838 | 49 850 | 1.012 | 2.07 | 68 | 2618 | 19 |
| Çaldıran | 62 530 | 63 133 | 603 | 0.96 | 70 | 1384 | 46 |
| Çatak | 20 592 | 20 337 | -255 | -1.24 | 33 | 1844 | 11 |
| Edremit | 127 505 | 128 557 | 1 052 | 0.83 | 30 | 353 | 364 |
| Erciş | 175 108 | 176 680 | 1 572 | 0.9 | 101 | 1854 | 95 |
| Gevaş | 28 235 | 28 242 | 7 | 0.02 | 40 | 1475 | 19 |
| Gürpınar | 34 393 | 34 956 | 563 | 1.64 | 79 | 3845 | 9 |
| İpekyolu | 326 007 | 334 470 | 8 463 | 2.6 | 50 | 970 | 345 |
| Muradiye | 50 206 | 50 247 | 41 | 0.08 | 48 | 918 | 55 |
| Özalp | 65 296 | 65 495 | 199 | 0.3 | 58 | 1417 | 46 |
| Saray | 20 498 | 20 843 | 345 | 1.68 | 27 | 917 | 23 |
| Tuşba | 162 848 | 162 153 | -695 | -0.43 | 67 | 1956 | 83 |
| Van | 1 136 757 | 1 149 342 | 12 585 | 1.11 | 691 | 19 922 | 58 |

## 2. Materials and methods

In this study, it is aimed to arrive at the concept of Compaction Index from agglomerations in sub-areas by defining densities and showing that the compaction index is an alternative to the traditional density. The Compaction Index is an indicator of the Compaction of a settlement and shows how many people actively interact with a person in a square kilometer area. For this reason, it offers very different values from the traditional population density.

TurkStat presents the population data of the provinces that have been granted metropolitan status after 2012, at the neighborhood level, within the scope of the Address Based Population Registration System (ADNKS). In this study, firstly, the population data of Van province for the year 2020 were obtained from TUIK at the neighborhood level. Likewise, the surface measurements of all neighborhoods were taken from the relevant institutions (Municipalities) and various websites using Google Earth. Traditional population densities were calculated for each district and neighborhood in Van. Then, the density indices of the settlements were calculated with the traditional population density data.

The data collected by the above methods were written using the Microsoft Office program “Microsoft Excel” software, and the neighborhood population was written in one column and the neighborhood areas in the other column for each district. Data were transferred using the same program and traditional population densities and compaction indices of the neighborhoods were calculated.

### *2.1. Traditional population density*

The density (D) of an urban area (referred to as "conventional density" to distinguish it from population-weighted density) is calculated by dividing the total population (P) by the total area (A) in Eqn. 2.1.

$$D = \frac{P}{A} \tag{2.1}$$

However, this generally does not give an ideal result for urban sprawl or urban compaction as it does not take into account unused land. Since the traditional density is not affected by the sub-areas, that is, it takes the average directly without distinguishing the most congested and rarest neighborhoods.

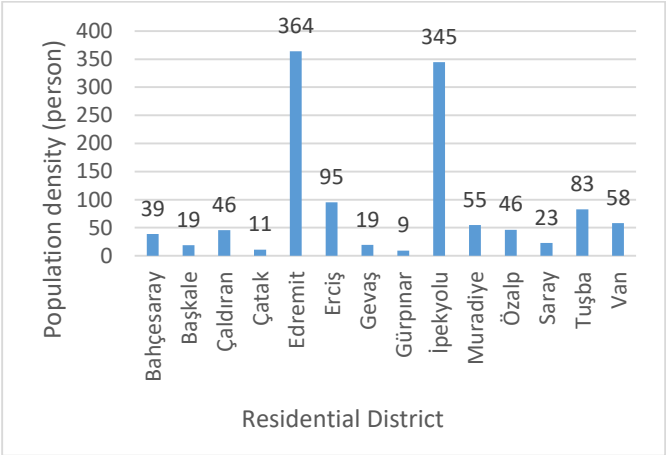


**Figure 2.** *Traditional population densities of Van province districts*

As can be seen from the above, the district with the highest traditional population density is Edremit, while the district with the lowest density is Gürpınar. It is clear that Edremit and İpekyolu districts are very dense compared to other districts.

### *2.2. Compaction index*

The size and configuration of the subdomains used in calculating the compaction index have important implications for the values obtained and their interpretation. The result is

to show what the 'Compaction Index' reached means for urban development.

This section presents the origin of the relationship between the Compaction index and conventional density. The density of an urban area is found by dividing the traditional density (D) by the total population (P) by the total area (A) as in Eqn. 2.2:

$$D = \frac{P}{A} \tag{2.2}$$

By definition, total population and total census area (or other sub-area) of area are population and areas:

$$P = \sum Pi \tag{2.3}$$

$$A = \sum ai \tag{2.4}$$

*Pi* is the population of region *i* and *ai* is the area of region *i*. *di* is the traditional population density of region *i*. The traditional population density of any region *i* is given in Eqn. 2.5.

$$d_i = \frac{P_i}{a_i} \tag{2.5}$$

The conventional density, which also applies to comparisons with the compaction index, is the average of the densities of the census regions (or other sub-areas) weighted by area, as shown in Eqn. 2.6.

$$D = \frac{1}{A}\sum a_i\, d_i = \frac{1}{A}\sum p_i = \frac{P}{A} \tag{2.6}$$

Therefore, conventional density is area-weighted density as opposed to compaction index.

The compaction index $C_i$ is the average of the census densities weighted by the population of the areas. The compaction index is calculated as in Eqn. 2.7.

$$C_i = \frac{1}{P}\sum p_i\, d_i \tag{2.7}$$

We can now show that the difference between the Compaction index and conventional density is a function of the density variance between census areas and conventional density.

Calculating variance requires the average density across areas. In order to calculate both the average density and the traditional density variance, it is necessary to weigh the regions according to their areas as in Eqn. 2.8.

$$\bar{D} = \frac{1}{A}\sum a_i d_i = \frac{1}{A}\sum p_i = D \tag{2.8}$$

Density variance $S_D^2$ is the weighted sum of the squares of the difference of the area densities and the mean intensity divided by the total area and is given as in Eqn. 2.9.

$$S_D^2 = \frac{1}{A}\sum di\ (d_i - \bar{D})^2 \tag{2.9}$$

We should note that we do not need to do the equivalent of (n - 1) correction for the weighted variance, since we have information about all domains and not just one sample.

Calculation of variance is done by squaring the binomial term in Parenthesis in Eqn. 2.9, dividing the sum, factoring the constants from the sums, and substituting the conventional density for the average density:

$$S_D^2 = \frac{1}{A}\left(\sum a_i\ d_i^2 - 2D\sum a_i d_i + D^2\sum a_i\right) \tag{2.10}$$

In Eqn. 2.10, the sum of the region's area multiplied by the density in the second term is the sum of the region's populations, the total population P equals the area times the density, A*D. Transforming this result together with the total area for the sum of the regional areas in the third term gives Eqn. 2.11.

$$S_D^2=\frac{1}{A}\left(\sum a_i d_i^2 - 2AD^2 + AD^2\right) = \frac{1}{A}\left(\sum a_i d_i^2 - AD^2\right) = \frac{1}{A}\sum a_i d_i^2 - D^2 \tag{2.11}$$

To show that this operation is related to the difference between the Compression index and density if we substitute $p_i/a_i = d_i$ for a $d_i$ in the first term in Eqn. 2.11, we get 'Eq. 2.12'.

$$S_D^2=\frac{1}{A}\sum a_i d_i\left(\frac{P_i}{a_i}\right) - D^2 = \frac{1}{A}\sum d_i p_i - D^2 \tag{2.12}$$

We can multiply the first term in Eqn. 2.13 by D/(D) and substitute P for AD,

$$S_D^2=\frac{D}{AD}\sum d_i p_i - D^2 = \frac{D}{P}\sum d_i p_i\ D^2 \tag{2.13}$$

If factor D is taken from both terms, Eqn. 2.14 is obtained.

$$S_D^2=D\left(\frac{1}{P}\sum d_i p_i - D\right) \tag{2.14}$$

The first term in parentheses is the formula for the Compaction index, this term is replaced by $C_i$ to get Eqn. 2.15.

$$S_D^2= D(C_i - D) \tag{2.15}$$

Thus, as seen in Eqn. 2.15, the variance in density is the difference between the compaction index and the conventional density multiplied by the conventional density. Therefore, the difference between compaction index density and conventional density is shown as in. 2.16.

$$C_i - D = \frac{S_D^2}{D} \tag{2.16}$$

This is obtained by dividing the density variance by the conventional density. As a result, the compaction index is the

sum of the traditional density and the ratio of the variance to the conventional density, as shown in Eqn. 2.17.

$$C_i = D + \frac{S_D^2}{D} \quad (2.17)$$

## 3. Results

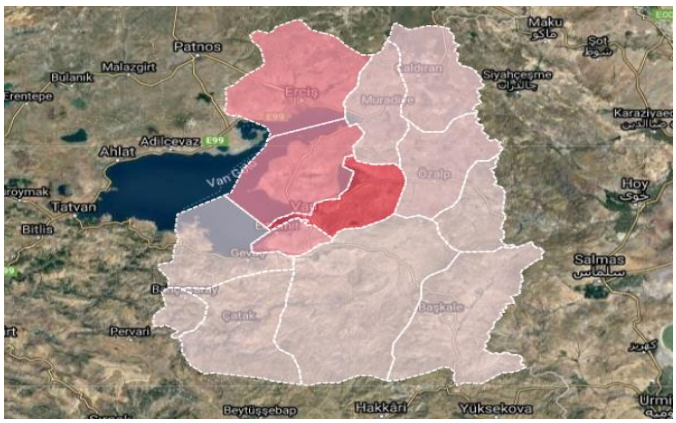


**Figure 3.** *District boundaries of Van province [12].*

The total population of Van province is 1 149 340 and its total area is 19 921.41 square kilometers. 63% of its population resides in urban areas and 37% in rural areas. The urban area constitutes 4% of the total area. While the most populous district of Van is the central İpekyolu district with 334 470 people, the district with the least population is Bahçesaray with 14 401 people.

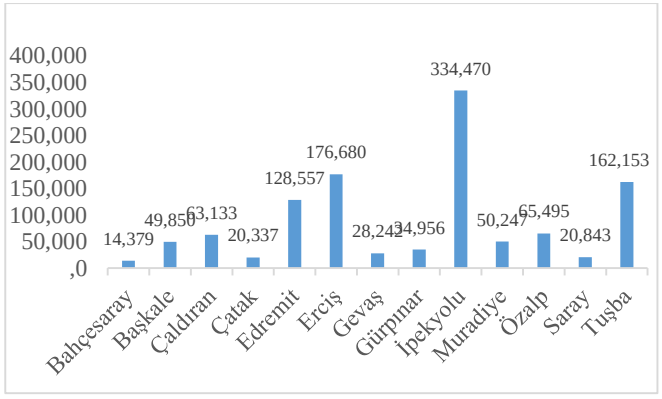


**Figure 4.** *The population of districts of Van province [18] (2020).*

While it is 57.69 per square kilometer throughout the province of Van, this value decreases to 3 788.67 per square kilometer with compaction.

The 3 central districts within the city center are İpekyolu, Edremit and Tusba districts. The total number of these three central neighborhoods is 548,590, and their area is 400.90 square kilometers.

There is a provincial town where 10 people outside the central districts of Van province are known. These districts are Bahçesaray, Başkale, Çaldıran, Çatak, Erciş, Gevaş, Gürpınar, Muradiye, Özalp and Saray districts.

**Table 2.** Traditional density and compaction indices of Van province and its districts

| District | Traditional Density | Compaction Index | Population | Area(km$^2$) | Ci/D Ratio |
|---|---|---|---|---|---|
| Bahçesaray | 39 | 55.82 | 14 379 | 372 | 1,43 |
| Başkale | 19 | 176.03 | 49 850 | 2618 | 9,26 |
| Çaldıran | 46 | 188.55 | 63 133 | 1384 | 9,26 |
| Çatak | 11 | 288.25 | 20 337 | 1844 | 4,10 |
| Edremit | 364 | 2 078.33 | 128 557 | 353 | 26,20 |
| Erciş | 95 | 1 894.41 | 176 680 | 1854 | 19,94 |
| Gevaş | 19 | 268.96 | 28 242 | 1475 | 14,16 |
| Gürpınar | 9 | 50.33 | 34 956 | 3845 | 5,59 |
| İpekyolu | 345 | 9350.78 | 334 470 | 970 | 27,10 |
| Muradiye | 55 | 257.55 | 50 247 | 918 | 4,68 |
| Özalp | 46 | 431.86 | 65 495 | 1417 | 9,39 |
| Saray | 23 | 79.05 | 20 843 | 917 | 3,44 |
| Tuşba | 83 | 3 363.86 | 162 153 | 1956 | 40,53 |
| Van | 58 | 3788.67 | 1 149 342 | 19 922 | 65,32 |

İpekyolu district, which is one of the central districts of Van, is both the most crowded and the most congested district of the city. According to the traditional population density in İpekyolu district, 344.81 people per square kilometer area, while according to the compaction index of the district, an average person lives with 9 350 people in a square kilometer area.
The total population of Tusba district is 162 151 and its area is 1955. 90 square kilometers.

According to the traditional population density in Tusba district, 82.90 people per square kilometer area, while according to the compaction index, one person in Tusba district lives with 3 363.86 people per square kilometer.

Edremit is the third crowded and last central district of Van. The total population of Edremit district is 128 557 people and its area is 353.17 square kilometers. According to the traditional population density in Edremit district, while 364.01 people per square kilometer area, this value shows that there are 2 078.33 people per square kilometer according to the compaction index. Its total population is 14 379 people and its area is 370.98 square kilometers. According to the traditional population density of the district, 38.76 people per square kilometer area, while according to the compaction index, there are 55.82 people per square kilometer throughout the county.

The population of Başkale district, which ranks second among the provincial districts of Van province in terms of surface area, is 49 850 people, and its area is 2 618.3 square kilometers. While

the traditional population density of Başkale district is 19.04 people per square kilometer area. According to this value compaction index, one person per square kilometer corresponds to 176.03 people.

The total population of Çaldıran District, which is a provincial district of Van province, is 63 133 and its area is 1384.37 square kilometers. The traditional population density of Çaldıran; while there are 45.60 people per square kilometer area, according to the compaction index, 1 person lives with 188.55 people in a square kilometer area.

Çatak district is a small town with a narrow settlement area on the river bed. The total population is 20 337 people and its total area is 1 843.65 square kilometers. The traditional population density of the Çatak district; while there are 11.03 people per square kilometer, according to the compaction index, one person lives with 288.25 people per square kilometer.

Erciş, the most populous district of the provincial districts of Van, has a total population of 176 680 people and an area of 1853,949 square kilometers. According to the traditional population density, 95.30 people per square kilometer in Erciş district, according to the central compaction index, one person lives with 1894.41 people.

Gevaş, a provincial town on the edge of Lake Van, has a population of 28242 people and an area of 1 474.88 square kilometers. Traditional population density of Gevaş district; 19.15 people per square kilometer area. According to the compaction index, one person in a square kilometer area in Gevaş district lives with 268.96 people.

The population of Gürpınar, the provincial district with the largest area in Turkey, is 34 956 people and this area is 3 844.69 square kilometers. The traditional population density of Gürpınar district; There are 9.09 people per square kilometer area. According to this value compaction index, one person lives with 50.33 people per square kilometer.

The total population of Muradiye district is 50 247 people and its total area is 917.51 square kilometers. While the traditional population density of Muradiye district is 54.76 people per square kilometer, this value is 257.55 people per square kilometer according to the compaction index.

The total population of Özalp district is 65 495 people and its total area is 1417.46 square kilometers. In Özalp district, according to the traditional population density, 46.21 people per square kilometer area, while this value is 431.86 people per square kilometer according to the compaction index.

The population of Saray district is 20 843 people. Its total area is 916.53 square kilometers. According to the traditional population density of Saray district, 22.74 people per square kilometer area, while this value increases to 79.05 people according to the compaction index.

## 4. Results and discussion

**Table 3.** *Traditional population densities of Van province by years (2007-2020)*

| 2007 | 2008 | 2009 | 2010 | 2011 | 2012 | 2013 | 2014 | 2015 | 2016 | 2017 | 2018 | 2019 | 2020 |
|---|---|---|---|---|---|---|---|---|---|---|---|---|---|
| 51 | 52 | 53 | 54 | 53 | 55 | 55 | 56 | 57 | 57 | 57 | 58 | 59 | 60 |

Mean = 55

The Compaction Index is a Different, alternative density scale. As shown, population-weighted density is equal to the conventional density and the density variance in the sub-areas used for its calculation, divided by the conventional density, which is simply the total population divided by the total area. Conventional density is also equivalent to the area-weighted density calculated across any sub-area set.

**Table 4.** *Comparison of compaction index, population and population density values*

| District | Compaction Index | Population Ranking | Popilation Density Ranking |
|---|---|---|---|
| İpekyolu | 9 350.78 | 2 | 2 |
| Van (overall) | 3 788.67 | 1 | 5 |
| Tuşba | 3 363.86 | 4 | 4 |
| Edremit | 2 078.33 | 5 | 1 |
| Erciş | 1 894.41 | 3 | 3 |
| Özalp | 431.86 | 6 | 7 |
| Çatak | 288.25 | 13 | 13 |
| Gevaş | 268.96 | 11 | 11 |
| Muradiye | 257.55 | 8 | 6 |
| Çaldıran | 188.55 | 7 | 8 |
| Başkale | 176.83 | 9 | 12 |
| Saray | 79.05 | 12 | 10 |
| Bahçesaray | 55.82 | 14 | 9 |
| Gürpınar | 50.33 | 10 | 14 |

While 57.69 people per 1 square kilometer area in Van province, the density generally applied throughout the province of Van, 3 788.67 people live in a square kilometer area according to the compaction zone. While the population census for the city center of Van is 1 368.39/km$^2$, this value is 7 164.92/km$^2$ according to the compaction data.

Ipekyolu district, which is in the 2nd place according to both the population amount and the population census, has been the most congested district of Van province. Edremit district ranks 5th in terms of compaction from a dense district until the census. We can better understand that the Çatak district is

in the last place with the 13th place in terms of both the population amount and the census, and the compaction demonstrations in the 6th place of the collision in the settlement. Preliminary preparations are made in the planning of all urban light contents.

It is located in an area that is a favorite of the crowds, gamers and closer than the eyes for its urban scales. This point of view is generally applied in general terms. Jam; related to health, life in education, education, fire, designing natural disasters. Although both types of density are positively correlated with the size of urban areas, the compaction index is more highly correlated than conventional density. The compaction index is not only related to the current size of an urban area, but also the size of the urban growth going back to past years.

To emphasize the point made in the introduction, the Compaction index takes a different density aspect compared to conventional density, it is a better density scale. For these reasons, it is a useful alternative in most situations.
According to the data obtained from TURKSTAT below [18], it is seen that the average population growth rate in Van province between 2007 and 2020 is 1.23% per year. According to these values, with the increase in the population of Van province, the compaction index will increase in the coming years.

**Table 5.** *Annual population growth rates in Van province by years (%) (2007-2020) [18]*

| 2007-2008 | 2008-2009 | 2009- 2010 | 2010-2011 | 2011-2012 | 2012-2013 | 2013-2014 | 2014-2015 | 2015-2016 | 2016-2017 | 2017-2018 | 2018-2019 | 2019-2020 |
|---|---|---|---|---|---|---|---|---|---|---|---|---|
| 2.49 | 1.77 | 1.27 | -1.25 | 2.84 | 1.71 | 1.43 | 1.00 | 0.35 | 0.61 | 1.51 | 1.15 | 1.10 |

Mean = %1.23

To other researchers; it can be suggested that they determine the relationship between the population growth rate and the compaction index, and make studies on the estimation and effects of the compaction index for the coming years.

## References


[1]. Avent. Ryan. (2011). The Gated City. Kindle Single. Amazon.

[2]. Barnes, G. (2001). Population and employment density and travel behavior in large US cities.

[3]. Başer. O. (2021). Population density index and its use for distribution of Covid-19: A case study using Turkish data. Health Policy. 125(2). 148-154.

[4]. Bradford. Chris. (2008). Perceived density. Austin Contrarian (website). Accessed from http:// austinzoning.typepad.com/austincontrarian/2008/03/perceived-densi.html on February 7. 2017.

[5]. Castro J.V. Regional convergence, polarisation and mobility in the European Union, 1980-1996. Journal of European Integration, 25(1), (2003). 73-86.

[6]. Coombes, M., & Raybould, S. (2001). Public policy and population distribution: developing appropriate indicators of settlement patterns. Environment and Planning C: Government and Policy, 19(2), 223-248.

[7]. Craig. John. (1984). Averaging population density. Demography 21. 3 (August): 405-412.

[8]. Craig. John. (1985). Better measures of population density. Population Trends No.39: 16-21.

[9]. Davies. Alan. (2012). Is Los Angeles really the densest city in the US? The Urbanist (website). Accessed from https://blogs.crikey.com.au/theurbanist/2012/10/17/is-los angeles-really-the-densest-city-in-the-us/ on February 8. 2017.

[10]. Dede. O. M.. & Şekeroğlu. A. (2019). Sağlıklı kent kavramı için nüfus kriterinin önemi. Kent Akademisi. 12(4). 703-713.

[11]. Dorling, D., & Atkins, D. J. (1995). Population density, change and concentration in Great Britain 1971, 1981 and 1991.

[12]. Endeksa Teknoloji A.Ş. (2021). Van İli demografik analizlerine yönelik veriler https://www.endeksa.com/tr/analiz/van/demografi Endeksa Teknoloji A.Ş. Ankara Erişim tarihi: 05.04.2021

[13]. Florida, Richard. 2012. America's truly densest metros. CityLab (website). Accessed from http:// www.citylab.com/housing/2012/10/americas-truly-densest-metros/3450/ on February 8. 2017.

[14]. Gülümser. A.A.. Baycan Levent. T.. & Nijkamp. P. (2011). Türkiye'nin kırsal yapısı: AB düzeyinde bir karşılaştırma. İTÜDERGİSİ/a. 9(2).

[15]. Lee, S., Lee, B. (2014). The influence of urban form on GHG emissions in the US household sector. Energy Policy, 68, 534-549.

[16]. Ottensmann. J. R. (2018). On population-weighted density. Available at SSRN 3119965.

[17]. Özçağlar. A. (2016). Büyükşehir belediyeli illerde kır ve kent nüfusunun tespiti mümkün mü. TÜCAUM

[18]. TÜİK, (2021). Türkiye İstatistik Kurumu Adrese dayalı nüfus kayıt sistemi sonuçları https://data.tuik.gov.tr/Bulten/Index?p=Adrese-Dayali-Nufus-Kayit-Sistemi-Sonuclari-2020-37210) Türkiye İstatistik Kurumu, Ankara, Erişim tarihi: 11.05.2021.

MANAS Journal of Engineering
ISSN 1694-7398 | e-ISSN 1694-7398

*Volume 10, Issue 1, (2022) Pages 60-65*
*https://doi.org/10.51354/mjen. 1034912*

# A glance at blockchain technology and cryptocurrencies as an application

Turgut Hanoymak[1,*], Ömer Küsmüş[2]

[1] Van Yüzüncü Yıl University, Van, Turkey, hturgut@yyu.edu.tr, ORCID: 0000-0002-3822-2202
[2] Van Yüzüncü Yıl University, Van, Turkey, omerkusmus@yyu.edu.tr, ORCID: 0000-0001-7397-0735

**ABSTRACT**

Blockchain technology, which includes cryptocurrencies such as Bitcoin, Ethereum, etc. [1,2] which has been evaluated as an investment tool by many people all over the world in recent years, needs to be examined in detail, both mathematically and conceptually [8,9]. In fact, it can be said that blockchain technology, which is characterized as an accounting system and database based on distributed ledgers in its most basic form, is extremely secure in terms of attacking. For this reason, we can say that technology has a more effective security mechanism than any central state-of-the-art authoritative system used today. However, as it is almost impossible to bring all of the security, speed and cost parameters to their full extent in a system at the same time, as in any cryptosystem, the security parameter from the distributed ledger structure in blockchain technology adversely affects the speed and cost parameters. In this article, we discuss the cryptographic working principles of cryptocurrencies, which is an application field of blockchain technology, together with blockchain technology and the features and structures of the blocks contained.

**ARTICLE INFO**

***Research article***

*Received: 9.12.2021*
*Accepted: 20.02.2022*

***Keywords:***
*Blockchain,*
*cryptocurrency,*
*bitcoin,*
*ethereum,*
*distributed ledger,*
*decentralized*

*Corresponding author

## 1 Introduction

Bitcoin, a financial instrument that almost everyone has been talking about recently, has attracted attention with its performance. Bitcoin and the technology of blockchain, which is the infrastructure of bitcoin, has become one of the most curious subjects of today due to its deflationary structure. Some people think that bitcoin is a pyramid scheme because it is illegal and virtual. However, others describe bitcoin and blockchain as the revolution of the future that affects almost everything, as both financial and social. As a result, some views regarding this technology have existed for a long time. Because of these two opposing views, it is possible for people to understand the essence of this technology only if the subject is studied by experts and the right information is transferred to people. Otherwise, people may continue to fall into financial difficulties by acting with the approach and advice of some malicious people due to the dark spots of this technology. People who are exposed to this situation also think that the technology is a fraud instead of protecting themselves from these malicious people. In our point of view, the people who have an interest in this technology should firstly read and study to have a technical understanding of its basics [3-8].

Blockchain technology was delivered to people in 2008 by an anonymous person or group of people named Satoshi Nakamoto with an article called Bitcoin written in academic language [1]. Understanding and adopting the essence of the business in the early days was really difficult for experts. This technological idea, which came to our minds with this theoretical article in 2008, started to become a financial instrument in 2009.

In order for people to understand why these developments actually took place in those years, they should closely follow the economic events that took place in the world at that time. The economic crisis, which started especially in the USA in 2008 and emerged as a result of an inflationary policy, caused people all over the world to question their management styles and seriously undermined the confidence in the financial policies of governments [11,12].

After this financial crisis, the concept of collateralized debt obligation began to be discussed and understood in society. Satoshi Nakamoto suggested that bitcoin should be seen as an alternative payment and exchange tool, not a derived money, in his article, which he published believing that the deflationary nature of money would protect societies from this crisis as a way to prevent such crises due to inflation. Thus,

for the first time in history, a definition of money, which was not under the control of the states and was a product of common intelligence, naturally aroused the reaction of the state authorities. Of course, bitcoin would not be like a commodity, a stock, or a fiat currency. The biggest criticism of governments for cryptocurrencies is that it is almost impossible to follow the transfer processes of cryptocurrencies and the potential of cryptocurrencies to be served for illegal groups or actions due to this following problem of cryptocurrencies. We actually do not think that cryptocurrencies have a tracking problem because, investigating the blockchain where the transfers are recorded, transactions in each block appear transparently with addresses specified in hexadecimal numbers. As a result of a rigorous criminal investigation, the state security forces can find out who these addresses belong to. In other words, it is very easy to follow the account numbers of the transactions made. However, at that time, it is not possible to track who have the accounts. Due to this feature, the ability of bitcoin to be used for money laundering and the underground economy is still a huge disgrace. The website Silkroad was founded in 2011 and was shut down twice in 2013 and 2014. On this site, it was possible to find illegal products such as various drugs, weapons, hired killers, credit card copying and child pornography. Bitcoin was used to pay for these illegal transactions on the site. However, it is argued that must emphasize that it is the business itself to be blamed here, not the use of bitcoin as the same accusations can be done for governmental printed money.

In terms of its working principle, in general, bitcoin or cryptocurrencies is a financial product based on blockchain technology, which aims to transfer money safely and quickly between two parties without any intermediary [12]. In the following sections, the structure of the blocks of the blockchain will be discussed in detail. However, to explain briefly now, it can be noticed that in order to ensure the security of this intended money transfer, the transactions must be recorded with more than one record holder. However, we realize that these transfer transactions, which are intended to be made quickly by peer-to-peer with a very low commission fee, contradict the genesis purpose of bitcoin due to problems such as the increase in commission fees and the prolongation of transfer times in recent years. Therefore, the technological solution proposal for each of the current problems of blockchain technology, called scalability, introduces new cryptocurrencies called alternative coins (altcoins).

As mentioned before, the biggest financial problem of current cryptocurrencies in the blockchain and the biggest obstacle to their use as a payment tool is the scalability problem which can be defined as slowness of transactions and high transaction fee.

## 2. The structure of blocks in a blockchain

In this section, we mention the mathematical structure of blocks in a blockchain. As mentioned in the previous section, we recall that blockchain technology is basically a database and this database is a technology with a distributed ledger structure. Data can be stored sequentially in blocks, and each block has a timestamp indicating when transactions are made. As the blocks fill their capacity, the next blocks are opened and the data starts to be recorded in this block. Each blockchain has some peculiarities of its own. With these features, the size (capacity) of the blocks contained in the blockchain and the information fields of the blocks (title, password, timestamp, version number, fingerprint of each record and the protocol to which it belongs) are determined. In every blockchain, it is necessary to know the structure of the blockchain in order to determine the way records are saved, which fields they will contain, how they will be ordered, what happens when the block is full, the conditions for generating new blocks, the characteristics of inter-block connections, how the blockchain will be distributed in the network, stored and controlled. If these features of the blockchain are secure, practical and useful, it is expected that the interest and demand for that blockchain will be higher. In a blockchain, the most important factor required for this security, practicality and usability among users on the network is mathematical hash functions.

Hash functions are very useful tools in the field of cryptology. A hash function by itself is not an encryption algorithm. It is essentially more convenient to think of hash functions as tools which satisfy authenticity and integrity. It is used to test and prove the authenticity of a data, message, document. The Secure Hash Algorithm (SHA) is an algorithm that creates a fixed-length output no matter what data it is [13]. A slightest change in a document causes a big change in the hash value. Hash value is the output or image of an input under a hash function. Therefore, when the hash value of the original document is compared with the hash value of the document that reaches us, it becomes clear whether the document is original or not. So, hash functions are used to determine the authenticity of a document.

An algorithm is required for encryption and decryption operations. For this, mathematical hard problems such as Integer Factorization Problem (IFP) [14], RSA Problem [15], Discrete Logarithm Problem (DLP) [16] are necessary. Asymmetric encryption algorithms are the only algorithms that meet the needs of the information world today. Asymmetric encryption algorithms contain a private and a public key.

The two main concepts required for the security of all transactions on the blockchain are confidentiality and integrity. An effective encryption algorithm against all kinds of attacks is required for confidentiality, and hash functions

with some features are required for integrity. The most popular among cryptographic hash functions is the SHA series hash algorithms developed by NSA. SHA-0 (in 1993), SHA-1 (in 1995) and SHA-2 (in 2002) are some of them. However, the most common and still used hash algorithm is SHA-256, which is 256 bytes long. Ideal hash functions have five key properties:

1. The same input should always produce the same output (hash value).
2. The function should be able to be calculated very quickly.
3. Input cannot be calculated using output.
4. A small change on the message or input should be able to produce a very different hash value.
5. Different inputs should not produce the same result (collision-resistant).

A hash function with these properties is a key element used to connect blocks and ensure immunity. The hash of a block appears as the input of the next block. This provides a very protective effect in terms of preventing attacks on basically any block, due to the feature of the ideal hash functions in the 4th item described above. Because even the slightest attack on a block, that is, its hash input, will change the output. Since this changing output is the input value of the next block, the hash value of the next block will also change, and as a result of this attack, the hash value of all blocks will change iteratively. This is an attack process that can be detected instantly across the entire blockchain, and the probability of the attack being successful is negligible. The first block created in a blockchain is usually called the genesis block, and since the previous block does not exist, a 256-byte-long hash input consisting of only 0 is systematically assigned.

In a blockchain, each block has a parent block because it is created by the hash output of the previous block. Except for the Genesis block, each block has a unique parent block. However, a parent block has more than one child block. Now, we examine the structure of blocks, which are the bricks of a blockchain. A block consists of 4 basic areas. These areas are shown as follows:

**Table 1.** *The Areas of Blocks*

| Field Name | Size | Context |
|---|---|---|
| Block Size | 4 Byte | shows the size of the block |
| Title | 80 Byte | consists of some fields |
| Counter | 1-9 Byte | Display number of the operations |
| Records | Variable | Saved operations |

Block size displays the total size of the operations which are realized in the block. Title consists of six subfields in itself. These subareas are given in the following table:

**Table 2.** *The Areas in the Title of a Block*

| Field Names in Title | Size | Context |
|---|---|---|
| Version | 4 Byte | follows updates |
| Hash of the previous block | 32 Byte | hash value of the parent block |
| Hash of the Merkle root | 32 Byte | hash value of the root of the Merkle tree in the block |
| Timestamp | 4 Byte | construction time (seconds) |
| Difficulty Level | 4 Byte | difficulty of proof of work (PoW) |
| Nonce | 4 Byte | A counter for PoW |

*Version* specifies which rules are valid in the relevant block of a blockchain. While creating a block, there are many rules to be followed such as its structure, length, record type, order of fields. One or more of these rules may be changed over time. Which blocks in the blockchain will be affected by this change and how will be determined by the version number.

*The hash of the previous block* is a key element which correlates the previous block with the next block. When a block is completed, its hash is generated. This hash is also one of the inputs for the next block. This feature ensures that the chain is unalterable, or in other words, protected against attacks. But that doesn't mean that blockchain registrants can't make the changes they want. The subject is directly related to the Merkle tree and the Merkle root.

*Merkle root* is actually a value obtained as a result of binary grouping of each transaction in the blockchain and calculating the hash values. The last value obtained as a result of these iterative operations by taking the hash is called Merkle root. Since transactions are hashed in pairs, if the number of records is odd, then the last record is hashed with itself. The reader who wants to better understand the Merkle tree and the Merkle root can refer to [17,18].

*Timestamp* indicates when a block was generated. It is displayed in Unix's epoch time format. This shows how many seconds have passed since January 1 1970, GMT 00:00. 4 bytes are reserved for the timestamp. This one is 32-bit. Since the first bit is reserved for the sign of the number (positive or negative), we have a 31-bit binary number. So the largest number that can be written is $2^{31} - 1 = 2147483647$.

*The degree of difficulty* is a concept directly related to the introduction of certain limitations and conditions on the hash value to be calculated. Even today's average computer is capable of calculating the hash value of a block in a short time.

It should be noted that finding the hash value of a block means creating that block. However, the blockchain system is programmed so that each block can be completed within 10 minutes. In other words, the computer does a job that finding the relevant hash value within 10 minutes. This is called mining by the miners in the blockchain. For example, the system identifies a problem when miners find an input whose first 40 bits are 0, and the miners try to be the first to complete the job. It is called Proof of Work (PoW) that the miner who completes the given job first is rewarded in the blockchain. If the time it takes to find these inputs, which we call the nonce value, in a way that meets the given conditions, that is, if the problem becomes more difficult, then an update is made on the timestamp of that blockchain.

*Nonce* is the generic name given to disposable numbers in computer language. In a blockchain, the difficulty level is based on finding the nonce value that meets the given conditions. The nonce discovery process by miners is essentially based on brute force. We now know that the time taken by this brute force operation varies directly with difficulty and timestamp. In PoW, miners compete with each other to be the first to find the nonce value. Recently, ethereum, which can be considered as the largest application of blockchains, uses PoS (Proof of Stake) method instead of PoW and develops an algorithm that adds smart contracts to the blockchain [19,20].

In PoS method, miners do not compete with each other using their computational power. Instead, each miner in the system has the right to be assigned the task of creating blocks according to his stake. In PoS method, miners collect their data in a pool and the next block creation task with this data is determined by a completely random function. However, the probability of a particular miner receiving this task is shaped by the help of this function and the stakes it has. One of the most distinctive features that distinguis PoS method from PoW method is that miners do not earn rewards after completing the block creation task in PoS method. He earns only commission fee based on his transactions. Another advantage of the PoS method over PoW method is the reduction of energy consumption, which is important for environmental health. In the PoS method, as in PoW method, each miner does not calculate for the nonce value. Since a selected person will do this calculation, there are direct energy savings. However, by the way, it should be noted that the selection of this single person in PoS method contradicts the distributed nature of the miners. This causes the task of creating blocks to be given to more stakeholders each time. It can be said that this is a contradiction in terms of centralization.

With all these advantages and disadvantages, we think that it is possible to prevent the block formation time, which is called the scalability problem of PoW or PoS method in the blockchain, which is still an open problem and cannot catch up with today's financial systems. In the next section, we will consider how blockchain can be used in finance and other business sectors when the scalability problem is solved.

## 3. Issues that will be affected by blockchain technology in the future

We now know that blockchain is a database where all records cannot be changed and only authorized persons can enter data within the framework of their authority and are kept in multiple copies in a distributed manner over the entire network. By placing smart contracts in this database, we can leave it entirely to the algorithm in which case what kind of ratio will be taken. There is no single center where all the data is collected due to the entire distributed storage of the database. Therefore, there is no such thing as a server crash, system hacking, malicious internal damage or deletion of data. It is also useless to destroy or replace a certain part of it, as losses are kept in multiple numbers. Because the terminals in the system have algorithms that check whether the records they have and other records are the same when using the blockchain. If two blockchains being compared to each other are different, the system queries which chain is present in the system. It discards the chain that is not in the system and continues processing the most common chain. All blocks in the blockchain are linked to each other by their hash values. The hash value of any block is one of the entries of the next block. Therefore, no matter which block is changed in the chain, the hash values of that block and all subsequent blocks change. This malicious terminal needs to calculate hash values of all communities one by one. The existing chain length of the system needs to be caught and crossed, which is unlikely. All records in the chain are stored sequentially. Recording or reading the chain is possible with passwords. In this way, data entry or data reading is provided at the depth of the chain, which is of interest to whomever. For example, the Bitcoin blockchain is an open chain. Anyone using a suitable application can read data from the system. In addition, anyone can enter data into the chain with appropriate applications using private key cryptography. Of course, this process is done within the framework of certain rules. However, for the blockchain that you will use, for example, in your shipping company, it is possible to set the read-only permissions and the data-write permissions and their depths. In our opinion, the most important feature of the blockchain, which we call the greatest invention after the establishment of the internet, is trust, which we say will cause great social, financial and legal changes. One of the most effective features of the blockchain is that the trading parties do not have to know and trust each other. It is possible to create such a platform without introducing a third party such as any central, notary, bank, referee, etc. The absence of a third party, that is, a centralized structure is very positive in terms of speed and cost of information confidentiality in transactions. Our general point of view on this issue is that the method of intermediary services and the institutions providing this service will either

disappear or undergo a structural transformation in the near future.

Banks that collect deposits from those with surplus resources and give loans to those in need, real estate agents who bring together those who want to sell their house and those who want to buy a house, an institution of notary public that witnesses any real estate purchase and sale and creates official records, letter of credit transactions that provide assurance in export and import, for example, intermediaries such as Swift, Western Union or MoneyGram that deliver the pocket money sent to a student studying abroad after 2 or 3 days or demand a high commission, security forces checking if a person is 18 years old, recruiters who had to check our manually prepared CV's during some job interviews, Music and art world people who want to protect their works from the pirate internet market, rental or logistics services, companies that provide hotel reservation services such as booking.com.

In short, the institutions, structures and services that provide brokerage services will change in the future. Moreover, blockchain technology may be used in electronic voting schemes such as the elections of governments by providing electronic and more secure systems. Blockchain technology promises to be quite a groundbreaking revolution such as printing presses, steam machines, airplanes, computers, the internet and e-mail have been in the past.

## 4. Conclusion and Discussion

In this article, we discuss blockchain technology, cryptocurrencies which is one of the applications of blockchains and their cryptological backgrounds such as private key cryptography, hash functions, etc. Also, we review technical informations about the structure of blocks in a blockchain and some items that the blocks and the header of a block carry.

In the end, we discuss which problems will be eliminated by blockchain technology and which problems of the companies that provide intermediary and brokerage services in social life will be facilitated in the future. We think that the glance at blockchain technology is like the glance at internet revolution in 1990s' Turkey for now. It still has many unknown features and many challenges or aspects to be applied for certain problems that need improvement. Unfortunately, due to its shortcomings, some abuses of blockchain technology, especially platforms in the cryptocurrency exchanges can be seen prominently against people. However, we think that states can prevent such abuses using constitutional regulations in capital markets laws. In this way, both cryptocurrencies and other applications of blockchain technology will provide more confidence to society being further integrated into the current financial system.

## References

[1]. Nakamoto S., "Bitcoin: A Peer-to-Peer Electronic Cash System". https://bitcoin.org/bitcoin.pdf , May-2009 (Accessed on 20.07.2018).

[2]. Vitalik Buterin. Ethereum white paper, 2013. https://github.com/ethereum/wiki/wiki/White-Paper

[3]. Polvora A., "Blockchain Now and Tomorrow, European Commission", Joint Research Centre, Brussels – Belgium, 2019.

[4]. Çarkacıoğlu A., Kripto-para Bitcoin. Research Report, Capital Markets Board of Turkey, Research Department, December-2016.

[5]. Antonopoulos A.M., Mastering Bitcoin. 1st Edition, O'Reilly Media, Inc., December-2014.

[6]. Prypto, Bitcoin for Dummies, A Wiley Brand. John Wiley & Sons, Inc., ISBN-13: 978-1119076131, 2016.

[7]. Rykwalder E., The Math Behind Bitcoin. https://www.coindesk.com/math-behind-bitcoin/ October-2014 (Accessed on 20.07.2018).

[8]. Sert T., Sorularla Blockchain, Türkiye Bilişim Vakfı, 2019.

[9]. Arvind Narayanan, Joseph Bonneau, Edward Felten, Andrew Miller, and Steven Goldfeder. Bitcoin and cryptocurrency technologies: A comprehensive introduction. 2016.

[10]. Bonneau J., Miller A., Clark J., Narayanan A., Kroll J.A., Felten E.W.. Sok: Research perspectives and challenges for bitcoin and cryptocurrencies. In 2015 IEEE Symposium on Security and Privacy, 104{121, May 2015.

[11]. Williams, Mark. Uncontrolled Risk. McGraw-Hill Education. s. 213. ISBN 978-0-07-163829-6(2010).

[12]. Andreas M. Antonopoulos, 2014, "Mastering Bitcoin", O'Reilly, 330 s.

[13]. Preneel B., Cryptographic Hash Functions, European Transactions on Telecommunications, 5, (1994), 431-448.

[14]. Pomerance C., Factoring, Cryptology and Computational Number Theory, 42, Proceedings of Symposia in Applied Mathematics, 27–47, American Mathematical Society, 1990.

[15]. Rivest R.L., Shamir A., Adleman L.M., A method for obtaining digital signatures and public-key cryptosystems", Communications of the ACM, 21 (1978), 120–126.

[16]. Mccurley K.S., The discrete logarithm problem", C. Pomerance, editor, Cryptology and Computational Number Theory, volume 42 of Proceedings of Symposia in Applied Mathematics, 49–74, American Mathematical Society, 1990.

[17]. Merkle R.C., "Protocols for public key cryptosystems," In Proc. 1980 Symposium on Security and Privacy, IEEE Computer Society, pages 122-133, April 1980.

[18]. Merkle R.C., A Certified Digital Signature, Advances in Cryptology - CRYPTO '89, 9th Annual International Cryptology Conference, Santa Barbara, California, USA, August 20-24, 1989, Proceedings.

[19]. Dwork, Cynthia; Naor, Moni "Pricing via Processing, Or, Combatting Junk Mail, Advances in Cryptology". CRYPTO'92: Lecture Notes in Computer Science No. 740. Springer. (1993), 139-147.

[20]. King S., Nadal S., Ppcoin: Peer-to-Peer crypto-currency with Proof of Stake, 2012, https://archive.org/details/PPCoinPaper.

MANAS Journal of Engineering
ISSN 1694-7398 | e-ISSN 1694-7398

*Volume 10, Issue 1, (2022) Pages 66-72*
*https://doi.org/10.51354/mjen. 1049851*

# Data hiding to the image with bit plane slicing and double XOR

Bilgi Özdemir[1], Nurettin Doğan[2] *

[1] Selçuk University, Graduate School of Natural and Applied Sciences, Department of Computer Engineering, Konya, Turkey, bilgig@hotmail.com, ORCID: 0000-0002-6841-0933

[2] Selçuk University, Faculty of Technology, Department of Computer Engineering, Konya, Turkey, ndogan@ymail.com, nurettin.dogan@selcuk.edu.tr, ORCID: 0000-0002-8267-8469

**ABSTRACT**

Data hiding is an important requirement in the history of humankind, whether internationally or personally. With the development of digital technologies, the types, and methods of data to be hidden are also very diverse. It is possible to hide any data sent via transmission channels. In this study, a new message hiding algorithm for a color image is described. In the developed algorithm, bit-plane slicing and double XOR operation are used as the basis. In the algorithm, the message to be hidden first is encrypted and then hidden. In this way, it is aimed to obtain a more secure data hiding algorithm. The keys used are selected from the most significant bitplane of the image to hide data. Thus, the algorithm becomes an adaptive algorithm. The least significant bitplane of the cover image is used to hide data. Performance criteria such as MSE, PSNR, and histogram distribution are used to measure the quality of the developed algorithm. Comparing the performance criteria with other studies shows that the developed algorithm can take its place in the field of data hiding in the literature.

**ARTICLE INFO**

***Research article***

*Received: 28.12.2021*
*Accepted: 7.06.2022*

***Keywords:***
*Bit Plane Slicing (BPS),*
*Steganography,*
*Cryptology,*
*Least Significant Bit (LSB) Method,*
*Most Significant Bit (MSB) Method,*
PSNR, MSE.

*Corresponding author

## 1. Introduction

The privacy and security of communication between people are of great importance. Due to the widespread use of digital communication over the internet, it is very important to ensure the secure transmission of information. Cryptography and Steganography are branches of science used to ensure information security and confidentiality [1]. Cryptography makes these messages unreadable to prevent unauthorized users from reading confidential or private messages. However, steganography deals with hiding hidden text data or other media in other media. Steganography is derived from the Greek words "steganos" and " Graphia", meaning cover and writing, respectively [2,3]. A carrier object is needed for use in steganography. The carrier object is called the cover-data in the environment where the data is hidden, and the resulting environment is called stegotext or stego-object, and it is called the cover-file [4]. The data to be hidden in cover objects can be text, image, or sound files [5]. The image obtained after embedding data into the cover image is called a "stego image". Hiding functions used in the process of embedding hidden data in the cover object and then retrieving the hidden data from the stego object are defined as keys [6]. The basic steganography process described above is graphically explained in Figure 1.

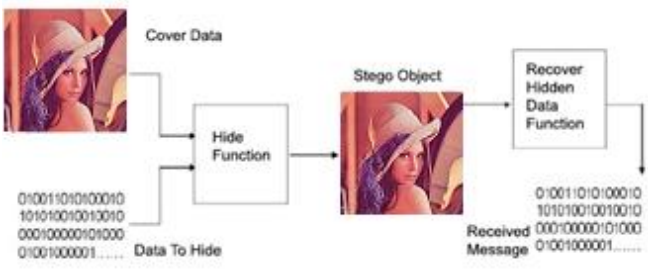


**Figure 1.** *Basic steganography system [7].*

Bit Plane Slicing (BPS) is a method of expressing an image in which each pixel is represented by one or more bits of the byte. To incorporate hidden data in any slice of eight slices, the BPS approach requires a bit slicing algorithm. Each pixel is represented by 8 bits in this approach. The combination of bit planes creates the whole image. Plane-0 is made up of LSB (Least Significant Bit) and Plane-7 is made up of MSB (Most Significant Bit) (Most Significant Bit). The value and role of each bit of the image may be determined by dividing the digital image into bitplanes. This approach, which is also

effective for image compression, defines the total amount of bits required to quantize each pixel [8]. Figure 2 shows the schematic view of bitplane slicing.

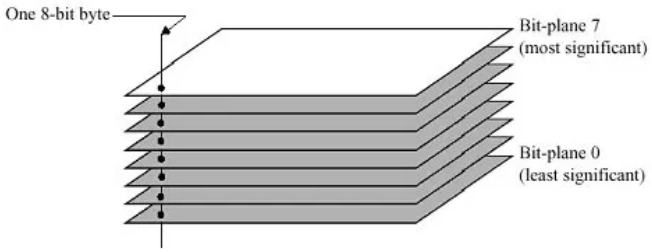


**Figure 2.** *Bit-Plane Slicing*

The security level is proportional to the number of bitplanes utilized to divide the image. The most preferred way is to hide data in the LSB bitplane, which results in less visual distortion. The risk of image corruption is lower when data is hidden in the LSB bitplane rather than the MSB bitplane. To avoid this distortion, it's important to properly hide in any plane without affecting the original image [8]. Figure 3 shows a binary display of each pixel's density value in bit plane slicing.

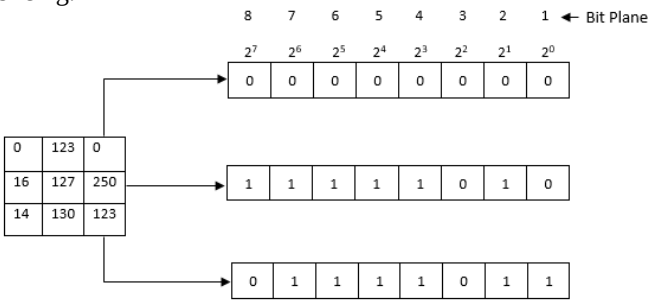


**Figure 3.** *Binary display of density value of each pixel in bit plane slicing [8]*

In the implementation of the Least Significant Bit (LSB), the least significant bits of the pixel values are used. Data bits are placed in each byte of the pixels that make up the image, one by one, respectively, starting from the beginning of the data [5]. The data to be hidden is written to the lowest-order pixel bits in order. It happens by changing the bits that will be placed in the least significant bit. This change in the image is very small and cannot be seen with the naked eye [9,10]. In the data hiding process with LSB, the hidden bit is written to the last bit of the related pixel in the binary system [11].

The most significant bit (MSB) is the highest bit of a string of numbers in binary [12]. Changing the LSB bits of an image creates a very small difference in the image that is not visible to the naked eye. Considering this situation for an image, the eye can't perceive it. When the MSB bit is changed, there is a huge color difference, and the eye can easily perceive it. Color and image distortions occur [13].

In this study, a combination method of cryptography and steganography is proposed. The encryption process proposed here is considered very efficient as it is obtained by performing a double XOR operation on a stream of message text stream with the stream of bits in the most significant MSB bit-slice obtained by the BPS method.

The outline of the proposed study is summarized as follows:

- The color cover image is divided into RGB channels and the pixel values of the R channel are obtained.
- To work on the R channel, the R channel is split into bit planes. Hiding is done on this channel determined in this way.
- In the MSB bitplane of the R channel, as many bits as the bit length of the message is determined as the key.
- The bits of the message information and the bits of the MSB are XORed. This is the first XOR operation.
- The second key is generated by inverting the MSB key bit. The result obtained from the first XOR operation with the second key is XORed. This is the second XOR operation.
- The resulting encrypted message is hidden in the LSB bitplane of the R channel.
- The hidden information in the Stego image is obtained by applying the above operations in reverse order.

In the encryption process, a more secure data hiding algorithm is obtained by using the bits in the most significant bit plane of the image's R channel as keys. In addition, an adaptive method is obtained by obtaining the key from the image. Three different images are used to evaluate the quality of the algorithm.

The remainder of this article is organized as follows:
Chapter 2 provides necessary information about the relevant study; Chapter 3 explains the basics behind the proposed combination schemes. Section 4 shows the results of the study and discussions. Finally, in Chapter 5, the conclusion of the article is presented

## 2. Literature Review

Wai et al., in their study, provide information hiding to the image by using LSB, MSB (Most significant bit), and NHB (New hybrid) techniques. Many different confidential data formats (txt, docx, xlsx, pdf) are hidden in the cover image [12].

Sharma et al., by explaining various steganography and cryptography techniques, revealed that steganography and cryptography alone are not sufficient for information security, therefore, the best of both techniques are combined to create a more secure and robust approach [14].

Neyeem proposed a new approach for reversible data hiding (RDH) using bitplane slicing. Instead of embedding data

directly in an input image, it provided hiding data in a pair of bit-plane sliced images of the input image [15].

Ahmed et al. suggested two encryption layers and a hiding stage. The message was encrypted using the double XOR operation and a secret key using binary representation, and then the encrypted bits were stored in the cover image using the LSB technique [16].

Astuti et al. have made some modifications to the LSB algorithms by adding a sequence algorithm for pixel selection. A three-time XOR operation is proposed on text messages and a three-bit MSB is used as the key in the encryption process [17].

Santosove et al. used image steganography, division, and module function, which was developed by first reducing the length of the message and then using the AES algorithm. Message security is increased as the messages are divided into two parts and sent separately [18].

A simple XOR binary-based operation used by Arindam et al. is implemented. In their work, some modifications of LSB algorithms have been made by adding a sequence algorithm for pixel selection. A three-time XOR operation is proposed on text messages and a three-bit MSB is used as the key in the encryption process [19].

Akbar et al. applied bit plane slicing to the fingerprints of the criminals and divided them into eight slices, and the criminal information of the criminals was kept in any of these eight slices. The secret message is encrypted and integrated into any bitplane after the bitplane image is rotated at various angles. Thus, it is not possible to understand which technique is used in encryption [8].

In this study, a simple and efficient way of double XOR operation with true random double key is performed before hiding the message using the BPS technique.

## 3. Proposed Method

In this study, an application is carried out on Lena, Pepper, and Babbon images as colored cover images. By using the BPS technique, the color cover image is divided into RGB channels and bit plane slicing is done for each channel. Message hiding work is carried out on the R channel from the obtained channels. A simple and efficient way of double XOR operation with a true random double key is performed before the MSB bit of the R channel of the cover image is hidden in the text. Encrypting the MSB bit is the most recommended method, as there is less cover image corruption. If encryption is selected for the LSB bit, the probability of the image being corrupted is higher than for the MSB bit encryption. The above-mentioned techniques are presented visually in the workflow chart given in Figure 4 below.

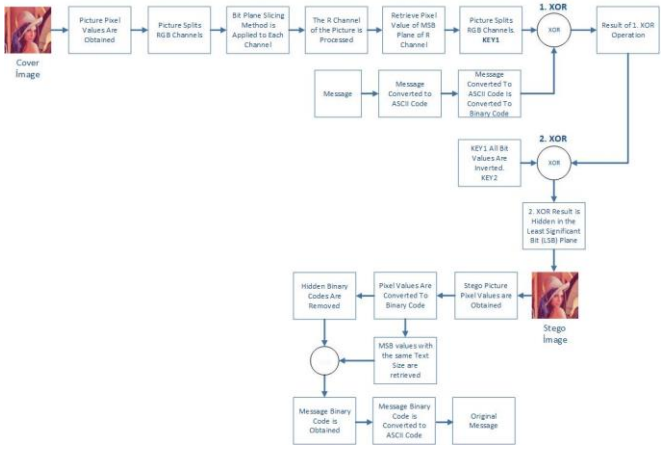


**Figure 4.** *Workflow of Recommended Security Method to Hide Encrypted Text Messages*

When Figure 4 is examined, a one-time (one-time pad (OTP)) symmetric encryption algorithm was used with the Double XOR process. This algorithm is very fast and unbreakable as the use of double keys performs in a one-bit stream in a single operation. The data hiding and decryption pseudo-codes of our algorithm are given below.

Data Hiding Algorithm:
Input: C is a color cover image. m is a message. R is C's Red channel.
Output:S is a stego image.

Start
1: size ← C's row, column, channel //Get the pixels of C.
2:Loop 1 to 8 BPS do // Do bit plane slicing
3: b ← R // Get bitplane slices of R channel.
4:end for
5: Bi_Msg=bin2dec(m) //Convert bits of m to binary code.
6: Loop 1 to length (m) do // Do the loop as many times as the m length.
7: msg←Bi_Msg //Get the binary bit string of m.
8: end for
9: key1 ← Get the bit string from MSBs of C of the same length m.
10: Loop i = 1 to length (msg) do // Do the loop as many times as the msg length.
11: EMtemp = msg-in-bits XOR Key1 // Do XOR m and KEY1 bits.
12: end for
13:Key2 = flip (Key1)) // Flip all the bits.
14: Loop i = 1 to length (msg) do // Do the loop as many times as the msg length.
15: EM = EMtemp-in-bits XOR Key2 // Do XOR the EMtemp and KEY2 bits.
16:Output1= LSB bit- in-bits BITSET EM //Hide EM encrypted message to LSB bit of R channel.
17: end for
end

Decryption Algorithm:
Input: S is an image.
Output: m is a message.

Start
1:size ← S's row, column, cannel //Get S's pixels.
2: bit plane slice ← R //Get bit plane slices of the R channel of the Stego image.

3: Loop i =1 to length (msg) // Do the loop as many times as the msg length.
4: Get the bit string for Lkey ← LSB(Si) message length.
5: length (msg)=bin2dec(Lkey) //convert bit string to binary.
6: end for
7: Loop i = 1 to length (msg) do // Do the loop as many times as the msg length.
8: Get the bit sequence from the MSBs of key1 ← S.
9: end for
10: Loop i = 1 to length (msg) do // Do the loop as many times as the msg length.
11: EM ← Extract string of bits from LSB1(Si) //Obtain bit string from LSB1 (Si).
12: end for
13:EMtemp = EM m-in-bits XOR Key1 // Do XOR EM m and bits Key1
14:Key2 = flip (Key1)) // Flip all the bits.
15: m-in-bits = EMtemp XOR Key2 //m is user message.
end

## 4. Experimental Result and Discussion

The suggested approach is evaluated using three alternative cover images. Each Cover image's original and hidden message images, as well as histogram graphs, are obtained. The histogram plot with Lena's original image and the histogram plot with the Stego image are shown in Figure 5. Bitplane slices of the Lena image are shown in Figure 6. The histogram plot with the original Pepper image and the histogram plot with the Stego image are shown in Figure 7. Bitplane slices of the R channel of the Pepper image are shown in Figure 8. The histogram plot with the original Babbon image and the histogram plot with the Stego image are shown in Figure 9. Bitplane slices of the R channel of the Babbon image are shown in Figure 10.


**Figure 5.** *Original Lena image, message hidden Lena image and their histogram plots.*

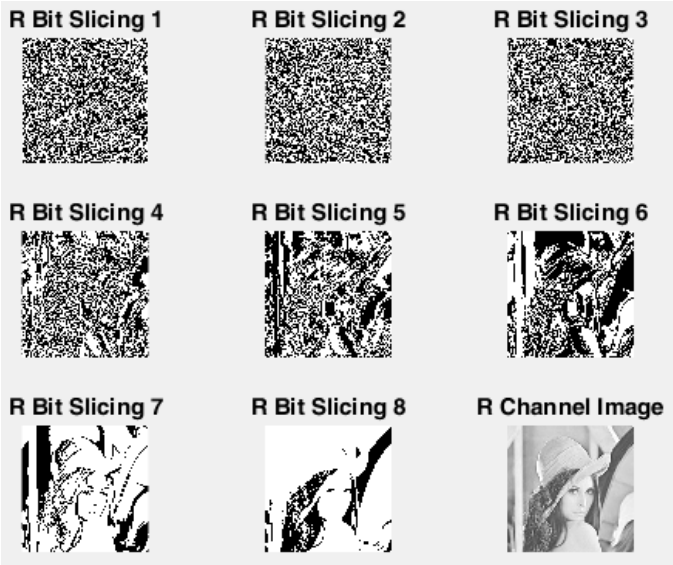


**Figure 6.** *8 Bit Plane View of R Channel of Lena image*


**Figure 7.** *Original pepper image, message hidden pepper image and their histogram plots.*

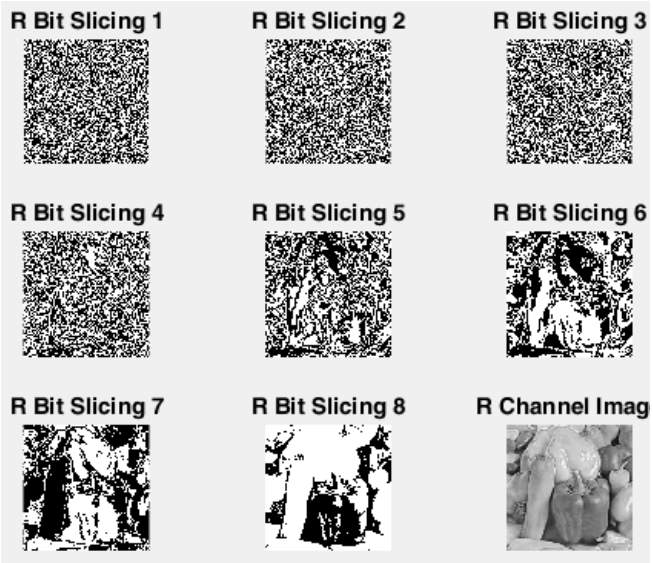


**Figure 8.** *8 Bit Plane View of R Channel of Pepper Image*

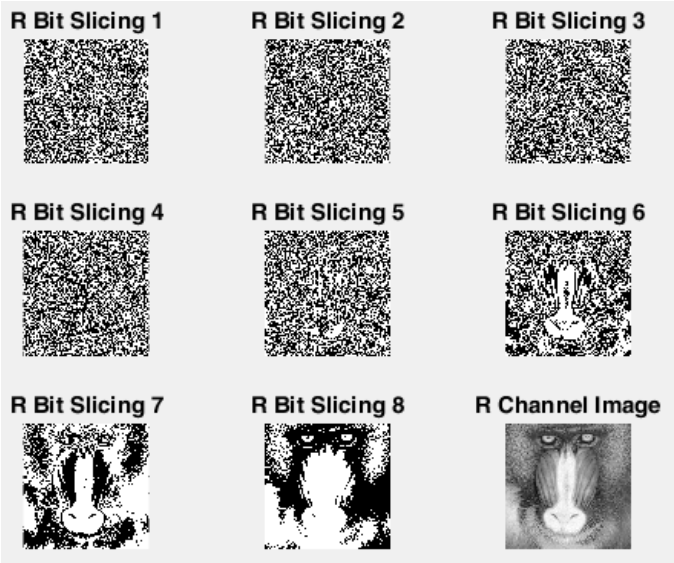


**Figure 10.** *8 Bit Plane View of R Channel of Baboon Image*

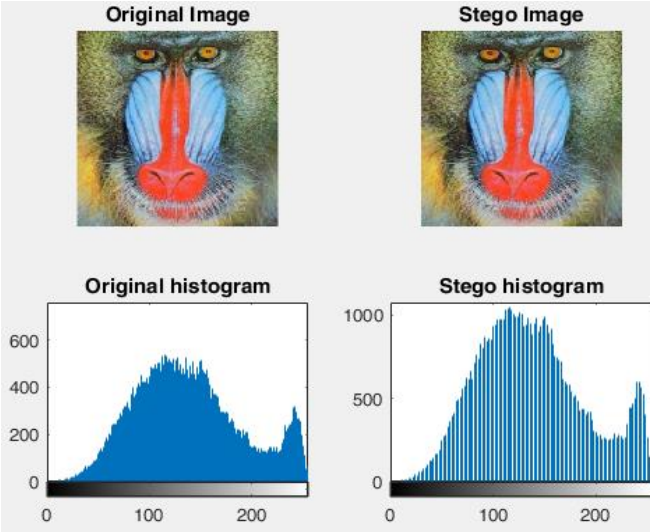


**Figure 9.** *Original Babbon image, message hidden Babbon image and their histogram plots.*

When the original and message-hidden stego images are examined, the changes in the pixels are too few to be distinguished by the human eye. However, when looking at the histograms of the images, the difference between the original and the message-hidden stego image histograms can be seen. This reveals the change made by the message in the pixels. It can be seen above that the R channel of each image is divided into bit plane slices.

For performance and evaluation measures, two common well-known metrics were used, mean square error (MSE) and peak signal-to-noise ratio (PSNR). MSE is the expected value of squared error loss or quadratic loss.

When the MSE value approaches zero, the PSNR value goes to infinity. A higher PSNR value represents better image quality. On the contrary, the smaller PSNR value indicates that the difference between cover and stego images is increased and there is no good embedding [20,21]. PSNR is usually expressed in decibels (dB) on a logarithmic scale. PSNR value greater than or equal to 30dB is difficult to detect by the human eye. PSNR value below 30 dB indicates very poor quality [22].

- MSE is between two images A (x, y) and B (x, y).
- Here, A and B are stego images and cover images, respectively, as given in the following equation [16]:

$$MSE = \sum_{i=1}^{x}\sum_{J=1}^{y}\frac{(|A_{iJ} - B_{iJ}|)^2}{x \times y}$$

- Here, x and y are the width and height of the image.
- PSNR is a well-known performance measure for image degradation that is always applied to the stego image and calculated by the following equation [16]:

$$PSNR = 10log_{10}\frac{C^2_{max}}{MSE}$$

- $C^2_{max}$, is the maximum value in the image as below:

$$C^2_{max} \leq \begin{cases} 1 \; in\; double\; precision\; intensity\; images \\ 255 - 8\; bit\; unsigned\; integer\; intensity\; images \end{cases}$$

- Images with double precision density 1 and unsigned integer density images must be less than or equal to $C^2_{max}$, values between 255 and 8 bits [16].

- These two criteria were already found by Eskicioğlu et al. [23]. In addition to image compression, they have been widely used in the field of image steganography.
- Experiments are conducted on MatLab2016b with 64-bit Microsoft Windows 10 operating system, Intel Core i5 platform with 2.5 processors, and 8 GB random access memory.

**Table 1.** *PSNR and MSE Values of the Proposed Method for Different Cover Images.*

| Images | PSNR | MSE |
|---|---|---|
| Lena | 55,903 | 0,166 |
| Pepper | 55,940 | 0,165 |
| Babbon | 55,929 | 0,165 |

Based on the values read and examined in Table 1, good results are seen for both MSE and PSNR values. Most PSNR values are greater than 40 dB, which is considered acceptable performance as reported by Nolkha et al. [24].

When our study for the colored Lena image is compared with other results in the literature, it is seen that the proposed method provides a quality stego image. Comparison results are shown in Table 2.

**Table 2.** *Results Of Image Quality Measures*

| Method | Hidden Data | PSNR | MSE |
|---|---|---|---|
| Recommended Method | 319 byte | 55.903 | 0.166 |
| Mahdi et al. [25] | 150 byte | 72.023 | 0.004 |
| Tiwari&Gangurde [26] | 112 byte | 45.865 | 1.684 |
| Ni et al. [27] | 682 byte | 48.20 | 0.980 |
| Ahmed et al. [16] | 500 byte | 51.95 | 0.420 |

## 5. Conclusion

In the study, a method is proposed to hide text messages on a colored cover image. In the proposed method, BPS steganography, which provides the capacity to hide large data, is studied. After the color cover image is first split into RGB channels, bitplane slicing is applied to R channel. At the beginning of the algorithm, the number of bit planes to be processed and the R color channel are determined and the ciphertext message is hidden in the LSB bit of the R channel. By using double encryption, secret data is sequentially embedded in LSB bit planes, preventing access to confidential information against external attacks in bit plane examination. Thanks to this process, hidden data is prevented from appearing as images in the least significant bit planes. In addition, data security is ensured with double encryption. The comparison of the proposed method with the current methods in the literature is given in Table 2. In the comparison, studies that hide data with the LSB method were used by using the Lena color image as the cover image. Looking at these results, it seems appropriate that the proposed algorithm can be used in the process of hiding information on the colored cover image. As a result, our method can take its place in the literature with other studies.

## Acknowledgment

We would like to thank the referees who read this study and made the necessary criticisms and contributed to the writing of the study in a better way.

## References

[1] Solak S., Altınışık U., A New Approach For Steganography: Bit Shifting Operation Of Encrypted Data In LSB (SED-LSB), Bilişim Teknolojileri Dergisi, 12(1), (2019), 75-81.

[2] Morkel, T., J.H. Eloff, M. S. Olivier., An Overview Of Image Steganography, in ISSA, (2005).

[3] Çelik, H. , Doğan, N. "K-En Az Anlamlı Bitlere Dayalı Kaotik Bir Harita Kullanan Renkli Görüntü Steganografisi". Politeknik Dergisi (2021 ): 1-1, https://doi.org/10.2339/politeknik.1008594 .

[4] Kurnaz H., "Hibrit Yaklaşımlı Yeni Bir Seganografi Yönteminin Geliştirilmesi," M.S. thesis, Kocaeli University, 2019.

[5] Esin E. M., Güvenoğlu E., Resim İçine Yazı Gizlenmesi Amacıyla Kullanılan LSB Ekleme Yönteminin Shuffle Algoritmasıyla İyileşitirilmesi.

[6] Patel Z. V., Gadhiya S. A., A Survey Paper On Steganography And Cryptography, International Multidisciplinary Research Journal (RHIMRJ), 2(5), (2015), 2349-7637.

[7] Özbilgin F., Durmuş F., Karagöl S., Yazılı Metni Şifreleyip LSB Yöntemi ile Gizleme, Bilim ve Teknoloji Dergisi, Düzce Üniversitesi Bilim ve Teknoloji Dergisi, (2018), 676-685.

[8] Akbar S., Dr. Rao K. N., Anand T., Bit-Plane Slicing Algorithm for Crime Data Security Using Fusion Technologies, International Journal of Recent Technology and Engineering (IJRTE), 7, (2019), 323-325.

[9] Yüksel K. [Online]. Available: https://www.youtube.com/watch?v=_-Ct3uV6AwM. [Accessed: Dec. 18, 2021]

[10] Doğan F., Daş R., Türkoğlu İ., İmgeler İçin Farklı Bir Veri Gizleme Yaklaşımı, Mühendislik Dergisi, .7(3), (2016), 501-514.

[11] Konyar Z., İlkin S., Çelik N., Sondaş A., Steganografi İçin En Uygun Resmi Belirleyen Uygulama Arayüz Tasarımı, İleri Teknoloji Bilimleri Dergisi, 1(7), (2018), 83-89.

[12] Wai Y. Y., Myat E. E., Comparison of LSB, MSB and New Hybrid (NHB) Of Steganography In Digital Image, International Journal of Engineering Trends and Applications (IJETA), 5(4), (2018).

[13] Gürel H., "Sayısal Resim İçerisine Veri Gizleme Uygulamaları," M.Sc. thesis, Kocaeli University, 2006.

[14] Sharma, H. and K. K. Sharma, S. Chauhan, "Steganography Techniques Using Cryptography-A Review Paper," 2015. pp.106-108.

[15] Neyeem H., "Reversible Data Hiding with Image Bit-Plane Slicing", 20th International Conference of Computer and Information Technology (ICCIT), 2017. pp. 22-24.

[16] Ahmed A., Ahmed A., A Secure Image Steganography Using LSB And Double XOR Operations, IJCSNS International Journal of Computer Science and Network Security, 20(5), 2020.

[17] Astuti, Y. P., E. H. Rachmawanto, and C.A. Sari,"Simple And Secure Image Steganography Using LSB And Triple XOR Operation Tn MSB," in 2018 International Conference on Information and Communications Technology (ICOIACT), 2018.

[18] Santoso H.A., Rachmawanto E. H., and Sari C. A., "An Improved Message Capacity And Security Using Divide And Modulus Function In Spatial Domain Steganography, " in 2018 International Conference on Information and Communications Technology (ICOIACT), 2018.

[19] Roy, A., Bhattacharya J., Kundu S., Sahana S., and Singh D., "Block Steganography Based Secure Key Encryption To Improve Data Security", in International Conference on Innovation in Modern Science and Technology, 2019.

[20] Horé A. and Ziou D., "Image Qualitymetrics: PSNR vs. SSIM," in International Conference on Pattern Recognition, 2010. pp. 2366-2369.

[21] Karakis R., Güler İ., Çapraz İ., Bilir E., A Novel Fuzzy Logic-Based Image Steganography Method To Ensure Medical Data Security, Computers in Biology and Medicine, 67(C), (2015), 172-183.

[22] Pund-Dange S., Desai C. G., A novel Approach of Steganography Using Bit Plane Slicing And Catalan-Lucas Number Sequence, International Journal on Recent and Innovation Trends in Computing and Communication, 6(6), (2018), 180-183.

[23] Eskicioglu A. M., Fisher P. S., Image Quality Measures And Their Performance", *IEEE Transactions on Communications*, 43(12), (1995), 2959-2965.

[24] Nolkha A., Kumar S., Dhaka V., Image Steganography Using LSB Substitution: A Comparative Analysis On Different Color Models, in Smart SystemsandIoT: Innovations in Computing, (2020), 711-718.

[25] Mahdi, S. A., Maisa'a, A. K., An Improved Method For Combine (LSB and MSB) Based On Color Image RGB, Engineering and Technology Journal, 39(1B), (2021), 231-242.

[26] Gangurde, S., Tiwari, K., LSB Steganography Using Pixel Locator Sequence With AES, arXiv e-prints, arXiv-2012., (2020).

[27] Ni, Z., Shi Y., Ansari N., Wei S., Reversible Data Hiding, IEEE Transactions on Circuits Systems and Video Technology, 16(3), (2006), 354-362.

MANAS Journal of Engineering
ISSN 1694-7398 | e-ISSN 1694-7398

*Volume 10, Issue 1, (2022) Pages 73-80*
*https://doi.org/10.51354/mjen. 1053446*

# Edge detection of aerial images using artificial bee colony algorithm

Elif Deniz Yelmenoğlu[1*], Nurdan Akhan Baykan[2]

[1] Işık University, İstanbul, Turkey, deniz.yelmenoglu@isikun.edu.tr, ORCID: 0000-0002-3645-3445,
[2] Konya Technical University, Konya, Turkey, nbaykan@ktun.edu.tr, ORCID: 0000-0002-4289-8889

**ABSTRACT**

Edge detection techniques are the one of the best popular and significant implementation areas of the image processing. Moreover, image processing is very widely used in so many fields. Therefore, lots of methods are used in the development and the developed studies provide a variety of solutions to problems of computer vision systems. In many studies, metaheuristic algorithms have been used for obtaining better results. In this paper, aerial images are used for edge information extraction by using Artificial Bee Colony (ABC) Optimization Algorithm. Procedures were performed on gray scale aerial images which are taken from RADIUS/DARPA-IU Fort Hood database. Initially bee colony size was specified according to sizes of images. Then a threshold value was set for each image, which related with images' standard deviation of gray scale values. After the bees were distributed, fitness values and probability values were computed according to gray scale value. While appropriate pixels were specified, the other ones were being abandoned and labeled as banned pixels therefore bees never located on these pixels again. So the edges were found without the need to examine all pixels in the image. Our improved method's results are compared with other results found in the literature according to detection error and similarity calculations'. All the experimental results show that ABC can be used for obtaining edge information from images.

**ARTICLE INFO**

***Research article***

*Received: 4.01.2022*
*Accepted: 22.05.2022*

***Keywords:***
*Image processing,*
*edge detection,*
*artificial bee colony optimization,*
*aerial ımages*

*corresponding author

## 1 Introduction

Nowadays, image processing techniques are quite advanced with the development of technology. Image is a concept that may be encountered in each area. Camera Systems are used in wide area such as military technology, education and training techniques, space science and in many areas like these ones. This system used in many different areas is open to continuous improvement.

Computer vision systems are also changed by the views of the nature of the images obtained in the field. For example, gray scale images, thresholded images and so on. On each image dependent upon the nature of the operations performed can be varied. All of these operations encountered appears as "**image processing**" in the literature. Image processing is being used also in many areas such as the industry of military, oil exploration, medical technology, security, criminal laboratories, satellite imagery, remote sensing applications, farming (for example; determination of the quality of meat), robotics, radar, astronomy [1-7]. Edge detection is one of the most important and indispensable step in image processing. Therefore, edge detection algorithms can be used wherever image processing is used [8-14].

In this paper, an "**edge detection method**" which is one of basic step of these operations, is used. Edges are the borders that are generated by abrupt diversities in the pixels of between two different areas [8-9, 11, 14]. Edge detection is so important because of the characterize the boundaries. Detecting the edges of an image preserves the major structural properties of the image. The recognition of edges of views is so important for human visual system because of the strong association between edge information and object attributes. For this reason, in image processing, edge detection algorithms try to identify where the object is. Edge detection reduces the amount of data to process in the image while provides important information about the shapes of objects [12]. It must be effective and trustworthy because it is very important for determining how successful following operation steps will be [15].

The existing edge extraction methods which are still used today, most of the common point is that they are dependent on

a mask. Without this mask information, edge detection process cannot be done. Derivative methods such as Laplacian, Canny, Roberts, Prewitt and Sobel are the common masks used for edge detection. Marr and Hildreth's method was developed by using edges of zero crossings with Gauss's Laplacian operator [9]. Haralick used the value of the gradient of the derivative to find a gradient of zero crossings in an image [8]. Canny's approach was based on the implementation of the Gaussian mask operator, which reduces the noise level on the image. This mask operator is produced by a sigma value. Then before the derivate process, a smoothing filter is applies on image. This method uses gradient value to find edge directions [16]. Roberts, Prewitt and Sobel methods are the some common techniques used in the image processing area. There is abundant literature [8-9, 11, 13, 16-18] on the subject of edge detection.

Optimization is to use available limited resources in the most optimal ways. Mathematically, it can be defined as maximizing or minimizing a function. It is a collection of processes comprising the best results. Optimization algorithms aim is to obtain the best results in the present circumstances. Because of the technology development and become more complex with each passing day, the problems raised by the optimization of the system also becomes more difficult to perform. For this reason, optimization algorithms must evolve with technology [19]. In the last years, new methods are developed by using modern global optimization algorithms such as the Genetic Algorithm (GA), Differential Evolution Algorithm (DE) and Simulated Annealing (SA). These kinds of algorithms are known as "**stochastic algorithms**". Yang describes the name of the all stochastic algorithms based on the randomization as "**metaheuristic**" [20].

The "**swarm**" definition is used for a group of animals. "Swarm intelligence", one of the metaheuristic approache's term, is an expression for a group behavior of decentralized and self-organized swarms. Artificial Bee Colony (ABC) is a metaheuristic algorithm inspired by the behavior of foraging bees. It was developed in 2005 by Derviş Karaboğa and has been applied in many fields [21-28].

Our improved edge detection method is based on ABC optimization algorithm and detects edges without using any mask operator. By using ABC algorithm, the pixels which are parts of an edge can be detected. This paper is organized as follows. Section 2 concerns used dataset, basic ABC and modified ABC algorithm that will be used in this work. Section 3 includes experimental results are provided by comparing between our implementation and other methods' performance. Conclusions are given in Section 4.

## 2. Material and methods

### *2.1. Dataset*

In this study, 10 gray level images taken from the RADIUS/DARPA-IU Fort Hood aerial image dataset [29] were used for testing accuracy of the proposed algorithm. All of the images size ranges between 476x477 and 645x667 pixels. The ground truth images of the test images are also included in the dataset. Figure 1 shows the 10 aerial images and their ground truths (GT: Ground Truths) used in this study.

### *2.2. Artificial Bee Colony (ABC) Optimization Algorithm*

Inspection of the occurring intelligent behavior in nature has directed researchers to produce new optimization techniques. Therefore, many metaheuristic algorithms like ABC based on behavior of the swarms are developed.

In nature, honey bees live in colonies. These bees have some features such as foraging, dancing, task sharing, decision making, navigating, positioning, mating and pheromone spreading behaviors. That features can be used as models for intelligent systems. ABC is one of the popular swarm-based algorithms developed by Karaboğa and Baştürk [30-32]. There are a lot of studies with ABC algorithms [21-24, 31, 33].

ABC algorithm has three types of bees consists of employed bees, scout bees and onlooker bees. In the ABC algorithm, there is one worker bee for each food source and the number of employed bees is equal to the number of onlooker bees. The case of the scout bees depends on the conditions of the food sources.

A food source is found randomly by each employed bee in the search space. These locations are found by Eq. (1).

$$x_{i,j} = x_j^{min} + rand(0,1)(x_j^{max} - x_j^{min}) \quad (1)$$

$x_i$ is a $D$-dimensional vector, $where\ i = 1,2,3,\ldots..,SN$ and $j = 1,2,3,\ldots.,D$ and $x_j^{max}, x_j^{min}$ are the maximum and minimum limits ($SN = number\ of\ the\ food\ source$).

All employed bees should complete their search steps, before they share their source information with the onlooker bees in the dancing area. Additionally this information includes and important data which is related the nectar amounts with onlookers.


(a1) Airfield

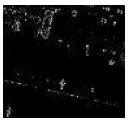
(b1) GT of Airfield


(a2) Baseball

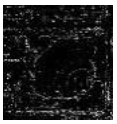
(b2) GT of Baseball

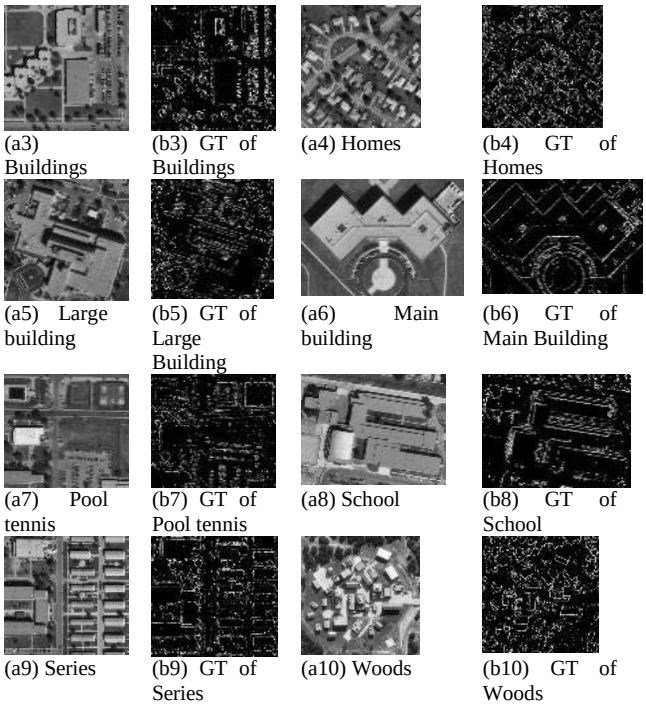


**Figure 1**. *Images from RADIUS/DARPA-IU with their ground truths.*

Each onlooker bee first selects a food source based on the probability value of the food sources. Then, following the waggle dance, it creates a new candidate solution, a new food source, in the neighborhood of this food source.

Each employed and onlooker bee tries to improve the quality of their food sources by choosing their neighbor by Eq. (2).

$$v_{i,j} = x_{i,j} + \varphi_{i,j}(x_{i,j} - x_{k,j}) \quad (2)$$

$v_i$ is randomly selected from neighbors of$x_i$ and it is called as candidate source. k is a random integer number between [1, SN] and it must be different from i. $\varphi_{i,j}$ is a real random number between [-1, 1] and j represents a random integer number between [1, D].

Works in the employed bees is done again by the greedy selection. If a resource's position cannot be improved after a certain number of cycles, that resource is banned. Meanwhile, the relevant worker bee becomes a scout bee. The banned and abandoned food source is replaced with a random food source [30-32].

The main steps are described below [28]:

1. Initial bee colony is $x = \{x_i | \, i = 1, 2, \ldots, n\}$, where n signify the population size, $x_i$ is the i'th bee in the bee colony.
2. Calculate the fitness $f_i$ of each employed bee $x_i$, and save the maximum source quality as well as the corresponding food source according to the fitness function.
3. Find a new solution $v_i$ in the neighborhood of the current solution. k is an integer near to i, k ≠i, and $\varphi$ is a random number between [−1, 1].
4. Greedy criterion is used for update $x_i$. Compute the fitness of$v_i$. If $v_i$is superior to $x_i$, $x_i$ is replaced with$v_i$; otherwise $x_i$ is remained.
5. Get the likelihood value $P_i$ by Eq. (3) and Eq. (4) according to the fitness $f_i$ of $x_i$ [34].
6. 

$$P_i = \frac{fit_i}{\sum_{i=1}^{n} fit_i} \quad (3)$$

$$fit_i = \begin{cases} \dfrac{1}{1+f_i}, & f_i \geq 0 \\ 1 + abs(f_i), & f_i < 0 \end{cases} \quad (4)$$

7. Depending on the probability$P_i$, onlookers choose food sources, search the neighborhood to generate candidate solutions, and calculate their fitness.
8. For updating the food sources, apply the greedy criteria.
9. Keep the best source data in memory.
10. Check the banned source situation. If located source is an abandoned source, replace it with a new random solution by using (1).
11. Repeat steps 3-9 until stopping criterion is satisfied.

The fitness function is so important factor in ABC algorithm. Also, control parameters of this algorithm, such as the value of limit criteria, the stopping condition and the number of employed bees or onlooker bees must be defined well. Because they affect the performance of convergence directly.

### *2.3. The proposed method*

Our method uses ABC algorithm for edge detection in images. In general, edges of an image are found with masks, and the dependency on masks can be eliminated by this improved method.

The initial image is taken for the process of edge detection with ABC and this image represents the solution space. The initial values for control parameters are set. The limit is the limit value that requires the abandonment of a resource in the ABC algorithm if it cannot be developed.

The maximum number of cycles is the number of iteration. Colony size is the number of individuals in the population and is formulated by Eq. (5) because it should not be a constant value for each image. The colony size is equal to the square root of the product multiplied by the number of rows and columns of the image.

$$K = \sqrt{NxM} \quad (5)$$

K is the total number of sources and is calculated using thee values N and M. N and M are the row and column numbers of the image, respectively [35].

After determining the all parameters' values, the sources are located. First, the number of located sources is equal to half the total number of sources given in Eq. (6). At the same time, emloyee bees are randomly located on the image.

$$LocatedSourceNumber = \frac{K}{2} \quad (6)$$

The attributes of the located sources, such as coordinates, gray level values, failure counters, probability and fitness values are kept in the memory. The fitness value for the source pixel is the value of the gray level value getting from the fitness function. Searching and using resources is still allowed to continue. If directed source is permitted source, the source's neighbor data is held as the directed source. If there is no better source adjacent to the located source, failure counter is increased. Banned resource is the source whose failure counter becomes equal to limit. The probability value of all sources is calculated by the fitness values.

In this study, fitness function is calculated by on grayscale value of each pixel. First, fitness and then likelihood values are computed according to these values. Located source's probability and one of its neighbor's are selected randomly before the probability values are compared. Failure values of current resources are controlled whatif it is equal or not to limit value in each comparison steps. If a failure value is the same with limit value, the current source is banned and the number of scout individual count is increased. None of the bees position on these banned sources again. In this study, our limit criteria is set as 5.

There are three cases about the comparison steps:

1. If current source's probability value is worse than probability boundary value, current source's failure counter increased by 1 (Figure 2.a).
2. If current source's probability value is better than probability boundary value, a random neighbor is selected from current source's neighborhood. If neighbor's value is worse than probability boundary value or current source's probability value, current source's failure counter increased by 1 (Figure 2.b).
3. If current source's probability value is better than probability boundary value, a random neighbor is selected from current source's neighborhood. If neighbor's value is better than probability boundary value and current source's probability value, and neighbor becomes new (current) source and old source's failure counter value is set as 0 (Figure 2.c).

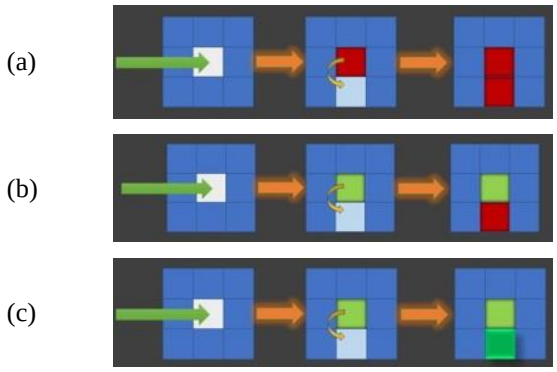


**Figure 2**. *Cases of comparison steps for neighbor pixels*

Then, located sources are controlled for belonging to any edge line or not by the examining pixels in directional aspects (Figure 3).

**Figure 3.** *Examining the neighbor pixels*

The threshold value for each image is specified by using the standard deviation of the image gray levels as given Eq. (7).

$$threshold\ value = \sqrt{\frac{1}{N}\sum_{i=1}^{N}(x_i - \bar{x})^2} \quad (7)$$

If the grayscale color difference is higher than the specified threshold value, this pixel can be belong to an edge line. If the current source is determined as an edge pixel and that pixel's value is set as 1 on the result image (Figure 4).

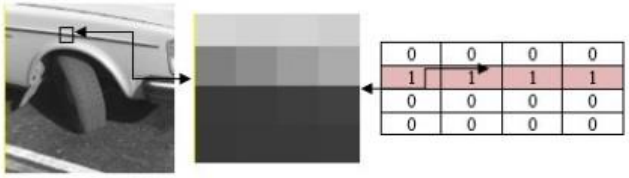


**Figure 4.** Labeling the edge boundary

## 3. Experimental results

In [36], algorithm was tested for gray scale images and compared with the Canny, Sobel and Roberts edge detection methods using Hamming Distance (HD).

(a1) Airfield (b1) ABC result of a1 (a2) Baseball (b2) ABC result of a2

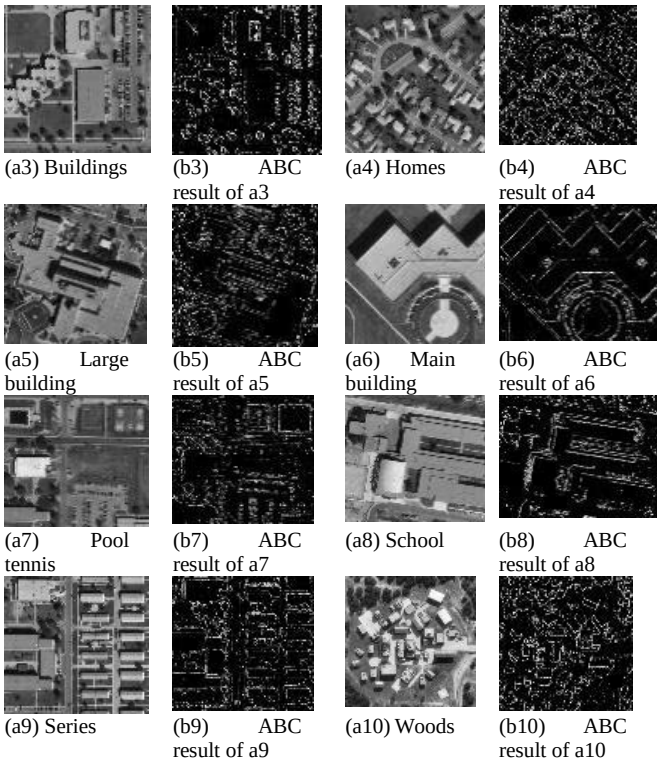


**Figure 5.** *Edge detection results of ABC*

The sizes of populations was specified according to images' width and height values by using Eq.6 and the maximum number of iterations criteria was set as 50000. Some iteration numbers such as 1000, 2000, 5000 and 50000 were compared to find the optimum iteration number and the best edge result was achieved with 50000 iteration. The limit parameter was set as 5 because a pixel has maximum 8 neighbors. Threshold and boundary probability values were computed for all tested images. RADIUS/DARPA-IU Fort Hood gray level object images and their ABC method's results are given in Figure 5. ABC method can be used as an alternative method for edge detection according to obtained experimental results.

Figure 6 shows operating times of test images which are given in Figure 4. Run time is increasing according to increasing the number of iteration.

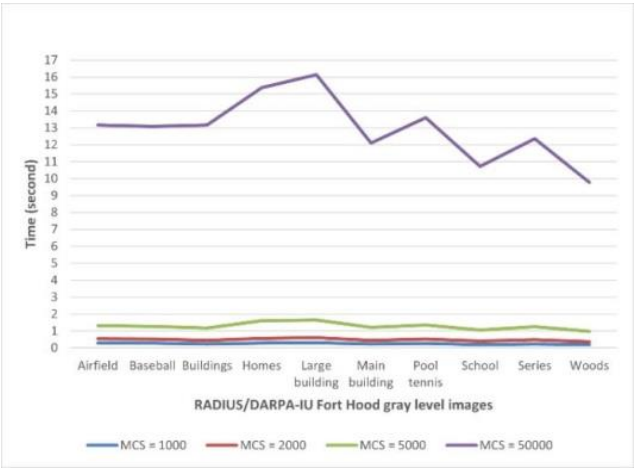


**Figure 6.** *Operating times for RADIUS/DARPA-IU Fort Hood aerial images*

Detection Error (DE) and Similarity (S) rates are used to compare results with the literature (Eq. 8-9). DE rate is computed according to result of values that are obtained from Specificity-Sensitivity analysis.

$$DE = \sqrt{(1 - TP)^2 + (FP)^2} \tag{8}$$

$$S = \frac{1}{N} \sum_{i=1}^{N} \frac{1}{1 + d_i^2} \tag{9}$$

Table 1 shows Sensitivity-Specificity analysis values for edge detection. Eq. (8) gives Detection Error rates.

**Table 1.** *Sensitivity-Specificity Analysis Values for Edge Detection*

| | **Edge (+)** | **Edge (-)** |
|---|---|---|
| **Test (+)** | True Positive (TP) | False Positive (FP) |
| **Test (-)** | False Negative (FN) | True Negative (TN) |

Our results obtained from ABC which are applied on 10 aerial gray scale images are compared with the ground truth images. The HD, DE and S results of these comparisons are given in Table 2 [37].

ABC method's DE results and S results (in Table 2) of RADIUS/DARPA-IU Fort Hood aerial images were compared with previous experimental research in the literature [15].

DE rates comparison shows that 6 of our results are worst findings and the others are acceptable values. The reason for such high rates of the developed algorithm, which environmental factors' edge information is not mentioned in the ground truth images. Our method's sensitivity is high for environmental factor's edge information on test images.

S rates comparison shows that one of our rates is the best result which is obtained from Airfield test image, the other results are acceptable values.

## 4. Conclusion

Most of the edge detection methods such as Sobel, Canny, etc. require a predefined mask. When masks are used, corner pixels of the image and pixels of the frame around the image are often either ignored or assumed to be zero. The edge extraction was done using the ABC without this kind of data loss and the dependency on the mask was removed. Its major components; i.e. graph representation, initial bee distribution, fitness function and likelihood values based on gray values of image were investigated and adapted to the underlying problem. The control of whether neighboring pixels belong to the edge was also compared with the proposed algorithm in three different stages, and the best result was tried to be obtained. Suitable values of the algorithm parameters were determined through empirical studies.

In this work, the positioning of the ABC optimization algorithm's swarm individuals was carried out on a random pixel in the input image.

In the basic ABC, first resource is specified by the formula, but in the study 8 adjacent pixels of the first resource are defined as new resources. Gray scale values of an image are used as knowledge about the quality. The numbers of populations vary according to the image size so it makes the algorithm adaptive. For maximum number of cycles, different iteration numbers between 1000 and 50000 was used and the best of them selected. Also, the limit parameter is equal to 5 after the experiments. The threshold value is computed based on the standard deviation of each image by using a formula.
In the study, run times for each number of iterations were tested and these times showed us that if maximum iteration number was increased, run time became longer. But on the other hand, if maximum iteration number was increased, result image showed us more edge information for related image.
Also improved method's results are compared with Ground Truth (GT) images according to Detection Error (DE) and Similarity (S) calculations' results. The obtained results show that the proposed method can be used for edge detection implementation as an alternative method.

Our goal for the future is to include the surrounding pixels of the image in the identification of the edges to achieve better results. For this aim, we are working on the modified ABC algorithm

**Table 2.** *Comparisons of Edge Detection Algorithms on Aerial Images*

| | | Airfield | Baseball | Buildings | Homes | Large building | Main building | Pool tennis | School | Series | Woods |
|---|---|---|---|---|---|---|---|---|---|---|---|
| **Rothwell** | ***DE*** | 0.4707 | 0.5710 | 0.5506 | 0.5991 | 0.5292 | 0.5608 | 0.5273 | 0.5638 | 0.4321 | 0.5634 |
| | ***S*** | 0.7692 | 0.6815 | 0.6886 | 0.6332 | 0.6844 | 0.6967 | 0.6722 | 0.6495 | 0.7577 | 0.6581 |
| **Bergholm** | ***DE*** | 0.4643 | 0.5968 | 0.6047** | 0.5703 | 0.5970** | 0.5651 | 0.5639 | 0.5844 | 0.5297 | 0.5846 |
| | ***S*** | 0.7651 | 0.6359 | 0.5895** | 0.5978** | 0.5401** | 0.6191 | 0.5923** | 0.5846** | 0.6084** | 0.5912 |
| **Canny** | ***DE*** | 0.5057 | 0.5668 | 0.5593 | 0.5712 | 0.5328 | 0.6180 | 0.5086 | 0.5571 | 0.4143 | 0.5526 |
| | ***S*** | 0.7593 | 0.6961 | 0.6892 | 0.6851 | 0.6976 | 0.6612 | 0.7208 | 0.6743 | 0.7682 | 0.6849 |
| **Schunck** | ***DE*** | 0.5147 | 0.5689 | 0.5640 | 0.5743 | 0.5459 | 0.6130 | 0.5367 | 0.5647 | 0.4276 | 0.5695 |
| | ***S*** | 0.7382 | 0.6848 | 0.6804 | 0.6762 | 0.6730 | 0.6499 | 0.6596 | 0.6474 | 0.7656 | 0.6748 |
| **Lacroix** | ***DE*** | 0.5340 | 0.5865 | 0.5736 | 0.4851 | 0.5180 | 0.5193 | 0.5396 | 0.5701 | 0.4522 | 0.5274 |
| | ***S*** | 0.7162 | 0.6579 | 0.6570 | 0.7143 | 0.6823 | 0.6988 | 0.6527 | 0.6419 | 0.7259 | 0.6760 |
| **Deriche** | ***DE*** | 0.5276 | 0.5726 | 0.5500 | 0.6302 | 0.5194 | 0.6677** | 0.4852 | 0.5928 | 0.5303 | 0.6856** |
| | ***S*** | 0.7516 | 0.6934 | 0.6871 | 0.6169 | 0.7082 | 0.6088** | 0.7100 | 0.6458 | 0.6810 | 0.5667** |
| **ROC** | ***DE*** | 0.4634 | 0.5505 | 0.5425 | 0.5177 | 0.5084 | 0.5439 | 0.5029 | 0.5444 | 0.4139 | 0.5241 |
| | ***S*** | 0.7760 | 0.6995 | 0.6946 | 0.7064 | 0.7014 | 0.6998 | 0.7046 | 0.6669 | 0.7767 | 0.6922 |
| **Kappa (r = 0.7)** | ***DE*** | **0.4126*** | **0.5183*** | **0.4885*** | **0.4402*** | **0.4440*** | **0.4561*** | **0.4343*** | **0.5001*** | **0.3619*** | **0.4602*** |
| | ***S*** | 0.8492 | **0.7249*** | **0.7355*** | **0.7599*** | **0.7506*** | **0.8357*** | **0.7639*** | **0.7835*** | **0.8090*** | **0.7448*** |
| **ABC** | ***DE*** | 0.86** | 0.76** | 0.59 | 0.64** | 0.59 | 0.54 | 0.63** | 0.66** | 0.63** | 0.68 |
| | ***S*** | **0.85*** | 0.63** | 0.69 | 0.68 | 0.73 | 0.73 | 0.66 | 0.74 | 0.70 | 0.64 |
| | ***HD*** | 0.0656 | 0.1406 | 0.1506 | 0.1988 | 0.1547 | 0.1086 | 0.1365 | 0.1335 | 0.1605 | 0.1561 |

**: Best for column **: Worst for column*

## Acknowledgements

This study is based on the Master Thesis of Elif Deniz Yigitbasi (Yelmenoglu) [37]. This paper has been presented at the 5th International Conference on Engineering Technologies (ICENTE-2021) held in Konya (Turkey), November 18-20, 2021.

## References

[1]. Bovik A (2010) Handbook of Image and Video Processing. Academic Press.

[2]. Gonzales RC, Woods RE (2007) Digital Image Processing. Pearson Press.

[3]. Umbaugh SE (1999) Computer Vision and Image Processing: A Practical Approach Using CVIPtools. Prentice Press.

[4]. Solomon C, Breckon T (2011) Fundamentals of Digital Image Processing : A Practical Approach with Examples in Matlab. Wiley Press.

[5]. Joyce KE, Bellis SE, Samsonov SV et al (2009) A review of the status of satellite remote sensing and image processing techniques for mapping natural hazards and disasters. Progress in Physical Geography 33(2): 183-207 DOI: 10.1177/0309133309339563

[6]. Huang J, Zhang S, Metaxas D (2011) Efficient MR image reconstruction for compressed MR imaging. Medical Image Analysis 15(5): 670-679 DOI:10.1016/j.media.2011.06.001

[7]. Liming X, Yanchao Z (2010) Automated strawberry grading system based on image processing. Computers and Electronics in Agriculture 71(1): 32-39 DOI: 10.1016/j.compag.2009.09.013

[8]. Haralick RM (1984) Digital step edges from zero crossing of second directional derivatives. IEEE Transactions on Pattern Analysis and Machine Intelligence 6(1): 58–68 DOI: 10.1109/TPAMI.1984.4767475

[9]. Marr D, Hildreth E (1980) Theory of edge detection. Proc. R. Soc. Lond. B 207: 187–217

[10]. Heath MD, Sarkar S, Sanocki T, Bowyer KW (1997) A Robust Visual Method for Assessing the Relative Performance of Edge-Detection Algorithms. IEEE Transactions on Pattern Analysis and Machine Intelligence 19 (12): 1338-1359 DOI: 10.1109/34.643893

[11]. Argyle E, Rosenfeld A (1971) Techniques for edge detection. Proceedings of the IEEE 59 (2): 285-287 DOI: 10.1109/PROC.1971.8136

[12]. Maini R (2011) Analysis and Development of Image Edge Detection Techniques. PhD Thesis, Punjabi University

[13]. Abdou IE, Pratt WK (1979) Quantitative design and evaluation of enhancement/ thresholding edge detectors. Proceedings of the IEEE 67(5): 753-763

[14]. Bhardwaj S, Mittal A (2012) A survey on Various Edge Detector Techniques. Procedia Technology 4: 220-226.

[15]. Giannarou S, Stathaki T (2011) Optimal edge detection using multiple operators for image understanding. EURASIP Journal on Advances in Signal Processing 28 DOI: 10.1186/1687-6180-2011-28

[16]. Canny J (1986) A computational approach to edge detection. IEEE Transactions on Pattern Analysis and Machine Intelligence PAMI-8(6): 679-698 DOI: 10.1109/TPAMI.1986.4767851

[17]. Roberts LG (1969) Machine perception of three-dimensional solids. US Government Printing Office Press.

[18]. Prewitt JM (1970) Object enhancement and extraction. Picture Processing and Psychopictorics: 75-149

[19]. Rao SS (2009) Engineering Optimization: Theory and practice (Fourth edition). Wiley Press

[20]. Yang XS (2010) Nature-Inspired Metaheuristic Algorithms: Second edition. Luniver Press.

[21]. Akay B (2009) Performance Analysis of Artificial Bee Colony Algorithm on Numerical Optimization Problems, Phd Thesis, Erciyes University.

[22]. Akay B, Karaboga D (2012) A modified Artificial Bee Colony algorithm for real-parameter optimization. Information Science 192: 120-142 DOI:10.1016/j.ins.2010.07.015

[23]. Karaboga D, Gorkemli B, Ozturk C, Karaboga N (2014). A comprehensive survey: Artificial Bee Colony (ABC) algorithm and applications. Artificial Intelligence Review 42(1): 21-57 DOI: 10.1007/s10462-012-9328-0

[24]. Pan Q, Tasgetiren MF, Suganthan P.N, Chua TJ (2011) A discrete artificial bee colony algorithm for the streaming flow shop scheduling problem. Information Science 181: 2455-2468 DOI:10.1016/j.ins.2009.12.025

[25]. Szeto WY, Wu Y, Ho SC (2011) An artificial bee colony algorithm for the capacitated vehicle routing problem. European Journal of Operational Research 215: 126-135 DOI: 10.1016/j.ejor.2011.06.006

[26]. Horng M (2011) Multilevel thresholding selection based on the artificial bee colony algorithm for image segmentation. Expert Systems with Applications 38: 13785-13791 DOI: 10.1016/j.eswa.2011.04.

[27]. Das P, Sadhu AK, Vyas RR, Konar A, Bhattacharyya D (2015) Arduino based multi-robot stick carrying by artificial bee colony optimization algorithm, Proceedings of the 2015 Third International Conference on Computer, Communication, Control and Information Technology (C3IT) IEEE Conference

[28]. Ma M, Liang J, Guo M, Fan Y, Yin Y (2011) SAR image segmentation based on Artificial Bee Colony algorithm. Applied Soft Computing 11: 5205–5214 DOI: 10.1016/j.asoc/2011.05.039

[29]. RADIUS/DARPA-IU Fort Hood Aerial image dataset (http://marathon.csee.usf.edu/edge/edgecompare_main.html (accessed in 2014))

[30]. Karaboga D (2005) An Idea Based on Bee Swarm for Numerical Optimization. Technical Report-TR06

[31]. Karaboga D, Basturk B (2007) A powerful and efficient algorithm for numerical function optimization: Artificial Bee Colony (ABC) algorithm. Journal of Global Optimization 39(3): 459–471 DOI: 10.1007/s10898-007-9149-x

[32]. Karaboga D, Basturk B (2008) On the performance of artificial bee colony (ABC) algorithm. Applied Soft Computing 8: 687–697 DOI: 10.1016/j.asoc.2007.05.007

[33]. Karaboga D, Akay B (2009) A survey: algorithms simulating bee swarm intelligence. Artificial Intelligence Review 31: 61–85 DOI: 10.1007/s10462-009-9127-4

[34]. Özkaya S, Conker Ç, Bilgiç H H (2021) Esnek Robot Kol Sistemi için LQR Denetleyici Parametrelerinin Metzsezgisel Algoritmalar Kullanılarak Belirlenmesi. Konya Mühendislik Bilimleri Dergisi (Konya Journal of Engineering Sciences) 9(3): 735-752 DOI: 10.36306/konjes.896087

[35]. Nezamabadi-pour H, Saryazdi S, Rashedi E (2006) Edge detection using ant algorithms. Soft Computing 10(7): 623-628

[36]. Yigitbasi ED, Baykan NA (2013) Edge detection using Artificial Bee Colony Algorithm (ABC). International Journal of Information and Electronics Engineering 3(6): 634-638 DOI: 10.7763/IJIEE.2013.V3.394

[37]. Yigitbasi ED (2014) Yapay arı kolonisi optimizasyonu ile kenar bulma [Edge detection with artificial bee colony optimization] Master thesis, The Graduate School of Natural and Applied Science, Selcuk University, Konya, Turkey (in Turkish) .

MANAS Journal of Engineering
ISSN 1694-7398 | e-ISSN 1694-7398

*Volume 10, Issue 1, (2022) Pages 81-87*
*https://doi.org/10.51354/mjen. 1076925*

# Novel indium(III) acetate phthalocyanine: synthesis and spectroscopic properties

Berra Gülem Gökçe[1], Hüseyin Kenan Soylu[1], Emir Gürel[2], Merve Cengiz[2], Fatih Mutlu[3], Mehmet Pişkin*[4]

[1] Anatolian High School, ISTEK 1915 Canakkale Schools, Çanakkale, Turkey
[2] Science High School, ISTEK 1915 Canakkale Schools, Çanakkale, Turkey
[3] Department of Chemistry, Faculty of Science, Çanakkale Onsekiz Mart University, Çanakkale, Turkey
[4] Department of Food Processing, Çanakkale Technical Sciences Vocational School, Çanakkale Onsekiz Mart University, 17020, Çanakkale, Turkey, mehmetpiskin@comu.edu.tr, ORCID: 0000-0002-4572-4905

**ABSTRACT**

A new phthalocyanine 1 was synthesized, containing 2-aminophenoxy groups as tetra from its peripheral positions and indium (III) acetate in its cavity. The structure of **1** was illuminated by elemental analysis, FTIR, UV-*vis* and fluorescence spectroscopy techniques It is well soluble in solvents such as polar and nonpolar solvent types. Its aggregation properties have been studied both in the solvents mentioned above and in Dimethyl sulfoxide at different concentrations. Its aggregation properties were examined in these solvents as well as in Dimethyl sulfoxide at certain different concentration ranges. With these determined spectroscopic properties, it can be a candidate for use in various technological applications.

**ARTICLE INFO**

***Research article***

*Received: 21.02.2022*
*Accepted: 25.04.2022*

***Keywords:***
*Phthalocyanine, indium(III) acetate, 2-aminophenol, spectroscopic, fluorescence*

**corresponding author*

## 1 Introduction

Phthalocyanines (Pcs) are synthetic molecules that are similar in structure to natural porphyrins but are not natural [1,2]. Pcs, which are formed by the cyclization of four iminoisoindoline groups over azo bridges, are generally with or without metal depending on the metal substitution in the space on the ring [1, 2]. According to the variety of metal bound to Pcs, their properties and usage areas vary [3,4]. By substituting different functional groups on the peripheral or non-peripheral positions of Pc, such as tetra or octa, as well as the presence of different metal species containing ligands in the axial position in its cavity, their aggregation can be prevented by increasing their solubility [5-9]. Pcs, which have high thermal and chemical stability, and light stability, have extraordinary physicochemical properties [5-9]. Therefore, they have different advanced technological application areas. The main areas of use are electrochemical applications [10, 11], gas sensors [12, 13], pigments and dye industry [14, 15], photovoltaic materials [16, 17], liquid crystals [18, 19], organic field transistors [20-22], non-linear optical materials [23-25], light-emitting devices [26, 27], optical switching and limiting devices [28-30], solar cells [31, 32] and as a photosensitizer for photodynamic therapy (PDT) [33-41]. The type of metal in the metal-containing phthalocyanine (MPc) cavity, changes MPc's planar geometry, solubility, thermal and optical stability, as well as electrical and chemical properties [42-50]. 2 -Aminophenol is a reducing agent, a useful reagent for the synthesis of dyes and heterocyclic compounds [51]. In this research work, a new phthalocyanine complex was designed, which can be used in different technological application areas, is well soluble in different solvent types, contains monomeric species, has fluorescent properties, and contains heavy metal ions. For this purpose, 2 (3), 9 (10), 16 (17), 23 (24)-tetra-(2-aminophenoxy) phthalocyaninato indium(III) acetate [In(OAc)Pc] **1** was synthesized and its properties were determined by widely known spectroscopic techniques (Scheme 1 ).

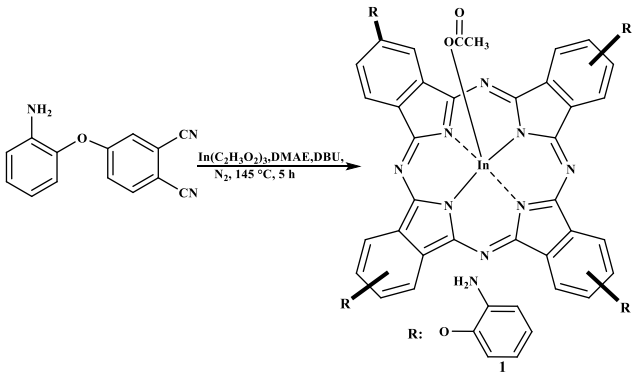


**Scheme 1.** *Synthesis of peripheral-tetra-2-aminophenoxy substituted indium(III) acetate phthalocyanine [In(OAc)Pc] 1*

## 2 Experimental section

### *2.1. Material and methods*

Indium(III) acetate metal salt and 4-(2-aminophenoxy)phthalonitrile compound were purchased from Sigma-Aldrich and ET Co.,Ltd., respectively. The solvents were purified, dried, and retained in molecular sieves, 4Å. All reactions were carried out under a dry nitrogen atmosphere. It was purified by successive washings with various solvents using a Soxhlet apparatus. The purity of the product was tested by thin layer chromatography after washing with each solvent and drying. FTIR and electronic spectra were recorded on a Shimadzu FTIR-8300 (ATR) and a Shimadzu UV–1601 spectrophotometer, respectively. Elemental analysis using LECO CHN 932 was carried out by TUBITAK Ankara Instrumental Analysis Laboratory. Fluorescent excitation and emission spectra were recorded on a Varian Eclipse spectrofluorometer using 1 cm path length cuvettes at 25 °C.

### *2.2. Synthesis of the In(OAc)Pc 1*

4-(2-aminophenoxy)phthalonitrile (0.15 g, 0.64 mmol), indium(III) acetate (0.09 g, 0.32 mmol) and and catalytic amount of 1,8-diazabicyclo[5.4.0]undec-7-ene (DBU) in 1.50 mL of 2-Dimethylaminoethanol (DMAE) was heated with stirring at 145 °C in a sealed glass tube for 5 hours under nitrogen atmosphere. The resulting suspensions were cooled to room temperature and then poured into 25 ml of ethanol. The precipitates were filtered and washed sequentially with water, ethyl acetate, hexane, acetone, dichloromethane (DCM), and diethyl ether and dried over phosphorus pentoxide in a vacuum desiccator. Mp>300° C. Yield: 54.56 mg (27.85%). Calculated for $C_{58}H_{39}InN_{12}O_6$. Elemental Analysis: C, 62.49; H, 3.53; N, 15.08%; found C, 64.65%; H, 3.18; N, 14.87%. FTIR (ATR) $\lambda_{max}$/cm$^{-1}$: 670-1058(C–H str.), 10165-1201(C–N str.), 1241-1371(C–O str.), 1469-1572 (C–H bend.), 1608 (C=N- str.),1722-1773(C=C str.), 3082(=C–H str.), 3200 (-$NH_2$ str.). UV–*vis* (DMSO, 1.00 ×10$^{-5}$ M): $\lambda_{max}$(nm), (log ε): 354 (4.83), 614 (4.43), 656 (4.50), 684 (5.08).

## 3 Results and discussion

### *3.1. Synthesis and characterization*

The In(OAc)Pc **1** was synthesized by cyclotetramerization reaction of 4-(2-amino phenoxy)phthalonitrile presence of DMAE as the solvent, DBU as the catalyzer and anhydrous indium(III) acetate under the nitrogen atmosphere (Scheme 1). It was isolated as dark green solids in 27.85% yield. It was washed sequentially with each of the solvents of water, ethyl acetate, hexane, acetone, DCM and diethyl ether. Its structure was illuminated by elemental analysis, FTIR, UV-*vis*, fluorescence spectroscopic techniques. The elemental compositions of C, H, and N obtained from its elemental analysis are in agreement with the proposed structure. The fact that the moderately sharp -C≡N stretching vibration band at 2233 cm$^{-1}$ belonging to 4-(2-aminophenoxy) phthalonitrile does not appear in the FTIR spectrum belonging to the In(OAc)Pc **1** confirms the proposed structure (Fig. 1). In its FTIR spectrum, respectively, at 3200 cm$^{-1}$ moderate NH stretching, at 3082 cm$^{-1}$ weak aromatic CH stretching, at 1722-1773 cm$^{-1}$ moderately sharp aromatic -C=C- stretching, at 1608 cm$^{-1}$ weak aromatic C=N- stretching, at 1469-1572 cm$^{-1}$ aromatic C–H bending, and at 1241-1371 cm$^{-1}$, moderate Ar–O-Ar stretching characteristic vibrational bands were observed, respectively (Fig. 1).

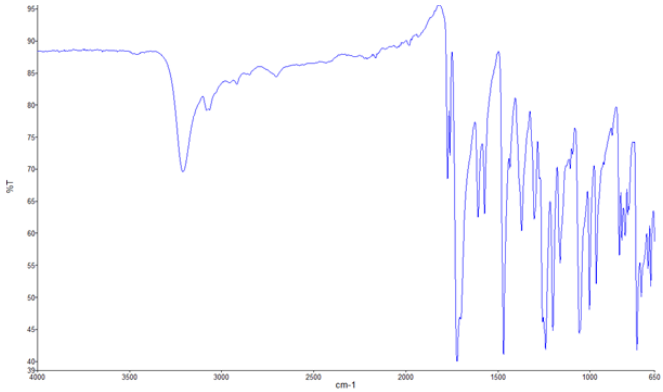


**Figure 1.** *FTIR spectrum of the In(OAc)Pc **1**.*

In its UV-*vis* absorption spectrum, a monomeric behavior was observed as evidenced by a single (narrow) Q band at 1.00 × 10$^{-5}$ M solution in DMSO. This is characteristic for metal-containing Pcs [47-50]. It demonstrated a single Q band due to the π-π* transition at 684 nm, with a high molar extinction coefficient of 5.08 L.mol$^{-1}$ cm$^{-1}$ (Fig. 2). It demonstrated another characteristic band, the Soret band (B band), at 354 nm due to n-π* electronic transitions (Fig. 2). It showed 3 nm blue-shifted Q band with respect to unsubstituted indium(III) acetate phthalocyanine [49, 50]. This is the type of substituent on the phthalocyanine skeleton, which is related to the presence of 2-aminophenoxy groups. The data and analyzes from these spectroscopic techniques for the In(OAc)Pc **1** are in agreement with the proposed structure.

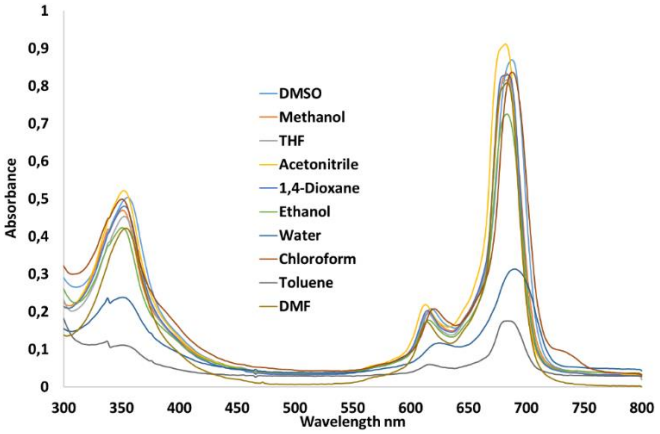


**Figure 2.** *UV-vis absorption spectra of the In(OAc)Pc **1** in different solvents. Concentration= ~1×10$^{-5}$ M.*

### *3.2. Aggregation studies*

Aggregation is known by the incorporation of monomers, dimers, and rings into higher-order complexes in different types of solvent. In this study, the aggregation behavior of the In(OAc)Pc **1** was investigated in different solvents It can dissolve well without aggregation in different kinds of solvents such as chloroform ($CHCl_3$), toluene and 1,4-dioxane as non-polar solvents and ethanol (EtOH and water as polar protic solvents, as well as tetrahydrofuran, N,N-dimethylformamide (DMF), dimethyl sulfoxide (DMSO) and acetonitrile as polar aprotic solvents (Fig. 2). In addition, its aggregation behavior was determined by investigating whether it obeys the Lambert-Beer law in DMSO at certain concentration ranges at room temperature. Ten solutions of its in DMSO with decreasing concentrations from 1.00 ×10$^{-6}$ M to 1.00×10$^{-6}$ M were prepared separately. The UV-*vis* spectra in Figure 3 show its aggregation behavior in DMSO. A linear regression analysis was performed between the intensity of its Q-band and its concentration. It has been determined that it obeys the Lambert-Beer law and contains monomeric species. It was also observed that the absorbance of the Q-band also increased due to the increase in its concentration and there were no new (normally blue or red shifted) bands. These obtained results confirm that it does not tend to aggregate and does not include aggregated species.

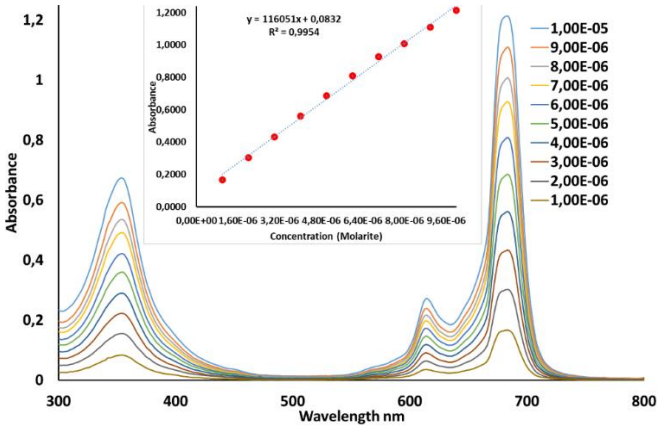


**Figure 3.** *Aggregation behavior of the In(OAc)Pc **1** in DMSO at different concentrations. (Inset: plot of absorbance vs. concentration).*

### *3.3. Fluorescence spectra*

Figure 4 displays fluorescence excitation and emission spectra of the In(OAc)Pc **1** in DMSO. Its bands with maximum intensity in the fluorescence spectrum were monitored at 690 nm for excitation and 702 nm for emission, respectively. It has a Stokes shift of 18 nm and is longer than that of unsubstituted In(OAc)Pc [27]. Its fluorescent emission in DMSO is low intensity and characteristic due to the heavy atom effect of indium metal [44-50].

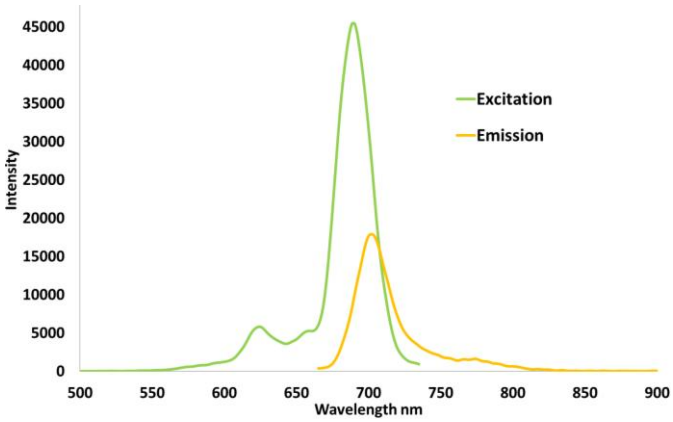


**Figure 4.** *Excitation, and emission spectra of the In(OAc)Pc **1** in DMSO. Excitation wavelength= 655 nm.*

## 4 Conclusions

In this research study, a novel phthalocyanine, containing heavy metal ion, which is 2(3),9(10),16(17),23(24)-tetra-(2-aminophenoxy)phthalocyaninato indium(III) acetate was synthesized. Its structure was illuminated and confirmed using elemental analysis, FTIR, UV-*vis*, and fluorescence spectroscopic techniques. It dissolves well in polar protic, polar aprotic and non-polar solvents, contains mainly monomeric species, and can absorb at long wavelengths with its high molar extinction coefficient. It showed low fluorescence emission due to the presence of indium metal ion as heavy metal in its cavity and with large atomic radius. It

can be used in various technological applications because it dissolves very well in different solvent types, has monomeric species and sufficient fluorescent properties, and can be useful for systems involving changes in forms similar to the studied complex.

## References


[1]. McKeown N.B., "Phthalocyanine Materials; Synthesis, Structure and Function" Cambridge University Press, (1998), Cambridge, 197.

[2]. Pişkin M., Odabaş Z., "Synthesis, Characterization and Spectroscopic Properties of Novel Mono-Lutetium(III) Phthalocyanines", Karaelmas Science and Engineering Journal, 6(2), (2016), 307-314.

[3]. Pişkin M., Özturk Ö.F., Odabaş Z., "Synthesis, spectroscopy, and photophysical properties of newly magnesium (II) phthalocyanine", Manas Journal of Engineering, 9 (1), (2021), 58-64.

[4]. Pişkin M., Özturk Ö.F., Odabaş Z., "Newly Soluble and Non-Aggregated Copper(II) and Tin(II) Phthalocyanines: Synthesis, Characterization and Investigation of Photophysical and Photochemical-Responsive", Karaelmas Science and Engineering Journal, 7(2), (2017), 627-637.

[5]. Demirbaş Ü., Pişkin M., Barut B., Bayrak R., Durmuş M., Kantekin H., "Metal-free, zinc(II) and lead(II) phthalocyanines functioning with 3-(2H-benzo[d][1,2,3] triazol-2-yl)-4-hydroxyphenethyl methacrylate groups: Synthesis and investigation of photophysical and photochemical properties", Synthetic Metals, 220, (2016), 276–285.

[6]. Çetinkaya M., Pişkin M., Altun, S., Odabaş Z., Durmuş M., "Do the positions of trimethyl groups on phthalocyanine photosensitizers improve their photochemical and photophysical properties?", Journal of Photochemistry and Photobiology A: Chemistry, 335, (2017), 17–25.

[7]. Demirbaş Ü., Pişkin M., Bayrak R., Durmuş M., Kantekin H., "Zinc(II) and lead(II) phthalocyanines bearing thiadiazole substituents: Synthesis, characterization, photophysical and photochemical properties", Journal of Molecular Structure, 1197, (2019), 594-602.

[8]. Makhseed S., Al-Sawah M., Samuel J., Mana H., "Synthesis, characterization and nonlinear optical properties of nonaggregating hexadeca-substituted phthalocyanines", Tetrahedron Lett., 50, (2009), 165.

[9]. Mutlu F., Pişkin M., Canpolat E., Öztürk Ö.F., "The new zinc(II) phthalocyanine directly conjugated with 4-butylmorpholine units: Synthesis, characterization, thermal, spectroscopic and photophysical properties", Journal of Molecular Structure, 1201, (2020), 127169.

[10]. Pişkin M., Öztürk N., Durmuş M., "Spectroscopic and electrochemical behavior of the novel tetra-2-methyl-pyrazinoporphyrazines", Journal of Molecular Structure, 1149 (2017) 893-899.

[11]. Orman E.B., Pişkin M., Odabaş Z., Özkaya A.R., "Electrochemical, Spectroelectrochemical, and Electrocatalytic Dioxygen Reducing Properties of Peripheral Tetra-2,6-dimethoxyphenoxy Substituted Phthalocyanines", Electroanalysis 33, (2021), 2310–2322.

[12]. Pişkin M., Can Nursel, Odabaş Z., Altındal A., "Toluene vapor sensing characteristics of novel copper(II),indium(III), mono-lutetium(III) and tin(IV) phthalocyanines substituted with 2,6-dimethoxyphenoxy bioactive moieties, Journal of Porphyrins and Phthalocyanines, 22, (2018), 1–9.

[13]. Yazıcı A., Dalbul N., Altındal A., Salih B., Bekaroğlu Ö., "Ethanol sensing property of novel phthalocyanines substituted with 3,4-dihydroxy-3-cyclobuten-1,2-dione", Sensors and Actuators B., 202, (2014), 14–22.

[14]. Mert S.A., Ilgün C., Gül A., "Preparation of heterogeneous phthalocyanine catalysts by cotton fabric dyeing", Dyes and Pigments, 89, (2011), 162–168.

[15]. Akçay H.T., Pişkin M., Demirbaş Ü., Bayrak R., Durmuş M., Menteşe E., Kantekin H., "Novel triazole bearing zinc(II) and magnesium(II) metallo-phthalocyanines: Synthesis, characterization, photophysical and photochemical properties", Journal of Organometallic Chemistry, 745 (746), (2013), 379-386.

[16]. Soylu M., Ocaya R., Tuncer H., Al-Ghamdi A.A., Dere A., Sari D.C., Yakuphanoglu F., "Analysis of photovoltaic behavior of Si-based junctions containing novel graphene oxide/nickel (II) phthalocyanine

composite films", Microelectronic Engineering, 154, (2016), 53–61.

[17]. Kantekin H., Yalazan H., Kahriman N., Ertem B., Serdaroğlu V., Pişkin M., Durmuş M.,"New peripherally and non-peripherally tetra-substituted metal-free, magnesium(II) and zinc(II) phthalocyanine derivatives fused chalcone units: Design, synthesis, spectroscopic characterization, photochemistry and photophysics", Journal of Photochemistry and Photobiology A: Chemistry, 361, (2018), 1-11.

[18]. Iino H., Hanna J., Bushby R.J., Movaghar B., Whitaker B.J., Cook M.J., "Very high time-of-flight mobility in the columnar phases of a discotic liquid crystal", Applied Physics Letters, 87, (2005), 132102.

[19]. Bayrak R., Akçay H.T., Pişkin M., Demirbaş Ü., Durmuş M., Değirmencioğlu İ., "Azine-bridged binuclear metallophthalocyanines functioning photophysical and photochemical-responsive", Dyes and Pigments 95, (2012), 330-337.

[20]. Dong S., Tian H., Huang L., Zhang J., Yan D., Geng Y., Wang F., "Non-Peripheral Tetrahexyl-Substituted Vanadyl Phthalocyanines with Intermolecular Cofacial π–π Stacking for Solution-Processed Organic Field-Effect Transistors", Advanced Materials, 23, (2011), 2850–2854.

[21]. Lu G., Kong X., Sun J., Zhang L., Chen Y., Jiang J., "Solution-processed single crystal microsheets of a novel dimeric phthalocyanine-involved triple-decker for high-performance ambipolar organic field effect transistors", Chemical Communications, 53, (2017), 12754–12757.

[22]. Demirbaş Ü., Bayrak R., Pişkin M., Akçay H.T., Durmuş M., Kantekin H., "Synthesis, photophysical and photochemical properties of novel tetra substituted metal free and metallophthalocyanines bearing triazine units" Journal of Organometallic Chemistry, 724, (2013), 225-234.

[23]. Ramya E., Momen N., Rao D.N., "Preparation of multiwall carbon nanotubes with zinc phthalocyanine hybrid materials and their nonlinear optical (NLO) properties", Journal of Nanoscience and Nanotechnology, 18 (7), (2018), 4764–4770.

[24]. Ghanem B.S., Pişkin M., Durmuş M., El-Khouly M.E., Al-Raqa S.Y., "Synthesis, photophysical and photochemical properties of novel phthalocyanines substituted with triptycene moieties", Polyhedron, 90, (2015), 85–90.

[25]. Al-Sohaimi B.R., Pişkin M., Ghanem B.S., Al-Raqa S.Y., Durmuş M., "Efficient singlet oxygen generation by triptycene substituted A3B type zinc(II) phthalocyanine photosensitizers" ,Tetrahedron Letters, 57, (2016) , 300–304.

[26]. Zheng L., Xu J., Feng Y., Shan H., Fang G., Xu Z.X., "Green solvent processed tetramethyl-substituted aluminum phthalocyanine thin films as anode buffer layers in organic light-emitting diodes", Journal of Materials Chemistry C, 6, (2018), 11471–11478.

[27]. Al-Sohaimi B.R., Pişkin M., Aljuhani A., Al-Raqa S.Y., Durmuş M.,"Enhancing photophysical and photochemical properties of zinc(II) Phthalocyanine dyes by substitution of triptycene moieties", Journal of Luminescence,173, (2016), 82–88.

[28]. Kumar A., Punia R., Gupta A.K., Mohan D., Kapoor K., "Study of all-optical switching properties of zinc phthalocyanine thin film by pump-probe technique", Optics & Laser Technology, 95, (2017), 100–104.

[29]. Pişkin M., "Synthesis, characterization, thermal and photophysical properties of novel strontium (II) phthalocyanine", Journal of Inclusion Phenomena and Macrocyclic Chemistry, 102, (2022), 35–44.

[30]. Pişkin M., Öztürk Ö.F., Odabaş Z., "Determination of photophysical, photochemical and spectroscopic properties of novel lead(II) phthalocyanines", Polyhedron, 182, (2020), 114480.

[31]. Sfyri G., Vamshikrishn N., Kumar C.V., Giribabu L., Lianos P.," Synthesis and characterization of tetratriphenylamine Zn phthalocyanine as hole transporting material for perovskite solar cells", Solar Energy, 140, (2016), 60–65.

[32]. Nas A., Demirbaş Ü., Pişkin M., Durmuş M., Kantekin H., "The photophysical and photochemical properties of new unmetallated and metalated phthalocyanines bearing four 5-chloroquinolin-8-yloxy substituents on peripheral sites", Journal of Luminescence, 145, (2014), 635–642.

[33]. Jia Y., Li J., Chen J., Hu P., Jiang L., Chen X., Huang M., Chen Z., Xu P., "Smart photosensitizer: tumor-triggered oncotherapy by self-assembly photodynamic nanodots", ACS Applied Materials & Interfaces, 10, (2018), 15369–15380.

[34]. Pişkin M., Durmuş M., Bulut M., "Highly soluble 7-oxy-3-(4-methoxyphenyl) coumarin bearing zinc phthalocyanines: Synthesis and investigation of photophysical and photochemical properties", Journal of Photochemistry and Photobiology A: Chemistry, 223, (2011), 37– 49.

[35]. Pişkin M., Durmuş M., Bulut M., "Synthesis and investigation on photophysical and photochemical properties of 7-oxy-3-methyl-4-phenylcoumarin bearing zinc phthalocyanines", Spectrochimica Acta Part A: Molecular and Biomolecular Spectroscopy, 97, (2012), 502–511.

[36]. Çakır V. Çakır D., Pişkin M., Durmuş M., Bıyıklıoğlu Z., "Water soluble peripheral and non-peripheral tetra substituted zinc phthalocyanines: Synthesis, photochemistry and bovine serum albumin binding behavior", Journal of Luminescence, 154, (2014), 274–284.

[37]. Çakır V. Çakır D., Pişkin M., Durmuş M., Bıyıklıoğlu Z., "New peripherally and non-peripherally tetra-substituted water-soluble zinc phthalocyanines: Synthesis, photophysics and photochemistry", Journal of Organometallic Chemistry, 783, (2015), 120-129.

[38]. Aktaş A., Pişkin M., Durmuş M., Bıyıklıoğlu Z., "Synthesis, photophysical and photochemical properties of zinc phthalocyanines bearing fluoro-functionalized substituents", Journal of Luminescence, 145, (2014), 899–906.

[39]. Şahal H., Pişkin, M., Organ G.A., Öztürk Ö.F., Kaya M., Canpolat E., "Zinc(II) phthalocyanine containing Schiff base containing sulfonamide: synthesis, characterization, photophysical, and photochemical properties", Journal of Coordination Chemistry, 71 (22), (2018), 3763–3775.

[40]. Pişkin, M., Canpolat E., Öztürk Ö.F., "The new zinc phthalocyanine having high singlet oxygen quantum yield substituted with new benzenesulfonamide derivative groups containing schiff base", Journal of Molecular Structure, 1202, (2020), 127181.

[41]. Demirbaş Ü., Pişkin M., Bayrak R., Ünlüer D., Düğdü E., Durmuş M., Kantekin H., "The determination of photophysical and photochemical parameters of novel metal-free, zinc(II) and lead(II) phthalocyanines bearing 1,2,4-triazole groups", Synthetic Metals, 219, (2016), 76–82.

[42]. Gargiani P., Rossi G., Biagi R., Corradini V., Pedio M., Fortuna S., Calzolari A., Fabris S., Cezar J.C., Brookes N.B., Betti M.G., "Spin and orbital configuration of metal phthalocyanine chains assembled on the Au(110) surface", Physical Review B Covering Condensed Matter and Materials Physics, 87, (2013), 165407.

[43]. Demirbaş Ü., Pişkin M., Akçay H.T., Barut B., Durmuş M., Kantekin H., "Synthesis, characterisation, photophysical and photochemical properties of free-base tetra-(5-chloro-2-(2,4-dichlorophenoxy)phenoxy)phthalocyanine and respective zinc(II) and lead(II) complexes", Synthetic Metals, 223, (2017), 166–171.

[44]. Pişkin M., "The novel 2,6-dimethoxyphenoxy substituted phthalocyanine dyes having high singlet oxygen quantum yields", Polyhedron, 104, (2016), 17-24.

[45]. Gürel E, Pişkin M., Altun S., Odabaş Z., Durmuş M., "Synthesis, characterization and investigation of the photophysical and photochemical properties of highly soluble novel metal-free, zinc(II), and indium(III) phthalocyanines substituted with 2,3,6-trimethylphenoxy moieties", Dalton Transactions, 44, (2015), 6202–6211.

[46]. Gürel E, Pişkin M., Altun S., Odabaş Z., Durmuş M., "The novel mesityloxy substituted metallo-phthalocyanine dyes with long fluorescence lifetimes and high singlet oxygen quantum yields", Journal of Photochemistry and Photobiology A: Chemistry, 315, (2016), 42–51.

[47]. Çapkın A., Pişkin M., Durmuş M., Bulut M., "Spectroscopic, photophysical and photochemical properties of newly metallo-phthalocyanines containing coumarin derivative", Journal of Molecular Structure 1213 (2020) 128145.

[48]. Pişkin M., Durmuş M., Bulut M., "Synthesis, characterization, photophysical and photochemical properties of 7-oxy-3-methyl-4-phenylcoumarin-substituted indium phthalocyanines", Inorganica Chimica Acta, 373, (2011), 107–116.

[49]. Pişkin M., Altun S., Durmuş M., Odabaş Z., "First investigation on the photophysical and photochemical properties of azo-bridged phthalocyanine photosensitizers", Journal of Luminescence,180, (2016), 219–223.

[50]. Alamin Ali H.E., Pişkin M., Altun S., Durmuş M., Odabaş Z., "Synthesis, characterization, photophysical, and photochemical properties of novel zinc(II) and indium(III) phthalocyanines containing 2-phenylphenoxy units", Journal of Luminescence,173, (2016), 113–119.

[51]. Watson D.C., Hill A.E., "Aminophenols". In Ullmann's Encyclopedia of Industrial Chemistry (2017), Wiley-VCH Verlag, 3, 59-77.

MANAS Journal of Engineering
ISSN 1694-7398 | e-ISSN 1694-7398

*Volume 10, Issue 1, (2022) Pages 88-94*
*https://doi.org/10.51354/mjen. 1083983*

# A core-shell magnetic layered double hydroxide composite material for the effective decolorization of phenol red

Şakir Yılmaz[1,2*]

[1] Van Yuzuncu Yil University, Faculty of Engineering, Department of Mining Engineering, 65080 Van Turkey
[2] Van Yuzuncu Yil University, Institute of Natural and Applied Sciences, Department of Chemical Engineering, 65080 Van Turkey, sakiryilmaz@yyu.edu.tr, ORCID: 0000-0001-9797-0959

**ABSTRACT**

The magnetic composite based on layered double hydroxide ($Fe_3O_4$/NiMn-LDH) was prepared by co-precipitation procedure and considered as a material to eliminate phenol red (PR) from aqueous environments. The characterization of $Fe_3O_4$/NiMn-LDH were recognized by Fourier transform infrared (FTIR) spectroscopy and scanning electron microscopy (SEM). Box-Behnken design (BBD) under response surface methodology (RSM) were applied to evaluate the effects of the process variables such as pH, adsorbent dosage, and initial PR concentration ($C_o$). The results indicated that a good correlation between the estimated and experimental values was found for the PR decolorization efficiency from aqueous media using $Fe_3O_4$/NiMn-LDH ($R^2$ = 0.99). Furthermore, the statistical model obtained from BBD was sufficient to estimate the PR decolorization on $Fe_3O_4$/NiMn-LDH ($p < 0.0001$). The optimal conditions for the PR decolorization efficiency were determined as 5.38, 24.59 mg, and 25.39 mg/L for pH, adsorbent dosage, and $C_o$, respectively which resulted in 86.93% the PR decolorization efficiency. Finally, this work demonstrated that BBD could easefully be utilized for the optimization of the PR decolorization using $Fe_3O_4$/NiMn-LDH.

**ARTICLE INFO**

***Research article***

*Received: 7.03.2022*
*Accepted: 2.05.2022*

***Keywords:***
*Decolorization, layered double hydroxide, magnetic, optimization, phenol red*

**corresponding author*

## 1 Introduction

The contamination of aquatic resources by industrial technologies is an issue of significant worry owing to rapid industrial development [1]. Dyestuffs, an industrial pollutant, are well known to affect the environmental ecosystem based on their serious health hazards and toxicity [2]. These wastes, which have wide applications in the rubber, textile, plastic, paper, food, cosmetics, pharmaceutical industries, are discharged into aqueous environments and cause great hazards for the environment [3]. Most of dyes in water bodies disrupts the esthetic nature and interferes from sunlight transmission, thus affecting the food web necessary for life. Moreover, these products lead to various disorders like lung, skin, and respiratory problems [1, 3]. Organic contaminants include various class of dyes and phenol derivatives. Among them, phenol red (PR) is one of the most harmful contaminant causing severe problems such as reducing light penetration, visibility in the water bodies, adjourning the growth of microorganisms, and increasing the chemical oxygen demand (COD) [4]. Consequently, it is significant to remove these colorants from water bodies.

The conventional technologies such as photocatalysis, chemical oxidation, coagulation, membrane filtration, photo degradation, and adsorption are applied to color removal from industrial effluents [4, 5]. Adsorption is one of the most efficient and reliable procedure for the decolorization of colorants [6, 7]. This treatment method has many advantages including high selectivity, easy handling, regeneration of adsorbent, and low cost effectiveness [6]. Adsorbent plays a significant role in separation and purification method in terms of capacity and selectivity [8]. Different materials have been utilized for the removal of organics from the water samples, however, layered double hydroxides (LDH), known anionic clays, have been promising adsorbent for wastewater treatment due to their interlayer ion exchange, high surface area, and layered structure, and thus the research focus of scientific application [9, 10]. Moreover, the materials utilized in adsorption applications are commonly powders and it is quite difficult to separate the solid from the solution. To overcome such limitations, magnetic separation technology has aroused great interest. Consequently, imparting magnetic properties to the material has attracted a lot of attention to the easy and efficient separation of materials from aquatic media after adsorption [11]. Therefore, it is of great significance to prepare the LDHs with a magnetic property for the removal of organic pollutants from aqueous environments.

Response surface methodology (RSM) is one of mathematical and statistical techniques and usually utilized to optimize of a process, minimize the error of tests, and decrease the number of tests [12]. When assessing the role of variables affecting the adsorption process, the RSM can be considered as a suitable statistical technique for improving, developing, and optimizing processes [9].

The aim of this research is to the synthesis of the magnetic LDH composite based on nickel (Ni) and manganese (Mn) ($Fe_3O_4$/NiMn-LDH) and its decolorization ability for PR. The influences of variables on decolorization of PR were studied and optimized by a Box-Behnken design (BBD) combined with RSM. The adsorption mechanism of PR decolorization on the prepared adsorbent was also investigated.

## 2 Materials and methods

### *2.1. Synthesis of magnetic composite*

$Fe_3O_4$ nanoparticles were synthesized by co-precipitation method in the presence of ammonia solution. Firstly, 2.2 g of ferric chloride hexahydrate ($FeCl_3 \cdot 6H_2O$) and 0.81 g of ferrous chloride tetrahydrate ($FeCl_2 \cdot 4H_2O$) were dissolved in 100 mL of deionized water. Afterwards, the mixture was stirred by adding 7 mL ammonium hydroxide ($NH_4OH$) for 30 min at ambient temperature. After the reaction process, black precipitate was separated by a magnet and washed several times with deionized water and ethanol, and then dried at 90 °C for 24 h. Magnetic composite material with a $Ni^{2+}/Mn^{3+}$ molar ratio of 2:1 was prepared by co-precipitation procedure. 0.5 g of $Fe_3O_4$ was dispersed in 100 mL of 1:1 methanol/water solution. Then, 2.91 g of nickel nitrate hexahydrate ($Ni(NO_3)_2 \cdot 6H_2O$) and 1.26 g of manganese nitrate tetrahydrate ($Mn(NO_3)_2 \cdot 4H_2O$) were dissolved in 100 mL of deionized water by addition of an alkaline solution (0.03 M sodium carbonate ($Na_2CO_3$) and 0.12 M sodium hydroxide (NaOH)). The obtained product was collected by a magnet and washed with deionized water and ethanol several times. Finally, $Fe_3O_4$/NiMn-LDH dried at 60 °C overnight (Scheme 1).

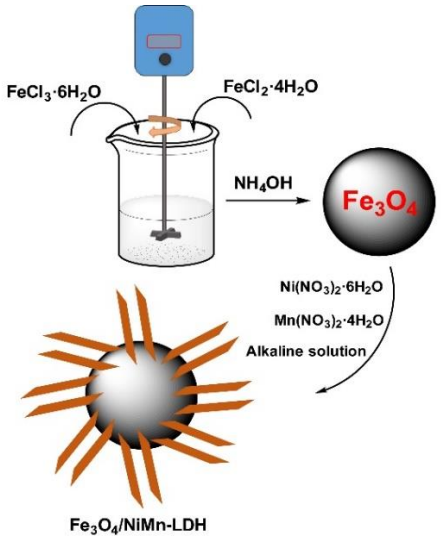


**Scheme 1.** *Synthesis of $Fe_3O_4$/NiMn-LDH by co-precipitation method.*

### *2.2. PR adsorption studies*

A stock solution of PR was prepared by dissolving required amount of PR in deionized water and the desired dilutions were prepared using deionized water. PR adsorption tests were performed under different pH of solution (2-8), adsorbent amount (5-30 mg), and initial PR concentration ($C_o$) (5-45 mg/L) at ambient temperature. The contact time was a fixed at 120 min. All experiments were conducted in a 20 ml flask with 10 ml of PR solution. The mixture was shaken in orbital shaker and samples were collected by a magnet after 120 min. Then, the supernatant was centrifuged at 7000 rpm for 10 min. The remaining PR concentration was measured by a UV–vis spectrophotometer (Genesys 10S, Thermo Scientific, USA) at 559 nm after centrifugation (Figure 1). The decolorization efficiency of PR (%) was calculated according to following equation.

$$\textit{The decolorization efficiency} = \frac{C_o - C_e}{C_o} \times 100 \qquad (1)$$

where, $C_o$ and $C_e$ (mg/L) are PR concentration at initial and at equilibrium, respectively.

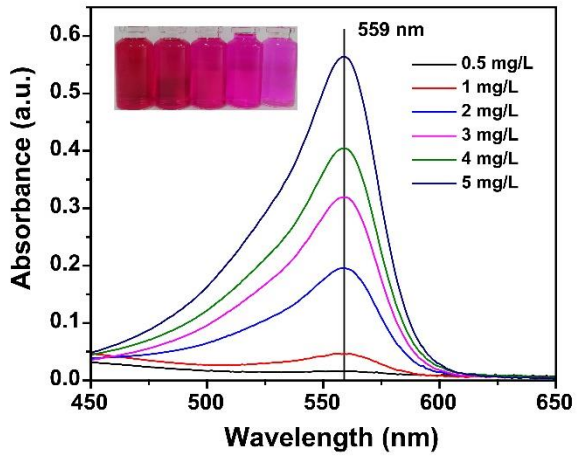


**Figure 1.** *UV-vis absorption spectra of PR.*

*2.3. Design methodology*

Among design of experiment models, Box-Behnken design (BBD) is the most mainly utilized in adsorption technologies [13]. BBD was applied to examine the effects of three independent variables pH of solution (A), adsorbent amount (B, mg), and $C_o$ (C, mg/L) on the PR decolorization efficiency onto $Fe_3O_4$/NiMn-LDH. A three-factor and level (*–1*, *0*, *1*) design consisting of *17* tests were designed to optimize PR decolorization efficiency. The following equation represented the quadratic polynomial model.

$$\hat{y}_n = \beta_o + \sum_{i=1}^{3} \beta_i x_i + \sum_{i=1}^{3} \beta_{ii} x_i^2 + \sum_{i=1}^{3} \sum_{j=i+1}^{3} \beta_{ij} x_i x_j \qquad (2)$$

where $\hat{y}_n$ represents PR decolorization efficiency; $\beta_0$ (intercept), $\beta_i$ (linear), $\beta_{ii}$ (quadratic), and $\beta_{ij}$ (interaction) are regression coefficients; $x_i$ and $x_j$ are the independent variables.

## 3. Results and discussion

*3.1. Characterization results*

Fourier transform infrared spectroscopy (FTIR) (Nicolet S10, Thermo Scientific, USA) was utilized to investigate changes in the functional groups of $Fe_3O_4$/NiMn-LDH with 500–4000 $cm^{-1}$ scanning spectra. Figure 2 shows the FTIR spectrum of $Fe_3O_4$/NiMn-LDH. The broad and strong band at 3300 $cm^{-1}$-3600 $cm^{-1}$ is originate from O–H stretching of hydroxyl group of $Fe_3O_4$/NiMn-LDH [14]. The bands at around 1635 $cm^{-1}$ and 1350 $cm^{-1}$ are due to the carbonate ($CO_3^{2-}$) and nitrate group ($NO_3^-$), respectively. The peaks at 500-700 $cm^{-1}$ are assigned to the stretching vibration of Ni-O and Mn-O bonds in the material [15]. Moreover, the band at around 890 $cm^{-1}$ is corresponded to $Fe_3O_4$ of the material [14].

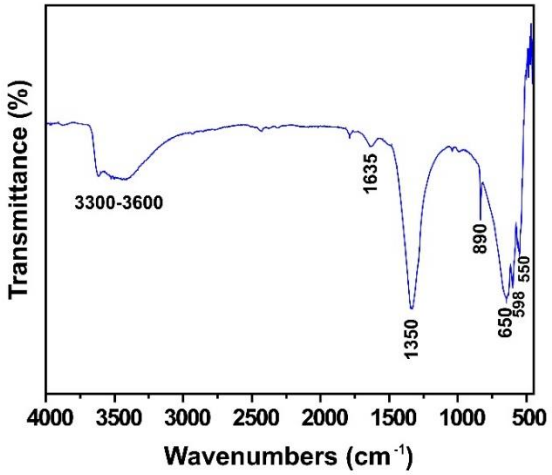


**Figure 2.** *FTIR spectrum of $Fe_3O_4$/NiMn-LDH.*

The surface morphology of $Fe_3O_4$/NiMn-LDH was analyzed using scanning electron microscopy (SEM) with a Zeiss GeminiSEM model (Germany). SEM image and elemental mapping of $Fe_3O_4$/NiMn-LDH is shown in Figure 3. The results indicate the layered surface and spherical structure of $Fe_3O_4$/NiMn-LDH [16]. Moreover, from the mapping analysis of the material, O, Ni, Mn, and Fe exist on the surface of $Fe_3O_4$/NiMn-LDH, confirming that the prepared material was successfully synthesized by co-precipitation method.

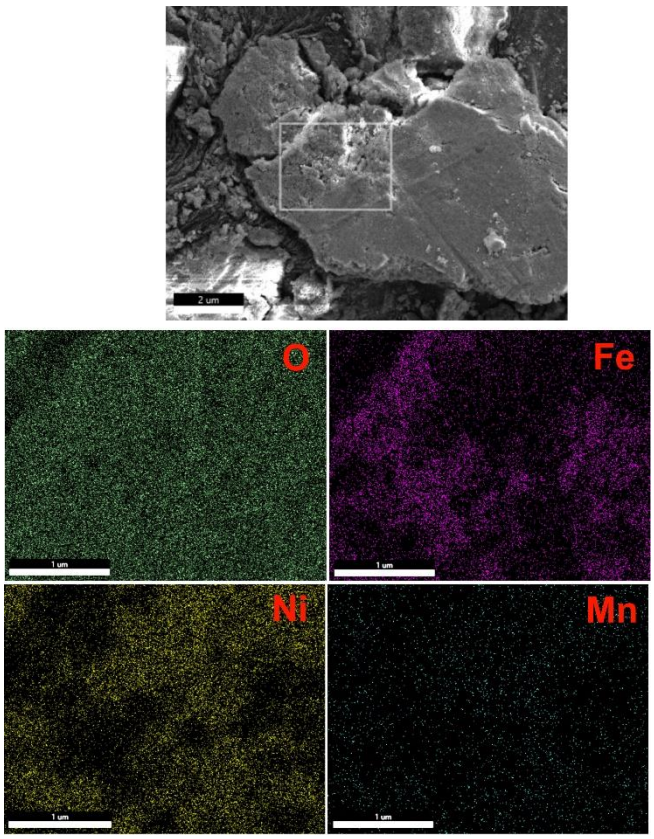


**Figure 3.** *SEM image and mapping results of $Fe_3O_4$/NiMn-LDH.*

*3.2. Process model and statistical analysis*

The BBD step executed for prediction of three independent variables including pH of solution (A), adsorbent dosage (B), and $C_o$ (C) at three levels were performed and their responses are given in Table 1. Totally *17* tests were designed to optimize the process variables on the PR decolorization efficiency. The quadratic model equation in terms of un-coded factors for the PR decolorization efficiency is displayed in the following equation.

$$\begin{aligned}&\textit{The PR decolorization efficiency} = \\ &-20.58133+19.25574[\text{pH}] +5.13985[\text{Ads. amount}] +1.01554[C_o] \\ &-0.029133[\text{pH}][\text{Ads. amount}] +1.87500E\text{-}003[\text{pH}][C_o] -0.018490[\text{Ads. amount}][C_o] - \\ &2.26086[\text{pH}]^2 \\ &-0.095570[\text{Ads. amount}]^2 -0.015394[C_o]^2\end{aligned} \quad (4)$$

**Table 1.** *The examined levels and ranges of variables and the responses based on BBD.*

| Variables | Levels | | |
|---|---|---|---|
| | *-1* | *0* | *+1* |
| pH (A) | 2 | 5 | 8 |
| Ads. amount (mg, B) | 5 | 17.5 | 30 |
| $C_o$ (mg/L, C) | 5 | 25 | 45 |

| Run | A | B | C | Response (%) |
|---|---|---|---|---|
| 1 | 2 | 5 | 25 | 44.23 |
| 2 | 8 | 5 | 25 | 25.71 |
| 3 | 8 | 17.5 | 45 | 46.26 |
| 4 | 5 | 17.5 | 25 | 85.39 |
| 5 | 5 | 5 | 5 | 47.51 |
| 6 | 5 | 5 | 45 | 51.33 |
| 7 | 5 | 30 | 45 | 71.50 |
| 8 | 5 | 17.5 | 25 | 84.91 |
| 9 | 2 | 17.5 | 5 | 71.39 |
| 10 | 8 | 17.5 | 5 | 46.08 |
| 11 | 5 | 30 | 5 | 86.17 |
| 12 | 2 | 30 | 25 | 76.35 |
| 13 | 5 | 17.5 | 25 | 85.67 |
| 14 | 5 | 17.5 | 25 | 85.27 |
| 15 | 5 | 17.5 | 25 | 84.85 |
| 16 | 2 | 17.5 | 45 | 71.12 |
| 17 | 8 | 30 | 25 | 53.46 |

Analysis of variance (ANOVA) was utilized to determine the significance of each variable (Table 2). Masoudian et al. [17] indicated that a p value lower than 0.05 was statistically important for each term. ANOVA results showed that the proposed model is significant with *p*-value of 0.0001, confirming that the statistical model best fit for $Fe_3O_4$/NiMn-LDH material to estimate the PR decolorization efficiency. Moreover, the regression coefficient value ($R^2$) of the model was 0.99, indicating that the model fits well.

**Table 2.** *ANOVA results.*

| Source | Sum of squares | df | Mean square | F value | p-value |
|---|---|---|---|---|---|
| Model | 6018.60 | 9 | 668.73 | 189.78 | < 0.0001 |
| A | 1048.36 | 1 | 1048.36 | 297.51 | < 0.0001 |
| B | 1761.21 | 1 | 1761.21 | 499.81 | < 0.0001 |
| C | 14.96 | 1 | 14.96 | 4.25 | 0.0783 |
| AB | 4.77 | 1 | 4.77 | 1.35 | 0.2826 |
| AC | 0.051 | 1 | 0.051 | 0.014 | 0.9080 |
| BC | 85.47 | 1 | 85.47 | 24.26 | 0.0017 |
| $A^2$ | 1743.29 | 1 | 1743.29 | 494.72 | < 0.0001 |
| $B^2$ | 938.89 | 1 | 938.89 | 266.44 | < 0.0001 |
| $C^2$ | 159.65 | 1 | 159.65 | 45.31 | 0.0003 |
| $R^2$ = 0.99 | | | | | |

The plot of the predicted responses versus experimental ones was shown in Figure 4a. It is seen that the estimated points are scatter close to experimental data. This confirm excellent compatibility between the estimated and experimental results by RSM modelling for the PR decolorization efficiency. On the other hand, the normal % probability plot of the residuals is given in Figure 4b. As observed in Figure 4b, the residuals are normally distributed, validating the adequacy and reliability of the proposed model.

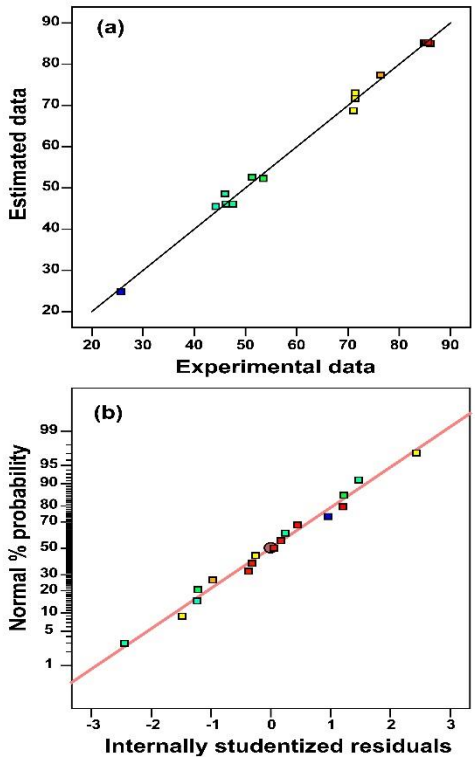


**Figure 4.** *(a) The estimated vs experimental values and (b) normal plot of residuals.*

The pH effect of PR onto $Fe_3O_4$/NiMn-LDH was investigated in the range of 2–8 (Figure 5a). It was found that the PR decolorization efficiency was increased as pH value of

solution increased from 2 to about 5. By changing pH value of solution from 5 to 8, the decolorization percentage of PR were significantly decreased. The increase in the decolorization percentage of PR at lower pH values is attributed to interaction between formation of negatively charged PR and the positively surface property of the material [2]. In basic conditions, $Fe_3O_4$/NiMn-LDH becomes more negative, resulting the decolorization percentage of PR progressively decreased owing to the electrostatic repulsion between negatively charged PR molecule and negative material surface [4]. The effect of adsorbent dosage on the PR decolorization efficiency was studied with varying adsorbent amount 5 to 30 mg (Figure 5a,b). The PR decolorization efficiency by $Fe_3O_4$/NiMn-LDH increased significantly as increases in the adsorbent dosage from 5 to about 20-25 mg and the maximum PR decolorization efficiency was achieved at 25 mg adsorbent dosage. This can be due to the available adsorption sites with increase in the adsorbent amount leading increase in removal efficiency [1]. The influence of $C_o$ was determined by changing $C_o$ from 5 to 45 mg/L (Figure 5b). The PR decolorization efficiency increased with increases in $C_o$ of PR. Then, the PR decolorization efficiency at high dye concentrations decreased. This may due to abundant adsorption sites at first resulting increased the removal of PR. However, at further concentrations of the dye molecules, the PR decolorization efficiency reduced based on the saturation of adsorbent sites [3].

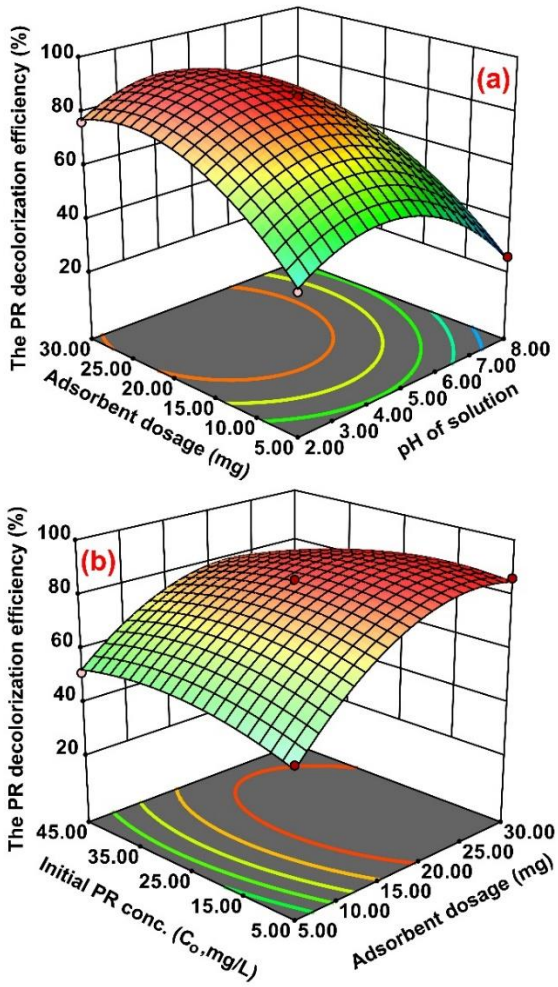


**Figure 5.** *3D plot for (a) pH of solution-adsorbent dosage and (b) adsorbent dosage-$C_o$.*

### *3.3. Optimization step*

Numerical optimization is a technique that is used to show the areas in which the maximum response values are obtained. The optimal point is determined based on the parameters, which is considered as the criterion for the maximum PR decolorization efficiency. Solving numerical analysis for an 86.93% PR decolorization efficiency predicted it occurrence at pH = 5.38, adsorbent dosage = 24.59 mg, and $C_o$ = 25.39 mg/L.

### *3.4. The decolorization mechanism of PR*

The decolorization mechanism are generally helpful for estimation of information about mechanism and nature of adsorption process. The decolorization mechanisms of PR molecules by $Fe_3O_4$/NiMn-LDH involved electrostatic interaction, ion exchange, hydrogen bonding and coordination with metal. Figure 6 displays a schematic representation of the decolorization mechanisms of PR onto $Fe_3O_4$/NiMn-LDH. The electrical charge of the material is positive under the

acidic conditions. The electrostatic interaction can be formed between the sulfonic group of PR molecule and the hydroxyl group in $Fe_3O_4$/NiMn-LDH [18]. $SO_3^-$ anion of dye might be replaced by $CO_3^{2-}$ anion, interlayer molecule of $Fe_3O_4$/NiMn-LDH via anion exchange [19]. H-bonding interaction can occur between the phenolic hydroxyl groups of PR molecule and the surface hydroxyls of $Fe_3O_4$/NiMn-LDH [20]. Moreover, the phenol hydroxyl groups of dye can capable of forming coordinate bonds with metal ions in $Fe_3O_4$/NiMn-LDH [21].

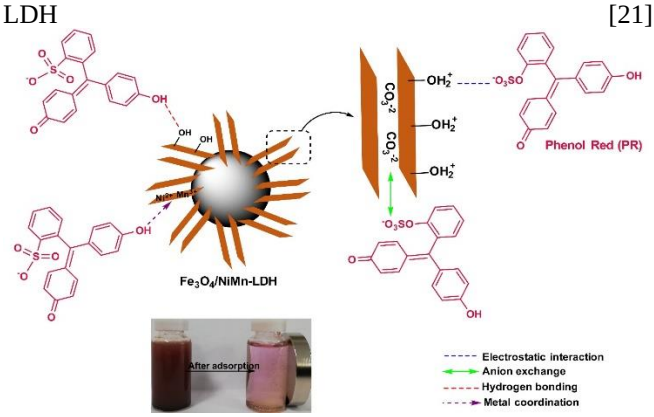


**Figure 6.** *Schematic representation of PR decolorization mechanism onto $Fe_3O_4$/NiMn-LDH.*

## 4. Conclusions

In this study, $Fe_3O_4$/NiMn-LDH with magnetic property was successfully synthesized via a co-precipitation synthesis approach. The prepared material was applied to the effective elimination of anionic dye (PR) from aqueous media. The PR decolorization experiments were performed as a function of pH, adsorbent amount, and $C_o$ using BBD based on RSM. The results of RSM showed that the model in the decolorization of PR was highly important within 99% confidence interval. The value of $R^2$ for the decolorization of PR indicates that the quadratic model is considerably appropriate for estimating the performance of PR decolorization on $Fe_3O_4$/NiMn-LDH. The optimum values for the maximum PR decolorization through numerical analysis were 5.38 of pH, 24.59 mg of adsorbent dosage, and 25.39 mg/L of $C_o$. Based on the obtained conditions, the maximum PR decolorization efficiency was determined as 86.93%. The PR decolorization process on $Fe_3O_4$/NiMn-LDH indicated that the prepared material would be a promising adsorbent for the decolorization of dyes.

## References

[1]. Mittal A., Kaur D., Malviya A., Mittal J., Gupta V.K., "Adsorption studies on the removal of coloring agent phenol red from wastewater using waste materials as adsorbents", Journal of Colloid and Interface Science, 337, (2009), 345-354.

[2]. Badhai P., Kashyap S., Behera S.K., "Adsorption of phenol red onto GO-Fe3O4 hybrids in aqueous media", Environmental Nanotechnology, Monitoring & Management, 13, (2020), 100282.

[3]. Ghaedi M., Daneshfar A., Ahmadi A., Momeni M.S., "Artificial neural network-genetic algorithm based optimization for the adsorption of phenol red (PR) onto gold and titanium dioxide nanoparticles loaded on activated carbon", Journal of Industrial and Engineering Chemistry, 21, (2015), 587-598.

[4]. Gautam A., Rawat S., Verma L., Singh J., Sikarwar S., Yadav B.C., Kalamdhad A.S., "Green synthesis of iron nanoparticle from extract of waste tea: An application for phenol red removal from aqueous solution", Environmental Nanotechnology, Monitoring & Management, 10, (2018), 377-387.

[5]. Iqbal M.J., Ashiq M.N., "Adsorption of dyes from aqueous solutions on activated charcoal", Journal of Hazardous Materials, 139, (2007), 57-66.

[6]. Masoudian N., Rajabi M., Ghaedi M., "Titanium oxide nanoparticles loaded onto activated carbon prepared from bio-waste watermelon rind for the efficient ultrasonic-assisted adsorption of congo red and phenol red dyes from wastewaters", Polyhedron, 173, (2019), 114105.

[7]. Thakur S., Singh S., Pal B., "Superior adsorptive removal of brilliant green and phenol red dyes mixture by CaO nanoparticles extracted from egg shells", Journal of Nanostructure in Chemistry, 12, (2021), 207-221.

[8]. He X., Wang B., Zhang Q., "Phenols removal from water by precursor preparation for MgAl layered double hydroxide: Isotherm, kinetic and mechanism", Materials Chemistry and Physics, 221, (2019), 108-117.

[9]. George G., Saravanakumar M.P., "Facile synthesis of carbon-coated layered double hydroxide and its comparative characterisation with Zn–Al LDH: application on crystal violet and malachite green dye adsorption—isotherm, kinetics and Box-Behnken design", Environmental Science and Pollution Research, 25, (2018), 30236-30254.

[10]. Zhou L., Slaný M., Bai B., Du W., Qu C., Zhang J., Tang Y., "Enhanced removal of sulfonated lignite from oil wastewater with multidimensional MgAl-LDH nanoparticles", Nanomaterials, 11, (2021), 861.

[11]. Shan R.-r., Yan L.-g., Yang K., Hao Y.-f., Du B., "Adsorption of Cd(II) by Mg–Al–CO3- and magnetic Fe3O4/Mg–Al–CO3-layered double hydroxides:

Kinetic, isothermal, thermodynamic and mechanistic studies", Journal of Hazardous Materials, 299, (2015), 42-49.

[12]. Dashamiri S., Ghaedi M., Asfaram A., Zare F., Wang S., "Multi-response optimization of ultrasound assisted competitive adsorption of dyes onto Cu (OH)2-nanoparticle loaded activated carbon: Central composite design", Ultrasonics Sonochemistry, 34, (2017), 343-353.

[13]. Yang Y., Ali A., Su J., Chang Q., Xu L., Su L., Qi Z., "Phenol and 17β-estradiol removal by Zoogloea sp. MFQ7 and in-situ generated biogenic manganese oxides: Performance, kinetics and mechanism", Journal of Hazardous Materials, 429, (2022), 128281.

[14]. Mardani H.R., "(Cu/Ni)–Al layered double hydroxides@Fe3O4 as efficient magnetic nanocomposite photocatalyst for visible-light degradation of methylene blue", Research on Chemical Intermediates, 43, (2017), 5795-5810.

[15]. Padmini M., Kiran S.K., Lakshminarasimhan N., Sathish M., Elumalai P., "High-performance solid-state hybrid energy-storage device consisting of reduced graphene-oxide anchored with NiMn-layered double hydroxide", Electrochimica Acta, 236, (2017), 359-370.

[16]. Shahabadi N., Razlansari M., Zhaleh H., Mansouri K., "Antiproliferative effects of new magnetic pH-responsive drug delivery system composed of Fe3O4, CaAl layered double hydroxide and levodopa on melanoma cancer cells", Materials Science and Engineering: C, 101, (2019), 472-486.

[17]. Masoudian N., Rajabi M., Ghaedi M., Asghari A., "Highly efficient adsorption of naphthol green B and phenol red dye by combination of ultrasound wave and copper-doped zinc sulfide nanoparticles loaded on pistachio-nut shell", Applied Organometallic Chemistry, 32, (2018), e4369.

[18]. Sriram G., Uthappa U.T., Losic D., Kigga M., Jung H.-Y., Kurkuri M.D., "Mg–Al-layered double hydroxide (LDH) modified diatoms for highly efficient removal of congo red from aqueous solution", Applied Sciences, 10, (2020), 2285.

[19]. Lu L., Li J., Ng D.H.L., Yang P., Song P., Zuo M., "Synthesis of novel hierarchically porous Fe3O4@MgAl–LDH magnetic microspheres and its superb adsorption properties of dye from water", Journal of Industrial and Engineering Chemistry, 46, (2017), 315-323.

[20]. Li Y., Bi H.-Y., Mao X.-M., Liang Y.-Q., Li H., "Adsorption behavior and mechanism of core–shell magnetic rhamnolipid–layered double hydroxide nanohybrid for phenolic compounds from heavy metal–phenolic pollutants", Applied Clay Science, 162, (2018), 230-238.

[21]. Wu Y., Zheng H., Li H., Sun Y., Zhao C., Zhao R., Zhang C., "Magnetic nickel cobalt sulfide/sodium dodecyl benzene sulfonate with excellent ciprofloxacin adsorption capacity and wide pH adaptability", Chemical Engineering Journal, 426, (2021), 127208.

MANAS Journal of Engineering
ISSN 1694-7398 | e-ISSN 1694-7398

*Volume 10, Issue 1, (2022) Pages 95-104*
*https://doi.org/10.51354/mjen. 1091207*

# Anion effect on obtaining nano-sized metal particules by reduction reaction

Sebati İlhan[1], Melda Bolat Bülter[2], Kadir Erol[3], Dursun Ali Köse[1*]

[1] Hitit University, Faculty of Science and Art, Department of Chemistry, Çorum, Turkey, dalikose@hitit.edu.tr, ORCID: 0000-0003-4767-6799
[2] Hitit University, Vocational School of Technical Sciences, Program of OHS, Çorum, Turkey.
[3] Hitit University, Health Sciences Vocational School, Environmental Health Program, Çorum, Turkey.

**ABSTRACT**

The word "nano" means; one in a billion of a physical mass. Nanotechnology has been frequently beneficial branch of science in recent years by applying nanoparticules to various fields. Synthesis of particules in nano is size, has increased the covered surface area in unit volume and this made expanding of using nanoparticules in many different areas. Especially the metal nanoparticules have many advantages leading to development of many ways of synthesis. One of these methods of synthesis is "chemical reduction". This work makes a research on the anion effects on the size mass nanoparticules of metals Cu(II), Ni(II), Co(II), Zn(II) and Mn(II) after reduction to nano size of sodium bor hidrur which belongs to salt of acetate and chloride, nitrate, sulfate. Depending on the radius ratios and solubility values of metal cations and anions, the nanoparticule obtained from $Cu(CH_3COO)_2$ salt has the smallest radius. Nanometal particules with the largest radius were obtained by reduction of $Cl^-$ ion salts. Size analysis and scanning electron microscope (SEM) analysis made about the characterization of synthesised nano particules.

**ARTICLE INFO**

***Research article***

*Received: 21.03.2022*
*Accepted: 2.05.2022*

***Keywords:***
*Nano,*
*metal,*
*sodium borohydride,*
*reduction anion effect*

**corresponding author*

## 1 Introduction

Nanotechnology, which is an up-to-date science, covers the production and applications of particules smaller than 100 nm [1]. The synthesis of nanostructured materials, especially metallic nanoparticules, has attracted great attention over the past decade due to their unique properties that make them applicable in different fields of science and technology [2]. Nanoparticule research is a fascinating science. The largely dimensional properties of nanoparticules offer countless opportunities for surprising discoveries. The often unexpected and unprecedented behavior of nanoparticules has great potential for innovative technological applications [3]. Nanoparticules have a surprisingly long history. Their preparation is neither a specific result of modern research nor limited to man-made materials. Naturally occurring nanoparticules, organic (proteins, polysaccharides, viruses, among others) as well as inorganic compounds Contains (iron oxyhydroxides, aluminosilicates, metals, among others) and are produced by weather conditions, volcano eruptions, forest fires, or microbial processes [4,5].
Transition metal nanoparticules are essential for the possible application of radiating diodes and nano centric chemical sensors in catalysis in quantum computers or other electronic devices. In addition, nanoparticules have important applications in optics, electronics, and magnetic devices. [6].

Metal oxide nanoparticules (MONs) are made entirely from metal precursors [7]. MONs are distinctive materials with properties such as catalytic, magnetic, UV absorption, fluorescent quenching and dielectric properties, photocatalyst oxidative catalyst, and drug release, biocompatibility, biomedical imaging, detection [8-14].

There are many studies on nanoparticules that have gained great attention in the last decade due to their unique properties [15-17]. In vivo and in vitro studies have shown that nanoparticules have toxic effects on living things [15,18-20]. Considering that nanotechnology, which has such fantastic features, will be used more widely in the future, people will come into contact with nanoparticules more. For this reason, the possible negative effects of nanoparticules on human health, especially the respiratory system, should be further investigated in order to prevent the repetition of the "fearful dream of asbestos" by human beings.

In this study, nanoparticule synthesis was carried out by reducing the sulfate, nitrate, chloride and acetate salts of Cu(II), Ni(II), Co(II), Zn(II) and Mn(II) metals with the help of sodium borohydride compound and in this way, the effects of the anion on the size of the nanoparticules were investigated. There is a gap in the literature on this issue and we think that the results of this study are important for the scientists who are interested in nanotechnology. For the characterization of obtained nanoparticules, size analysis and scanning electron microscopy (SEM) analysis was performed.

## 2 Materials and methods

### *2.1. Chemicals*

Sulfate, nitrate, chloride, and acetate salts of copper, nickel, cobalt, zinc, manganese, and sodium borohydride ($NaBH_4$) are supplied from Sigma-Aldrich. All other chemicals used in the study are of analytical purity.

### *2.2. Synthesis of Nanoparticules*

In this study, metal oxide nanoparticule synthesis was applied following the processes. 0.001 mol of transition metal salt and 0.005 mol of $NaBH_4$ were dissolved in 100 mL of distilled water. The pH of the solution was brought to around 6.50 with HCl solution. The solution was then taken into a flask and placed in the assembly consisting of a water bath and a mechanical stirrer. The transition metal solution was stirred for 2.5 hours at 85 °C, 700 rpm. In the last stage, the large particules and unwanted impurities settled at the bottom were filtered under vacuum and the metal oxide nanoparticule solid remaining at the bottom of the flask after the water was removed by the evaporator device was dried with a vacuum oven.

### *2.3. Characterization Studies*

#### *2.3.1. Scanning electron microscope (SEM)*

The surface morphology of the synthesized nanoparticules was investigated using scanning electron microscopy (SEM; FEI / Quanta 450 FEG, USA). The sample attached to the SEM holder by double-sided carbon tape was then coated under vacuum with a thin layer of gold. Then the resulting SEM sample was placed in the device and the image was taken.

#### *2.3.2. Size analysis*

The size of the nanoparticules in the aqueous solution was analyzed. The scattering angle of the laser light passing through the particule depends on the particule size. As the particule size decreases, the scattering angle increases logarithmically. The scattering angles of large particules are low, and the intensity of the scattered laser light is high. In small particules, the scattering angle is high and the intensity of the scattered laser light is low.

## 3 Results and discussions

### *3.1. Scanning Electron Microscope (SEM)*

SEM images of metal oxide nanoparticules are given in the figures (Fig. 1-5). The images of the nanoparticules obtained by reducing them in 2+ oxidation step with $NaBH_4$ by scanning electron microscopy are given.

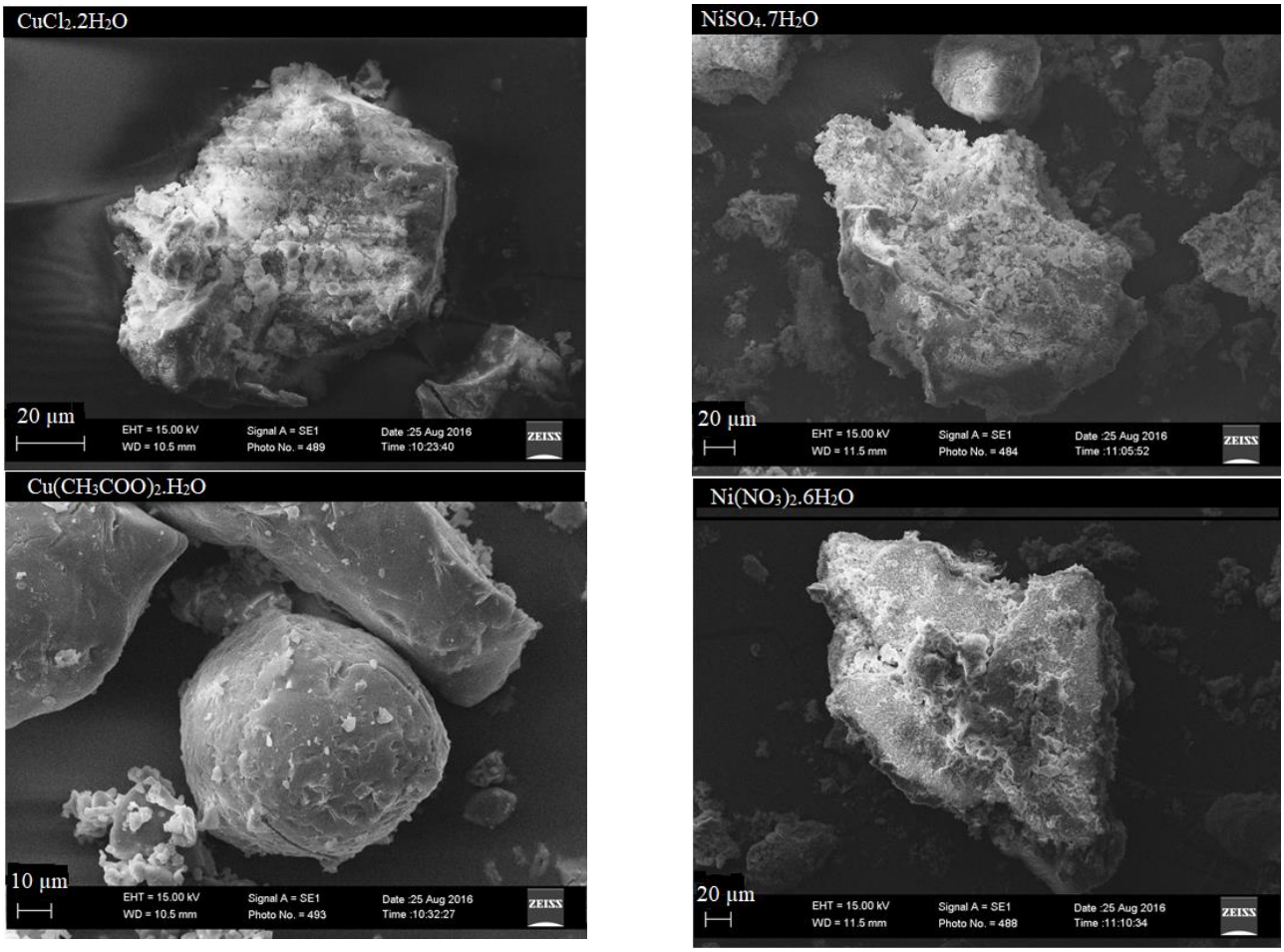


**Figure 1**. *SEM images of nanoparticules taken from Cu(II) salts.*

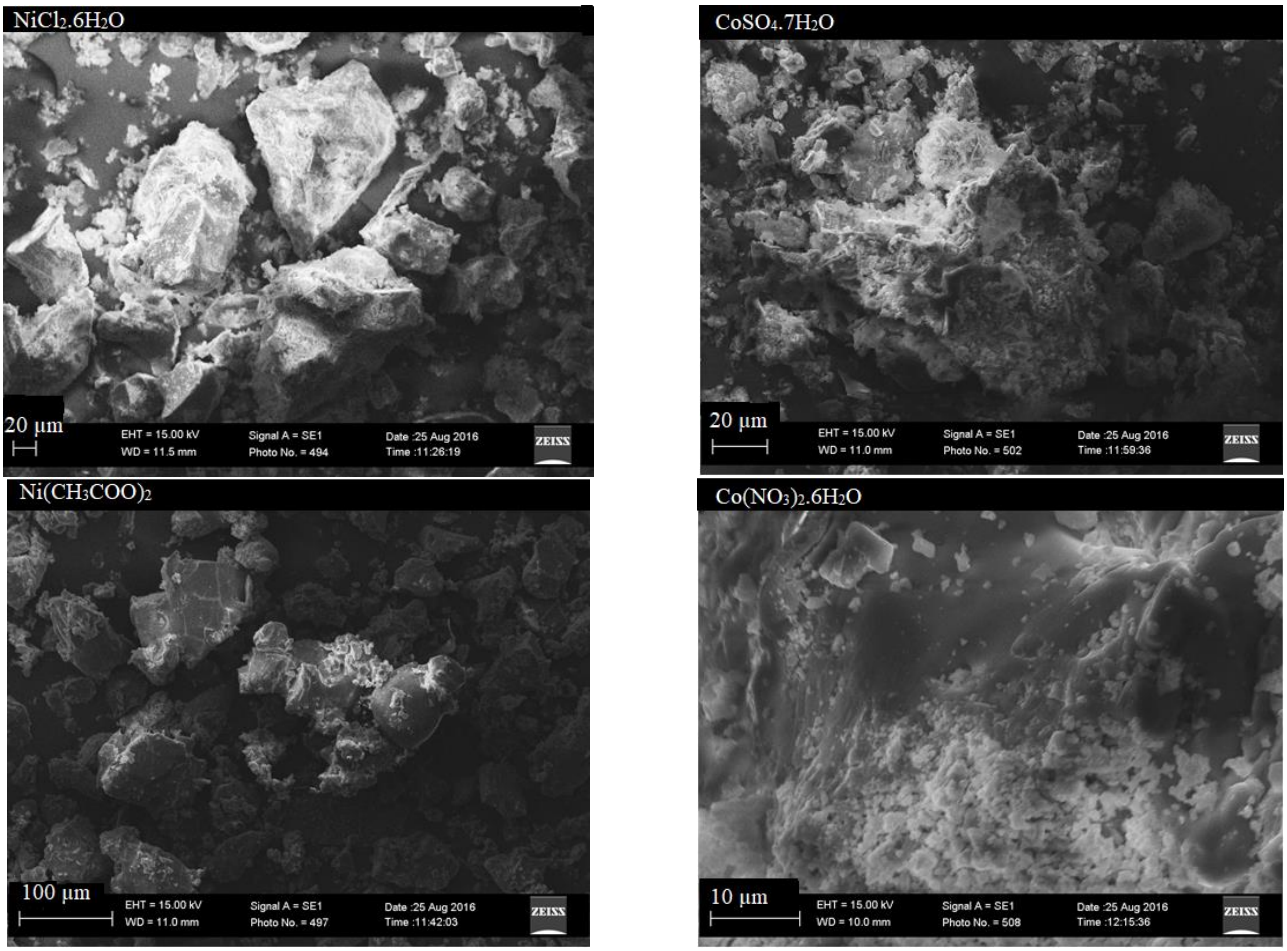


**Figure 2**. *SEM images of nanoparticules taken from Ni(II) salts*

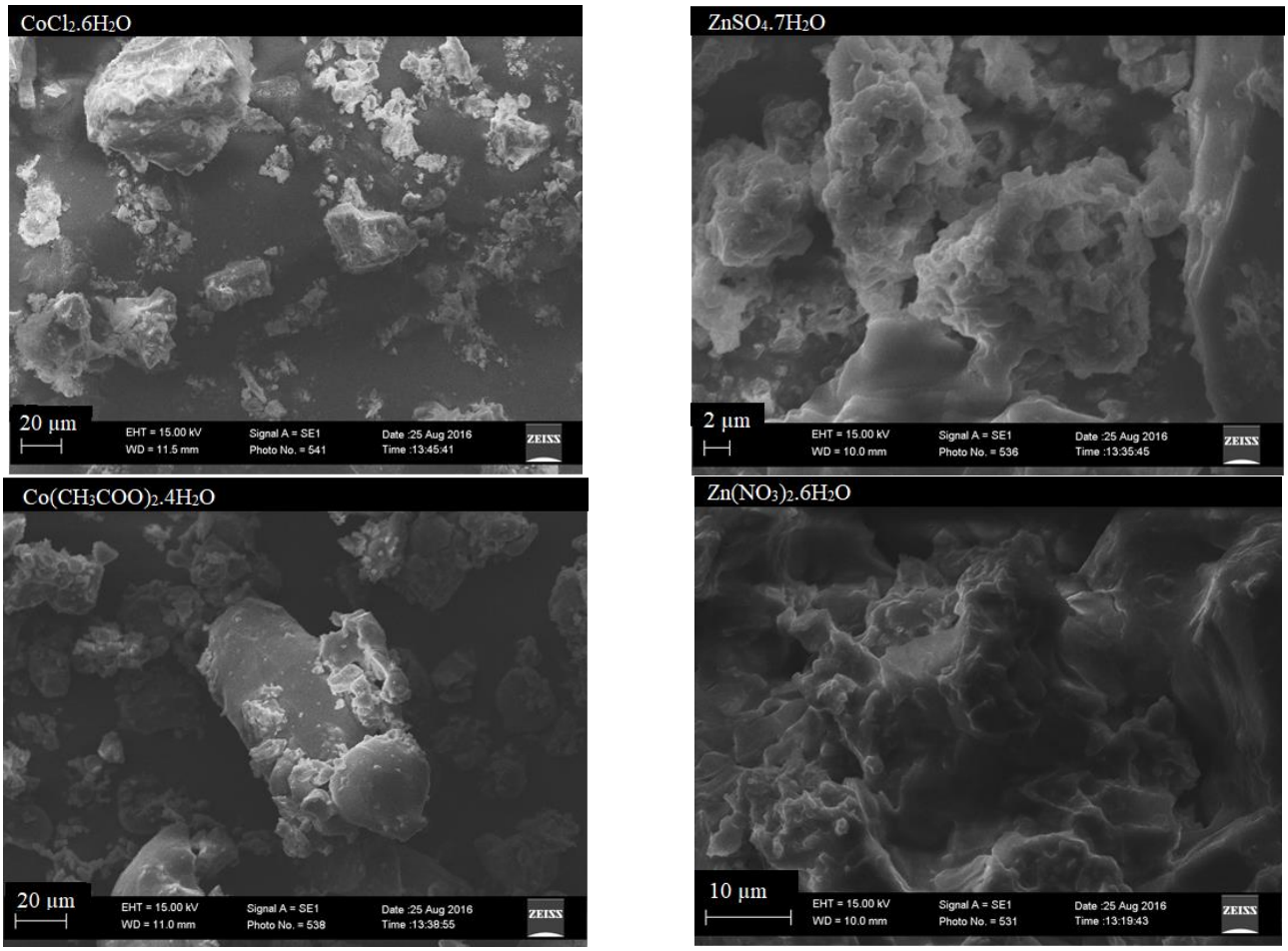


**Figure 3**. *SEM images of nanoparticules taken from Co(II) salts*

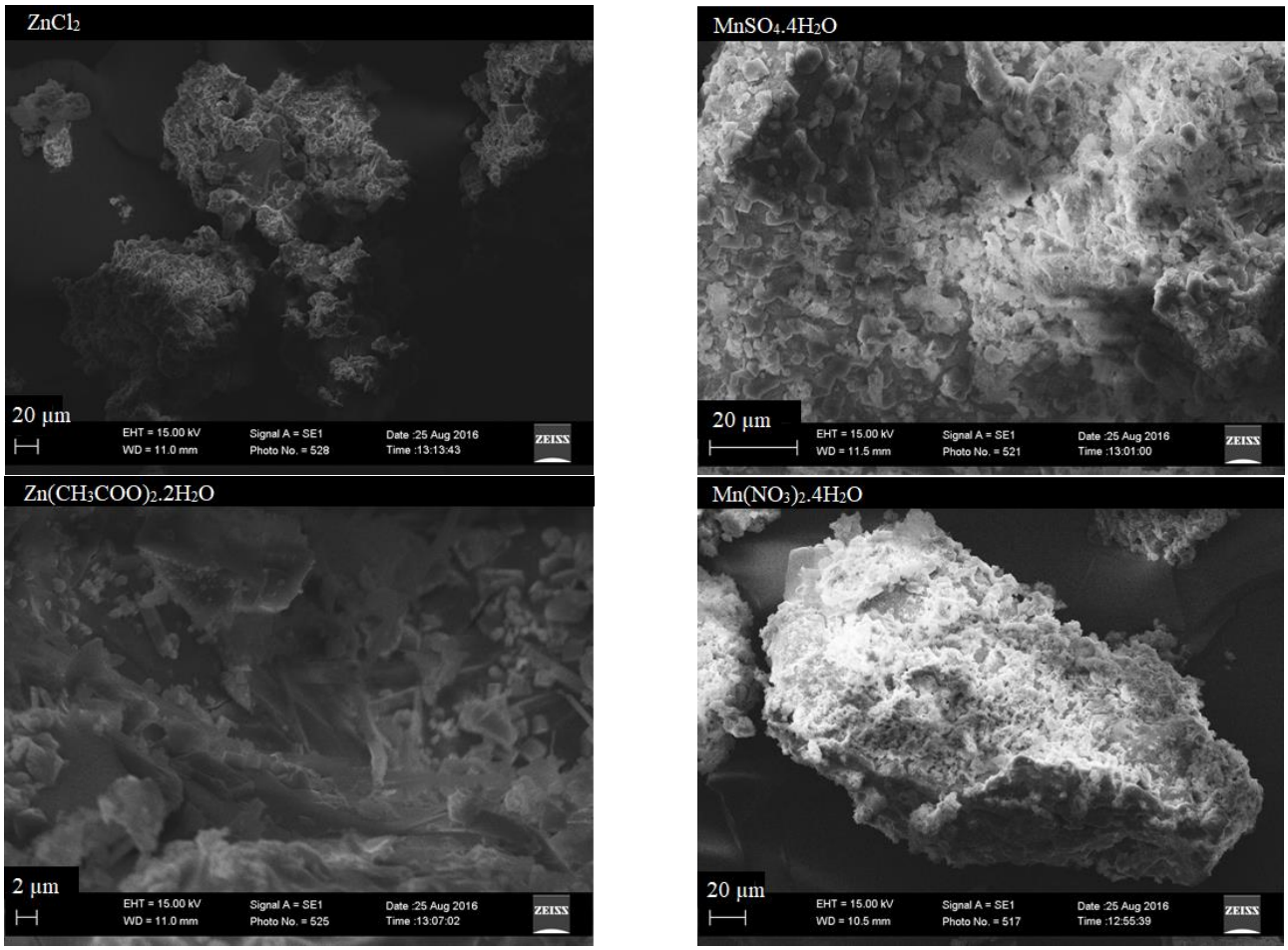


**Figure 4**. *SEM images of nanoparticules taken from Zn(II) salts*

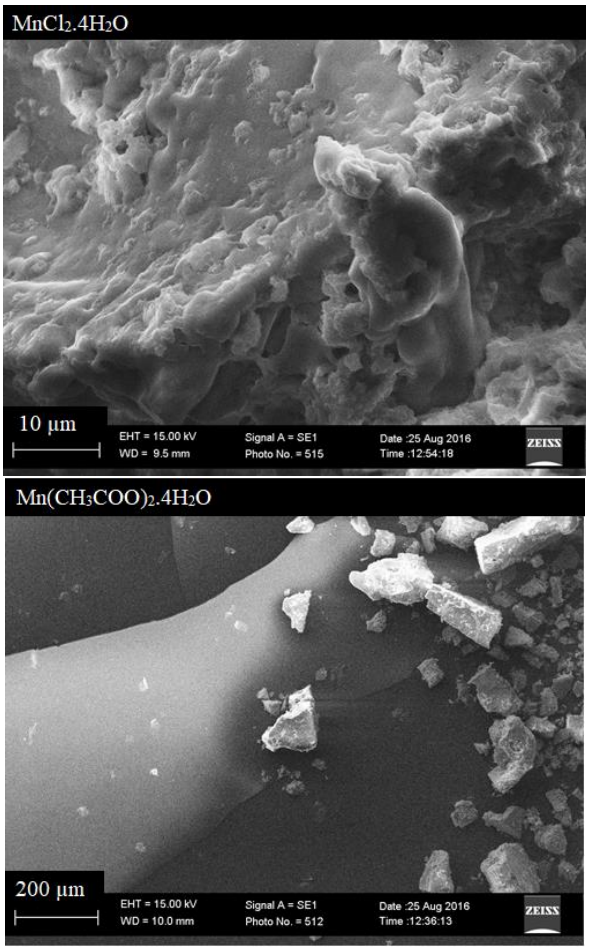


**Figure 5**. *SEM images of nanoparticules taken from Mn(II) salts*

### *3.2. Size Analysis*

The results of the size analysis of nanoparticule metal powders performed by the Zeta-Sizer method are given in Table 1. The smallest size nanoparticule Zeta-Sizer plots are shown in Figure 6. The largest size nanoparticule Zeta-Sizer plot is shown in Figure 7.

**Table 1.** *Size analysis of nanoparticules.*

| Anion | Cu (nm) | Ni (nm) | Co (nm) | Zn (nm) | Mn (nm) | Ave. (nm) |
|---|---|---|---|---|---|---|
| Sulfate | 40.49 | 369.2 | 1.553 | 0.8212 | 0.8907 | 82.59 |
| Nitrate | 281.0 | 2.171 | 0.6823 | 0.7146 | 770.4 | 210.99 |
| Chloride | 546.9 | 243.4 | 307.4 | 338.8 | 543.7 | 457.52 |
| Acetate | 0.6393 | 2.710 | 364.2 | 0.6835 | 0.6696 | 73.78 |
| *Average* | 294.11 | 154.37 | 168.45 | 85.26 | 328.92 | |

When the size analysis of metal salts is examined in the light of the data summarized in table 1, the following order of salts from small to large is formed according to the size of the particules obtained.

$$Cu(CH_3COO)_2 < Mn(CH_3COO)_2 < Co(NO_3)_2 < Zn(CH_3COO)_2 < Zn(NO_3)_2 < ZnSO_4 < MnSO_4 < CoSO_4 < Ni(NO_3)_2 < Ni(CH_3COO)_2 < CuSO_4 < NiCl_2 < Cu(NO_3)_2 < CoCl_2 < ZnCl_2 < Co(CH_3COO)_2 < NiSO_4 < MnCl_2 < CuCl_2 < Mn(NO_3)_2$$

When anion-based size analysis is examined, the following order is formed from small to large.

$$CH_3COO^- < SO_4^{-2} < NO_3^- < Cl^-$$

When the cation-based size analysis is examined, the following order is formed from small to large.

$$Zn^{+2} < Ni^{+2} < Co^{+2} < Cu^{+2} < Mn^{+2}$$

4

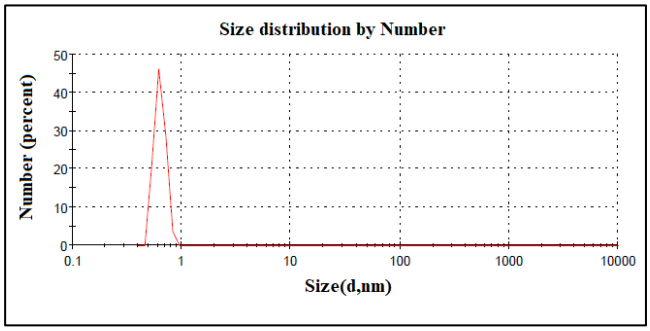


**Figure 6**. *Smallest size nanoparticule particules $Cu(CH_3COOH)_2$*

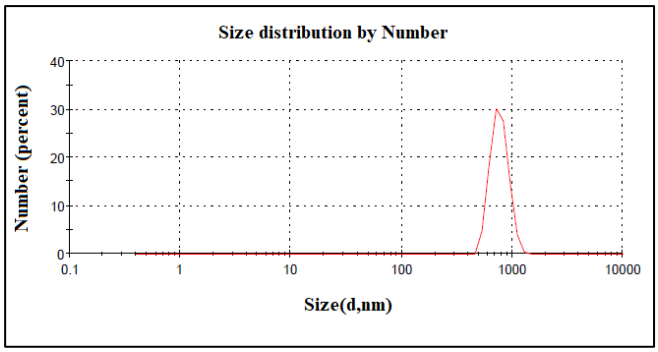


**Figure 7.** *Largest size nanoparticule particule $Mn(NO_3)_2$*

In Table 2 of the metal salts we used in our study, the radius values of the cations with 2+ oxidation steps are given. When these values are examined, it is seen that they change differently from the expected order in the periodic table.

$Mn^{2+} < Co^{2+} < Ni^{2+} < Cu^{2+} < Zn^{2+}$ expected order in the periodic table

$Co^{2+} < Cu^{2+} < Mn^{2+} < Ni^{2+} < Zn^{+2}$ actual size order of metal cations with +2 charge valence

**Table 2**. *Cation radius values [21]*

| Cation | Radius(pm) |
|---|---|
| $Co^{+2}$ | 65(ls), 74,5(hs) |
| $Cu^{+2}$ | 73 |
| $Mn^{+2}$ | 81(ls), 97(hs) |
| $Ni^{+2}$ | 83 |
| $Zn^{+2}$ | 88 |

ls: low spin, hs: high spin

The behavior they show differently from what is expected in the periodic table can be attributed to the change in electronic configurations of the metal cations when they turn into the +2 oxidation step form. The $Mn^{2+}$ cation, which is expected to have the smallest radius, becomes stable by distributing all the electrons it has in the form of $d^5$ semi-full stability to the *3d* orbitals one by one, which causes its radius to increase. The fact that the $Ni^{2+}$ cation is smaller than the $Cu^{2+}$ cation can also be attributed to the difference in the expected +2 metal cation electronic configuration compared to the lean electronic configurations of the metal [22], [23].

When the radius values of the anions given in Table 3 are compared, it has been determined that $SO_4^{2-}$ anion has the largest radius value and $CH_3COO^-$ anion has the smallest value according to the expected conventions.

**Table 3.** *The radius values of anions [24]*

| Anion | Radius (nm) |
|---|---|
| $CH_3COO^-$ | 162 |
| $NO_3^-$ | 179 |
| $Cl^-$ | 184 |
| $SO_4^{2-}$ | 258 |

As the cation / anion ratio of the ionic salts formed by the hard acid - hard base and soft acid - soft base binary compounds approaches 1, the solubility properties are expected to decrease due to the increasing covalent character. When the solubility values of the metal salts given in g / ml in an aqueous medium at 20 °C in Table 4 are examined, they show the expected changes (due to the periodic table exceptions), including small deviations.

**Table 4.** *The solubility values of the metal salts [16]*

| Metal Salt | Solubility (g/100mL, 20°C) |
|---|---|
| $Zn(CH_3COO)_2.2H_2O$ | 43.0 |
| $Zn(NO_3)_2.6H_2O$ | 184.0 |
| $ZnSO_4.7H_2O$ | 96.0 |
| $ZnCl_2$ | 395.0 |
| $Cu(CH_3COO)_2.H_2O$ | 7.2 |
| $Cu(NO_3)_2.3H_2O$ | 125.0 |
| $CuSO_4.5H_2O$ | 32.0 |
| $CuCl_2.2H_2O$ | 73.0 |
| $Co(CH_3COO)_2.4H_2O$ | 38.0 |
| $Co(NO_3)_2.6H_2O$ | 134.0 |
| $CoSO_4.7H_2O$ | 36.2 |
| $CoCl_2.6H_2O$ | 52.9 |
| $Ni(CH_3COO)_2.4H_2O$ | 182.0 |
| $Ni(NO_3)_2.6H_2O$ | 238.5 |
| $NiSO_4.7H_2O$ | 75.6 |
| $NiCl_2.6H_2O$ | 254.0 |
| $Mn(CH_3COO)_2.4H_2O$ | 23.3 |
| $Mn(NO_3)_2.4H_2O$ | 380.0 |
| $MnSO_4.4H_2O$ | 70.0 |
| $MnCl_2.4H_2O$ | 198.0 |

Comparisons of metal salts based on +2 metal cations are as follows, but the anion salts with the highest solubility are salts with $Ni^{2+}$ metal cations, and the anion salt group with the lowest solubility is salted with $Cu^{2+}$ metal cation.

| | |
|---|---|
| $Cu(NO_3)_2 > CuCl_2 > CuSO_4 > Cu(CH_3COO)_2$ | 59,30 |
| $Co(NO_3)_2 > CoCl_2 > Co(CH_3COO)_2 > CoSO_4$ | 65,28 |
| $Mn(NO_3)_2 > MnCl_2 > MnSO_4 > Mn(CH_3COO)_2$ | 167,82 |
| $ZnCl_2 > Zn(NO_3)_2 > ZnSO_4 > Zn(CH_3COO)_2$ | 179,50 |
| $NiCl_2 > Ni(NO_3)_2 > Ni(CH_3COO)_2 > NiSO_4$ | 187,53 |

Unlike $NO_3^-$, $Cl^-$ and $CH_3COO^-$ anions with 1- oxidation step, $SO_4^{2-}$ anion with -2 oxidation step will create a desire to give stronger electrons than other anions in order to reduce the electronic stress caused by the -2 charge in its structure. For this reason, compared to the radius ratios of other anions, it will perform a stronger ionic interaction with metal cations, and consequently, the solubility of the salt compounds it creates will be higher than expected.

As a result of the interaction of the aqueous solutions of the metal salts with the strong reducing sodium borohydride ($NaBH_4$), the order of the particule size of the metal oxide nanoparticules obtained from the reduction of the metals from the $M^{2+}$ oxidation step to the $M^0$ plain metal form is as follows:

$$Cu(CH_3COO)_2 < Mn(CH_3COO)_2 < Co(NO_3)_2 < Zn(CH_3COO)_2 < Zn(NO_3)_2 < ZnSO_4 < MnSO_4 < CoSO_4 < Ni(NO_3)_2 < Ni(CH_3COO)_2 < CuSO_4 < NiCl_2 < Cu(NO_3)_2 < CoCl_2 < ZnCl_2 < Co(CH_3COO)_2 < NiSO_4 < MnCl_2 < CuCl_2 < Mn(NO_3)_2$$

When the anion radius order of the salts from which the metal nanopowder is obtained was examined, it was determined that the salts with acetate anion formed the smallest particules, while the radius average of the metal nanopowder from the chloride anion-containing salts was the largest.

The anion-based particule size order of nanopowders obtained from metal cation salts by reduction with $NaBH_4$ is as follows.

$$CH_3COO)_2^- < SO_4^{2-} < NO_3^- < Cl^-$$

The cation-based particule size order of nanopowders obtained from metal cation salts by reduction with $NaBH_4$ is as follows.

$$Zn^{2+} < Ni^{2+} < Co^{2+} < Cu^{2+} < Mn^{2+}$$

The smallest particule size among the cations was obtained in Zn(II). Among the anions, the smallest size is reached in the acetate anion. Accordingly, it can be said that the higher solubility of zinc acetate in aqueous media compared to other salts caused the nanoparticules to be smaller in size. Based on the same idea, copper(II) chloride salt, which dissolves relatively slowly in aqueous media, was also identified as the largest particule.

The smallest metal oxide nanoparticules were formed as a result of the reduction of the salt compounds containing the lowest solubility of $CH_3COO^-$ anion according to the radius ratios of the cations and anions given above accordingly increasing or decreasing solubility values. In particular, the nanoparticule obtained from the $Cu(CH_3COO)_2$ salt has the smallest radius. Metal oxide nanoparticules with the largest radius were obtained by reducing the $Cl^-$ ion salts in contrast to those obtained from the $NO_3^-$ ion salts with the highest solubility. The reason is that the average solubility values of the salts formed by chloride and nitrate anions are very close to each other.

## 5 Conclusion

As a result of the study, metal oxide nanoparticules of the smallest size were obtained from metal salts formed by metal cations and acetate anions. Although the solubility of the metal salts formed by the acetate anions is less than that of the others, the controlled reduction of the metal cations in the solution may have caused this result. We think, metal oxide nanoparticules obtained by reducing metal salts that have a higher solubility in an aqueous medium with $NaBH_4$ are grown as a result of agglomeration.

When the cation radius of the salts from which metal nanopowders are obtained is examined, it is expected that the particule size of the nanopowders obtained from the $Zn^{2+}$ cations with a radius greater than the other cations is the smallest, and the radiuses of the nanometal powders obtained from the $Co^{2+}$ cation salts with the smallest radius are expected to have the largest average. However, nanoparticules obtained from $Cu^{2+}$ and $Mn^{2+}$ metal cations were found to be smaller in size. This behavior, which develops differently than expected, can be attributed to the behavior of the $Co^{2+}$ metal cation with high spin and radii of $Co^{2+}$ (with high spin), $Cu^{2+}$, and $Mn^{2+}$ metal cations very close to each other. According to the anion / cation radius ratio, the particule sizes of the nanopowders obtained from the $Ni(CH_3COO)_2$ and $Mn(CH_3COO)_2$ salts with the lowest solubility are the smallest, and the particule size of the nanopowder obtained from the $Mn(NO_3)_2$ salt with the highest solubility is found to be the highest. The particule sizes of the other metal oxide nanoparticules were also found to be changing (including the exceptions) in parallel with the change in the solubility of the ionic salts.

## References

[1]. A.G. Mamalis, Recent advances in nanotechnology, J. Mater. Process Technol., 181(1-3) (2007) 52-58. doi:10.1016/j.jmatprotec.2006.03.052

[2]. N. Kulkarni, U. Muddapur, Biosynthesis of Metal Nanoparticles: A Review, J. Nanotechnol., (2014) 510246. doi:10.1155/2014/510246

[3]. F. J. Heiligtag, M. Niederberger, The fascinating world of nanoparticule research, materialstoday, 16(7-8) (2013) 262-271. doi:10.1016/j.mattod.2013.07.004

[4]. J. R. Lead and K. J. Wilkinson, Aquatic colloids and nanoparticules: Current knowledge and future trends, Environ. Chem., 3(3) (2006) 159-171. doi:10.1071/EN06025

[5]. R. M. Hough, R. R. P. Noble, M. Reich, Natural gold nanoparticules, Ore Geol. Rev., 42(1) (2011) 55-61. doi:10.1016/j.oregeorev.2011.07.003

[6]. R. Dittrich, S. Stopić, B. Friedrich, Mechanism of nanogold formation by ultrasonic spray pyrolysis, Proc.-Eur. Metall. Conf. EMC 2011, 3 (2011) 1065-1076.

[7]. T. Naseem, T. Durrani, The role of some important metal oxide nanoparticules for wastewater and antibacterial applications: A review, J. Environ. Chem. Ecotoxicol., 3 (2021) 59-75. doi:10.1016/j.enceco.2020.12.001

[8]. Y. H. Kim, D. K. Lee, H. G. Cha, C. W. Kim, Y. S. Kang, Synthesis and characterization of antibacterial Ag - SiO2 nanocomposite, J. Phys. Chem. C, 111(9) (2007) 3629-3635. doi:10.1021/jp068302w

[9]. S. Chandra, P. Das, S. Bag, D. Laha, P. Pramanik, Synthesis, functionalization and bioimaging

applications of highly fluorescent carbon nanoparticles, Nanoscale, 3(4) (2011) 1533-1540. doi:10.1039/c0nr00735h

[10]. H. Rui, R. Xing, Z. Xu, Y. Hou, S. Goo, S. Sun, Synthesis, functionalization, and biomedical applications of multifunctional magnetic nanoparticles, Adv. Mater., 22(25) (2010) 2729-2742. doi:10.1002/adma.201000260

[11]. T. Montini, M. Melchionna, M. Monai, P. Fornasiero, Fundamentals and Catalytic Applications of CeO2-Based Materials, Chem. Rev., 116(10) (2016) 5987-6041. doi:10.1021/acs.chemrev.5b00603

[12]. M. Rizwan, S. Ali, M.F. Qayyum, Y. S. Ok, M. Adrees, M. Ibrahim, M. Z. Rehman, M. Farid, F. Abbas, Effect of metal and metal oxide nanoparticules on growth and physiology of globally important food crops: A critical review, J. Hazard. Mater., 322 (2017) 2-16. doi:10.1016/j.jhazmat.2016.05.061

[13]. H.S. Tuli, D. Kashyap, S.K. Bedi, P. Kumar, G. Kumar, S.S. Sandhu, Molecular aspects of metal oxide nanoparticule (MO-NPs) mediated pharmacological effects, Life Sci., 143 (2015) 71-79. doi:10.1016/j.lfs.2015.10.021

[14]. P. Falcaro, R. Ricco, A. Yazdi, I. Izmaz, S. Furukawa, D. Maspoch, R. Ameloot, J.D. Evans, C.J. Doonan, Application of metal and metal oxide nanoparticules at MOFs', Coord. Chem. Rev., 307(2) (2016) 237-254. doi:10.1016/j.ccr.2015.08.002

[15]. S.S. Sana, H. Li, Z. Zhang, M. Sharma, Z. Usmani, T. Hou, V.R. Netala, X. Wang, V.K. Gupta, Recent advances in essential oils-based metal nanoparticules: A review on recent developments and biopharmaceutical applications, J. Mol. Liq., 333 (2021) 115951. doi:10.1016/j.molliq.2021.115951

[16]. G. Yang, W. Lin, H. Lai, J. Tong, J. Lei, M. Yuan, Y. Zhang, C. Cui, Understanding the relationship between particule size and ultrasonic treatment during the synthesis of metal nanoparticules, Ultrason. Sonochem., 73 (2021) 105497. doi:10.1016/j.ultsonch.2021.105497

[17]. D.K. Kumar, J. Kříž, N. Bennett, B. Chen, H.U. Kakarla, R. Reddy, V. Sadhu, Functionalized metal oxide nanoparticules for efficient dye-sensitized solar cells (DSSCs): A review, Mater. Sci. Energy Technol., 3 (2020) 472-481. doi:10.1016/j.mset.2020.03.003

[18]. S. Khan, M. M.N. Babadaei, A. Hasan, Z. Edis, F. Attar, R. Siddique, Q. Bai, M. Sharifi, M. Falahati, Enzyme–polymeric/inorganic metal oxide/hybrid nanoparticule bio-conjugates in the development of therapeutic and biosensing platforms, J. Adv. Res., 4(33) (2021) 227-239. doi:10.1016/j.jare.2021.01.012

[19]. I. Khan, K. Saeed, I. Khan, Nanoparticules: Properties, applications and toxicities, Arab. J. Chem., 12(7) (2019) 908-931. doi:10.1016/j.arabjc.2017.05.011

[20]. A.C. Anselmo, S. Mitragotri, Nanoparticules in the clinic, Bioeng. Transl. Med., 1(1) (2016) 10-29. doi: 10.1002/btm2.10003

[21]. R.D. Shannon, Revised effective ionic radii and systematic studies of interatomic distances in halides and chalcogenides, Acta Cryst., A32 (1976) 751-767. doi:10.1107/S0567739476001551

[22]. R.G. Pearson, Hard and soft acids and bases, J. Am. Chem. Soc., 85(22) (1963) 3533-3539. doi:10.1021/ja00905a001

[23]. R.G. Pearson, Hard and soft acids and bases, HSAB, Part I: Fundamental principles, J. Chem. Educ., 45(9) (1968) 581-587. doi:10.1021/ed045p581

[24]. H.D.B. Jenkins, K.P. Thakur, Reappraisal of thermochemical radii for complex ions, J. Chem. Educ., 56(9) (1979) 576-577. doi:10.1021/ed056p576.

MANAS Journal of Engineering
ISSN 1694-7398 | e-ISSN 1694-7398

*Volume 10, Issue 1, (2022) Pages 105-109*
*https://doi.org/10.51354/mjen. 1097668*

# Efficiency analysis of BLDC motor for variable magnetic field

Yıldırım Özüpak

[1], yildirimozupak@gmail.com, ORCID: 0000-0001-8461-8702

**ABSTRACT**

With the developing technology, direct current motors have been widely used in industrial applications. The limited use of brushed models in some areas has made Brushless Direct Current Motors stand out. In this paper, the design and analysis of an efficient, high power density, brushless direct current motor (BLDC) for use in electric vehicles is carried out. In this direction, studies have been carried out to reduce the reverse induced voltage, which is the biggest problem of electric motors in the electric vehicle sector. Analyzes were carried out with ANSYS subprograms, which realized a Finite Element Method (FEM) based solution to change the nominal values of the BLDC motor by changing the distance between the rotor and the stator. According to the results of the analysis, it was concluded that the method used in the study can also be used in high speed applications of brushless direct current motors.

**ARTICLE INFO**

***Research article***

*Received: 2.04.2022*
*Accepted: 10.06.2022*

***Keywords:***
*BLDC*
*efficiency*
*FEM*

*corresponding author

## 1 Introduction

Direct Current (DC) motors are widely used in industrial applications. The limited use of brushed models in some areas has brought Brushless Direct Current Motors (BLDC) to the fore. The constant need for maintenance of brushed type motors creates a disadvantage in variable conditions and in areas that are used continuously. For this reason, brushless DC motors have a wide range of uses. Brushless DC motors stand out with their high performance values. Brushless DC motors with outer rotor type are used in applications that require high torque and inertia. These types of motors are used in many areas such as vehicle wiper motors, automatic windows, robotics, generators, electric vehicles, unmanned aerial vehicles, and the white goods sector. Although there are various disadvantages such as motor protection and resistance to vibrations in applications with outer rotor, they do not require any transmission organ because they provide direct drive, they are preferred in applications that require higher efficiency than other types of motors (especially in electric vehicles). Apart from this, the motor drivers used for brushless direct current motors have a more complex structure compared to other motors. Due to the high torque values of brushless DC motors with outer rotor, they can be used especially in electric vehicles.

In this sector, which is in the process of development worldwide, various competitions are held in various countries in order to raise awareness about electric vehicles. The increase in interest in these competitions, which are mostly university-participated, paved the way for the organization of these races in every country. Improvements are being made in electric motors. In such motor applications, the load against the system creates an opposite force depending on the distance between the rotor and the stator. Optimization studies on this radial gap have increased the efficiency [1]. Reducing torque ripple in permanent magnet motors significantly affects efficiency [3-5]. In motors, the voltage induced by the rotation of the rotor in idling state adversely affects the efficiency. This induced voltage is an important factor in motor design. Figure 1 shows the rate-dependent variation of this induced voltage [6-9]

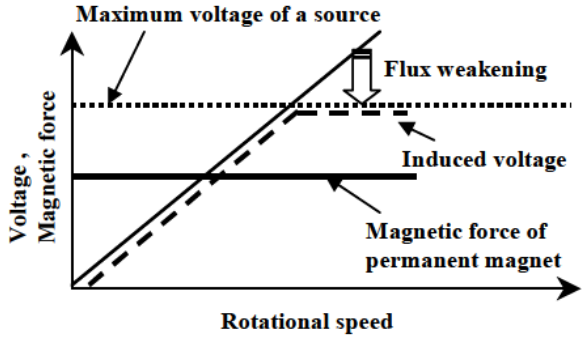


**Figure 1.** *Voltage regulation at variable-speed using flux-weakening control for a conventional permanent magnet motor [6].*

Today, there are various replaceable magnetic field applications in permanent magnet motors. In these applications, in order to reduce the reverse induced voltage, magnetic coercive force is created with different types of

magnets on the permanent magnets of the motor. Figure 2 shows the configuration of the machine created in this way.

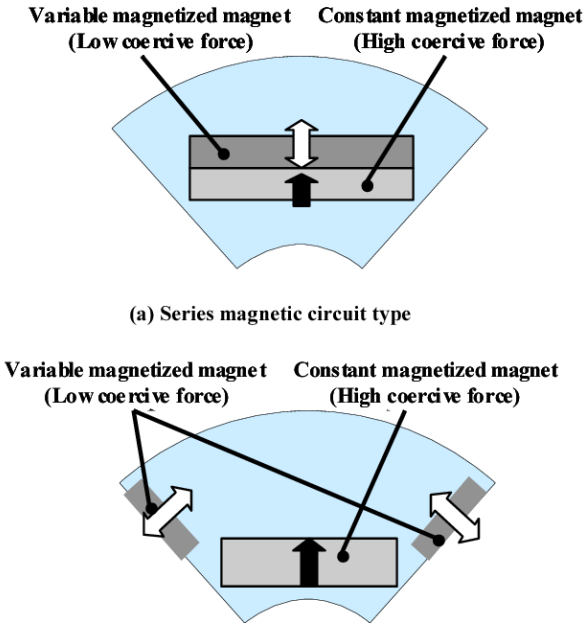


**Figure 2.** *Configuration of the magnetically forced motor*

In the mentioned application, four magnets with low coercive force, that is, four magnets with high coercive force, whose magnetization amount varies according to the magnetic field force it is exposed to, were used at the corner points. It is desired to create a forcing magnetic field force on permanent magnets with magnets with low coercive force. Applied for machines with internal rotor. This practice has some negative effects. The stator flux density was adversely affected in regions with low coercive magnets. This reduces high motor torque and causes flux loss. As a result, these triggered values increase the speed of the machine, but affect the efficiency negatively.

In this study, different from the application mentioned above, in BLDC motors, a variable magnetic field application has been made depending on the distance between the stator and the rotor. As a result, it is aimed to reduce the reverse induction and to make the maximum velocity threshold changeable.

## 2 Methods and materials

### *2.1. General Structure and Model of BLDC Motor*

As a general structure, position sensors are used in brushless direct current motor to be driven according to the state variables. The basic features of the machine are shown in Table 1.

**Table 1.** *The basic features of the machine*

| Parameter | Value |
|---|---|
| Rated Voltage | 134 V |
| Rated Output Power | 15 W |
| Rated Speed | 187.5 rpm |
| Number of Pole | 16 |
| Rotor Position | Outer |
| Rotor Length | 26 mm |
| Number of Slots | 12 |
| Operating Temperature | 75 ℃ |

The modeling of the machine used was carried out in the RMxprt design module of the ANSYS Maxwell program. Complete electrical and mechanical modeling of the motor has been applied. Modeling as close to reality as possible was carried out, and the graphics and values used in the next section were made according to this modeling. The mentioned machine model is shown in Figure 3.

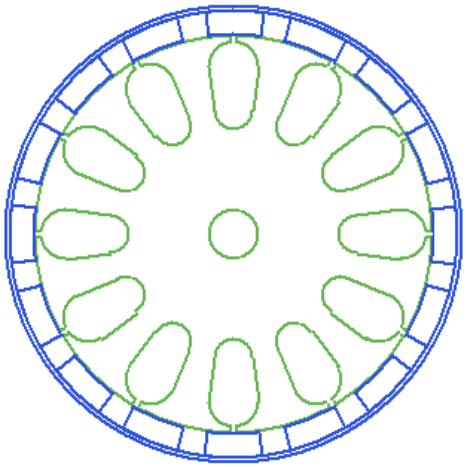

**Figure 3.** *Modeled brushless DC motor*.

In the mentioned motor, a magnet type called superficially inclined diameter magnetized magnet is used. The need for hard magnetic materials has brought developments in this field.

### *2.2. Exchangeable magnetic field definition*

Brushless DC motor with Switchable Magnetic Field, which will be applied in prototype models designed for electric vehicle races, will provide a purpose to increase the speed threshold of the applied vehicle. In the study, it is aimed to reduce the back electromotive force that will occur in the armature part depending on the vehicle rotor rotation speed in cases where the efficiency of the vehicle is not a priority. The change of magnetic flux applied by hard magnetic materials at the peak value of the efficiency-speed curve to be determined will be realized by means of movable connectors. Thus, it is aimed to reduce the back electromotive force (back-EMF) on the stator [10-11].

*2.3. Magnetic effect calculation*

The back electromotive force created by the magnets is equal to the voltage induced in the stator tooth due to rotor motion and can be calculated as follows [5].

$$e_T = \frac{\partial \Phi}{\partial t} = \omega_m \frac{\partial \Phi}{\partial \xi} \quad (1)$$

Where, Φ is the flux due to the magnet when there is no current flowing in the stator, $e_T$ is the induced voltage, $\omega_m$ is the angular velocity, N is the number of turns, t is the time index, and $\xi$ is the rotor position. The equation of the flux to be obtained depending on the flux density is as follows.

$$\Phi = NRL \int_{\theta_2}^{\theta_1} B(\theta) d\theta \quad (2)$$

Where, B is the flux density generated by the magnets on the active tooth. R is the axial stator radius, L is the depth in the axial direction, $N_s$ is the number of slots, $\theta_1$ and $\theta_2$ are expressed as the transition positions of a pole on a slot. Using Equation 1 and Equation 2, the following expression can be reached;

$$e_T = N\omega_m RL \frac{\partial}{\partial \xi} \int_{\theta_2}^{\theta_1} B(\theta) d\theta \quad (3)$$

$V=\omega_m R$ indicates the linear speed of the motor. $B_1$ and $B_2$ are opposite magnetic flux densities of magnets. If $\xi$ and θ values are equal or there is a constant difference, the induced voltage is shown as in Equation 4;

$$e_T = NV(B_2 - B_1)L \quad (4)$$

*2.4. Permanent magnet distance effect*

By creating a special design, Neodymium N50M class magnets are used in order to provide the high torque requirement at the start of the motor and the properties of these magnets are as given in Table 2.

**Table 2.** *Properties of these magnets*

| Material Type | Residual Flux Density (Br) | Coercive Force (Hc) | Intrinsic Coercive Force (Hci) | Max.Energy Product (BH)max |
|---|---|---|---|---|
| N48 | 13.8-14.2 KGs | >11.0 KOe | >12 KOe | 45-48 MGOe |

The magnetic density provided by hard magnetic materials changes according to the distance. A superficially curved diameter magnetized magnet type is used in the brushless direct current motor that is aimed to be applied. The calculation of the change with respect to this magnet is given in the following equation [2].

$$B_{(z)} = \frac{\mu_0 M}{\pi}\left[arct\frac{ab}{(z-c)\sqrt{a^2+b^2+(z-c)^2}} - arct\frac{ab}{(z+c)\sqrt{a^2+b^2+(z-c)^2}}\right] \quad (5)$$

Magnetic field calculations for any point in space are as shown in the equations below [2].

$$B_x(x,y,z) = \frac{\mu_0 M}{\pi}\ln\frac{F_2(-x,y,-z)F_2(x,y,z)}{F_2(x,y,-z)F_2(-x,y,z)} \quad (6)$$

$$B_y(x,y,z) = \frac{\mu_0 M}{\pi}\ln\frac{F_2(-y,x,-z)F_2(x,y,z)}{F_2(y,x,-z)F_2(-y,x,z)} \quad (7)$$

$$B_y(x,y,z) = \frac{\mu_0 M}{\pi}[F_1(-x,y,z) + F_1(-x,y,-z) + F_1(-x,-y,z) + F_1(-x,-y,-z) + F_1(x,y,z) + F_1(x,y,-z) + F_1(x,-y,z) + F_1(x,-y,-z)] \quad (8)$$

$$F_1(x,y,z) = arct\frac{(x+a)(y+b)}{(z+c)\sqrt{(x+a)^2+(y+b)^2+(z+c)^2}} \quad (9)$$

$$F_2(x,y,z) = \frac{\sqrt{(x+a)^2+(y-b)^2+(z+c)^2}+b-y}{\sqrt{(x+a)^2+(y+b)^2+(z+c)^2}-b-y} \quad (10)$$

In Figure 4, the space of the magnet, whose calculations are given above, is shown. μ0 represents the permeability of the air, the coordinate axes of the X,Y,Z three-dimensional space, r the center of the magnet, r' the magnetic flux density that will fall on it, the point to be calculated, x, y, z the distance from the magnet center of the point to be calculated in its own coordinates. 2a, 2b, 2c show the dimensions of the magnet [2].

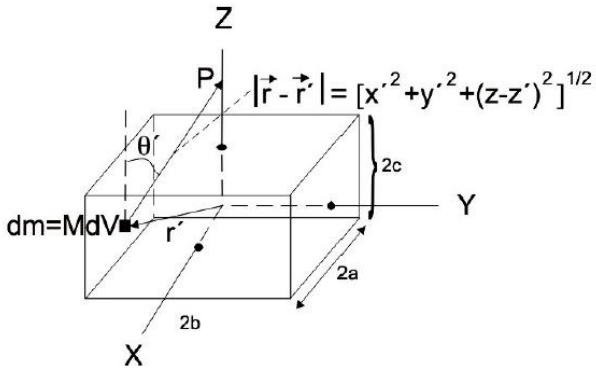


**Figure 4.** *Block magnet area calculation scheme.*

## 3. Results and discussion

The infrastructure of the mobile system to be applied to the BLDCM is currently being worked on and the majority of it is mechanical systems. In this study, the results to be obtained in the case of the physical application of the aforementioned

system are simulated. The basic structural movements that will enable the formation of the system have been determined gradually. In these stages, it is planned to separate the rotor from the stator part by a mechanical design. The remaining dimensions of the rotor in the stator according to the steps to be provided by the designed system.

There is a section called the air gap between the stator and the rotor. While designing the motor, the magnetic flux density affected by this field should be considered. This gap affects the induced voltage and the current generated on the coils. The air gap of the system to be applied in the machine changes axially at each stage. In the previous section, the calculation of the magnetic flux created by the distance on the coils is shown. In the initial state of the modeled brushless direct current motor, this air gap was determined as 2 mm and the air gap of the modeled motor is shown in Figure 5.

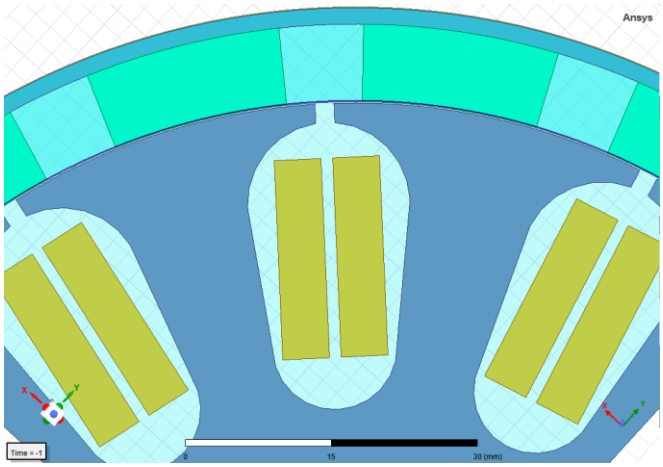


**Figure 5.** *The air gap of the machine modeled with ANSYS Maxwell 2D Design.*

## 4. Simulation results

Assuming that the movable rotor system of the modeled brushless direct current motor is applied, necessary analyzes are made in the analysis section of the ANSYS Maxwell program. According to the first case, the peak and maximum velocity value of the yield curve were determined and shown in Figure 6.

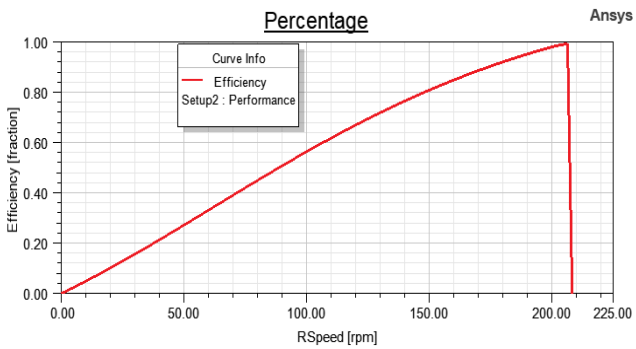


**Figure 6**. *Yield-Speed graph in the first case (Rotor length =26 mm).*

Accordingly, it is expected that the speed will increase with the next step change after the transition points are the points where the motor efficiency is maximum. It is thought that the rotor position should change step. With this approach, it was determined that the transition points to be made between the stages should be as shown in Figures 7-9.

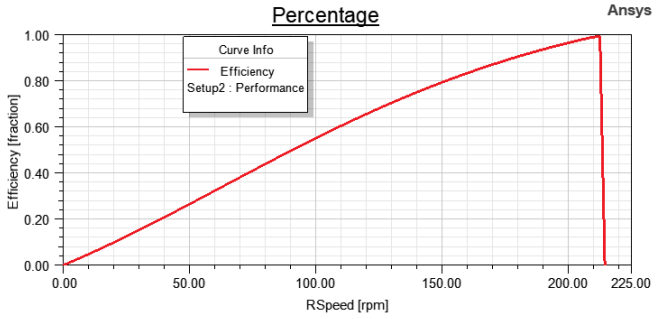


**Figure 7.** *Efficiency-Speed curves for rotor length=30 mm position in the modeled system.*

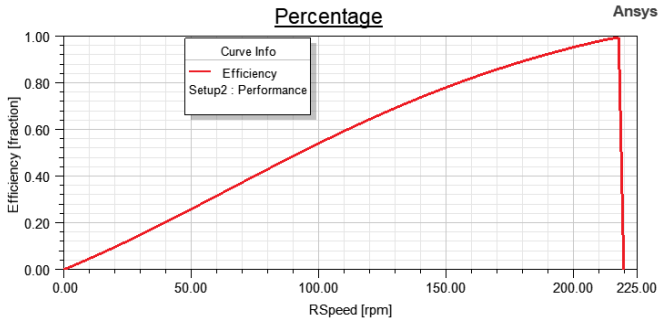


**Figure 8.** *Efficiency-Speed curves for rotor length=34 mm position in the modeled system.*

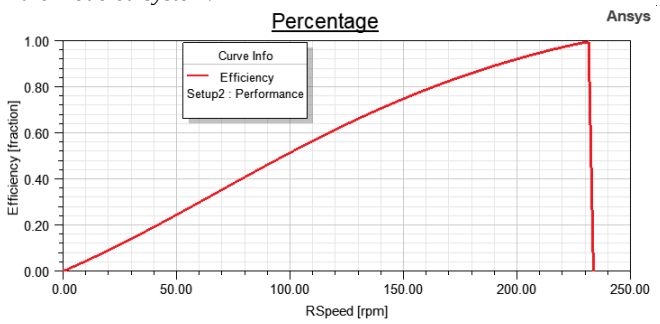


**Figure 9**. *Efficiency-Speed curves for rotor length=38 mm position in the modeled system.*

The values obtained when the rotor length is increased gradually while keeping the stator length constant are presented in Table 4.

**Table 4.** *Efficiency-speed values obtained depending on the rotor length*

| Rotor Length (mm) | Speed (rpm) | Efficiency (%) |
|---|---|---|
| 26 | 206.8 | 98.3 |
| 30 | 218.1 | 98.1 |
| 34 | 223.2 | 97.6 |
| 38 | 235.1 | 98.4 |

## 5. Conclusion

Motor designers should first determine the area where the brushless DC motor will be used and the main expectation before starting the design work. While designing the machine, the limitations of the area to be used, ease of production and cost expectations should also be considered. Performance expectations such as speed, output power and efficiency may also vary depending on the area to be used. In addition, since situations such as variable speed request may occur during operation, it may be important to examine the machine performance in the entire operating range according to the number of revolutions of the machine. At this point, the design of how the designer will use his machine is important. In this study, the application of the changeable magnetic field, which is created as a result of physical motion, is examined. An machine with different characteristics has emerged at each stage. This has shown that a variable speed motor can be achieved by applying a variable magnetic field system. As a result, the switchable magnetic field system, which is considered to be applied, has revealed that it can be used in race organizations where the speed factor is important or in passenger and commercial electric vehicles.

## References

[1]. Ajith H. Wiyenayake, J.M. Bailey, Patrick J. McCleerDesing, Optimization of an Axial Gap Permanent Magnet Brushless DC Motor For Electric Vehicle Applications. IEEE. (1995). doi: 10.1109/IAS.1995.530366.

[2]. Camacho J. M., V. Sosaa. Alternative method to calculate the magnetic field of permanent magnets with azimuthal symmetry. Revista Mexicana de Fisica E 59. (2013) Universidad Autonoma de Yucat ´ an.

[3]. Hanselman Dr. Duane. Brushless Permanent Magnet Motor Design(2 Edition). Magna Physics Publishing. (2003), ISBN: 1-881855-15-5. USA: Lebanon.

[4]. Hanselman, D, Minimum torque ripple, maximum efficiency excitation of brushless permanent magnet motors. IEEE .(1994). doi: 10.1109/41.293899.

[5]. Hendershot Jr., T.J.E Miller, Desingn of Brushless Permenant-Magnet Motors. Magna Physics Publishing. (1994). ISBN: 1-881855-03-1. USA: Hillsboro.

[6]. Kazuto Sakai, Kazuaki Yuki, Yutaka Hashiba, Norio Takahashi, Kazuya Yasui.(2009). Principle of the Variable-Magnetic-Force Memory Motor. IEEE. doi: 10.1109/ICEMS.2009.5382812.

[7]. Yedemale P., (2003), Brushless DC (BLDC) Motor Fundamentals(App. Note: DS00885A).USA:Microchip Technology Inc.

[8]. Lequesne B., Automotive Electrification: The Nonhybrid Story, IEEE Transactions on Transportation Electrification, 2015, 1(1), 40-53.

[9]. Chaudhari, A., Mahajan, G., Implementation of BLDC Motor Based Water Pump for Automotive Vehicle, The International Journal of Engineering and Science, 4(6), (2015), 34-41.

[10]. Ooshima, M., Takeuchi, C., Magnetic suspension performance of a bearingless brushless DC motor for small liquid pumps, 2009 International Conference on Electrical Machines and Systems, (2010), 1-4.

[11]. Dusane, P., Simulation of a Brushless DC Motor in ANSYS – Maxwell 3D, Master Thesis, Czech Technical University and Department of Power Engineering, (2016).

MANAS Journal of Engineering
ISSN 1694-7398 | e-ISSN 1694-7398

*Volume 10 (Issue 1) (2022) Pages 110-115*
*https://doi.org/10.51354/mjen.937100*

# Generalized fermi derivative on the hypersurfaces

**Ayşenur Uçar**[1], **Fatma Karakuş**[2]

[1] Dept. of Mechanical Engineering,Dogus University, Istanbul, Turkey, aucar@dogus.edu.tr, ORCID: 0000-0002-7498-6752, [2]Dept. of Mathematics, Sinop University, Sinop, Turkey, fkarakus@sinop.edu.tr, ORCID: 0000-0003-0379-4232

**ABSTRACT**

In this paper, generalized Fermi derivative, generalized Fermi parallelism, and generalized non-rotating frame concepts are given along any curve on any hypersurface in $E^{n+1}$ Euclidean space. The generalized Fermi derivative of a vector field and being generalized non-rotating conditions are analyzed along the curve on the surface in Euclidean 3-space. Then a correlation is found between generalized Fermi derivative, Fermi derivative, and Levi-Civita derivative in $E^3$. Then we examine generalized Fermi parallel vector fields and conditions of being generalized non-rotating frame with the tensor field in $E^4$. Generalizations have been made in $E^n$.

**ARTICLE INFO**

***Research article***

*Received*: 14.05.2021
*Accepted*: 07.06.2022

***Keywords***: Generalized Fermi derivative, generalized Fermi parallelism, generalized non-rotating frame, Frenet frame, tangent space

**Corresponding author*

## 1. Introduction

To interpret the universe, it needs to be observed. An observer needs an appropriate frame construction for the definition of its location and its geometric analysis at a proper time. Rest spaces of an observer $\gamma$ are transported through Levi-Civita parallelism when $\gamma$ is freely falling, so a fix direction has a null covariant derivative. If $\gamma$ is not freely falling, the rest space also is not transported by Levi-Civita parallelism anymore. So in order to define "constant" directions a new connection was defined for accelerated observers [5, 7, 15, 19, 20]. This connection which is called Fermi-Walker connection is an isometry between tangent spaces along the curve [5, 7, 9, 13]. But the Fermi-Walker connection is only relevant for accelerating observers. Also this connection and Levi-Civita connection coincide along $\gamma$ if and only if $\gamma$ is geodesic. Starting from this point, many scientists have given extensions for the Fermi-Walker transport with several physical motivations [8, 11]. Then in [13] and [14] Pripoae enlarged the context by defining a rich class of generalized Fermi-Walker connections which are relevant for both accelerating and non-accelerating observers. According to the new connection, $\gamma$ must be able to choose between several parallel transports and not resume itself to the Fermi-Walker one. In [17], we have shown the conditions of generalized Fermi-Walker parallelism along any curve and generalized non-rotating frame in Euclidean 3-space.

In this study, we enlarge the concepts of Fermi derivative to generalized Fermi derivative by using the definition of generalized Fermi-Walker derivative along any curve which was given by Pripoae [13, 14]. Generalized Fermi derivative and generalized Fermi parallelism concepts are considered for Frenet and Darboux frames along curves. Also the generalized non-rotating frame is defined by using the definition of non-rotating frame and the conditions of being generalized non-rotating frame are analyzed along the curve in Euclidean 3-space. Similarly we investigate generalized Fermi-derivative along any curve on hypersurface in $E^4$ and generalized Fermi parallelism conditions has been obtained. Generalizations have been made in Euclidean $n-$space.

## 2. Preliminaries

We now recall some basic concepts of Fermi derivative and give the definition generalized Fermi derivative.

Definition 2.1. Let $M$ be a n-hypersurface, $\alpha : I \to M$ be a unit speed curve and $X$ be a vector field, which is tangent to $M$ along $\alpha$ and also orthogonal to $\alpha$ everywhere. $\frac{\delta X}{\delta s}$ Fermi derivative is defined as

$$\frac{\delta X}{\delta s} = \nabla_T X - \langle \nabla_T X, T \rangle T.$$

Here, $\nabla$ is the Levi-Civita connection of $M$ [2, 10].

Definition 2.2. Let $M$ be a n-hypersurface, $\alpha : I \to M$ be a unit speed curve and $X$ be a vector field, which is tangent to $M$ along $\alpha$ and also orthogonal to $\alpha$ everywhere. If the Fermi derivative of the vector field $X$ vanishes, i.e., $\frac{\delta X}{\delta s} = 0$, then the vector field $X$ is called Fermi parallel along the curve [2, 10].

Definition 2.3. Let $\alpha : I \to M$ be unit-speed curve in a n-hypersurface and $U, V, W$ are orthonormal vectors along $\alpha$. If the Fermi derivative of the vector fields vanish, then $\{U, V, W\}$ is called non-rotating frame [2, 10].

We can give the definition below by using definition 2.1. and definition of generalized Fermi-Walker derivative by Pripoae [13, 14].

Definition 2.4. Let $M$ be a n-hypersurface, $\alpha : I \to M$ be a unit speed curve and $X$ be a vector field, which is tangent to $M$ along $\alpha$ and also orthogonal to $\alpha$ everywhere. Then there exists a unique $(1, 1)$ −tensor field $A$ along the curve such that

$$\frac{\widetilde{\delta} X}{\widetilde{\delta} s} = \frac{\delta X}{\delta s} + A(X) \tag{1}$$

and

$$\langle A(Z), T \rangle = 0, Z \in \chi^{\perp}(M). \tag{2}$$

Thus, the formulaes 1 and 2 are defined as generalized Fermi derivative. Here, $\frac{\delta X}{\delta s}$ is the Fermi derivative of the vector field $X$ [18].

Definition 2.5. Let $M$ be a n-hypersurface, $\alpha : I \to M$ be a unit speed curve and $X$ be a vector field, which is tangent to $M$ along $\alpha$ and also orthogonal to $\alpha$ everywhere. If the generalized Fermi derivative of vector field $X$ vanishes, then the vector field $X$ is called generalized Fermi parallel along the curve [18].

Definition 2.6. Let $\alpha : I \to M$ be unit-speed curve in a n-hypersurface and $U, V, W$ are orthonormal vectors along $\alpha$. If the generalized Fermi derivative of the vector fields vanish, then $\{U, V, W\}$ is called non-rotating frame with the generalized Fermi terms or shortly generalized non-rotating frame [18].

In the light of these concepts let us continue our study the main subject of the paper.

## 3. Generalized Fermi Derivative on the Surface

In this section, we investigate generalized Fermi derivative along any unit speed curve on the surface in $E^3$. Let $\alpha : I \subset \mathbb{R} \to M$ be unit-speed curve and $\{T, Y, n\}$ be the Darboux frame of the surface, and $X$ is a vector field along the curve $\alpha$ with the corresponding connection $\nabla$. According to Darboux frame we will give a lemma of generalized Fermi derivative and investigate the vector field $X$, whether it is a generalized Fermi parallel vector field along the curve or not.

Lemma 3.1. Let $M$ be a surface in $E^3$, $\alpha : I \to M$ be a unit speed curve and $X$ be a vector field, which is tangent to $M$ along $\alpha$ and also orthogonal to $\alpha$ everywhere, $A$ be $(1, 1)$ −tensor field along $\alpha$. Generalized Fermi derivative of the vector field $X$ can be expressed as

$$\frac{\widetilde{\delta} X}{\widetilde{\delta} s} = \frac{d(\ln \lambda(s))}{ds} X + A(X).$$

**Proof** In [10] Karakuş and Yaylı obtained the Fermi derivative as

$$\frac{\delta X}{\delta s} = \frac{d(\ln \lambda(s))}{ds} X.$$

Then from the definition of the generalized Fermi derivative, we obtain the result. □

Theorem 3.2. Let $M$ be any surface in $E^3$ and $\alpha : I \to M$ be a unit speed curve. $X = \lambda(s) Y$ vector field along the curve, is generalized Fermi parallel if and only if

$$A(X) = -\frac{d(\ln \lambda(s))}{ds} X.$$

Here $\lambda(s)$ is continuously differentiable function of a real parameter $s$.

**Proof** In [10], the Fermi derivative of $X = \lambda(s) Y$ was obtained as

$$\frac{\delta X}{\delta s} = \frac{d(\ln \lambda(s))}{ds} X.$$

Then from the equality $\frac{\widetilde{\delta} X}{\widetilde{\delta} s} = \frac{\delta X}{\delta s} + A(X)$,

$$A(X) = -\frac{d(\ln \lambda(s))}{ds} X$$

is obtained. □

Now, by using Theorem 3, we will give more specifical vector field with constants.

Corollary 3.3. If $\lambda$ is constant, the Fermi derivative of the vector field $X = \lambda Y$ coincides with the generalized Fermi derivative of $X$.

Corollary 3.4. Let $M$ be any surface in $E^3$ and $\alpha : I \to M$ be a unit speed curve. If $\alpha$ is an asymptotic curve, the normal vector field of the curve $N$ is generalized Fermi parallel along the curve. Moreover, if $\alpha$ is a geodesic curve,

the binormal vector field of the curve $B$ is generalized Fermi parallel along the curve.

**Proof** Let $\alpha$ be an asymptotic curve, since the normal curvature of the curve $\kappa_n = 0$,

$$Y = N$$

and then

$$\frac{\widetilde{\delta}N}{\widetilde{\delta}s} = \frac{\widetilde{\delta}Y}{\widetilde{\delta}s} = 0$$

is obtained. On the other hand, let $\alpha$ be a geodesic curve. Since the geodesic curvature of the curve $\kappa_g = 0$,

$$Y = B$$

and

$$\frac{\widetilde{\delta}B}{\widetilde{\delta}s} = \frac{\widetilde{\delta}Y}{\widetilde{\delta}s} = 0$$

is obtained which gives the result. □

Corollary 3.5. Let $M$ be any surface in $E^3$ and $\alpha : I \to M$ be a unit speed geodesic curve. The vector field $X = \lambda Y$ is Levi-Civita parallel along the curve if and only if the vector field is generalized Fermi parallel, also Fermi parallel, along the curve. Here, $\lambda$ is constant.

**Proof** Let $X = \lambda Y$ be Levi-Civita parallel along the curve. In that case the generalized Fermi derivative of $X$ is

$$\frac{\widetilde{\delta}X}{\widetilde{\delta}s} = A(X).$$

Since $\lambda$ is constant,

$$A(X) = 0$$

is obtained.

On the other hand, Let $X$ be generalized Fermi parallel along the curve. The Levi-Civita derivative of $X$ is

$$\nabla_T X = -\kappa_g \lambda T,$$

since $\alpha$ is a geodesic curve

$$\nabla_T X = 0$$

is obtained. □

Theorem 3.6. Let $\lambda$ be a constant and $A$, $(1,1)$ −tensor field be $A(X) = t_r(X \wedge T)$. $X$ vector field is generalized Fermi parallel along the curve if and only if curve $\alpha$ is curvature of line.

**Proof** Let $X$ vector field be generalized Fermi parallel along the curve. By using the Lemma 3.1 we obtain

$$\frac{\widetilde{\delta}X}{\widetilde{\delta}s} = \frac{d(\ln\lambda(s))}{ds}X + t_r(X \wedge T).$$

Thus the generalized Fermi derivative along the curve of $X$ vector field is

$$\frac{\widetilde{\delta}X}{\widetilde{\delta}s} = -t_r \lambda n.$$

Since $X$ is generalized Fermi parallel along the curve

$$t_r = 0.$$

On the other hand, let the curve $\alpha$ be a curvature of line. Since $\lambda$ is a constant

$$\frac{\widetilde{\delta}X}{\widetilde{\delta}s} = 0.$$

□

## 4. Generalized Fermi Derivative on the Hypersurface

In this section we will get any curve on the hypersurface in $E^4$. We will analyze generalized Fermi derivative along any curve on the hypersurface. Then we will examine generalized Fermi parallelism of a vector field along the curve by using Frenet frame and also we will investigate which vector fields are generalized parallel along the curve on the hypersurface in $E^4$.

Lemma 4.1. Let $M$ be a hypersurface in $E^4$, $\alpha : I \to M$ be a unit speed curve and $X$ be a vector field, which is tangent to $M$ along $\alpha$ and also orthogonal to $\alpha$ everywhere, $A$ be $(1,1)$ −tensor field along $\alpha$. The generalized Fermi derivative $\frac{\widetilde{\delta}X}{\delta s}$ can be expressed as

$$\frac{\widetilde{\delta}X}{\widetilde{\delta}s} = \frac{dX}{ds} - \left\langle \frac{dX}{ds}, n \right\rangle n - \left\langle \frac{dX}{ds}, T \right\rangle T + A(X).$$

**Proof** In [10], Karakuş and Yaylı obtained the Fermi derivative as

$$\frac{\delta X}{\delta s} = \frac{dX}{ds} - \left\langle \frac{dX}{ds}, n \right\rangle n - \left\langle \frac{dX}{ds}, T \right\rangle T$$

by using Levi-civita derivative. Thus from the definition of the generalized Fermi derivative, we obtain the result.

□

Theorem 4.2. Let $M$ be a hypersurface in $E^4$, $\alpha : I \to M$ be a unit speed curve. $X = \lambda_1 N + \lambda_2 B$ vector field along the curve, is generalized Fermi parallel if and only if

$$A(X) = -\left[\left(\frac{d\lambda_1}{ds} - \tau\lambda_2\right)N + \left(\frac{d\lambda_2}{ds} + \tau\lambda_1\right)B\right].$$

Here $\lambda_1, \lambda_2, \lambda_3$ are continuously differentiable functions of a real parameter $s$ and $\{T, N, B\}$ is Frenet frame along the curve $\alpha$.

**Proof** In [10], the Fermi derivative of $X = \lambda_1 N + \lambda_2 B$ was obtained as

$$\frac{\delta X}{\delta s} = \left[\left(\frac{d\lambda_1}{ds} - \tau\lambda_2\right) N + \left(\frac{d\lambda_2}{ds} + \tau\lambda_1\right) B\right]$$

by using $\{T, N, B\}$ . Thus by using (1)

$$A(X) = -\left[\left(\frac{d\lambda_1}{ds} - \tau\lambda_2\right) N + \left(\frac{d\lambda_2}{ds} + \tau\lambda_1\right) B\right]$$

is obtained. □

In Theorem 4.2 we gave a general choise of $(1,1)-$ tensor field. Now, let us find it with more specific way.

Corollary 4.3. Let $M$ be any hypersurface in $E^4$, $\alpha : I \to M$ be unit-speed on any curve. $X = \lambda_1 N + \lambda_2 B$ vector field along the curve, is generalized Fermi parallel if and only if

$$A(X) = \tau(X \wedge T).$$

Here $\lambda_1, \lambda_2$ are constants and $\tau$ is torsion of the curve.

**Proof** By using Lemma 4.1, we get

$$\frac{\widetilde{\delta} X}{\widetilde{\delta} s} = -\lambda_2\tau N + \lambda_1\tau B + A(X).$$

Let $\frac{\widetilde{\delta} X}{\widetilde{\delta} s} = 0$. Then

$$\begin{aligned} A(X) &= \tau(\lambda_2 N - \lambda_1 B), \\ A(X) &= \tau(\lambda_2 (B \wedge T) + \lambda_1 (N \wedge T)), \\ A(X) &= \tau(X \wedge T) \end{aligned}$$

is obtained.

On the other hand let $(1,1)-$ tensor field be $A(X) = \tau(X \wedge T)$ . From the generalized Fermi derivative

$$\begin{aligned} \frac{\widetilde{\delta} X}{\widetilde{\delta} s} &= -\lambda_2\tau N + \lambda_1\tau B + A(X), \\ \frac{\widetilde{\delta} X}{\widetilde{\delta} s} &= -\lambda_2\tau N + \lambda_1\tau B + \tau(X \wedge T), \\ \frac{\widetilde{\delta} X}{\widetilde{\delta} s} &= 0 \end{aligned}$$

is obtained which gives the result. □

So, if we choose $(1,1)-$ tensor field as $A(X) = \tau(X \wedge T)$, we can give some results about the vector field.

Corollary 4.4. Let $M$ be any hypersurface in $E^4$, $\alpha : I \to M$ be unit-speed on any curve. If $(1,1)-$ tensor field is $A(X) = t_r(X \wedge T)$, the vector fields $\{N, B\}$ are generalized Fermi parallel along the curve $\alpha$. Here $N$ is the normal vector field and $B$ is the binormal vector field.

**Proof** From the Corollary 4 the generalized Fermi derivative of the vector field $N$ is

$$\begin{aligned} \frac{\widetilde{\delta} N}{\widetilde{\delta} s} &= \tau B + A(N), \\ \frac{\widetilde{\delta} N}{\widetilde{\delta} s} &= \tau B + \tau(N \wedge T), \\ \frac{\widetilde{\delta} N}{\widetilde{\delta} s} &= 0. \end{aligned}$$

Similarly it can be shown that the vector field $B$ is also generalized Fermi parallel along the curve. □

## 5. Generalized Fermi Derivative in Euclidean $n-$Space

In this section, we investigate generalized Fermi derivative along the curve in $M$ which is a Riemannian manifold in $E^n$ $(n \geq 4)$. We examine $X$ generalized Fermi parallelism of any vector field along the curve $\alpha : I \to M$ which is a unit speed W-curve in $M$ by considering the tangent space $\{V_1, V_2, ..., V_{n-1}\}$ of $M$ and the Levi-Civita connection $\nabla$ of $M$.

Theorem 5.1. Let $X = \sum_{i=1}^{n-2} \lambda_i V_{i+1}$ be a vector field along the W-curve $\alpha$. $X$ is generalized Fermi parallel along the curve if and only if

$$\begin{aligned} A(X) = -\Bigg[&\left(\frac{d\lambda_1}{ds} - k_2\lambda_2\right) V_2 \\ &+ \sum_{i=3}^{n-2} \left(\frac{d\lambda_{i-1}}{ds} + k_{i-1}\lambda_{i-2} - k_i\lambda_i\right) V_i \\ &+ \left(\frac{d\lambda_{n-2}}{ds} + k_{n-2}\lambda_{n-3}\right) V_{n-1}. \end{aligned}$$

Here $\lambda_i$ $(1 \leq i \leq n-2)$ are continuously differentiable functions of a real parameter $s$ and $k_i$ are curvatures of the curve $\alpha$ according to the Levi-Civita connection..

**Proof** In [9] the Fermi derivative of $X = \sum_{i=1}^{n-2} \lambda_i V_{i+1}$ was obtained as

$$\begin{aligned} \frac{\delta X}{\delta s} = &\left(\frac{d\lambda_1}{ds} - k_2\lambda_2\right) V_2 + \sum_{i=3}^{n-2} \left(\frac{d\lambda_{i-1}}{ds} + k_{i-1}\lambda_{i-2} - k_i\lambda_i\right) V_i \\ &+ \left(\frac{d\lambda_{n-2}}{ds} + k_{n-2}\lambda_{n-3}\right) V_{n-1}, \end{aligned}$$

Here, if $3 > n-2$, then $\sum_{i=3}^{n-2} \left(\frac{d\lambda_{i-1}}{ds} + k_{i-1}\lambda_{i-2} - k_i\lambda_i\right) V_i = 0$.

Let $X$ be generalized Fermi parallel. Then from the definition of generalized Fermi derivative

$$\frac{\widetilde{\delta} X}{\widetilde{\delta} s} = 0$$

is obtained. The rest is obvious. □

If we take $n = 4$ in Theorem 5.1 we get Theorem 4.2.

Corollary 5.2. Let $(1,1)-$ tensor field be

$$A(X) = -\left[\left(\frac{d\lambda_1}{ds} - k_2\lambda_2\right)V_2 + \sum_{i=3}^{n-2}\left(\frac{d\lambda_{i-1}}{ds} + k_{i-1}\lambda_{i-2} - k_i\lambda_i\right)V_i + \left(\frac{d\lambda_{n-2}}{ds} + k_{n-2}\lambda_{n-3}\right)V_{n-1}.\right.$$

$\{V_2, V_3, ..., V_{n-1}\}$ is generalized non-rotating along the curve.

**Proof** Let $(1,1)-$ tensor field be

$$A(X) = -\left[\left(\frac{d\lambda_1}{ds} - k_2\lambda_2\right)V_2 + \sum_{i=3}^{n-2}\left(\frac{d\lambda_{i-1}}{ds} + k_{i-1}\lambda_{i-2} - k_i\lambda_i\right)V_i + \left(\frac{d\lambda_{n-2}}{ds} + k_{n-2}\lambda_{n-3}\right)V_{n-1}.\right.$$

Then

$$\begin{aligned}
\frac{\widetilde{\delta}V_2}{\widetilde{\delta}s} &= k_2V_3 + A(V_2), \\
\frac{\widetilde{\delta}V_i}{\widetilde{\delta}s} &= -k_{i-1}V_{i-1} + k_iV_{i+1} + A(V_i), \ 3 \le i \le n-2, \\
\frac{\widetilde{\delta}V_{n-1}}{\widetilde{\delta}s} &= -k_{n-2}V_{n-2} + A(V_{n-1})
\end{aligned}$$

are obtained. By considering $A(X)$,

$$\frac{\widetilde{\delta}V_i}{\widetilde{\delta}s} = 0$$

for all $2 \le i \le n-1$. □

## 6. Conclusions

In this paper, we have explained the concepts of generalized Fermi derivative, generalized Fermi parallelism, the generalized non-rotating frame along the curve in Euclidean space.

By recalling the concept of Fermi-Walker derivative, which is used for defining "constant" directions and shows us one strict method, that may contain lots of condition to have Fermi-Walker parallelism or non-rotating frame. For example, the condition of Femi-Walker parallelism depends on a solution that contains differential equation system which is not always easy to find a solution [9]. But the generalized case has more flexible way and depends on only one condition which contains choice of (1,1)-tensor field. Moreover, generalized Fermi-Walker derivative is more suitable than the Fermi-Walker one in the terms of the movement of the observer and qualifying conditions [13, 14]. Therefore it is important to analyse this concept.

From this point of view in [17], we analysed the generalized Fermi-Walker derivative and the conditions of being generalized non-rotating frame along any curve in Euclidean space. We have shown that generalized Fermi-Walker derivative has more options. The conditions of generalized Fermi-Walker parallelism and non-rotating frame along the curves weaker than the Fermi-Walker derivative. For example unlike the Fermi-Walker case, Frenet frame is generalized non-rotating frames along all types of curves.

In this study, we enlarged the definition of Fermi derivative to generalized Fermi derivative by using the concept of generalized Fermi-Walker derivative, which has defined by Pripoae [13, 14] before. And also we defined generalized non-rotating frame by using the concept of generalized Fermi derivative. Thus a derivative has obtained which is relevant for both accelerating and non-accelerating observers on the hypersurfaces.

By using these concepts, initially we got a curve on the surface in Euclidean 3-space. We have shown which tensor field is necessary for generalized Fermi parallel vector fields. We proved that if the curve is asymptotic curve, the normal vector field of the curve is generalized Fermi parallel along the curve. Also if the curve is geodesic, its binormal vector field is generalized Fermi parallel vector field along the curve. We have shown the conditions of coinciding Levi-Civita parallelism, Fermi paralellism and generalized Fermi parallelism.

Then we examined any curve on the hypersurface in Euclidean 4-space. We have shown the choise of the tensor field to establish whether the vector field is generalized Fermi parallel along the curve or not. We proved that the normal vector field and the binormal vector field of the curve are generalized Fermi parallel along the curve.

Finally, generalizations have been made in Euclidean n-space. We gave the conditions which are necessary in order that any vector field is Fermi parallel along the curve and the tangent space of the manifold is generalized non-rotating along the curve.

## References

[1] Balakrishnan R., "Space curves, anholonomy and nonlinearity," Pramana Journal of Physics., 64(4), 2005, 607-615.

[2] Benn I.M. and Tucker R.W., "Wave mechanics and inertial guidance," Bull. The American Physical Society, 39(6),

(1989), 1594-1601.

[3] Berry M.V., "Quantal phase factors accompanying adiabatic changes," Proc. R. Soc. London A 392, (1984).

[4] Dandoloff R., "Berrys phase and Fermi-Walker parallel transport," Elsevier Science Publishers, 139(1-2), (1989), 19-20.

[5] Fermi E., Atti Accad. Naz. Lincei Cl. Sci. Fiz. Mat. Nat., 31 (1922) 184-306.

[6] H. W. Guggenheimer, Differential Geometry. McGraw-Hill, New York, 1963.

[7] Hawking S.W. and Ellis G. F. R., The Large Scale Structure of Spacetime. Cambridge Univ. Press, 1973.

[8] Hehl F.W., Lemke J., and Mielke E.W., "Two lectures on Fermions and Gravity," Geometry and Theoretical Physics. J. Debrus and A.C. Hirshfeld (eds.), Springer Verlag, N.Y., (1991), 56- 140.

[9] Karakuş F. and Yaylı Y., "On the Fermi-Walker derivative and non-rotating frame," Int. Journal of Geometric Methods in Modern Physics, 9(8), (2012), 1250066(11 pp.).

[10] Karakuş F. and Yaylı Y., "The Fermi derivative in the hypersurfaces," Int. Journal of Geometric Methods in Modern Physics, 12, (2015), 1550002 (12 pp.).

[11] Manoff S., "Fermi derivative and Fermi-Walker transports over (Ln;g) spaces," Internat. J. Modern Phys. A, 13(25), (1998), 4289-4308.

[12] O'Neill B., Elementary Differential Geometry. Academic Press, New York, 1966.

[13] Pripoae G. T., "Generalized Fermi-Walker transport," LibertasMath., XIX, 1999, 65-69.

[14] Pripoae G. T., "Generalized Fermi-Walker parallelism induced by generalized Schouthen connections," in Proceedings of the Conference of Applied Differential Geometry-General Relativity and the Workshop on Global Analysis Balkan Society of Geometers. Differential Geometry and Lie Algebras, Balkan Society of Geometers, 2000, 117–125.

[15] Sachs R. K. and Wu H., General Relativity for Mathematicians. Springer Verlag, N.Y., 1977.

[16] Thorpe J. A., Elementary Topics in Differential Geometry. SpringerVerlag, Berlin, 1979, pp. 45-52.

[17] Uçar A., Karakuş F., and Yaylı Y., "Generalized Fermi-Walker derivative and non-rotating frame," Int. Journal of Geometric Methods in Modern Physics, 14(09), (2017), 1750131-1750141, Doi: 10.1142/S0219887817501316.

[18] Uçar, A. "Genelleştirilmiş Fermi-Walker türevi ve geometrik uygulamaları," Ph. D. thesis, Sinop University, Sinop, Turkey, (2019).

[19] Walker A. G., Relative co-ordinates. Proc. Royal Soc. Edinburgh, 52 (1932) 345-353.

[20] Weinberg S., Gravitation and Cosmology. J. Wiley Publ., N.Y, 1972.